Development of New Materials and Methods for Dye Sensitized and Perovskite Solar Cells

A dissertation submitted in partial fulfilment of requirements for the degree of

Doctor of Philosophy

by

Mohammad Adil Afroz

Roll No. 136122028

Department of Chemistry

Indian Institute of Technology Guwahati

Guwahati-781039, Assam, India

January 2020

Abstract

A number of sources have been discovered and techniques developed in pursuit of renewable energy to overcome the energy crisis and reduce carbon foot print. Solar energy is considered as the most sustainable renewable energy source owing to the large amount of energy supply from the sun to the earth. Among photovoltaic technologies, dye-sensitized solar cells and perovskite solar cells are very attractive due to their lower production cost and easy fabrication. Dye-sensitizer is a key component in dye-sensitized solar cells and it has a similar role as the chlorophyll in plants. It harvests the sunlight and transfer the energy via electron transfer to an appropriate material (TiO_2 in this case) for the production of electricity. With the aim to further enhance the conversion of sunlight to electricity, perovskite solar cells have been developed from dye-sensitized solar cells by replacing the sensitizer with perovskite materials having comparatively better charge transport properties. These solar cell devices fabricated with cheap and abundant materials seems a significant contributor to commercial photovoltaic technology in the near future.

This thesis is broadly organized into two parts. The first part focuses on the development of new sensitizers using several strategies to further advance the performance of dye-sensitized solar cells. The second part covers regulation of crystallization and trap states in perovskite through additive engineering to achieve high efficiency, stability and reproducibility of perovskite solar cells. Firstly, with the aim to achieve high efficiency in the dye-sensitized solar cells and understand the structure property relationship, a series of organic dyes having a carbazole donor, cyanoacrylic acid as an acceptor, and phenylene ring as a spacer with the difference in the positions and number of fluorine substitution were synthesized. The study revealed that fluorine substitution leads to a red shift in the absorption spectra of the dyes and reduces the band gap. As a result, the dye MA1F-o with *o*-fluoro substitution outperformed other dyes with a power conversion efficiency of 4.02%. Subsequently, to study and control the aggregation effect of sensitizers, mono- and di-anchor dyes having carbazole donor were synthesized. The results demonstrated that the presence of two acceptor groups provide efficient electron extraction from carbazole donor, reduces dye aggregation, and improves charge transfer. Therefore, an attractive power conversion efficiency of 5.35% was observed for di-anchor dye with iodide based redox electrolyte. A comparatively lesser efficiency was achieved in solid state dye sensitized solar cell.

Later, with the objective to regulate the crystallization process that could provide smooth perovskite films with large grains, Lewis acid-base adduct formation approach in concurrence with hot casting technique was employed. Uniform films of $MAPbCl_xI_{3-x}$ having large grain size were formed reproducibly on addition of 1.5 equivalents of dimethyl sulfoxide to the precursor solution. Perovskite solar cells fabricated using this solution resulted in power conversion efficiency of 14.11% with enhanced stability. Following this work, oxalic acid was used as additive in perovskite solution to regulate the crystallization, minimize ion migration and charge recombination in perovskite solar cells. As a result, 17.12% power conversion efficiency was obtained. Finally, benzene carboxylic acid derivatives (benzoic, isophthalic, and trimesic acids) were utilized to simultaneously control crystallization kinetics and passivate trap states in perovskite film resulting in maximum power conversion efficiency of 18.08%.

The efforts made in this thesis highlights the usefulness of molecular engineering of sensitizers as well as additive engineering of perovskites and provides the basis for facilitating the commercialization of dye sensitized and perovskite solar cells in the near future.

Dedicated to my parents

Statement

I do hereby declare that the work incorporated in this thesis entitled, "**Development of New Materials and Methods for Dye Sensitized and Perovskite Solar Cells**" is the result of investigations carried out by me under the guidance of Prof. Parameswar Krishnan Iyer, at the Department of Chemistry, Indian Institute of Technology Guwahati, Guwahati, Assam, India.

In keeping with the general practice of reporting scientific observations, due acknowledgements have been made wherever the work described is based on the findings of other investigators. I further declare that this work has not been submitted in part or full to any other university or institute for award of any degree or diploma.

IIT Guwahati **Mohammad Adil Afroz**

January 2020

Certificate

This is to certify that the work included in this thesis entitled "**Development of New Materials and Methods for Dye Sensitized and Perovskite Solar Cells**" by Mr. Mohammad Adil Afroz, Department of Chemistry, Indian Institute of Technology Guwahati has been carried out under my supervision. I further certify that this work has not been submitted to any other University or Institution in part or full for the award of any degree or diploma.

IIT Guwahati

January 2020

Parameswar Krishnan Iyer

Thesis supervisor

Department of Chemistry

Indian Institute of Technology Guwahati

Guwahati – 781039, Assam, India

Acknowledgements

I feel pleased to express my sincere appreciation and gratitude to those who have contributed to this thesis and supported me in one way or the other during this truly memorable and overwhelming journey. It is really hard to list all who sincerely helped me, and I would like to thank all of them who have made this thesis possible.

First of all, I am extremely grateful to my supervisor Prof. Parameswar K. Iyer for providing me a precious opportunity to work in his group. His continuous support, scientific guidance, deep insights, patience and motivation encouraged me to take up the tasks that otherwise were hard and demanding. I earnestly thank him for having trust in me and giving me total freedom in choosing the direction of my research. I feel fortunate to having him as my mentor who always motivated me with his hard work, dedication and optimism.

Besides my supervisor, I am highly indebted to my doctoral committee members, Prof. Mohammad Qureshi, Prof. Aditya Narayan Panda, Prof. Subhendu Sekhar Bag, Dr. D. Pamu and Dr. Akshai Kumar A. S. for assessing my research work regularly. Their insightful advices, suggestions and crucial comments helped me to widen my research from various perspectives and improve my thesis.

The completion of this thesis became possible only with the help of my collaborators, who had provided strong support and guidance along with lab facilities. I sincerely thank my collaborators, Dr. Saurabh S. Soni, Dr. Keval K. Sonigara and Dr. Jayraj V. Vaghasiya, Sardar Patel University, Gujarat, India for their continuous help and support. My sincere thank also goes to Dr. Arun Tej M., department of EEE, IIT Guwahati. I found him available whenever I was having a query related to the charge transport kinetics of solar cell devices.

I am also thankful to all the researchers and the staff of the Department of chemistry, center for nanotechnology, central instrument facility, IIT Guwahati for their kind cooperation and support. I am indebted to the staff of student affairs, academic affairs and finance sections of IIT Guwahati for being kind enough to advise and help in their respective roles.

Without a modicum of doubt, my research team deserve the best and utmost respect for their hard work, diligence and indispensable input into the overall research work. I would like to thank Bhim bhaiya, Ritesh, Rabindra, and Mamiur.

I would like to thank all my past and present lab mates Muthu da, Subbarao bhaiya, Priyanka mam, Himani di, Jupitara mam, Ekta di, Radha bhaiya, Bhim bhaiya, Suresh bhaiya, Anamika mam, Ashish bhaiya, Sameer, Akhtar, Arvin, Sayan, Dipjyoti, Anamika, Gopi, Niranjan, Rahul, Raman, Indrani, Subrata, Ramesh ji, Maimur, Debasish, Rabindra, Nehal, Ritesh, Retwik, Anwesha, Nasima, Biki, Anita, Kavita, Rajdikshit, Paromita, Muzaffer bhai, Tamal, Priyam, Debika and Dibash for their timely help and support. I would also like to thank them for creating a pleasant and vibrant laboratory atmosphere and making my days memorable. I especially thank Bhim bhaiya and Ashish bhaiya for sharing their enormously broad knowledge and showing endless patience. They taught me all the basics, experiments and techniques that were needed.

I extend my sincere thanks to my friends Tariq, Firoz, Ahmad, Usman, Osama, Sajjad, Saquib, Masih, Mobaid, Junaid, Ron, Sauraj, Abhishek, Nilesh, Vignesh, Anil, Reshu, Jyoti, Anzar, Sabera di, Afsana di, Randeep, Kamal, Joydeep, Gattu, Chandan, Mustakim, Anjali, Renu and other friends for their constant unfailing support, their encouragement and all the help they extended whenever required.

My sincere thanks to Dr. Sameer Hussain, Dr. Wajid Ali, Dr. M Shaad Ansari, Dr. Randeep Singh, Mahboob Alam for their brotherly caring nature, sharing all kinds of moments and helping to improve my thinking approach.

I sincerely express my gratitude towards entire fraternity from my school and university especially Mr. Neyaz Sir, Mr. T. Ali Sir, Dr. Mohammad Shahid Sir and Prof. Suhail Sabir Sir for imbibing good values and knowledge in me.

A special thanks to all my seniors and juniors from AMU; Palash da, Ajaz bhai, Sameer, Akhtar, Sahnawaz, Wajid, Kripa, Zia bhai, Faheem bhai, Shaad, Kafeel, Tasleem, Mahboob bhai, Maimur, Adil Rather, Tarique bhai, Akhtar Alam, Munendra, Suhaib, Shavez, Nehal, Saghir, Tipu, Altaf, Tarik and Masud for giving me unforgettable moments and delightful experiences. I will specially miss the memorable moments shared with Sameer, Wajid bhai, Shaad, Akhtar, Kafeel and Suhaib during my stay at IIT Guwahati.

I am thankful to Department of Science and Technology (DST) and The Indo-US Science and Technology Forum (IUSSTF) for providing me an opportunity to work at South Dakota State University (SDSU), in the United States of America through Bhaskara Advanced Solar Energy (BASE) fellowship 2018 to carry out an internship of six months (April 2018 – September 2018). I am grateful to Prof. Qiquan Qiao for hosting me in his

group at Department of Electrical Engineering (EECS), Center for Advanced Photovoltaics, South Dakota State University (SDSU) to pursue the internship. I would also like to thank the group members and staff at EECS, SDSU for their help and encouragement. I will never forget the time spent at SDSU with my friends Shamiq, Nabin, Dr. Mahesh, Reza, Rajesh, Tawabur Rahman and Ashraful.

My Ph. D. endeavor could not have been completed without the endless love, support, tolerance and blessings from my family. I am fortunate and blessed enough to have such a caring and supportive parents. It is because of their prayers, sacrifice and struggle, I am able to live my dream to complete my higher education from a prestigious institute. I am also grateful to my sisters and brother for their eternal love, cooperation and emotional support which had immensely needed to complete this work.

Finally, I thank almighty Allah for giving me a great life, strength to chase my dreams, and being with me in all my failure and success!

Mohammad Adil Afroz

Table of Contents

Abbreviations

2D	Two-dimensional
3D	Three-dimensional
AC	Alternating current
AFM	Atomic force microscopy
Ag	Silver
AM	Air mass
BA	Benzoic acid
BCA	Benzene carboxylic acid
BMImI	1-butyl-3-methylimidazolium iodide
CB	Conduction band
CDCA	Chenodeoxycholic acid
CdS	Cadmium sulfide
CdSe	Cadmium selenide
CdTe	Cadmium teluride
CIGS	Cadmium Indium Gallium Sulfide
CPE	Constant phase element
CV	Cyclic voltammetry
DC	Direct current
DCA	Deoxycholic Acid
DCM	Dichloromethane
DFT	Density functional theory
DMF	N,N-dimethylformamide
DMSO	Dimethylsulfoxide
DOS	Density of state
DPV	Differential pulse voltametry
DSSC	Dye sensitizes solar cell
EIS	Electrochemical impedance spectroscopy
ETA	Extremely thin absorber
ETL	Electron transporting layer
eV	Electrovolt
FA	Formamidinium
FESEM	Field Emission Scanning Electron Microscope
FF	Fill factor
FTIR	Fourier-transform infrared spectroscopy
FTO	Fluorine-doped tin oxide, SnO2:F
GBL	Gamma butyrolactone
HOMO	Highest occupied molecular orbital
HRMS	High resolution mass spectrometry
HTL	Hole transporting layer
Hz	Heartz
ICT	Intramolecular charge transfer
IPCE	Incident Photon to Current Efficiency
ITA	Isophthalic acid
ITO	Tin-doped indium oxide
J_o	Exchange current density
LUMO	Lowest unoccupied molecular orbital
M	Molar
MA	Methylammonium

mA	milliampere
mg	milligram
mV	millivolt
mW	milliwatt
NBS	N-Bromosuccinimide
NiOx	Nickel oxide
NIR	Near infrared
nm	nanometer
NMR	Nuclear magnetic resonance
NREL	National renewable energy laboratory
ns	nanosecond
OA	Oxalic acid
OCVD	Open circuit voltage decay
OLED	Organic light emitting diode
PCBM	[6,6]-Phenyl-C61- methyl ester
PCE	Power conversion efficiency
PEDOT:PSS	Poly(3,4-ethylenedioxythiophene)-poly(styrenesulfonate)
PL	Photoluminescence
PSC	Perovskite solar cell
Pt	Platinum
RMS	Root mean square
Ru	Ruthenium
s	second
SEM	Scanning electron microscope
SSC	Steady state current
TA	Trimesic acid
TBP	4-Tert. butylpyridine
TCO	Transparent conducting oxide
TFT	Thin film transistor
THF	Tetrahydrofuran
TiO_2	Titanium dioxide
TMTA	Trimethylolpropanetriacrylate
TPC	Transient photocurrent
TPV	Transient photovoltage
TRPL	Time-resolved photoluminescence
UV-Vis	Ultraviolet visible
V	Volt
v/v	Volume/volume
X	Halogen
XRD	X-ray diffraction
ZnO	Zinc oxide
μm	micrometer
Ω	Ohm
$\Omega\ \square^{-1}$	Ohm per square

List of Figures

List of Figures in Appendices

List of Tables

List of Tables in Appendices

CHAPTER 1

Introduction

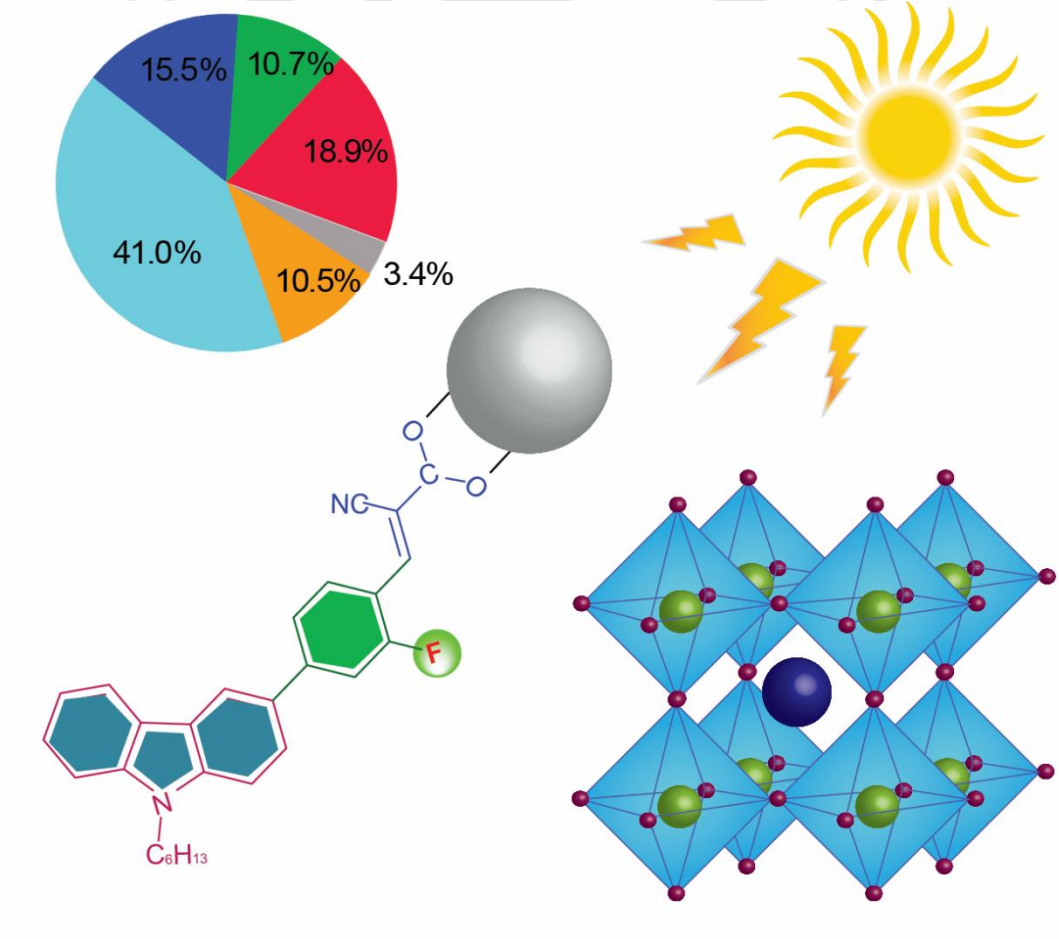

Abstract

Energy is one of the most important resources in this world. It is required for all our daily needs such as; for lighting, cooking food, and to improve the living standards. In addition, energy is required to power industrial machinery and transport. Fortunately, a wide range of energy resources are available in nature. The available natural resources are divided as primary and secondary energy. The fuels that provide energy without undergoing any conversion process are termed as primary, for example coal, natural gas and fuel wood. On the other hand, secondary energy like electricity and petrol is made from the processing of primary fuels. In the modern society, without a doubt, electricity is the leading source of energy. The available natural resources are also classified as non-renewable and renewable energy source. The nonrenewable energy sources such as coal, oil and gas are destroyed after use. The energy sources discovered relatively lately, such as wind, tidal and solar are considered as renewable. Therefore, they are sustainable, and are seems to play an increasingly significant role in the future to overcome energy requirements. The energy demand across the world including India is increasing continuously. The energy consumption used by a country indicates its level of development. India being a developing country, consumes more energy in activities such as manufacturing, transport and provision of services. Hence, this chapter discusses the need for the development of technologies to produce renewable and clean energy, especially solar energy followed by a brief explanation on dye sensitized and perovskite solar cells, and different measurement techniques of solar cells. Further an account on engineering of photosensitizer dye and perovskite materials is presented. Finally, the chapter end with a synopsis of this thesis.

1.1 Introduction

The increasing global need for energy arising from modern lifestyle based on extensive use of electronic and electrical equipment coupled with the depletion of easily accessible, hence cheap, fossil fuel reserves, poses a serious threat to the human global economy in the near future.[1] Considering, in addition, the harmful ecological impact of conventional energy sources leading to global warming and climate change, it becomes obvious that development of clean, efficient, and cost-effective alternative energy sources is a necessity.[2] Among the renewable energy sources available such as hydropower, wind, solar, biomass and geothermal, solar energy is the only sustainable source to fulfill energy requirements of growing population. The supply of energy from the sun to the earth is enormous, i.e., 3×10^{24} joule a year or about ten thousand times more than what mankind consumes currently. This means that only 0.1% of the earth's surface covered with solar cells with an efficiency of 10% would be sufficient to satisfy our current needs. Therefore, solar power is considered to be one of the best sustainable energies for future generations.[3] Current commercially available photovoltaic technologies are based on inorganic materials (monocrystalline and polycrystalline silicon used in wafer technology, and CdTe and CIGS for thin film technologies). However, their fabrication requires high costs and large amounts of energy. Many features of dye sensitized solar cells (DSSCs) and perovskite solar cells (PSCs) are unique and advantageous over the solar cells based on crystalline or amorphous silicon. Nearly all the components of these solar cells are "tunable", including the semiconducting electron transport layers (ETLs), the active layer (dyes and perovskites), the electrolytes/hole transporting layers (HTLs) and the counter electrode. Therefore, the dominance of the photovoltaic field by such kind of inorganic solid-state junction devices is now being challenged by the emergence of the third-generation solar cells based on interpenetrating network structures, such as dye-sensitized and perovskite solar cells. Dye-sensitized and perovskite solar cells have received intense interest due to their potential advantages like low production cost, easy fabrication, transparency, multi-color options, flexibility, light weight and short energy payback time. Transparency and multi-color design alone offer huge potential for the integration of DSSCs/PSCs as part of the building architecture.[1-2] On the contrary, the bulk heterojunction solar cells have not been demonstrated with reasonable efficiency suitable for practical device manufacturing. They suffer largely due to the limited number of n-type organic semiconductors available.

1.2 Dye Sensitized and Perovskite Solar Cells

The dye sensitized solar cell (DSSC) is a photoelectrochemical device containing a nanostructured mesoporous large bandgap semiconductor sensitized with a dye. First report on dye sensitization of the large band gap semiconductor can be found in the late 19th century. The photographic silver halide emulsion was sensitized by a dye in 1873 by Vogel, a German scientist, to extend its spectral sensitivity from UV to green.[4] The first dye sensitized photoelectrode was observed by Moser in 1887 when erythrosin dye was used on silver halide electrodes.[5] The phenomenon of photo-electrochemistry could be linked to photography in 1964 when Namba and Hishiki used same dye to demonstrate both the processes.[6] The involvement of charge transfer process rather than energy transfer from the dye to semiconductor could be established during sixties and seventies.[7-8] At that time, very low photocurrents were obtained as the monolayer of dye was poorly anchored (mostly physisorbed) on the planar surface and could absorb only small amount of light. The overall efficiency was enhanced to 1.5% under monochromatic irradiance at 563 nm by Tsubomura and coworkers by using porous ZnO with an enhanced surface area available for sensitization. Following this, incremental developments were accomplished in the chemisorption of dyes,[9-11] electrolyte redox chemistry and photoelectrode materials.[11-16] Many of the semiconductors like CdSe, CdS, GaP etc. were prone to photo corrosion, therefore, with the successful demonstration of photolysis of water with TiO_2, it became the prime choice.[17-18] All these improvements finally led to development of dye sensitized nanocrystalline solar cell in 1991, with a PCE of 7.1-7.9% under solar illumination.[19] The DSSCs have now achieved PCE of 14.3% (certified PCE of 11.9%) by different molecular engineering of dyes and device modifications.[20-21]

Solar cells using perovskite as light absorbing material have recently emerged from DSSCs.[22] The conventional DSSC with liquid electrolyte generally requires 10 μm thick TiO_2 layer to capture almost complete light in the absorbing region of the dye.[19] But they suffer from the leakage and drying of electrolyte. To solve this problem, solid-state DSSCs (ss-DSSCs) with solid hole transport layer/ electrolyte came into existence. Use of solid-state electrolyte limited the thickness of the TiO_2 layer to less than 2 μm because of a number of factors, such as poor infiltration of hole transport materials into the mesoporous structure and relatively fast charge recombination.[23] A solution to facilitate almost complete absorption of the incident light in thin films is to utilize sensitizers with high

molar absorption coefficient. The concept of extremely thin absorbers (ETA) based solar cells has been found to solve the limitation of thin mesoporous layers of TiO_2 up to some extent. Examples of ETA are CdTe and CdSe.[24] The motivation to find more advanced light absorbers as compared to dyes led Miyasaka and co-workers for the first time to report perovskite-sensitized solar cells between 2006 and 2008. They employed $CH_3NH_3PbI_3$ and $CH_3NH_3PbBr_3$ absorbers with either an iodide triiodide redox couple or a polypyrrole carbon black composite solid-state hole conductor and measured full sun power conversion efficiency varying between 0.4 and 2% for solid-state and liquid electrolyte cells, respectively.[25-26] The first peer-reviewed journal publication of a perovskite-sensitized solar cell came in 2009, where the $CH_3NH_3PbI_3$ absorber resulted in a 3.5% efficient sensitized solar cell employing the iodide/triiodide redox couple.[22] While investigating the charge-transport properties of the perovskite-sensitized solar cells, Snaith and co-worker noticed that the charge extraction rates were significantly faster for the perovskite-sensitized solar cell in comparison to conventional DSSCs. This could have been due to either the perovskite having an influence upon the surface states, and hence trap site density in the TiO_2, or a significant fraction of the long-range electron transport occurring through the perovskite phase itself. To confirm this, they constructed solar cells where the mesoporous TiO_2 was replaced with insulating mesoporous Al_2O_3, with a very similar meso-morphology. They found that not only was the charge transport faster and the photocurrent unaffected when the TiO_2 was replaced by the insulating Al_2O_3, but for a like-to-like comparison, the open-circuit voltage increased by 200 to 300 mV, leading very quickly to a 10.9% efficiency solar cell. This discovery also suggested that perovskite planar structures can also be used in a positive (p)−intrinsic (i)−negative (n) architecture.[27]

1.3 Device Architecture and Working Principle

1.3.1 Dye Sensitized Solar Cells

DSSC is typically composed of five major components (Figure 1.1), namely, (i) transparent conducting oxide (TCO), (ii) a mesoporous semiconductor metal oxide (such as TiO_2 or ZnO) film, (iii) a sensitizer, (iv) an electrolyte layer (I^-/I_3^- couple, Co(II)/Co(III) couple or Fc/Fc^+ couple), (v) counter electrode (platinum or carbon coated glass substrate). Five basic processes which occur during the operation of the DSSC are instrumental in governing the efficiency of the device. They are: (1) absorption of solar light by the dye

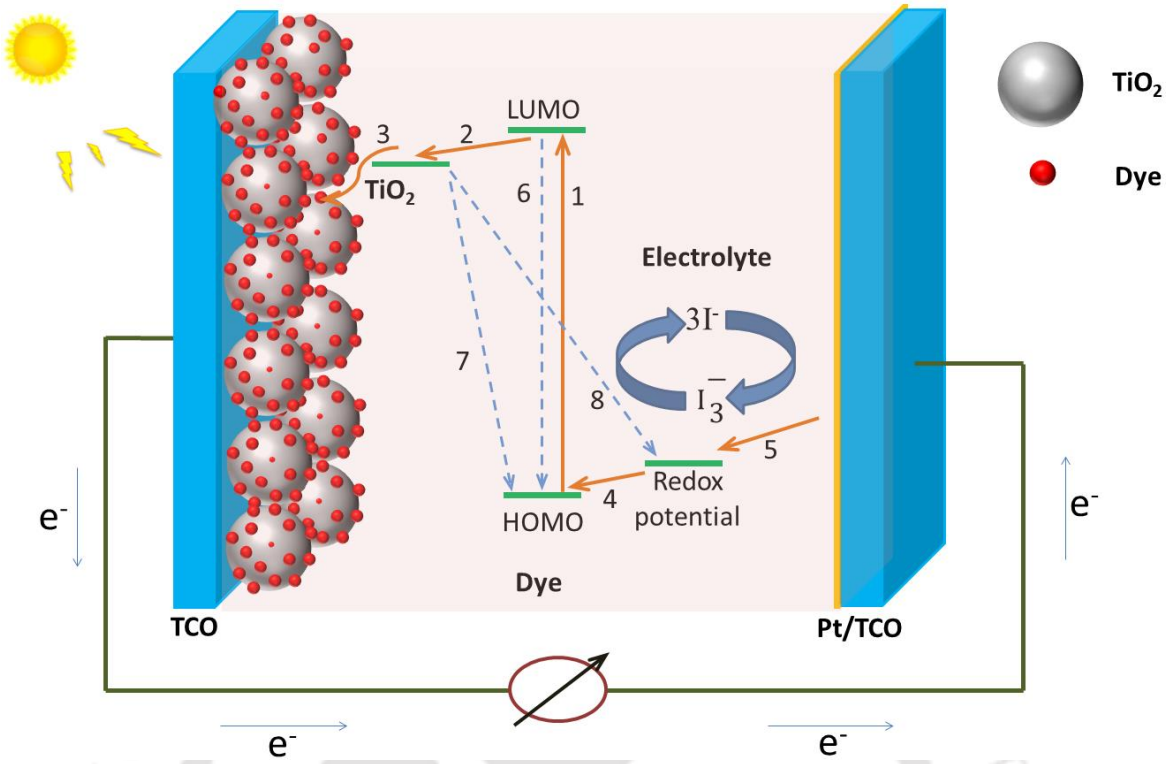

Figure 1.1: Schematic diagram showing different processes involved during the operation of a DSSC(idea of the illustration taken from reference 28).[28]

anchored on TiO_2, (2) injection of electrons into the conduction band (CB) of TiO_2, (3) charge collection at the anode, (4) reduction/regeneration of the oxidized dye by redox couple, (5) regeneration of redox couple by electron injection from cathode. The following three processes are detrimental for the efficiency of the DSSC (6) relaxation of the excited dye to ground state by non-radiative processes such as internal conversion, aggregation-induced quenching, etc., (7) recombination of electrons from the CB of TiO_2 with the oxidized dye, (8) recombination of electrons in CB of TiO_2 with the electrolyte.

1.3.2 Perovskite Solar Cells

The architecture of commonly used single junction perovskite solar cells can be classified into mesoscopic and planar heterojunction structure (Figure 1.2). The mesoscopic structure involves infiltration of perovskite into a mesoporous metal oxide scaffold.[27] On the other hand, taking advantage of ambipolar nature of perovskites, a planar configuration can also be afforded. The planar devices could have a regular (n-i-p)[29] or inverted (p-i-n)[30] configuration, depending on the selective contact (n-type or the p-type, respectively) used

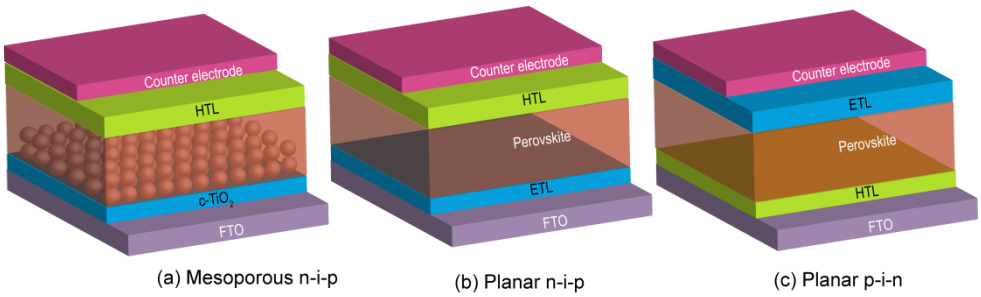

Figure 1.2: Device architectures of perovskite solar cells (a) mesoporous n-i-p, (b) planar (n–i–p) and (c) planar (p–i–n).

towards the transparent electrode. Similar to DSSC, typically a PSC is also composed of five layers, namely (1) transparent conducting oxide (TCO) (2) an electron transporting layer (ETL), (3) photoactive perovskite layer, (4) a hole transporting layer (HTL) and (5) the counter electrode/back contact.

The operation of both the planar as well as mesoscopic PSCs occurs through the same charge transfer mechanism. First electrons and holes are being generated following the photoexcitation of perovskite layer by sunlight (Figure 1.3). Then the generated electrons are injected into the conduction band or LUMO of ETL and the holes are transferred to the valence band or HOMO level of the hole transporting layer. These charges are then migrating to their respective electrodes. The injection of electrons and holes occur efficiently owing to the long diffusion lengths of charge carriers in perovskite solar cells. However, similar to DSSC, undesirable charge transfer process such as charge

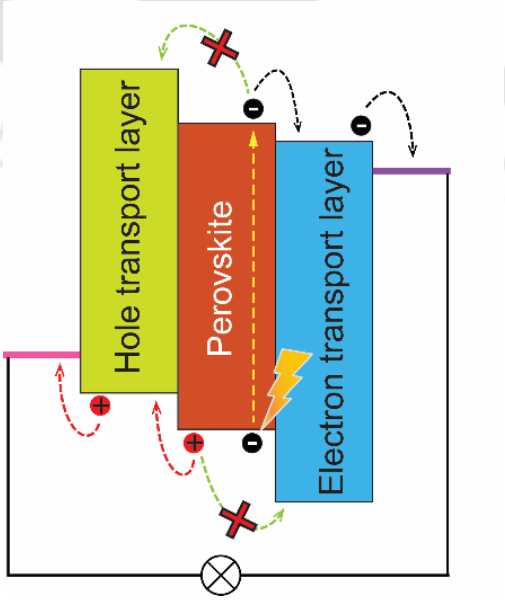

Figure 1.3: Schematic showing working principle of perovskite solar cells.

recombination occurs in PSCs also. These detrimental recombination processes may occur at the interfaces between different layers as well as at the grain boundaries of perovskite layer. Therefore, to reduce carrier recombination at the interfaces the ETL and HTL should be compact and perovskite films should have large grains.

1.4 Components of Typical Dye Sensitized and Perovskite Solar Cells

1.4.1 Working Electrode

The solar cell devices are generally fabricated over transparent conducting oxide (TCO) substrates, such as tin-doped indium oxide (ITO) or fluorine-doped tin oxide (SnO_2: F, FTO), which is coated on a plastic or glass substrate to provide electrical conductivity. The transparency of these substrates allows the sunlight to pass through it to the active layer while the electrical conductivity helps in charge transport. FTO substrate was used in all the studies performed in this thesis due to its relatively superior qualities over ITO. FTO substrate is recognized to have relatively better stability under atmospheric conditions. It is chemically inert, mechanically robust and shows resistance to high temperature. Moreover, it has high transparency, high abrasion resistance, low reflection and absorption as well as low cost.

1.4.2 Electron Transporting Material

The main role of electron transporting layer (ETL) is to extract and transport the photo-generated electrons. It also aligns the interfacial energy level and prevents recombination of photo-injected electrons in the conductive substrate with the holes. The mesoporous TiO_2 (m-TiO_2) has been used as ETL for the fabrication of DSSCs. The ETL layer that also acts as hole blocking layer was deposited on the TCO substrate using doctor blade technique from a TiO_2 paste. It is well known that the m-TiO_2 provides high surface area for enhanced dye loading and improved electron injection. It also improves the external quantum efficiency of DSSCs.[31-32] [6,6]-Phenyl-C61- methyl ester (PCBM) has been utilized as ETL for PSC fabrication as it is the most widely used ETL in inverted PSCs.[33]

1.4.3 Active Layer

The photoactive layer of a solar cell is the key component which absorbs the light and starts the whole process of electricity generation. New dyes were developed to fabricate DSSCs and their materials property relationships were examined. The performance of

DSSCs was improved by tuning the optical and electrochemical properties of the dyes through molecular engineering. Similarly, quality of perovskite layer was also enhanced through chemical additives utilizing Lewis acid base interaction. The perovskite layer was then used to fabricate PSCs with high performance and stability. The details of material design strategy will be discussed in section 1.6.

1.4.4 Hole Transporting Materials/Electrolyte

The main function of electrolyte is to regenerate the photo-excited dye/sensitizer.[34] An electrolyte usually consists of a redox mediator such as iodide/tri-iodide (I^-/I_3^-) or Cobalt (II/III) in an organic solvent. Through an oxidation reduction reaction, the electrolyte takes electron from counter electrode and regenerates the dye. These electrolytes are generally used with some additives like tert-butyl pyridine (TBP), chenodeoxycholic acid and guanidium thiocyanate (GuSCN) etc. for optimum performance. The hole transporting layer (HTL) is used in PSCs to collect the holes and transport to the anode. Additionally, it blocks the electrons to recombine with holes present in the anode. The HTL should have high mobility value, ideally higher than 10^{-3} cm^2 $(V \times s)^{-1}$.[35] Poly(3,4-ethylenedioxythiophene)-poly(styrenesulfonate) (PEDOT:PSS) was used as HTL for first two works on perovskite solar cells (Chapter 4 and 5). However, to further reduce the cost and improve the performance and stability of PSC, Nickel oxide (NiOx) was used as HTL for the last work (Chapter 6).

1.4.5 Counter Electrode/Back Contact

Counter electrode completes the internal circuit and work as an electrode that provides voltage and current for the external electrical work. Generally, counter electrode of DSSC is formed by thin layer of platinum (Pt) coated on an FTO or ITO and catalyze the redox reaction of electrolyte. However, metal sulfides, carbon-based materials (graphene composites) etc. can also be utilized as an alternative to Pt. The back contact of PSCs is commonly made by thermal evaporation of a metal such as aluminum, silver, or gold etc. The metal should have high work function to achieve high open circuit voltage for the devices.

The above listed components are basic constituents of a dye sensitized and perovskite solar cells that are commonly used. Some additional layers may also be used to further enhance the performance and/or stability of a device. Owing to poor stability of PSCs, they need to be encapsulated for operation under ambient conditions.

1.5 Device Measurements

1.5.1 *J-V* Characterization

The current density-voltage (*J-V*) measurement is one of the most important techniques that enables the determination of PCE of a solar cell. The *J-V* measurements are performed by illuminating the solar cell under standard AM 1.5G illumination (1 Sun illumination). The current density is recorded by linearly sweeping the voltage across electrodes to provide *J-V* curve as shown in Figure 1.4(a). Following parameters are extracted from the *J-V* curves:

Short circuit current density (Jsc)

The short circuit current density is obtained from the *J-V* curve at short circuit condition that is when there is no photo-voltage (at zero volts). The *J*sc value depends on the absorption properties and bandgap of dye or perovskite layer, charge transportation and collection in the complete device. *J*sc is the maximum current generated in a solar cell (Figure 1.4(a)).

Open circuit voltage (Voc)

The open circuit voltage is determined as the potential in the open circuit condition that is when no current flows in the circuit. It mainly depends on the built-in potential and the band positions of active layer. It is the maximum voltage obtained in a solar cell (Figure 1.4(a,b)).

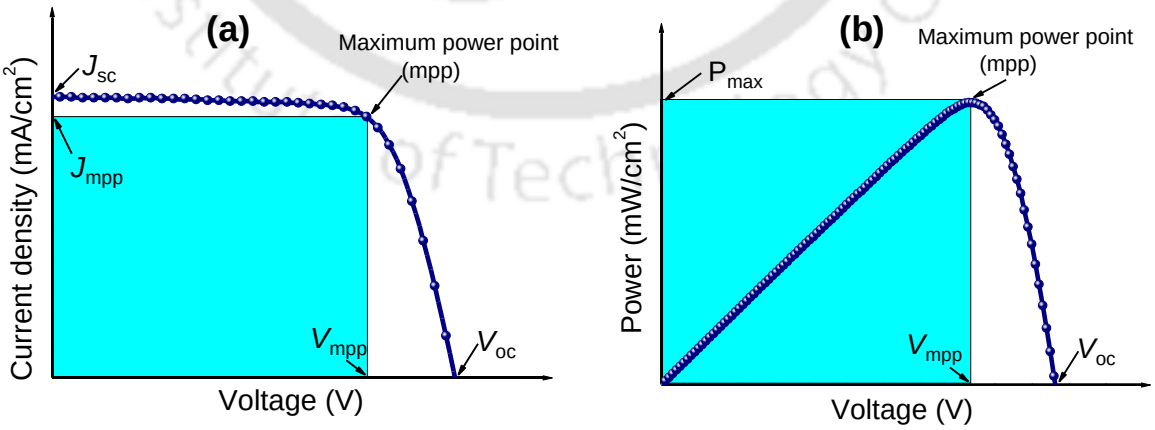

Figure 1.4: A typical example of (a) *J-V* curve and (b) power output versus voltage curve recorded under light illumination.

Power conversion efficiency (PCE, η)

The overall power conversion efficiency of a solar cell is defined as the ratio of maximum power extracted from solar cell to the power of incident light (P_{in}) and can be expressed as equation 1.1:

$$PCE\ (\eta) = \frac{P_{max}}{P_{in}} = J_{sc}V_{oc}\mathrm{FF}P_{in} \qquad (1.1)$$

The value of maximum power (P_{max}) can be found from the product of photocurrent and voltage at its maxima (J_{mpp} x V_{mpp}) as illustrated in Figure 1.4(b). The *J-V* curve of PSCs often depends on the scan direction resulting in hysteresis behavior.[36] Therefore, the scan direction (*V*oc to *J*sc or *J*sc to *V*oc sweep of voltage) and the scan rate are important for obtaining reliable photovoltaic parameters.

Fill factor (FF)

Fill factor is a parameter which is used to evaluate the deviation of real solar cell sample efficiency from the maximum power output estimated theoretically. High value of FF indicates good quality of solar cells. The FF of a solar cell can be calculated using equation 1.2.

$$FF = \frac{J_{mpp}V_{mpp}}{J_{sc}V_{oc}} \qquad (1.2)$$

1.5.2 Incident Photon to Current Efficiency (IPCE)

Incident photon to current efficiency is a parameter which determines how efficiently the incoming photons are converted into electrons by the PSC. It is usually measured to confirm the reliability of *J*sc obtained from *J-V* characterization. The IPCE spectrum (Figure 1.5) is obtained by recording the photocurrent response of PSC by applying monochromatic light with continuously varying the wavelength of the excitation light. IPCE is the ratio of charge carriers collected from a solar cell to the number of photons shining over the cell and is calculated utilizing equation 1.3.

$$IPCE(\lambda) = \frac{n_{electrons}(\lambda)}{n_{photons}(\lambda)} = \frac{J_{sc}(\lambda)/q}{P_{in}/hf} = \frac{h\nu}{q\lambda} \times \frac{J_{sc}(\lambda)}{P_{in}} = \frac{1240}{\lambda} \times \frac{J_{sc}(\lambda)}{P_{in}} \qquad (1.3)$$

Where, $n_{electrons}$ & $n_{photons}$ are number of electrons & photons, respectively. *J*sc is photocurrent density in mA cm^{-2}, q stands for an elementary charge, P_{in} is the power of incident light (mW cm^{-2}), h is the Planck's constant, f is the frequency of light in vacuum (Hz), υ is the speed of light in vacuum (nm s^{-1}) and λ is the wavelength of incident light

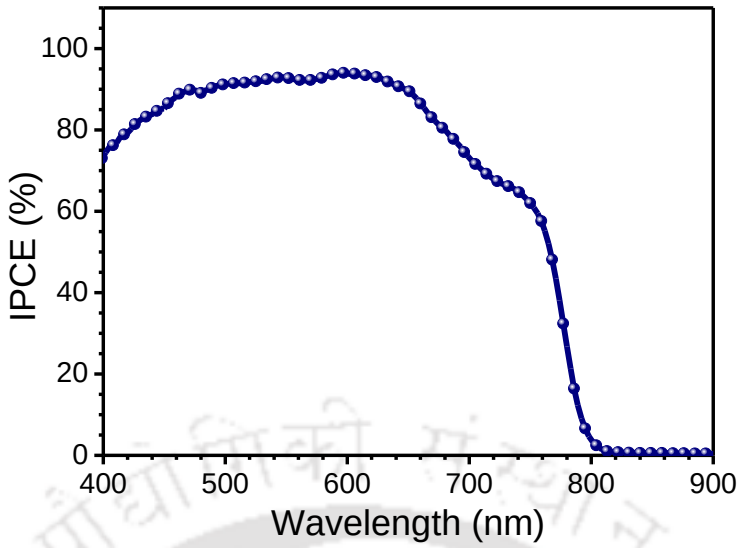

Figure 1.5: A typical IPCE spectrum of a perovskite solar cell.

(nm). The expected short-circuit photocurrent density that is to be generated by the solar cell is calculated by integrating the product of IPCE and *J*sc (λ) over the wavelength of the incoming light.

1.5.3 Impedance Spectroscopy Measurements

Impedance spectroscopy is a useful technique to track charge transport and kinetics of different process involved in a solar cell.[37-38] The impedance spectroscopic measurement of DSSC and PSCs is performed, generally, in the frequency range of 1 Hz–1 MHz with sinusoidal voltage amplitude of 10 mV in dark condition. The impedance data can be represented in the form of either Bode plot or Nyquist plot. By fitting the impedance spectrum, many parameters such as sheet resistance, shunt resistance, capacitance, and density of trap states can be estimated.

1.6 Engineering Dye-sensitizer and Perovskite Layer

Dye or photosensitizer is one of the crucial parts of a DSSC and for achieving high performance of the device it should accomplish some essential features:

(1) It should have strong absorption means high molar absorption coefficient and panchromatic absorption covering whole visible region and even the part of the near-infrared (NIR).

(2) It should possess anchoring group, such as –COOH, –SO_3H, –H_2PO_3, etc. for strong binding onto the semiconductor surface.

(3) The LUMO energy level of the photosensitizer should be higher than the conduction band edge of n-type semiconductor in case of n-type DSSC. Whereas, the HOMO energy level of the photosensitizer should be lower than the valence band level of p-type semiconductor so that an efficient charge transfer can take place between the excited dye and the semiconductor.

(4) The photosensitizer must have its oxidized state level more positive than the redox potential of electrolyte for dye regeneration.

(5) Dye aggregation on the semiconductor surface, which is an unfavorable process, should be avoided through molecular structure designing of the dye or by coadsorbers addition that prevent aggregation.

(6) The photosensitizer should have good photostability along with good electrochemical and thermal stability.

Many photosensitizers have been designed based on the above criteria and applied to DSSCs in the past two decades. These dyes are broadly categorized into metal complexes and metal-free organic sensitizers. Metal complex such as zinc porphyrin[39-40] and ruthenium polypyridine[41-42] complexes are the photosensitizers with the best performance in terms of the efficiency and stability. However, the problem associated with ruthenium dyes is the metal toxicity, high cost and inadequate resource availability, whereas zinc porphyrin dyes have limited yields and involve poisonous chemicals during the synthesis. On the other hand, metal-free organic dyes are attracting researchers attention owing to the advantage of abundant raw materials, high molar absorption coefficient, flexible molecular modification, and relatively low cost.[43] Most of the organic sensitizers consist of a push–pull combination of a donor (D) and an acceptor (A) linked with a π-spacer. This design of photosensitizer enhances intra-molecular charge transfer (ICT) and results in broad absorption to effectively harvest sunlight.[44] The properties of D–π–A sensitizers can be easily regulated by selecting different combinations of the constituents (i.e. D, π and A) and different substitutions.[45-47]

Though several chromophores such as triarylamine[43], coumarin[48], fluorene[49], phenothiazine [50], benzothiadiazole [51], benzotriazole[52], indoline[53], etc., have been used in the assembly of organic dyes, carbazole-based organic materials are exceptionally

interesting due to their promising properties such as relatively low oxidation potentials, thermal and photo-stability and hole-conducting capabilities.[54] Moreover, a variety of nuclear positions available for functionalization expand the scope and utility of carbazole-derived materials. Carbazole containing molecular materials have been successfully demonstrated for application as hole-transporting emitters in organic light-emitting diodes (OLED),[55] organic semiconductor in thin-film transistors (TFT)[56] and electron donors in photovoltaics.[57] The first report on the use of carbazole-based organic dyes came in 2006 and was authored by Koumura and co-workers (D1-D3, Figure 1.6).[58] Several dyes featuring carbazole as either donor or π-linker have been synthesized and demonstrated as sensitizers in DSSC (Chemical structure of some representative dyes are presented in Figure 1.6). Efforts to improve open circuit voltage was made by Teng and co-workers.[59] They developed two new dyes (D4-D5) where carbazole was used as donor linked to its nitrogen atom and applied in a DSSC with Br^-/Br_3^- redox couple. The dyes were designed in a manner to have more positive oxidation potentials than Br^-/Br_3^-. Another dye was developed with alkoxysilyl anchoring group to afford open-circuit photovoltages higher than 1 V with $Co^{3+/2+}$-complex redox electrolyte. It was found that dye with alkoxysilyl anchor (D6) have robust linkage with TiO_2 compared to the –COOH group (D7, D8).[60] Two series of symmetrical acceptor–donor–acceptor sensitizers (D9-D14) with two cyanoacrylic acid anchoring terminals were developed. One series was containing 3,6-functionalized carbazole cores whereas the second series had 2,7-functionalized carbazole. The effect of molecular planarity was investigated and it was found that the non-planar carbazole dye with 3,6-substitution gave better performance in DSSC. The enhancement in the performance was attributed to the suppression of π–π stacking, superior binding with TiO_2 and relatively higher dye loadings.[61] D–π–A dyes based on carbazole with cyanoacrylic acid (D15) and rhodanine-3-acetic acid (D16) as anchoring groups were designed and their performance was compared. D15 showed better performance compared to the D16 owing to better electron injection to the CB of TiO_2 and lower recombination between the injected electrons from the dye with the oxidized electrolyte. Also, LUMO of D16 dye has better orbital overlap with the conduction band of TiO_2.[62] Dyes with twisted donors were developed (D17, D18) to block electrolyte from reaching TiO_2 surface and reduce recombination reactions. The influence of carbazole (Cz) and triphenylaime (NPh_3)

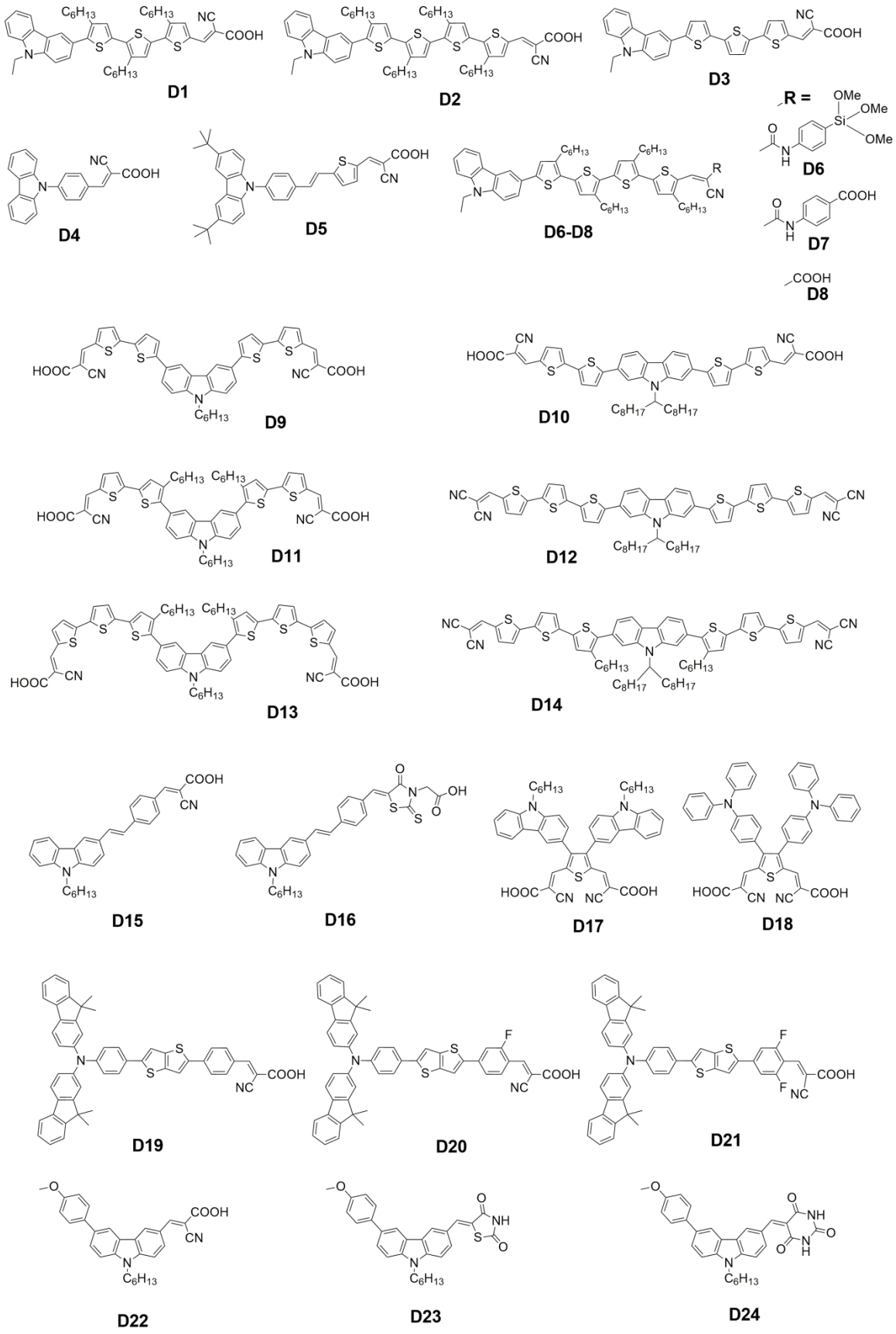

Figure 1.6: Chemical structure of carbazole based dyes utilized in DSSCs.

unit substitution at 3,4-position of thiophene was studied and it was observed that the dye aggregation and charge recombination gets retarded.[63] Aimed to achieve efficient dye-sensitized solar cells (DSSCs), D-π-A organic dyes with tailored energy levels were obtained through fluorination of their acceptor units. One or two fluorine atoms were incorporated at the *ortho*-positions of the cyanoacetic acid as additional acceptor units (D19-D21). The LUMO energy level of the organic dye was gradually lowered as the number of fluorine atoms increased owing to the electron-withdrawing nature of fluorine, which ultimately resulted in a gradual reduction of band gap and improved spectral response.[64] Another report presented three D-D-π-A type dyes that comprised of carbazole as donor, 4-methoxyphenyl group as auxiliary donor and three different acceptors/anchoring units, viz. cyanoacetic acid (D22), 2,4-thiazolidinedione (D23) and barbituric acid(D24). Here also, the dye carrying strong cyanoacetic acid moiety showcased highest PCE compared to other anchoring groups containing dyes.[65]

Perovskites are the series of materials having general formula ABX_3, where A and B are cations (size of A is larger than B) and X is an anion. The cell structure of perovskite has cubic geometry and consists of a backbone of corner-sharing octahedral formed by X atoms with B atom at the center and cuboctahedra voids occupied by the A-cations (Figure 1.7). Usually, it forms three-dimensional networks of cells. There is a large class of perovskite compounds out of which the methylammonium lead iodide, $CH_3NH_3PbI_3$ (or $MAPbI_3$), has been most extensively investigated and can, therefore, be seen as a standard perovskite and a model compound. Still, there is a possibility to change cations and anions and accordingly, their optoelectronic properties can be tuned. The major advantages of

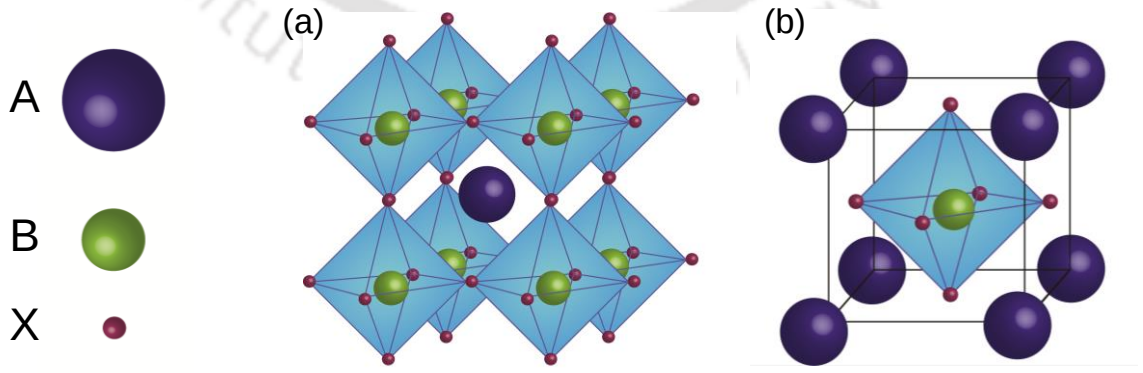

Figure 1.7: Scheme of perovskite crystal unit cell (a) A-cation centered and (b) B-cation centered.

these three-dimensional perovskite materials are its ease of fabrication, strong solar absorption, high carrier mobility, long-lived charge carriers and low non-radiative carrier recombination rate.[66] However, the negative aspect of perovskites is that the precursors of perovskite contain lead, raising the toxicity issues. Nevertheless, the even greater issue associated with perovskite is extreme moisture sensitivity due to which they tend to hydrolyze, undergoing irreversible degradation and decomposing back to its precursors. It is also sensitive to ultraviolet light and thermal stress. The degradation is catalyzed in the presence of heat, light and moisture.[67] The qualities of perovskite film crystallinity, morphology and defect density significantly impact the PSC performance and depend on the fabrication conditions. Rapid improvement in the performance of PSCs has been achieved through development of new methods for perovskite preparation.[29,68-71] The additive engineering is a widely used method among them, and involved in various breakthroughs of PSCs. Additives are efficient in modulating the morphology, stabilizing the perovskite phase, adjusting energy level alignment, suppressing non-radiative recombination, eliminating hysteresis, and enhancing operational stability. A representative list of additives utilized to improve the performance and stability of PSCs is presented in Table 1.1.

The morphology, which refers to coverage, uniformity, roughness and determined usually by the texture, grain size, and pinholes in films can be modulated with additives. Some molecular additives, such as methylamine or DMSO can form intermediate with the perovskite precursor and result in improved morphology through crystallization control. DMSO, which is a high polarity solvent, was usually applied to dissolve perovskite precursor for the formation of halide perovskites. DMSO could form complex with MAI and PbI_2[72] and regulate the morphology of perovskite film to result in high efficiency PSC. A mixed solvent system of γ-butyrolactone (GBL) and DMSO was developed through solvent engineering to prepare uniform, high quality perovskite film. This resulted in high performance PSCs with a certified PCE of 16.2%.[69] The improvement in the morphology was ascribed to the formation of CH_3NH_3I–PbI_2–DMSO intermediate phase. Use of chloride additives in the form of $PbCl_2$ or MACl into the precursor solution resulted in formation of $MAPbCl_3$ perovskite due to their lower solubility.[73] Upon annealing, iodide-based perovskite with improved morphology was formed due to chloride volatilization from the film.[74] Chloride additives were used along with antisolvent method or sequential deposition for record efficiency of 23.3% and 22.7%, respectively.[71,75] Very recently,

Table 1.1: A representative list of additives utilized to improve the performance and stability of PSCs

Additive	Structure	Device configuration	The role of additive			Perovskite material	Efficiency %	Year/Reference
			Film formation	Passivation	Stability (test conditions/ retained PCE)			
Dimethylsulfoxide (DMSO)		FTO/bl-TiO_2/mp-TiO_2/Perovskite/spiro-MeOTAD/Ag	Solvent and morphology controller	-	-	$MAPbI_3$	19.7	(2015)/[72]
Methylammonium Chloride (MACl)	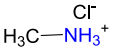	ITO/Y-TiO_2/Perovskite/spiro-OMeTAD/Au	Morphology and phase purity controller	-	devices stored in dry air without encapsulation /~98% after216 h	$MAPbI_3$	17.91	(2015)/[76]
Lead chloride	$PbCl_2$	ITO/PEDOT:PSS/perovskite/PC61BM/PFN/Ag	Morphology controller	-	stored in a glovebox without encapsulation /75% after 3 months	$MAPbI_3$	14.91	(2015)/[77]
Poly(methyl methacrylate) (PMMA)	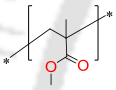	FTO/c-In-TiO_x/m-TiO_2/PMMA:PCBM/perovskite/PMMA/Spiro-OMeTAD/Au	-	Surface defects	-	$Cs_{0.07}Rb_{0.03}FA_{0.765}MA_{0.135}PbI_{2.55}Br_{0.45}$	≈20.8	(2018)/[78]
(Iodopentafluorobenzene) IPFB	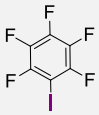	FTO/c-TiO_2/mp-Al_2O_3/perovskite/Spiro-OMeTAD/silver	-	Surface defects	-	$MAPbI_{3-x}Cl_x$	15.7	(2014)/[79]
Thiophene		FTO/c-TiO_2/perovskite/spiro-OMeTAD/gold	-	Surface defects	-	$MAPbI_{3-x}Cl_x$	15.3	(2014)/[80]
Pyridine		FTO/c-TiO_2/perovskite/spiro-OMeTAD/gold	-	Surface defects	-	$MAPbI_{3-x}Cl_x$	16.5	(2014)/[80]
trimethylolpropane triacrylate (TMTA)	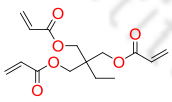	ITO/P_3CT-N/perovskite/PCBM/C_{60}/BCP/Cu	-	Surface defect	storing the non-encapsulated devices on a hot plate setting at 85 °C in glovebox/~80 % after 11h	$MAPbI_3$	19.2	(2018)/[81]
Benzylamine	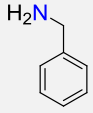	FTO/TiO_2/Perovskite/spiroMeOTAD/Au	-	Surface defects	Shelf life test, in air at 55 ± 5% RH in the dark, > 50% after 2900 h	$FAPbI_3$	19.2	(2016)/[82]
Pyrazine		FTO/bl-TiO_2/mp-TiO_2/Perovskite/spiro-MeOTAD/Au	Morphology Controller	-	Shelf life test, encapsulated cells stored in the dark under ambient condition, > 98% after 100 d	$FASnI_3$	4.80	(2016)/[83]

Table 1.1 continued…..

Additive	Structure	Device configuration	The role of additive			Perovskite material	Efficiency %	Year/Reference
			Film formation	Passivation	Stability (test conditions/ retained PCE)			
PCDTBT	See Figure 1.8	ITO/PEDOT:PSS/Perovskite/PCBM/BPhen/Ag	Morphology controller	Bulk defects	Shelf life test, unencapsulated cells stored in ambient atmosphere (RH 30%, 28 °C), > 80% after 192 h	$MAPbI_{3-x}Cl_x$	14.62	(2017)/[84]
2-Pyridylthiourea		FTO/bl-TiO_2/mp-TiO_2/Perovskite/spiro-MeOTAD/Au	Morphology controller	Bulk and surface defects	Shelf life test, under ambient air of 55 ± 5% RH in the dark and under 65 °C, > 90% after 30 d	$MAPbI_3$	18.2	(2017)/[85]
Nitrogen doped reduced graphene oxide (N-RGO)	See Figure 1.8	FTO/bl-TiO_2/mp-TiO_2/Perovskite/spiro-OMeTAD/Au	Morphology controller	Surface and bulk defects	-	$FA_{0.85}MA_{0.15}Pb(I_{0.85}Br_{0.15})_3$	18.73	(2016)/[86]

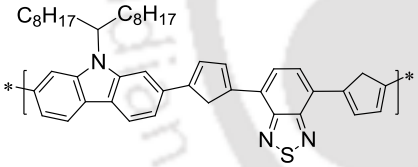

PCDTBT

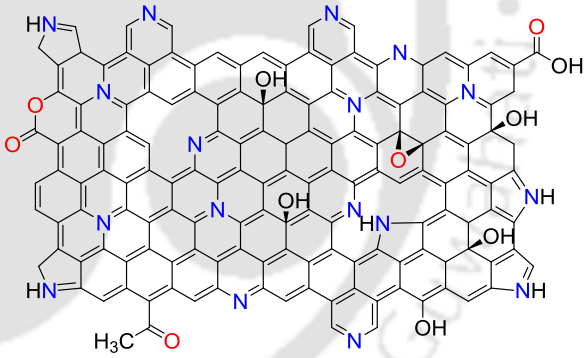

N-RGO

Figure 1.8: The molecular structure of some large ligands listed in Table 1.1.

crystal size were increased from 250 to 1500 nm using the MACl additive with $FAPbI_3$ perovskite via antisolvent method, resulting in a certified efficiency of 23.48%.[87]

Non-radiative recombination drastically affects the efficiency of solar cells. Generally, defects cannot be avoided as the perovskite films are polycrystalline in nature. These defects present in the perovskite film induce carrier recombination centers, which results in non-radiative recombination and hence loss of open circuit voltage and fill factor. In addition to the formation of perovskite film with good morphology, defect passivation of

perovskite film is a powerful approach to suppress the non-radiative recombination loss and thus improve the performance of PSC.[88] Ultrathin PMMA films were introduced and it was observed that the carbonyl (C=O) groups present on PMMA could passivate both perovskite/HTL as well as perovskite/ETL interface via Lewis-Base interaction with of Pb^{2+} ions.[78] An ultrahigh V_{OC} of 1.22 V was obtained using this approach with a 1.6 eV bandgap perovskite material. Another report also demonstrated similar approach to enhance the performance of PSC.[89] Lewis acid iodopentafluorobenzene (IPFB) was employed to passivate surface trap states, which was induced by under-coordination of halide ions. The perovskite was passivated via supramolecular halogen bonding to give a PCE of 15.7%.[79] Lewis bases, such as thiophene and pyridine were also utilized that coordinate with under coordinated Pb atoms. This could also reduce the rate of non-radiative recombination significantly in the perovskite films.[80]

Before its commercialization, the stability of PSCs is a major bottleneck among other issues. Many additives including small molecules and polymers have been proven to improve the moisture stability of the perovskite films. Generally, the additives opted for stability improvement contains a functional group which can coordinate with perovskite along with a hydrophobic core. The additive coordinates with perovskite during film formation and its functional groups come over the surface or at the grain boundaries. The hydrophobic part protects it from moisture. Incorporation of trimethylolpropanetriacrylate (TMTA), a hydrophobic additive into $MAPbI_3$ perovskite films that anchor chemically to grain boundaries and then in situ crosslink, after thermal treatment to a robust continuous network polymer[81] showed enhanced thermal, UV and moisture stability. The PSC with TMTA retained nearly 80% of its initial efficiency after 400 h at maximum power point under full-sun AM 1.5 G illumination of Xenon lamp without any UV filter. It also demonstrated excellent stability under moisture or thermal (85 °C) conditions, with over 90% of their initial efficiency after 1000 h of aging.

1.7 Thesis Synopsis

Motivated from the energy crisis and climate change, the focus of this thesis is to achieve clean and sustainable energy generation by further advancing the development of dye sensitized and perovskite solar cells in terms of performance and stability. The first part of the thesis deals with the design and development of new sensitizers and analysis of

their structure property relationship as well as photovoltaic performance. The second part is an effort to progress and understand the crystallization process of perovskite material. In addition, control of trap states and ion migration in perovskite layer has also been performed through additive engineering. The results obtained during the course of these developments are divided into five chapters. Finally, a summary and future prospect is presented. A brief outline of these chapters is given below

Chapter 2 aims to enhance the absorption property of metal-free sensitizers. The absorption spectra of sensitizer may be broadened by either increasing the conjugation length using an additional spacer, donor, and acceptor or introducing different substituents. The extension of π-conjugation causes unfavorable π–π stacking and aggregation that results in low photo-stability. With the aim to avoid this, fluorine atom was substituted on organic sensitizers, which provided an inverted charge density distribution with respect to the analogous non-fluorinated molecule due to its strong electron-withdrawing nature. Moreover, it strongly impacted on inter- and intra-molecular interaction via hydrogen bonding. As a result, broad absorption and high electron injection rates were achieved, and hence the dye MA1F-o outperformed other dyes with a power conversion efficiency of 4.02%. Thus, this has been revealed that fluorination could be used as a tool to optimize the optical, electrochemical and electron injection properties to obtain high-efficiency DSSCs.

Chapter 3 focuses to reduce the dye aggregation on the TiO_2 photoanode and correlate it with the molecular design. With this goal two new *o,m*-di fluoro substituted phenylene spacer dyes with mono- or di-anchoring groups have been synthesized having carbazole donor. The molecular properties of the newly synthesized dyes were extensively studied and correlated with the photovoltaic performance for both liquid as well as solid state DSSCs (ss-DSSCs). Further, electrochemical impedance spectroscopy (EIS) measurements were used to estimate carrier transport and interfacial charge recombination in the solar cell devices. The dye having presence of two acceptor groups (Cz-D2) showed lower LUMO level, efficient electron extraction, lesser aggregation, high molar extinction coefficient and better charge transfer. Therefore, without using any additive, Cz-D2 exhibited an attractive PCE of 5.35%. Hence, molecular engineering of sensitizers could be used to solve the problem of dye aggregation.

Chapter 4 deals with the crystallization control and the grain growth of perovskite films. The precise control of perovskite crystallization process that could provide smooth

films with large grains is a prerequisite for solar cell fabrication to achieve higher efficiencies. To accomplish this the Lewis acid base approach was combined with the hot casting technique to control the grain growth of perovskite films by varying the amount of DMSO added in the perovskite precursor solution of lead iodide (PbI_2) and methyl ammonium chloride (MACl) in dimethylformamide (DMF) carefully. Uniform films of $MAPbCl_xI_{3-x}$ having large grain size were formed reproducibly on addition of 1.5 equivalents DMSO to the precursor solution. Perovskite solar cells fabricated using this solution resulted in maximum PCE of 14.11% with enhanced stability. Further improvement in PSC performance could be achieved by using a mixture of A site cations in perovskite.

Chapter 5 discusses the issue of perovskite crystallization and stability of perovskite solar cells. Although improvements have been achieved in the crystallization process by incorporation of additives into the perovskite precursors to attain high-quality large-grain perovskite films with uniform morphology and smooth surface, the poor stability of PSCs has still remained a key challenge that need to be solved. Oxalic acid (OA) was introduced as an effective additive into perovskite precursor solution to positively impact both photovoltaic performance and stability of PSCs. The bidirectional OA assisted growth enabled a substantial improvement in the quality of perovskite films, leading to an enhancement in PCE to 17.12%. Furthermore, a remarkable improvement in stability under heat at 100 ^oC was obtained with OA incorporation, where the OA modified PSCs exhibited much higher PCE retention of 70% after 19 h. This study provides an effective way to prepare perovskite film with superior morphology and low recombination to achieve high efficiency and stability of PSCs.

Chapter 6 demonstrates simultaneously improvement of perovskite film morphology and passivation of trap states. The solution processed polycrystalline perovskite films have multiple times higher defect density compared to the single-crystalline film. In this work, improved perovskite morphology with effective defect passivation has been achieved by adding benzene carboxylic acid (BCA) derivatives in the perovskite precursor solution. Three different BCA derivatives, viz. benzoic acid (BA), isophthalic acid (ITA), and trimesic acid (TA), have been used in this study. TA incorporated device, gave highest PCE of 18.08% with a significant improvement in the open circuit voltage to 1.063 V (an enhancement of ≈110 mV). In addition, the device with TA exhibited enhanced thermal

stability. Besides, a unique property of these additives to use higher concentration of –COOH group by substituting it on the same aromatic core has been established. Thus, this approach to use BCA functionalized molecules to reduce trap states through passivation along with crystallization control further extends the knowledge of selective chemical additives to enhance perovskite based solar cells.

Chapter 7 discusses conclusions of the thesis and prospects. A brief summary of research work carried out and possibilities of investigations required towards the commercialization of perovskite solar cells in the near future is presented.

1.8 References

(1) Armaroli, N.; Balzani, V. *Angew. Chem., Int. Ed.* **2007,** *46*, 52-66.

(2) Gust, D.; Moore, T. A.; Moore, A. L. *Acc. Chem. Res.* **2009,** *42*, 1890-1898.

(3) Grätzel, M. *Nature* **2001,** *414*, 338-344.

(4) West, W. *Proc. Vogel Cent. Symp. Photogr. Sci.* **1974,** *18*, 35-48.

(5) Moser, J. *Monatsh. Chem.* **1887,** *8*, 373-373.

(6) Namba, S.; Hishiki, Y. *J. Phys. Chem.* **1965,** *69*, 774-779.

(7) Gerischer, H.; Tributsch, H. *Berichte der Bunsengesellschaft für physikalische Chemie* **1968,** *72*, 437-445.

(8) Hauffe, K.; Danzmann, H. J.; Pusch, H.; Range, J.; Volz, H. *J. Electrochem. Soc.* **1970,** *117*, 993-999.

(9) Tsubomura, H.; Matsumura, M.; Nomura, Y.; Amamiya, T. *Nature* **1976,** *261*, 402-403.

(10) Clark, W. D. K.; Sutin, N. *J. Am. Chem. Soc.* **1977,** *99*, 4676-4682.

(11) Anderson, S.; Constable, E. C.; Dare-Edwards, M. P.; Goodenough, J. B.; Hamnett, A.; Seddon, K. R.; Wright, R. D. *Nature* **1979,** *280*, 571-573.

(12) Gerischer, H. *J. Electroanal. Chem.* **1975,** *58*, 263-274.

(13) MEMMING, R. *Photochem. Photobiol.* **1972,** *16*, 325-333.

(14) Fujishima, A.; Watanabe, T.; Tatsuoki, O.; Honda, K. *Chem. Lett.* **1975,** *4*, 13-18.

(15) Hamnett, A.; Dare-Edwards, M. P.; Wright, R. D.; Seddon, K. R.; Goodenough, J. B. *J. Phys. Chem.* **1979,** *83*, 3280-3290.

(16) Dare-Edwards, M. P.; Goodenough, J. B.; Hamnett, A.; Seddon, K. R.; Wright, R. D. *Faraday Discuss. Chem. Soc.* **1980,** *70*, 285-298.

(17) Akira, F.; Kenichi, H. *B. Chem. Soc. Jpn.* **1971,** *44*, 1148-1150.

(18) Fujishima, A.; Honda, K. *Nature* **1972,** *238*, 37-38.

(19) O'Regan, B.; Grätzel, M. *Nature* **1991,** *353*, 737-740.

(20) Kakiage, K.; Aoyama, Y.; Yano, T.; Oya, K.; Fujisawa, J.-i.; Hanaya, M. *Chem. Commun.* **2015,** *51*, 15894-15897.

(21) National Renewable Energy Laboratory (NREL). https://www.nrel.gov/pv/assets/pdfs/best-research-cell-efficiencies.20190923.pdf (accessed 02 November 2019).

(22) Kojima, A.; Teshima, K.; Shirai, Y.; Miyasaka, T. *J. Am. Chem. Soc.* **2009,** *131*, 6050-6051.

(23) Snaith, H. J.; Schmidt-Mende, L. *Adv. Mater.* **2007,** *19*, 3187-3200.

(24) Bang, J. H.; Kamat, P. V. *ACS Nano* **2009,** *3*, 1467-1476.

(25) Kojima, A.; Teshima, K.; Shirai, Y.; Miyasaka, T., Novel Photoelectrochemical Cell with Mesoscopic Electrodes Sensitized by Lead-Halide Compounds. In *210th ECS Meeting*, Cancun, Mexico, 2006; p 397.

(26) Kojima, A.; Teshima, K.; Shirai, Y.; Miyasaka, T., Novel Photoelectrochemical Cell with Mesoscopic Electrodes Sensitized by Lead-Halide Compounds. In *214th ECS Meeting*, Honolulu, Hawaii, 2008.

(27) Lee, M. M.; Teuscher, J.; Miyasaka, T.; Murakami, T. N.; Snaith, H. J. *Science* **2012,** *338*, 643-647.

(28) GAMRY INSTRUMENTS. https://www.gamry.com/application-notes/physechem/dssc-dye-sensitized-solar-cells/ (accessed 06 Januaru 2020).

(29) Liu, M.; Johnston, M. B.; Snaith, H. J. *Nature* **2013,** *501*, 395.

(30) Jeng, J.-Y.; Chiang, Y.-F.; Lee, M.-H.; Peng, S.-R.; Guo, T.-F.; Chen, P.; Wen, T.-C. *Adv. Mater.* **2013,** *25*, 3727-3732.

(31) Xing, G.; Mathews, N.; Sun, S.; Lim, S. S.; Lam, Y. M.; Grätzel, M.; Mhaisalkar, S.; Sum, T. C. *Science* **2013,** *342*, 344-347.

(32) Zhao, Y.; Nardes, A. M.; Zhu, K. *J. Phys. Chem. Lett.* **2014,** *5*, 490-494.

(33) Urbani, M.; de la Torre, G.; Nazeeruddin, M. K.; Torres, T. *Chem. Soc. Rev.* **2019,** *48*, 2738-2766.

(34) Kalyanasundaram, K.; Grätzel, M. *Coord. Chem. Rev.* **1998,** *177*, 347-414.

(35) Bakr, Z. H.; Wali, Q.; Fakharuddin, A.; Schmidt-Mende, L.; Brown, T. M.; Jose, R. *Nano Energy* **2017,** *34*, 271-305.

(36) Unger, E. L.; Hoke, E. T.; Bailie, C. D.; Nguyen, W. H.; Bowring, A. R.; Heumüller, T.; Christoforo, M. G.; McGehee, M. D. *Energy Environ. Sci.* **2014,** *7*, 3690-3698.

(37) Zaban, A.; Meier, A.; Gregg, B. A. *J. Phys. Chem. B* **1997,** *101*, 7985-7990.

(38) Kern, R.; Sastrawan, R.; Ferber, J.; Stangl, R.; Luther, J. *Electrochim. Acta* **2002,** *47*, 4213-4225.

(39) Urbani, M.; Grätzel, M.; Nazeeruddin, M. K.; Torres, T. *Chem. Rev.* **2014,** *114*, 12330-12396.

(40) Bessho, T.; Zakeeruddin, S. M.; Yeh, C.-Y.; Diau, E. W.-G.; Grätzel, M. *Angew. Chem., Int. Ed.* **2010,** *49*, 6646-6649.

(41) Wang, P.; Zakeeruddin, S. M.; Moser, J. E.; Nazeeruddin, M. K.; Sekiguchi, T.; Grätzel, M. *Nat. Mater.* **2003,** *2*, 402-407.

(42) Chen, C.-Y.; Wang, M.; Li, J.-Y.; Pootrakulchote, N.; Alibabaei, L.; Ngoc-le, C.-h.; Decoppet, J.-D.; Tsai, J.-H.; Grätzel, C.; Wu, C.-G.; Zakeeruddin, S. M.; Grätzel, M. *ACS Nano* **2009,** *3*, 3103-3109.

(43) Liang, M.; Chen, J. *Chem. Soc. Rev.* **2013,** *42*, 3453-3488.

(44) Mishra, A.; Fischer, M. K. R.; Bäuerle, P. *Angew. Chem., Int. Ed.* **2009,** *48*, 2474-2499.

(45) O'Regan, B. C.; Walley, K.; Juozapavicius, M.; Anderson, A.; Matar, F.; Ghaddar, T.; Zakeeruddin, S. M.; Klein, C.; Durrant, J. R. *J. Am. Chem. Soc.* **2009,** *131*, 3541-3548.

(46) Chang, Y. J.; Chow, T. J. *J. Mater. Chem.* **2011,** *21*, 9523-9531.

(47) Clifford, J. N.; Martínez-Ferrero, E.; Viterisi, A.; Palomares, E. *Chem. Soc. Rev.* **2011,** *40*, 1635-1646.

(48) Hara, K.; Sayama, K.; Ohga, Y.; Shinpo, A.; Suga, S.; Arakawa, H. *Chem. Commun.* **2001**, 569-570.

(49) Baheti, A.; Singh, P.; Lee, C.-P.; Thomas, K. R. J.; Ho, K.-C. *J. Org. Chem.* **2011,** *76*, 4910-4920.

(50) Tian, H.; Yang, X.; Chen, R.; Pan, Y.; Li, L.; Hagfeldt, A.; Sun, L. *Chem. Commun.* **2007**, 3741-3743.

(51) Velusamy, M.; Justin Thomas, K. R.; Lin, J. T.; Hsu, Y.-C.; Ho, K.-C. *Org. Lett.* **2005,** *7*, 1899-1902.

(52) Cui, Y.; Wu, Y.; Lu, X.; Zhang, X.; Zhou, G.; Miapeh, F. B.; Zhu, W.; Wang, Z.-S. *Chem. Mater.* **2011,** *23*, 4394-4401.

(53) Horiuchi, T.; Miura, H.; Sumioka, K.; Uchida, S. *J. Am. Chem. Soc.* **2004,** *126*, 12218-12219.

(54) Justin Thomas, K. R.; Lin, J. T.; Tao, Y.-T.; Ko, C.-W. *J. Am. Chem. Soc.* **2001,** *123*, 9404-9411.

(55) Lai, S. L.; Tong, Q. X.; Chan, M. Y.; Ng, T. W.; Lo, M. F.; Ko, C. C.; Lee, S. T.; Lee, C. S. *Org. Electron.* **2011,** *12*, 541-546.

(56) Han, J.; Thirupathaiah, B.; Kwon, G.; Kim, C.; Seo, S. *Dyes Pigm.* **2015,** *114*, 78-84.

(57) Li, J.; Grimsdale, A. C. *Chem. Soc. Rev.* **2010,** *39*, 2399-2410.

(58) Koumura, N.; Wang, Z.-S.; Mori, S.; Miyashita, M.; Suzuki, E.; Hara, K. *J. Am. Chem. Soc.* **2006,** *128*, 14256-14257.

(59) Teng, C.; Yang, X.; Yuan, C.; Li, C.; Chen, R.; Tian, H.; Li, S.; Hagfeldt, A.; Sun, L. *Org. Lett.* **2009,** *11*, 5542-5545.

(60) Kakiage, K.; Aoyama, Y.; Yano, T.; Otsuka, T.; Kyomen, T.; Unno, M.; Hanaya, M. *Chem. Commun.* **2014,** *50*, 6379-6381.

(61) Chu, H.-C.; Sahu, D.; Hsu, Y.-C.; Padhy, H.; Patra, D.; Lin, J.-T. S.; Bhattacharya, D.; Lu, K.-L.; Wei, K.-H.; Lin, H.-C. *Dyes Pigm.* **2012,** *93*, 1488-1497.

(62) Soni, S. S.; Fadadu, K. B.; Vaghasiya, J. V.; Solanki, B. G.; Sonigara, K. K.; Singh, A.; Das, D.; Iyer, P. K. *J. Mater. Chem. A* **2015,** *3*, 21664-21671.

(63) Raju, T. B.; Vaghasiya, J. V.; Afroz, M. A.; Soni, S. S.; Iyer, P. K. *Org. Electron.* **2017,** *50*, 25-32.

(64) Lee, M.-W.; Kim, J.-Y.; Son, H. J.; Kim, J. Y.; Kim, B.; Kim, H.; Lee, D.-K.; Kim, K.; Lee, D.-H.; Ko, M. J. *Sci. Rep.* **2015,** *5*, 7711.

(65) Naik, P.; Su, R.; Elmorsy, M. R.; El-Shafei, A.; Adhikari, A. V. *Dyes Pigm.* **2018,** *149*, 177-187.

(66) Green, M. A.; Ho-Baillie, A.; Snaith, H. J. *Nat. Photonics* **2014,** *8*, 506.

(67) Grancini, G.; Roldán-Carmona, C.; Zimmermann, I.; Mosconi, E.; Lee, X.; Martineau, D.; Narbey, S.; Oswald, F.; De Angelis, F.; Graetzel, M.; Nazeeruddin, M. K. *Nat. Commun.* **2017,** *8*, 15684.

(68) Kim, H.-S.; Lee, C.-R.; Im, J.-H.; Lee, K.-B.; Moehl, T.; Marchioro, A.; Moon, S.-J.; Humphry-Baker, R.; Yum, J.-H.; Moser, J. E.; Grätzel, M.; Park, N.-G. *Sci. Rep.* **2012,** *2*, 591-591.

(69) Jeon, N. J.; Noh, J. H.; Kim, Y. C.; Yang, W. S.; Ryu, S.; Seok, S. I. *Nat. Mater.* **2014,** *13*, 897.

(70) Li, X.; Bi, D.; Yi, C.; Décoppet, J.-D.; Luo, J.; Zakeeruddin, S. M.; Hagfeldt, A.; Grätzel, M. *Science* **2016,** *353*, 58-62.

(71) Jung, E. H.; Jeon, N. J.; Park, E. Y.; Moon, C. S.; Shin, T. J.; Yang, T.-Y.; Noh, J. H.; Seo, J. *Nature* **2019,** *567*, 511-515.

(72) Ahn, N.; Son, D.-Y.; Jang, I.-H.; Kang, S. M.; Choi, M.; Park, N.-G. *J. Am. Chem. Soc.* **2015,** *137*, 8696-8699.

(73) Williams, S. T.; Zuo, F.; Chueh, C.-C.; Liao, C.-Y.; Liang, P.-W.; Jen, A. K. Y. *ACS Nano* **2014,** *8*, 10640-10654.

(74) Zhao, Y.; Zhu, K. *J. Phys. Chem. C* **2014,** *118*, 9412-9418.

(75) Jiang, Q.; Zhao, Y.; Zhang, X.; Yang, X.; Chen, Y.; Chu, Z.; Ye, Q.; Li, X.; Yin, Z.; You, J. *Nat. Photonics* **2019,** *13*, 460-466.

(76) Chen, Q.; Zhou, H.; Fang, Y.; Stieg, A. Z.; Song, T.-B.; Wang, H.-H.; Xu, X.; Liu, Y.; Lu, S.; You, J.; Sun, P.; McKay, J.; Goorsky, M. S.; Yang, Y. *Nat. Commun.* **2015,** *6*, 7269.

(77) Xu, M.-F.; Zhang, H.; Zhang, S.; Zhu, H. L.; Su, H.-M.; Liu, J.; Wong, K. S.; Liao, L.-S.; Choy, W. C. H. *J. Mater. Chem. A* **2015,** *3*, 14424-14430.

(78) Peng, J.; Khan, J. I.; Liu, W.; Ugur, E.; Duong, T.; Wu, Y.; Shen, H.; Wang, K.; Dang, H.; Aydin, E.; Yang, X.; Wan, Y.; Weber, K. J.; Catchpole, K. R.; Laquai, F.; De Wolf, S.; White, T. P. *Adv. Energy Mater.* **2018,** *8*, 1801208.

(79) Abate, A.; Saliba, M.; Hollman, D. J.; Stranks, S. D.; Wojciechowski, K.; Avolio, R.; Grancini, G.; Petrozza, A.; Snaith, H. J. *Nano Lett.* **2014,** *14*, 3247-3254.

(80) Noel, N. K.; Abate, A.; Stranks, S. D.; Parrott, E. S.; Burlakov, V. M.; Goriely, A.; Snaith, H. J. *ACS Nano* **2014,** *8*, 9815-9821.

(81) Li, X.; Zhang, W.; Wang, Y.-C.; Zhang, W.; Wang, H.-Q.; Fang, J. *Nat. Commun.* **2018,** *9*, 3806.

(82) Wang, F.; Geng, W.; Zhou, Y.; Fang, H.-H.; Tong, C.-J.; Loi, M. A.; Liu, L.-M.; Zhao, N. *Adv. Mater.* **2016,** *28*, 9986-9992.

(83) Lee, S. J.; Shin, S. S.; Kim, Y. C.; Kim, D.; Ahn, T. K.; Noh, J. H.; Seo, J.; Seok, S. I. *J. Am. Chem. Soc.* **2016,** *138*, 3974-3977.

(84) Zhang, C.-C.; Li, M.; Wang, Z.-K.; Jiang, Y.-R.; Liu, H.-R.; Yang, Y.-G.; Gao, X.-Y.; Ma, H. *J. Mater. Chem. A* **2017,** *5*, 2572-2579.

(85) Sun, M.; Zhang, F.; Liu, H.; Li, X.; Xiao, Y.; Wang, S. *J. Mater. Chem. A* **2017,** *5*, 13448-13456.

(86) Hadadian, M.; Correa-Baena, J.-P.; Goharshadi, E. K.; Ummadisingu, A.; Seo, J.-Y.; Luo, J.; Gholipour, S.; Zakeeruddin, S. M.; Saliba, M.; Abate, A.; Grätzel, M.; Hagfeldt, A. *Adv. Mater.* **2016,** *28*, 8681-8686.

(87) Kim, M.; Kim, G.-H.; Lee, T. K.; Choi, I. W.; Choi, H. W.; Jo, Y.; Yoon, Y. J.; Kim, J. W.; Lee, J.; Huh, D.; Lee, H.; Kwak, S. K.; Kim, J. Y.; Kim, D. S. *Joule* **2019,** *3*, 2179-2192.

(88) Zhang, H.; Nazeeruddin, M. K.; Choy, W. C. H. *Adv. Mater.* **2019,** *31*, 1805702.

(89) Yang, F.; Lim, H. E.; Wang, F.; Ozaki, M.; Shimazaki, A.; Liu, J.; Mohamed, N. B.; Shinokita, K.; Miyauchi, Y.; Wakamiya, A.; Murata, Y.; Matsuda, K. *Adv. Mater. Interfaces* **2018,** *5*, 1701256.

CHAPTER 2

Effect of Fluorine Substitution and Position on Phenylene Spacer in Carbazole Based Organic Sensitizers for Dye Sensitized Solar Cells

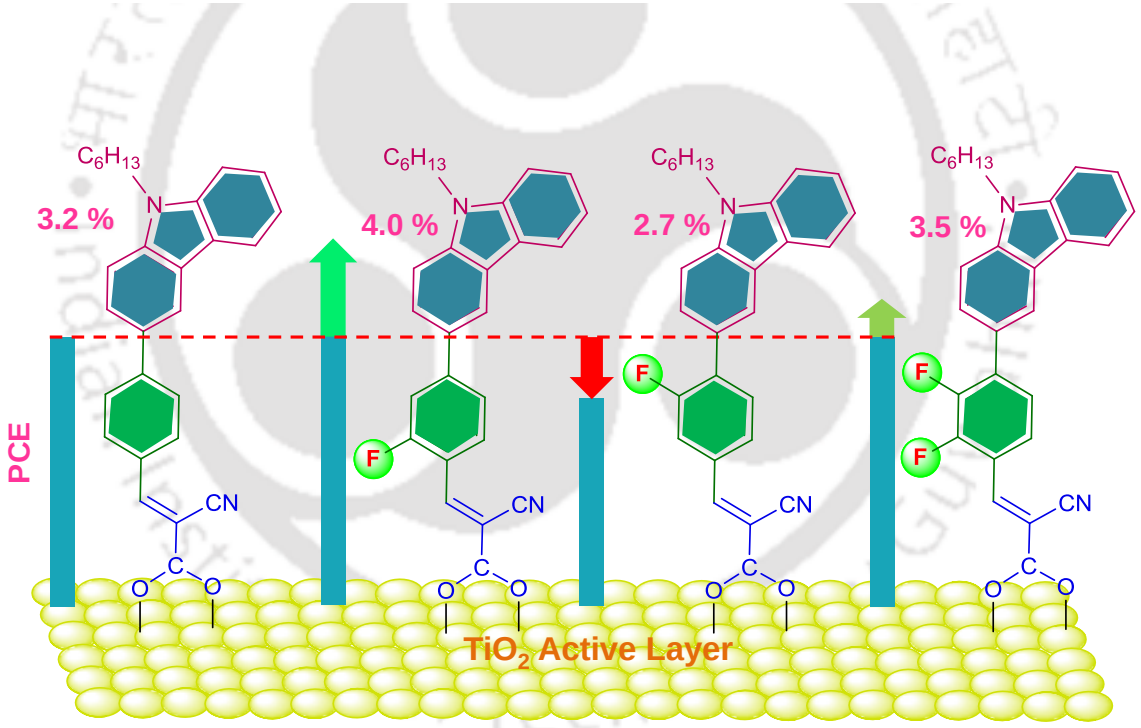

Afroz, M. A.; Sonigara, K. K.; Raju, T. B.; Soni, S. S.; Iyer, P. K. *Phys. Chem. Chem. Phys.* **2017,** *19*, 28579-28587, DOI: 10.1039/c7cp05226j.

Abstract

The preparation of a series of organic dyes having a carbazole donor, cyanoacrylic acid as an acceptor, and phenylene ring as a spacer with the influence of fluorine substitution at different positions on the photophysical and device properties is presented in this chapter. Due to its unique properties of small size and high electronegativity, fluorine is now being extensively used to control the optoelectronic properties of organic conjugated materials. In this study, the results revealed that the specific position and number of fluorine substitution were very crucial to control the optical as well as the electrochemical properties of organic dyes. It was found that fluorine substitution led to a red shift in the absorption spectra of the dyes and reduced the band gap. The injection rate of photoexcited electrons was measured using time-resolved photoluminescence and the *o*-fluoro substituted dye MA1F-o showed the best electron injection dynamics. As a result of broad absorption and high electron injection rate, the dye MA1F-o outperformed other dyes with a power conversion efficiency of 4.02% (Jsc = 8.28 mA cm^{-2}, Voc = 0.745 V and FF = 0.64). The non-fluorinated dye MA0F exhibited a power conversion efficiency of 3.23% (Jsc = 6.80 mA cm^{-2}, Voc = 0.720 V and FF = 0.67). The dye MA1F-m exhibited the least molar absorption coefficient and a lower power conversion efficiency because of the *meta* inductive effect.

2.1 Introduction

Considering the efficiency and stability, zinc porphyrin[1-5] and ruthenium polypyridine[6-8] complexes are the dyes with the best performance. However, ruthenium dyes have a drawback of metal toxicity and inadequate resource availability, whereas zinc porphyrin dyes have the complications of giving low yields and handling of highly poisonous chemicals during the synthesis.[9] DSSCs have recently achieved the record in the power conversion efficiency (PCE) of more than 14% based on organic sensitizers, which is higher than the maximum reported efficiency of metal complex dyes.[10] Organic sensitizers have the advantage of abundant raw materials, flexible molecular modification, and high molar absorption coefficient.[11] Organic sensitizers mostly consist of a push–pull combination of a donor (D) and an acceptor (A) linked with a π-spacer to enhance intra-molecular charge transfer (ICT), resulting in effective sunlight harvesting.[12] The properties of D–π–A sensitizers can be easily tuned by choosing different combinations of the components (i.e. D and A) and different substitutions.[13-18] Photovoltaic characteristics of a sensitizer can be enhanced by broadening the absorption spectra. This may be achieved by either increasing the conjugation length using an additional spacer, donor, and acceptor or introducing different substituents. The extension of π-conjugation causes unfavorable π–π stacking and aggregation that results in low photo-stability.[19] Fluorine atom, when substituted on organic sensitizers, provides an inverted charge density distribution with respect to the analogous non-fluorinated molecule due to its strong electron-withdrawing nature. Moreover, fluorine has a strong impact on inter- and intra-molecular interaction via hydrogen bonding. It is also beneficial in lowering the energy level as well as reducing the band gap.[20] The method based on fluorine substitution to obtain a narrow band gap sensitizer also has the advantage that fluorinated sensitizers are more hydrophobic, creating a large shielding that curtails the direct contact between the electrolyte and the photoanode. Several studies have been reported on the effects of fluorination, which includes either the effect of fluorine position (*ortho*- or/and *meta*- to cyanoacrylic acid)[21-23] or the effect of fluorine content.[24-26] It has a observed that when fluorine was substituted at an *ortho*-position, a superior PCE was obtained, while it hampered the efficiency when incorporated at a *meta* position. When mono and di-*ortho* substitutions were considered, the highest efficiency in mono-substitution was observed with vinyl spacer dyes, whereas di-substituted dye gave the highest efficiency with thieno[3,2-b]thiophene spacer.[21-25]

In this chapter, fluorine containing metal-free organic sensitizers MA1F-o, MA1F-m and MA2F (Figure 2.1) were designed and synthesized. These sensitizers contain carbazole donor, cyanoacrylic acid as an acceptor and different fluorine substitutions at a phenylene unit that acted as a spacer. Both the number and the position of fluorine on phenylene spacer were changed. The properties of these dyes were compared with those of the fluorine-free reference dye MA0F. Fluorination can lower the LUMO level relative to that of the non-fluorinated dye because of its electron withdrawing nature, resulting in a narrower band gap and a red shift in the absorption. It was observed that mono fluorine substitution at the *ortho* position improves the photovoltaic properties of the dye significantly. The improvement in the photovoltaic properties was correlated with the positions and number of fluorine using UV-vis absorption spectroscopy, differential pulse voltammetry, time-resolved photoluminescence and electrochemical impedance spectroscopy.

2.2 Results and Discussion

Fluorine substitution at *ortho* (MA1F-o), *meta* (MA1F-m) and *ortho–meta* positions (MA2F) on phenyl spacer to cyanoacrylic acid of the reference dye MA0F was carried out to design the dyes. The synthesis method of MA dyes involved two steps (Figure 2.1). First, the Suzuki coupling reaction of 3-bromo-9-hexyl-9H-carbazole with **1 (a, b, c, or d)** gave the corresponding aldehyde **2 (a, b, c, or d)**. The second step involved the Knoevenagel reaction of **2 (a, b, c, or d)** with cyanoacetic acid to afford the corresponding dye.

The UV-vis absorption spectra of all dyes in chloroform solution are illustrated in Figure 2.2(a) and the parameters are summarized in Table 2.1. All the dyes exhibited

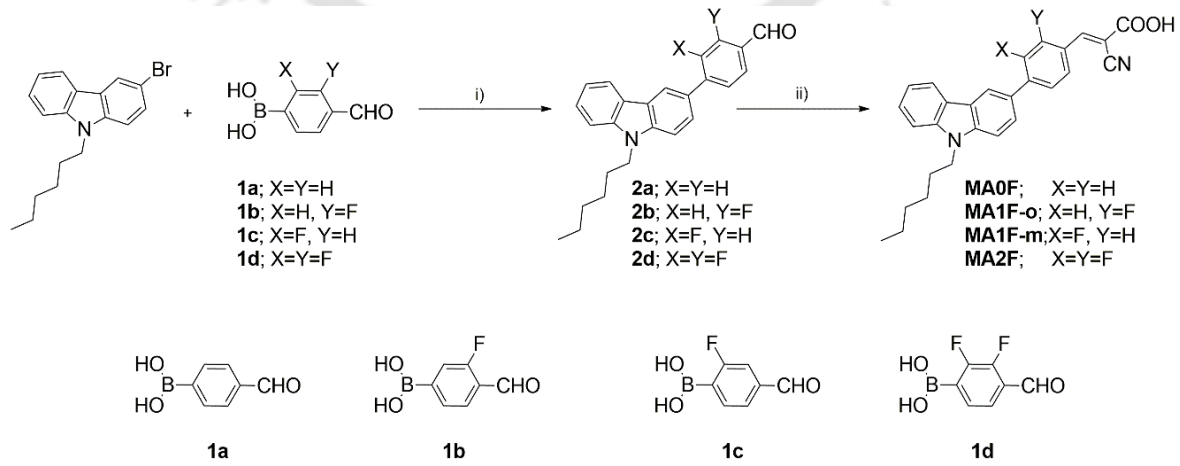

Figure 2.1: Synthesis of MA dyes: (i) $Pd(PPh_3)_4$, K_2CO_3, THF : H_2O (3 : 1, v/v), 85 °C, Argon, 12 h; (ii) cyanoacetic acid, piperidine, CH_3CN, 85 °C, 8 h.

similar spectra with the localized π–π* transition peaks in the range of 260–360 nm and the intra-molecular charge transfer (ICT) transition from carbazole to the cyanoacrylic acid group in the range of 360–500 nm. The reference dye MA0F exhibited a λmax at 380 nm (ε = 24 957 M^{-1} cm^{-1}) for the lowest energy peak. As expected, fluorine substitution resulted in a red shift of the absorption maxima to 396, 400, and 402 nm for MA1F-o, MA1F-m, and MA2F, respectively. The observed red shift was attributed to the reduction in the band gap because of the electronegative fluorine substitution.[22] However, a moderate decrease in the molar absorption coefficient of MA1F-o (19 869 M^{-1} cm^{-1}) and MA2F (19 251 M^{-1} cm^{-1}) as well as a dramatic decrease in case of MA1F-m (11 489 M^{-1} cm^{-1}) were observed. As compared to the absorption onset of other fluorinated dyes, the absorption onset of MA1F-m was blue-shifted due to the *meta* inductive effect of the fluorine atom and was almost equal to that of MA0F. Figure 2.2(b) shows the absorption

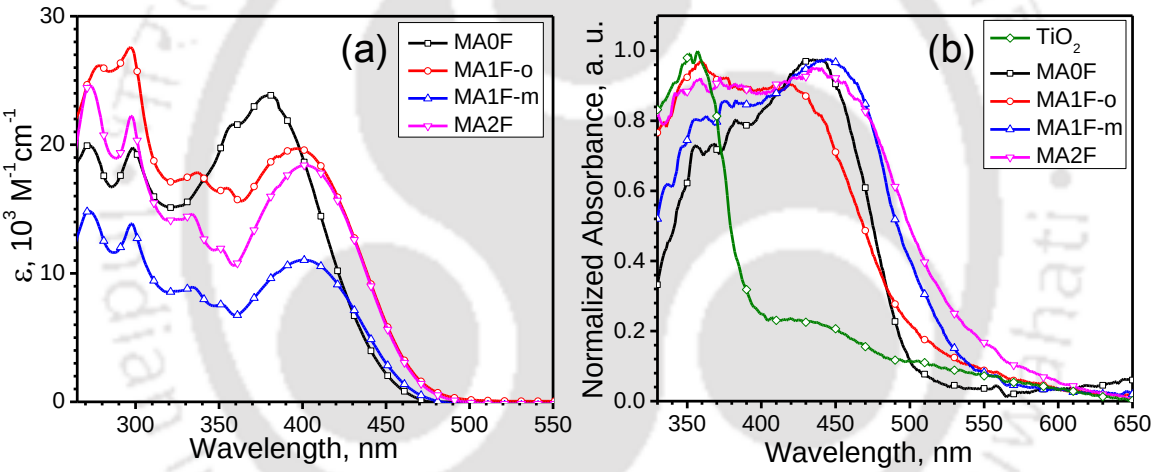

Figure 2.2: (a) UV-vis absorption spectra of the dyes in chloroform solution and (b) normalized UV-vis absorption spectra of the dyes absorbed on TiO_2 film.

Table 2.1: Optical and electrochemical data of the sensitizers.

Dye	λmax (nm)	Ɛmax ($M^{-1}cm^{-1}$)	EHOMO (eV)	ELUMO (eV)	E*g* (eV)
MA0F	380	24957	-5.35	-3.43	1.92
MA1F-o	396	19896	-5.38	-3.54	1.84
MA1F-m	400	11489	-5.44	-3.49	1.95
MA2F	402	19251	-5.34	-3.56	1.78

spectra of the dyes absorbed on 6 μm TiO_2 films, where the maximum absorption peaks are located at 435, 418, 446, and 440 nm for MA0F, MA1F-o, MA1F-m, and MA2F, respectively. When dyes are loaded onto TiO_2 surface, the aggregation and deprotonation affect the UV-vis absorption. The aggregation of the sensitizers may be of H-type or J-type. The H-type aggregates along with deprotonation always resulted in the blue shift of the absorption peak, while the J-type aggregates mainly led to the red shift.[27] The red shift in the absorption maxima for the dyes coated onto TiO_2 as compared to those in the chloroform solution, in this study, proved the dominance of J-type aggregates. A blue shift in the absorption peak of MA1F-o as compared to that of other dyes may be attributed to better deprotonation and anchoring to the TiO_2 layer.

Cyclic voltammetry (CV) was performed to calculate energy levels of the sensitizers. However, the reduction peak was not observed (Figure 2.3(a)). Therefore, a more sensitive technique, differential pulse voltammetry (DPV), was used to obtain the energy level. Quasi-reversible oxidation and reduction peaks were observed for all the sensitizers (Figure 2.3(b)). The energy levels of all MA dyes were calculated using the formulae E_{HOMO} = (−4.8 − Eox) eV and E_{LUMO} = (−4.8 − Ered) eV, as reported in the literature.[28] The HOMO level of all the dyes matched well with the redox potential of I^-/I_3^- present in the electrolyte. The electron-withdrawing nature of fluorine led to an enhanced charge separation between the donor and the acceptor parts.[22] As a result of fluorination, the LUMO level of MA0F (−3.43 eV) was lowered to −3.54, −3.49, and −3.56 eV for MA1F-o, MA1F-m and MA2F, respectively. These values were above the conduction band (CB) level of the TiO_2 electrode (−3.9 eV), providing a sufficient driving force for the electron injection from the oxidized sensitizer to the CB of the mesoporous TiO_2 layer. The electron injection from the dye to the CB of TiO_2 was analyzed by dynamic fluorescence. The lifetime decay curves of the dyes coated on 6 μm thin film of TiO_2 and Al_2O_3 are illustrated in Figure 2.3(c,d). The decay was found to be biexponential in case of TiO_2 and triexponential for Al_2O_3. The fluorescence decays of the dyes absorbed on alumina films showed only the intermolecular energy transfer due to the aggregation of the dye on the alumina surface. However, in case of the dyes absorbed on TiO_2 films, both processes, the aggregation induced energy transfer and the electron injection from the excited dye into the conduction band of TiO_2, occurred simultaneously. Therefore, if same aggregation is assumed in both the cases (i.e. Al_2O_3 and TiO_2) as the same thickness of Al_2O_3 and TiO_2 films were used, the rate constant for the electron injection from the excited state of the dye into the conduction band of TiO_2 can be

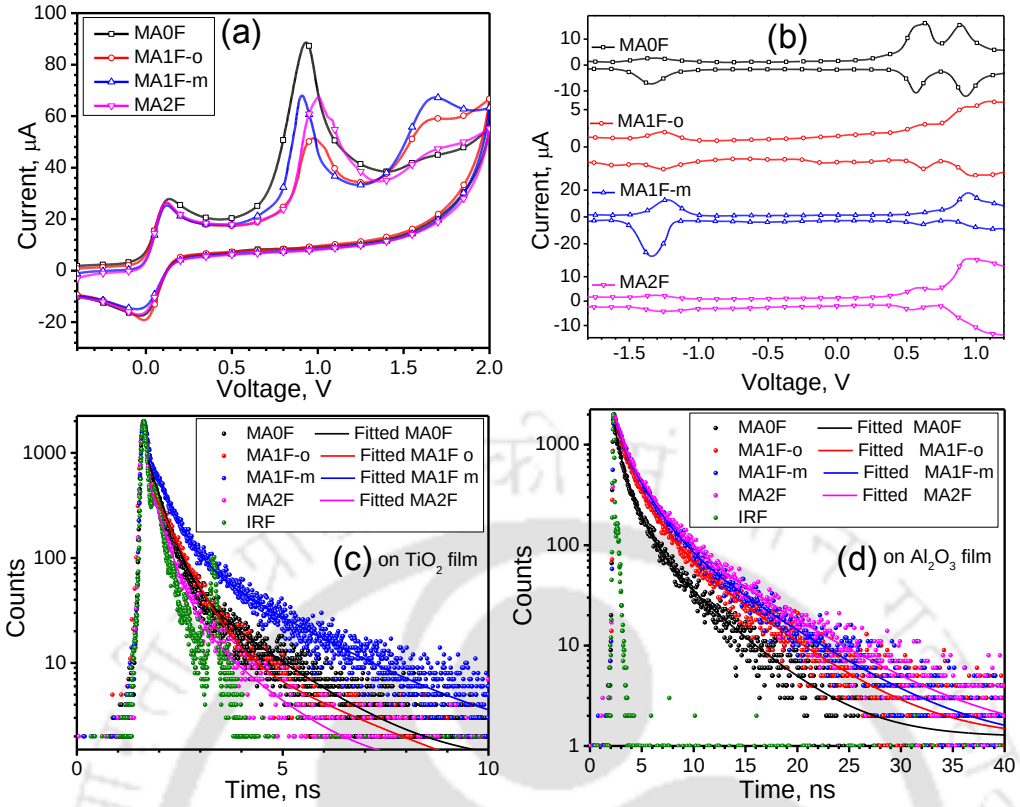

Figure 2.3: (a) Cyclic voltammetry, (b) Differential pulse voltammetry, (c) time resolved photoluminescence on TiO_2 films and (d) on Al_2O_3 films of MA dyes.

evaluated using equation $k_{inj} \approx k_{TiO2} - k_{Al2O3}$.[29-30] The average lifetime (τ), rate coefficient (k), and rate constants for the electron injection (k_{inj}) are listed in Table 2.2. Monofluoro-substitution at the *ortho* position (MA1F-o) and difluoro-substitution (MA2F) resulted in an increase in the rate constant for the electron injection to 9.10×10^8 and 9.48×10^8 s^{-1}, respectively. Moreover, a decrease in the rate constant was observed in case of MA1F-m (3.95×10^8 s^{-1}) when compared with that of the reference dye MA0F which has the rate

Table 2.2: Electron injection kinetics data of the sensitizers.

Dye	$\langle\tau\rangle TiO_2$ (ns)	$\langle\tau\rangle Al_2O_3$ (ns)	$kTiO_2$ (x 10^8 s^{-1})	kAl_2O_3 (x 10^8 s^{-1})	k_{inj} (x 10^8 s^{-1})
MA0F	1.15	3.69	8.70	2.71	5.99
MA1F-o	0.88	4.41	11.36	2.27	9.10
MA1F-m	1.66	4.83	6.02	2.07	3.95
MA2F	0.88	5.31	11.36	1.88	9.48

constant of 5.99×10^8 s^{-1}. The rate constant is a measure of electron transfer between the dye and the CB of TiO_2.

Electron density of frontier molecular orbitals was analyzed using Gaussian 09 software package. Density functional theory (DFT) calculations were carried out at B3LYP/6-31G(d,p) level. The distribution of electrons was similar in all the dyes as seen in Figure 2.4. The dyes were almost planar (Appendix A, Figure A-1, maximum dihedral angle 37.4°) and HOMO electrons are mainly distributed on the carbazole unit with partial spreading over the phenyl ring. LUMO electrons are spread from cyanoacrylic acid up to the phenyl spacer. The analogous HOMO and LUMO levels could be attributed to the same backbone structure of the dyes. Fluorine substitution lowered both the HOMO and LUMO level and reduced the band gap.

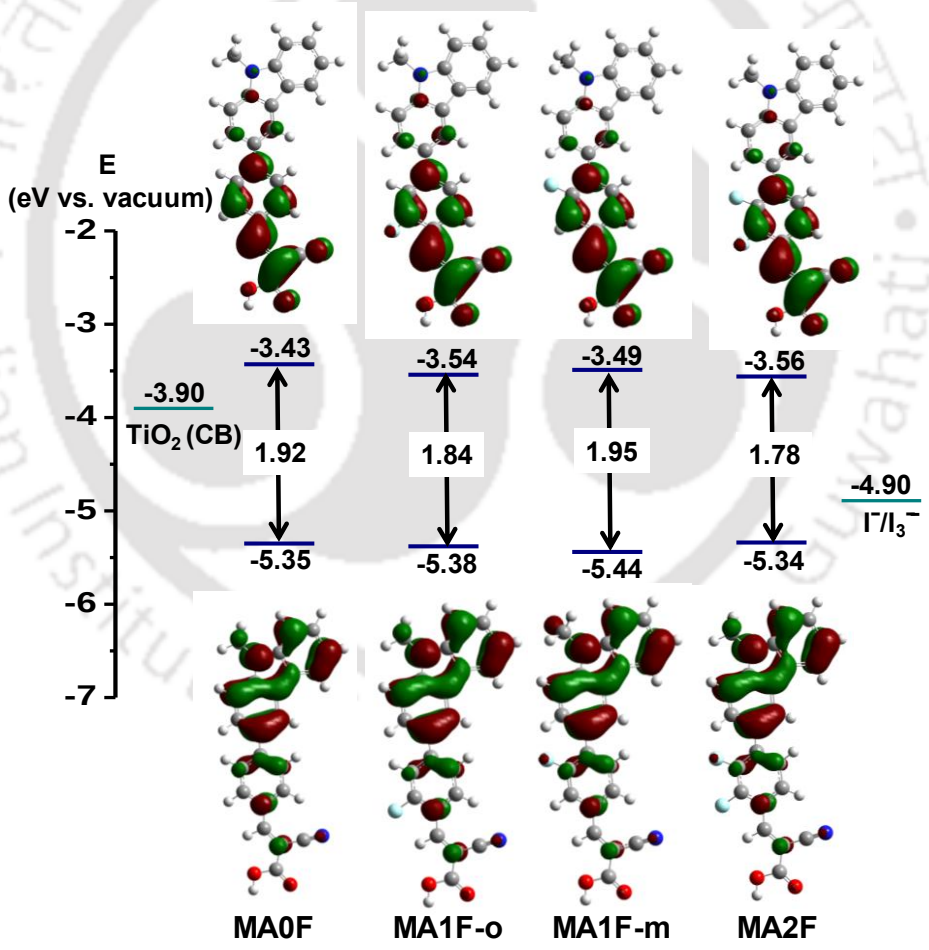

Figure 2.4: Frontier molecular orbitals of the dyes (HOMO-bottom, LUMO-top) calculated from Gaussian B3LYP/6-31G(d,p) level and the experimental energy level diagram.

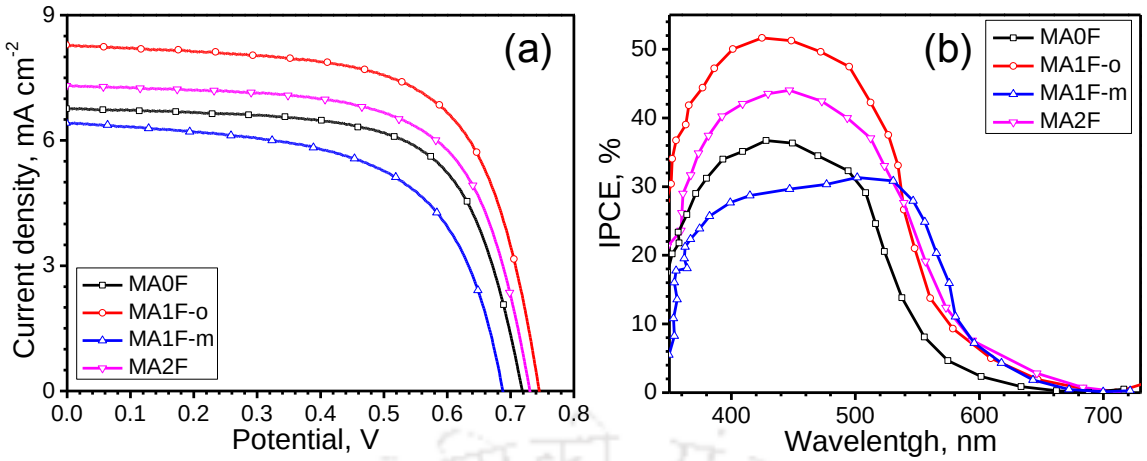

Figure 2.5: (a) Current–voltage measurements and (b) IPCE spectra of all DSSC devices.

Based on an earlier report where the effect of the thickness of the TiO_2 film sensitized with different fluorine containing dyes was investigated,[31] 12 μm thick TiO_2 film was selected due to its suitability with the dyes of these series. The devices with the N719 dye were also fabricated to understand the quality of our dyes. Figure 2.5(a) shows the *J*–*V* curves of DSSCs under light and dark conditions (the *J*–*V* curve of DSSC with N719 dye is presented in Appendix A, Figure A-2). The results show that the power conversion efficiency (PCE) of the DSSC changed clearly with the position of fluorine substitution in the phenyl ring of the dyes. Various photovoltaic parameters of DSSC with different sensitizers are depicted in Table 2.3. Photovoltaic parameters in terms of *J*sc, *V*oc and PCE of DSSC based on the reference dye MA0F (i.e. without fluorine substitution) were 6.76 mA cm^{-2}, 0.718 V and 3.23%, respectively. The introduction of a single fluorine atom at

Table 2.3: Photovoltaic parameters of different sensitizers based DSSC devices.[a]

Dye	*J*sc (mA cm^{-2})	Voc (V)	FF	η (%)
MA0F	6.8± 0.1	0.72± 0.02	0.67 ± 0.08	3.2 ± 0.2
MA1F-o	8.3± 0.1	0.75± 0.01	0.64 ± 0.06	4.0 ± 0.2
MA1F-m	6.4± 0.1	0.69± 0.01	0.59 ± 0.04	2.7 ± 0.3
MA2F	7.3± 0.1	0.73± 0.02	0.63 ± 0.03	3.5 ± 0.1
N719	13.05± 0.1	0.72± 0.02	0.72± 0.05	6.5± 0.2

[a]Average of 5 devices is presented

the *ortho* position on the phenyl ring (MA1F-o) led to a red shift in the absorbance (Figure 2.2(a)) due to the pronounced charge transfer, in the presence of fluorine atom, towards the acceptor end along with the subsequent H-type aggregation inducing the blue shift on the TiO_2 film, which led to an enhancement in *J*sc (8.28 mA cm^{-2}). To analyze the increase in the photovoltage of the dyes MA1F-o, MA2F and the decrease in the case of MA1F-m compared to that of reference dye MA0F, the dipole moment of the dyes was analyzed using DFT. The energetics of titania electrode depends on the dipole moment of the sensitizers in a DSSC. Therefore, the dipole moment of these dyes was compared. The dipole moment normalized to the surface of TiO_2 (μ_z) is among three components that can cause a shift in the conduction band potential of TiO_2. A higher positive value of μ_z can upshift the conduction band of TiO_2, which could lead to an increase in the photovoltage.[25] As listed in Table 2.4, the order of μ_z was MA1F-o > MA2F > MA0F > MA1F-m. This increase in the μ_z led to the increment of the photovoltage. The increase in the photovoltage coupled with the increase in the photocurrent resulted in the enhancement of PCE in the same order. The incident photon-to-current conversion efficiency (IPCE) spectra, which reflects the efficiency of photoelectric conversion at various wavelengths, are depicted in Figure 2.5(b). Because of the strong absorption bands in the visible range (400–500 nm), these molecules had a good IPCE in a wide range of the solar spectrum, which is in good agreement with the absorption spectra of the dyes. Furthermore, it can be observed that the IPCE plateaus of the MA1F-o and MA2F dyes are higher than that of the MA0F dye, whereas that of MA1F-m is lower, indicating the significant effect of fluorine unit on the light harvesting capability.

The *V*oc value depends on the conduction band edge (Ec) of the TiO_2 electrode and the electron recombination process at the TiO_2/dye/electrolyte interface.[32-34] The electrochemical impedance spectroscopy (EIS) measurement was performed to evaluate the recombination in the DSSC devices and correlate it with the difference in the *V*oc values. Typical EIS Nyquist plots measured in the dark under forward bias (−0.7 V) are shown in Figure 2.6(a). The larger semicircle at lower frequencies represents the interfacial charge-recombination resistances (R_{rec}) at the TiO_2/dye/electrolyte interface.[35] The fitted R_{rec} increased in the order of MA1F-m < MA0F < MA2F < MA1F-o, which is consistent with the sequence of the *V*oc values in the devices. The larger R_{rec} value indicates that the electron recombination from the conduction band to the electrolyte occurred with more difficulty. Clearly, the electron recombination in the devices based on MA1F-m and MA0F

Table 2.4: Dipole moment of the sensitizers calculated using density functional theory.

Dye	Components of dipole moment (Debye)		
	μ_x	μ_y	μ_z
MA0F	-1.5	-6.3	6.3
MA1F-o	-0.8	-5.6	7.0
MA1F-m	-0.9	-5.3	5.5
MA2F	-0.3	-4.6	6.2

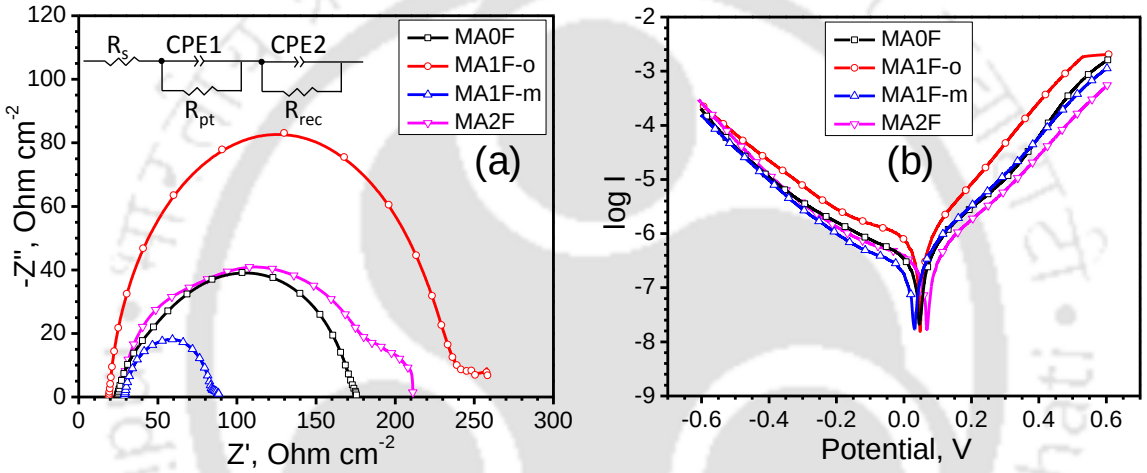

Figure 2.6: (a) Electrochemical impedance spectroscopy spectra (EIS) of DSSC performed at −0.7 V bias under dark condition and (b) Tafel polarization curve of the devices under dark condition.

was faster than that in devices based on MA2F and MA1F-o. By fitting the EIS curves, another important parameter for DSSCs, the electron lifetime (τ), could be extracted from the chemical capacitance (Cμ) and R_{rec} using the equation $\tau = CPE2 \times R_{rec}$. The fitted τ increased in the same order as the recombination resistance, providing an explanation of the difference in *V*oc yielded by the DSSCs based on these four dyes.

The Tafel polarization curves, used to study the back-electron transfer reaction in the DSSC devices, are shown in Figure 2.6(b). This technique is used to analyze the interface charge transfer of the iodine/triiodide redox mediator on the photoanode surface. The kinetics of the anodic reactions occurring at the electrolyte and TiO_2 photoanode interface can be represented using the Butler–Volmer equation (equation 2.1).[36-37]

$$j = -J_0 \left(\exp \frac{\alpha_c nF}{RT} (E - E_{eq}) \right) - \left(\exp \frac{\alpha_a nF}{RT} (E - E_{eq}) \right) \qquad (2.1)$$

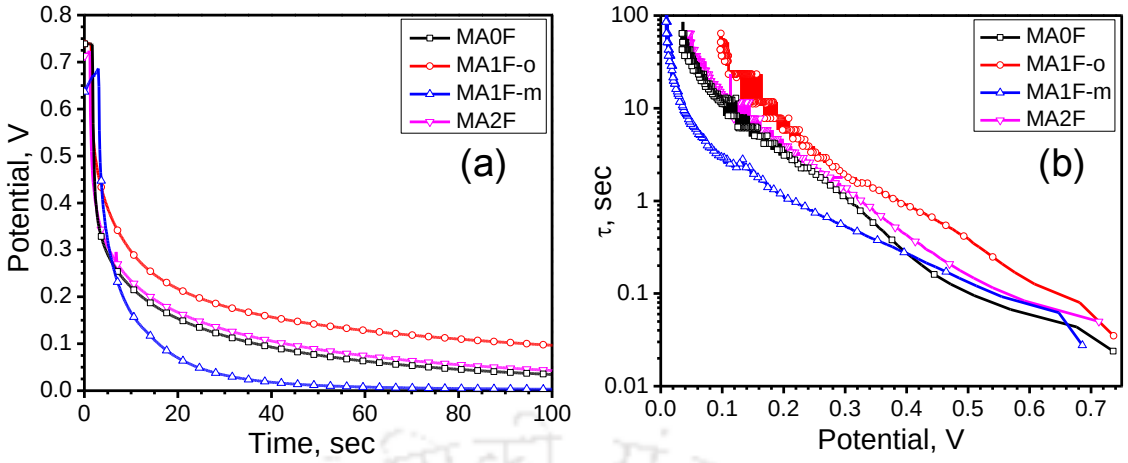

Figure 2.7: (a) Open-circuit voltage decay spectra of the DSSC devices. (b) Decay curves after illumination are turned off.

where J_0 is the exchange current density; Eeq is the equilibrium potential of the iodide/triiodide redox system; E is the applied voltage; α_a and α_c are the anodic and cathodic transfer coefficients, respectively. It is clear from this equation that $J = J_0$ as E = Eeq in the dark condition. Tafel measurement data were fitted using the CorrView software and J_0 was estimated for all the devices and summarized in Table 2.5. From the results obtained, it can be concluded that the trend of J_0 value fits best with R_{pt} and R_{rec} from EIS study and the highest exchange current density of MA1F-o confirms the better performance over the other sensitizers.

Open-circuit voltage decay (OCVD) method is a useful tool to evaluate the electron lifetime and the electron recombination velocity kinetics in DSSCs.[38] To support the mechanism from EIS study, OCVD measurements were performed, where the simulated

Table 2.5: Charge transfer kinetic parameters of the DSSC devices.

Dye	R_{pt} (Ω cm^{-2})[a]	R_{rec} (Ω cm^{-2})[a]	CPE2 (mF)[a]	τ_r (ms)	J_o (μA cm^{-2})[b]
MA0F	24.4	157.1	721.2	113.4	0.581
MA1F-o	19.0	251.7	675.8	170.0	0.995
MA1F-m	28.3	78.18	707.4	62.3	0.397
MA2F	26.7	190.4	601.3	114.0	0.613

[a]From EIS measurements, [b]From Tafel polarization.

solar light was illuminated on the device and a steady-state voltage was obtained after interrupting the illumination (Figure 2.7). This result indicated that the equilibrium between the electron injection and the electron recombination was attained at the TCO surface. A potentiostat monitored the decay of *V*oc of the photoanode with different sensitizer-based devices. Herein, the exponentially fitted decay behavior of MA1F-o was the slowest, suggesting the superior photovoltaic performance.

2.3 Conclusions

In this study, a strong connection between the fluorine substitution and the optoelectronic properties of the dyes have been shown. Four carbazole-based dyes (MA0F, MA1F-o, MA1F-m and MA2F) having the same structure, but different fluorine substitution at phenylene spacer were synthesized involving a simple two-step reaction (Suzuki coupling followed by Knoevenagel condensation reaction). UV-Vis absorption spectroscopic analysis revealed that the dyes with fluorine substitution exhibited red-shifted absorption maxima as compared to the non-fluorinated reference dye MA0F. TRPL studies of the dyes coated onto the TiO_2 and Al_2O_3 film elucidated the role of fluorine in the electron injection. The results indicated that when fluorine substitution was aligned towards the TiO_2 surface, the dye showed a higher electron injection rate. It has also been illustrated that the position and the content of fluorine have a direct influence on the photovoltaic performance of DSSC. As expected from the optical and electrochemical data, with respect to the reference dye MA0F, the dyes MA1F-o and MA2F with a better absorption near the absorption onset resulted in an increased short circuit current, while the dye MA1F-m with the absorption onset almost equal to that of MA0F and very low extinction coefficient resulted in a lower *J*sc. The DSSC device based on the dye MA1F-o gave the best solar cell performance among those based on the other dyes with a PCE of 4.02%, corresponding to a *J*sc = 8.28 mA cm^{-2}, *V*oc = 0.745 V and FF = 0.64. Thus, fluorine substitution could be used as a tool to optimize the optical, electrochemical and electron injection properties to obtain high-efficiency DSSCs.

2.4 Experimental Section

2.4.1 Materials

All the materials used in this work were purchased from different commercial sources and used as received. Precursor 3-bromo-9-hexyl-9H-carbazole was synthesized according

to the reported literature.[39] All the reactions were performed under argon atmosphere. Moisture sensitive reactions were carried out with dried and freshly distilled solvents.

2.4.2 Synthesis

The synthetic procedure and the chemical structure of the dyes are shown in Figure 2.1. The dye MA1F-o was synthesized earlier in our lab.[31] The synthesis of dyes was confirmed by ^{1}H, ^{13}C, ^{19}F NMR and HRMS analysis. (Appendix A, Figure A-3 to 24).

General synthesis of compounds 2a–2d

3-Bromo-9-hexyl carbazole (300 mg, 0.91 mmol), 1 (1.37 mmol) [1a–1d], tetrakis(triphenylphosphine) palladium (30 mg, 0.03 mmol) and potassium carbonate (500 mg, 3.62 mmol) were added in THF/H_2O (3: 1, v/v, 12 mL) solution under an Argon atmosphere and the mixture was refluxed for 12 h. After the completion of the reaction, the mixture was cooled to room temperature and THF was evaporated under a reduced pressure. The compounds were then extracted with chloroform, washed with water, dried over anhydrous sodium sulphate and purified over column chromatography (silica gel, 4–6% ethyl acetate in hexane).

4-(9-Hexyl-9H-carbazol-3-yl)benzaldehyde (2a) ^{1}H NMR (600 MHz, $CDCl_3$): δ (ppm) 9.98 (s, 1H), 8.30 (s, 1H), 8.08 (d, 1H, J = 7.8 Hz), 7.89 (d, 2H, J = 7.8 Hz), 7.80 (d, 2H, J = 7.8 Hz), 7.68 (d, 1H, J = 8.4 Hz), 7.44–7.40 (m, 2H), 7.36 (d, 1H, J = 8.4 Hz), 7.19 (t, 1H, J = 7.2 Hz), 4.25 (t, 2H, J = 7.2 Hz), 1.82 (q, 2H, J = 7.2 Hz), 1.34–1.18 (m, 6H), 0.79 (t, 3H, J = 7.2 Hz). ^{13}C NMR (150 MHz, $CDCl_3$): δ (ppm) 192.23, 148.47, 141.18, 140.81, 134.63, 130.65, 130.58, 127.74, 126.33, 125.35, 123.72, 123.05, 120.67, 119.49, 119.45, 109.39, 109.22, 43.48, 31.78, 29.17, 27.18, 22.75, 14.21. HRMS (ESI) m/z: $[M + H]^+$ calcd for $C_{25}H_{26}NO$ 356.2014, found 356.2001.

3-Fluoro-4-(9-hexyl-9H-carbazol-3-yl)benzaldehyde (2c) ^{1}H NMR (600 MHz, $CDCl_3$): δ (ppm) 9.93 (s,1H), 8.25 (s, 1H), 8.05 (d, 1H, J = 7.8 Hz), 7.68–7.60 (m, 4H), 7.43–7.40 (m, 2H), 7.35 (d, 1H, J = 7.8 Hz), 7.18 (t, 1H, J = 7.2 Hz), 4.24 (t, 2H, J = 7.2 Hz), 1.81 (q, 2H, J = 7.8 Hz), 1.35–1.18 (m, 6H), 0.79 (t, 3H, J = 7.2 Hz). 13C NMR (150 MHz, $CDCl_3$): δ (ppm) 190.91, 161.12, 159.47, 141.09, 140.69, 136.62, 136.53, 131.76, 131.74, 126.89, 126.32, 125.14, 123.36, 122.97, 121.41, 120.68, 119.48, 116.68, 116.52, 109.19, 109.02, 43.45, 31.77, 29.16, 27.17, 22.74, 14.21. ^{19}F NMR (565 MHz, $CDCl_3$): δ

(ppm) −116.43. HRMS (ESI) m/z: $[M + H]^+$ calcd for $C_{25}H_{25}FNO$ 374.1920, found 374.1932.

2,3-Difluoro-4-(9-hexyl-9H-carbazol-3-yl)benzaldehyde (2d) ^{1}H NMR (600 MHz, $CDCl_3$): δ (ppm) 10.29 (s, 1H), 8.25 (s, 1H), 8.05 (d, 1H, J = 7.8 Hz), 7.62 (t, 2H, J = 8.4 Hz), 7.44–7.36 (m, 5H), 7.21–7.17 (m, 1H), 4.25 (t, 2H, J = 7.2 Hz), 1.81 (q, 2H, J = 7.2 Hz), 1.33–1.21 (m, 6H), 0.79 (t, 3H, J = 7.2 Hz). ^{13}C NMR (150 MHz, $CDCl_3$): δ (ppm) 186.20, 154.73, 152.87, 148.95, 147.28, 141.12, 140.93, 138.42, 138.36, 126.68, 126.48, 121.36, 120.71, 119.64, 109.26, 109.17, 43.48, 31.76, 29.16, 27.17, 22.74, 14.20. ^{19}F NMR (565 MHz, $CDCl_3$): δ (ppm) −143.24 (d, 1F, J = 20.4 Hz), −146.60 (d, 1F, J = 20.4 Hz). HRMS (ESI) m/z: $[M + H]^+$ calcd for $C_{25}H_{24}F_2NO$ 392.1826, found 392.1837.

General synthesis of dyes (MA0F, MA1F-o, MA1F-m, and MA2F)

In a clean and dry round bottom flask, a mixture of the compound **2** (0.25 mmol) [2a–2d] and cyanoacetic acid (0.3 mmol) was dissolved in acetonitrile and sparged with Argon. Finally, piperidine (0.03 mmol) was added to the reaction mixture and it was refluxed for 10 h. The solution was then allowed to cool to room temperature and acetonitrile was evaporated using a rotary evaporator. The compound was finally extracted with chloroform, washed with 0.1 M HCl, and dried over anhydrous Na_2SO_4. The solid was finally washed with hexane and 2% ethyl acetate in hexane to get the pure compounds.

2-Cyano-3-(4-(9-hexyl-9H-carbazol-3-yl)phenyl)acrylic acid (MA0F) M.p. 228–230 °C. IR (KBr, cm^{-1}): 3450, 2955, 2927, 2854, 2216, 1700, 1596, 1478, 1352, 1192. ^{1}H NMR (600 MHz, DMSO-d6): δ (ppm) 8.60 (s, 1H), 8.26 (d, 1H, J = 7.2 Hz), 8.00–7.93 (m, 5H), 7.86 (d, 1H, J = 8.4 Hz), 7.69 (d, 1H, J = 8.4 Hz), 7.62 (d, 1H, J = 8.4 Hz), 7.47 (t, 1H, J = 7.8 Hz), 7.23 (t, 1H, J = 7.2 Hz), 4.42 (t, 2H, J = 6.6 Hz), 1.78 (q, 2H, J = 7.2 Hz), 1.31–1.20 (m, 6H), 0.81 (t, 3H, J = 7.2 Hz). ^{13}C NMR (150 MHz, $CDCl_3$): δ (ppm) 152.30, 144.32, 140.39, 139.73, 131.16, 130.04, 126.53, 125.07, 124.87, 122.95, 122.73, 120.53, 118.64, 118.16, 114.26, 108.36, 108.11, 42.45, 31.42, 28.58, 26.73, 22.52, 14.04. HRMS (ESI) m/z: $[M + H]^+$ calcd for $C_{28}H_{27}N_2O_2$ 423.2073, found 423.2079.

2-Cyano-3-(3-fluoro-4-(9-hexyl-9H-carbazol-3-l)phenyl)acrylic acid (MA1F-m) M.p. 134–136 °C. IR (KBr, cm^{-1}): 3439, 2956, 2924, 2852, 2222, 1711, 1594, 1491, 1383, 1249, 1082. ^{1}H NMR (600 MHz, DMSO-d6): δ (ppm) 8.45 (s, 1H), 8.23 (d, 1H, J = 7.2 Hz), 8.13 (bs, 1H), 7.91 (bs, 2H), 7.83 (t, 1H, J = 7.8 Hz), 7.72 (s, 2H), 7.64 (d, 1H, J = 7.8 Hz), 7.49 (t, 1H, J = 7.2 Hz), 7.23 (t, 1H, J = 7.2 Hz), 4.43 (bs, 2H), 1.79 (bs, 2H), 1.29–

1.22 (m, 6H), 0.81 (t, 3H, J = 6.6 Hz). ^{13}C NMR (150 MHz, DMSO-d6): δ (ppm): 142.73, 140.52, 139.93, 129.96, 129.80, 128.02, 127.33, 126.81, 125.99, 124.65, 123.00, 122.75, 122.24, 120.62, 118.94, 118.66, 109.78, 109.46, 42.35, 30.95, 28.48, 26.10, 21.98, 13.82. ^{19}F NMR (565 MHz, $CDCl_3$): δ (ppm) −117.30. HRMS (ESI) m/z: $[M + H]^+$ calcd for $C_{28}H_{26}FN_2O_2$ 441.1978, found 441.1866.

2-Cyano-3-(2,3-difluoro-4-(9-hexyl-9H-carbazol-3-yl)phenyl)acrylic acid (MA2F) M.p. 196–198 °C. IR (KBr, cm^{-1}): 3451, 2957, 2924, 2852, 2227, 1701, 1588, 1492, 1428, 1358, 1270. ^{1}H NMR (600 MHz, $CDCl_3$): δ (ppm) 8.45 (s, 1H), 8.22 (d, 1H, J = 7.8 Hz), 8.11 (bs, 1H), 8.02 (t, 1H, J = 7.8/7.2 Hz), 7.70 (s, 2H), 7.61 (t, 2H, J = 8.4 Hz), 7.48 (t, 1H, J = 7.8 Hz), 7.22 (t, 1H, J = 7.2 Hz), 5.75 (s, 1H), 4.40 (t, 2H, J = 7.2 Hz), 1.76 (q, 2H, J = 7.2 Hz), 1.29–1.18 (m, 6H), 0.79 (t, 3H, J = 7.2 Hz). ^{13}C NMR (150 MHz, DMSO-d6): δ (ppm) 149.83, 148.02, 146.60, 140.50, 140.05, 137.07, 133.08, 126.46, 126.21, 125.58, 123.83, 122.93, 122.43, 122.03, 121.41, 120.94, 120.62, 119.18, 118.63, 109.62, 42.40, 30.98, 28.50, 26.13, 22.02, 13.84. ^{19}F NMR (565 MHz, $CDCl_3$): δ (ppm) −139.70 (d, 1F, J = 20.3 Hz), −143.84 (d, 1F, J = 21.55 Hz). HRMS (ESI) m/z: $[M + H]^+$ calcd for $C_{28}H_{25}F_2N_2O_2$ 459.1884, found 459.1876.

2.4.3 Fabrication of solar cell

The TiO_2 photoelectrodes were prepared by following the previously reported process.[31] In brief, a transparent layer of TiO_2 with a thickness of 12 μm was used as a photoanode. A TCO glass substrate on deposition of TiO_2 blocking (ethanolic titanium tetraisopropoxide) layer was calcined in a tubular furnace at 450 °C for 10 min. Then, ethyl cellulose and α-terpineol were dispersed to make a paste and the film was prepared by doctor blade method on the prepared TiO_2 thin film as the TCO blocking layer. The electrode was cooled to 60 °C and soaked into various sensitizer solutions (20 mM in dichloromethane and ethanol mixture) for 24 h. The counter electrode was prepared by a spin coating method using Pt salt (50 mM H_2PtCl_6 solution in IPA) and the electrode was calcined at 450 °C for 10 min. DSSC was assembled in a sandwich type configuration and sealed. The electrolyte consisted of 0.6 M BMImI (1-butyl-3-methylimidazolium iodide), 0.03 M iodine and 0.5 M 4-tert-butyl pyridine. 0.1 M guanidium thiocyanate (GuSCN) in 3-methoxy propionitrile was inserted through the predrilled holes onto the counter electrodes. The devices were stored in the dark for 24 h prior to the photovoltaic measurements.

2.4.4 Characterization

^{1}H, ^{13}C and ^{19}F NMR spectra were recorded on a Varian AS400 (400 MHz) or Brucker Ascend 600 (600 MHz) spectrometers, using solvent $CDCl_3$ or DMSO-d6. HRMS spectra were recorded on a Waters (Micro mass MSTechnologies) Q-Tof MS Analyzer spectrometer. The UV-vis absorption spectra for solution were recorded on a Perkin-Elmer Lambda 35 spectrometer and that for film/dye coated TiO_2 films on a Perkin-Elmer Lambda 75 spectrometer. Electrochemical measurements were carried out using a CH Instruments 760D electrochemical workstation at a scan rate of 50 mV s^{-1}. A three-electrode cell with platinum wire counter electrode, glassy carbon working electrode and Ag/Ag+ reference electrode was employed. Tetrabutylammonium hexafluorophosphate (0.1 M) in acetonitrile was used as supporting electrolyte and Fc^{+}/Fc couple was used as internal reference. A thin film was casted from 10 µL, 1 mM solution of dye in DCM on the working electrode and the measurements were performed at room temperature under inert atmosphere. Time-resolved fluorescence studies were performed using an Edinburgh Life Spec II instrument. Veeco Dektak 150 Surface Profilometer was used for the measurement of the TiO2 film thickness. Oriel Sol 3A solar simulator from Newport, with a 500 W xenon lamp, connected to AM 1.5 Globe filter and a Keithley-2400 digital source meter was used for *IV* measurements. A Solartron 1287 gain phase analyzer was used for Impedance Spectroscopy (EIS) measurements and analysis was performed by sweeping frequency from 120 KHz to 0.1Hz in dark condition under a bias of -0.65V DC with a small AC perturbation (10 mV). Open-circuit voltage decay (OCVD) and Tafel polarization plot were obtained using a Solartron electrochemical analyzer by sweeping potential +0.65 in dark with 25mV s^{-1} scan rate. IPCE measurement was carried out on Optosolar SR 300, Gemany, where a 250 W xenon lamp was used as the light source. Electronic distribution of frontier molecular orbitals was investigated in Gaussian 09 software package. Calculations were carried out using Density functional theory (DFT) with B3LYP/6-31G(d,p) level.

2.5 References

(1) Bessho, T.; Zakeeruddin, S. M.; Yeh, C.-Y.; Diau, E. W.-G.; Grätzel, M. *Angew. Chem., Int. Ed.* **2010,** *49*, 6646-6649.

(2) Yella, A.; Mai, C.-L.; Zakeeruddin, S. M.; Chang, S.-N.; Hsieh, C.-H.; Yeh, C.-Y.; Grätzel, M. *Angew. Chem., Int. Ed.* **2014,** *53*, 2973-2977.

(3) Urbani, M.; Grätzel, M.; Nazeeruddin, M. K.; Torres, T. *Chem. Rev.* **2014,** *114*, 12330-12396.

(4) Higashino, T.; Imahori, H. *Dalton Trans.* **2015,** *44*, 448-463.

(5) Higashino, T.; Fujimori, Y.; Sugiura, K.; Tsuji, Y.; Ito, S.; Imahori, H. *Angew. Chem., Int. Ed.* **2015,** *54*, 9052-9056.

(6) Wang, P.; Zakeeruddin, S. M.; Moser, J. E.; Nazeeruddin, M. K.; Sekiguchi, T.; Grätzel, M. *Nat. Mater.* **2003,** *2*, 402-407.

(7) Kuang, D.; Klein, C.; Ito, S.; Moser, J.-E.; Humphry-Baker, R.; Evans, N.; Duriaux, F.; Grätzel, C.; Zakeeruddin, S. M.; Grätzel, M. *Adv. Mater.* **2007,** *19*, 1133-1137.

(8) Chen, C.-Y.; Wang, M.; Li, J.-Y.; Pootrakulchote, N.; Alibabaei, L.; Ngoc-le, C.-h.; Decoppet, J.-D.; Tsai, J.-H.; Grätzel, C.; Wu, C.-G.; Zakeeruddin, S. M.; Grätzel, M. *ACS Nano* **2009,** *3*, 3103-3109.

(9) Yao, Z.; Zhang, M.; Wu, H.; Yang, L.; Li, R.; Wang, P. *J. Am. Chem. Soc.* **2015,** *137*, 3799-3802.

(10) Kakiage, K.; Aoyama, Y.; Yano, T.; Oya, K.; Fujisawa, J.-i.; Hanaya, M. *Chem. Commun.* **2015,** *51*, 15894-15897.

(11) Liang, M.; Chen, J. *Chem. Soc. Rev.* **2013,** *42*, 3453-3488.

(12) Mishra, A.; Fischer, M. K. R.; Bäuerle, P. *Angew. Chem., Int. Ed.* **2009,** *48*, 2474-2499.

(13) Liyanage, N. P.; Yella, A.; Nazeeruddin, M.; Grätzel, M.; Delcamp, J. H. *ACS Appl. Mater. Interfaces* **2016,** *8*, 5376-5384.

(14) Kakiage, K.; Aoyama, Y.; Yano, T.; Otsuka, T.; Kyomen, T.; Unno, M.; Hanaya, M. *Chem. Commun.* **2014,** *50*, 6379-6381.

(15) Clifford, J. N.; Martínez-Ferrero, E.; Viterisi, A.; Palomares, E. *Chem. Soc. Rev.* **2011,** *40*, 1635-1646.

(16) O'Regan, B. C.; Walley, K.; Juozapavicius, M.; Anderson, A.; Matar, F.; Ghaddar, T.; Zakeeruddin, S. M.; Klein, C.; Durrant, J. R. *J. Am. Chem. Soc.* **2009,** *131*, 3541-3548.

(17) Chang, Y. J.; Chow, T. J. *J. Mater. Chem.* **2011,** *21*, 9523-9531.

(18) Soni, S. S.; Fadadu, K. B.; Vaghasiya, J. V.; Solanki, B. G.; Sonigara, K. K.; Singh, A.; Das, D.; Iyer, P. K. *J. Mater. Chem. A* **2015,** *3*, 21664-21671.

(19) Hara, K.; Sato, T.; Katoh, R.; Furube, A.; Ohga, Y.; Shinpo, A.; Suga, S.; Sayama, K.; Sugihara, H.; Arakawa, H. *J. Phys. Chem. B* **2003,** *107*, 597-606.

(20) Brédas, J. L.; Heeger, A. J. *Chem. Phys. Lett.* **1994,** *217*, 507-512.

(21) Chen, D.-Y.; Hsu, Y.-Y.; Hsu, H.-C.; Chen, B.-S.; Lee, Y.-T.; Fu, H.; Chung, M.-W.; Liu, S.-H.; Chen, H.-C.; Chi, Y.; Chou, P.-T. *Chem. Commun.* **2010,** *46*, 5256-5258.

(22) Chen, B.-S.; Chen, D.-Y.; Chen, C.-L.; Hsu, C.-W.; Hsu, H.-C.; Wu, K.-L.; Liu, S.-H.; Chou, P.-T.; Chi, Y. *J. Mater. Chem.* **2011,** *21*, 1937-1945.

(23) Scrascia, A.; De Marco, L.; Laricchia, S.; Picca, R. A.; Carlucci, C.; Fabiano, E.; Capodilupo, A. L.; Della Sala, F.; Gigli, G.; Ciccarella, G. *J. Mater. Chem. A* **2013,** *1*, 11909-11921.

(24) Lin, Y.-D.; Chow, T. J. *J Photochem. Photobiol. A* **2012,** *230*, 47-54.

(25) Lee, M.-W.; Kim, J.-Y.; Son, H. J.; Kim, J. Y.; Kim, B.; Kim, H.; Lee, D.-K.; Kim, K.; Lee, D.-H.; Ko, M. J. *Sci. Rep.* **2015,** *5*, 7711.

(26) Mathew, S.; Iijima, H.; Toude, Y.; Umeyama, T.; Matano, Y.; Ito, S.; Tkachenko, N. V.; Lemmetyinen, H.; Imahori, H. *J. Phys. Chem. C* **2011,** *115*, 14415-14424.

(27) Zhu, W.; Wu, Y.; Wang, S.; Li, W.; Li, X.; Chen, J.; Wang, Z.-s.; Tian, H. *Adv. Funct. Mater.* **2011,** *21*, 756-763.

(28) Sek, D.; Bijak, K.; Grucela-Zajac, M.; Filapek, M.; Skorka, L.; Siwy, M.; Janeczek, H.; Schab-Balcerzak, E. *Synth. Met.* **2012,** *162*, 1623-1635.

(29) Lu, H.-P.; Tsai, C.-Y.; Yen, W.-N.; Hsieh, C.-P.; Lee, C.-W.; Yeh, C.-Y.; Diau, E. W.-G. *J. Phys. Chem. C* **2009,** *113*, 20990-20997.

(30) Chetia, T. R.; Ansari, M. S.; Qureshi, M. *J. Mater. Chem. A* **2016,** *4*, 5528-5541.

(31) Bhim Raju, T.; Vaghasiya, J. V.; Afroz, M. A.; Soni, S. S.; Iyer, P. K. *Phys. Chem. Chem. Phys.* **2016,** *18*, 28485-28491.

(32) Li, L.-L.; Chang, Y.-C.; Wu, H.-P.; Diau, E. W.-G. *Int. Rev. Phys. Chem.* **2012,** *31*, 420-467.

(33) Mane, S. B.; Hu, J.-Y.; Chang, Y.-C.; Luo, L.; Diau, E. W.-G.; Hung, C.-H. *Chem. Commun.* **2013,** *49*, 6882-6884.

(34) Griffith, M. J.; Sunahara, K.; Wagner, P.; Wagner, K.; Wallace, G. G.; Officer, D. L.; Furube, A.; Katoh, R.; Mori, S.; Mozer, A. J. *Chem. Commun.* **2012,** *48*, 4145-4162.

(35) van de Lagemaat, J.; Park, N. G.; Frank, A. J. *J. Phys. Chem. B* **2000,** *104*, 2044-2052.

(36) Soderberg, J. N.; Co, A. C.; Sirk, A. H. C.; Birss, V. I. *J. Phys. Chem. B* **2006,** *110*, 10401-10410.

(37) Petrii, O. A.; Nazmutdinov, R. R.; Bronshtein, M. D.; Tsirlina, G. A. *Electrochim. Acta* **2007,** *52*, 3493-3504.

(38) Bisquert, J.; Zaban, A.; Greenshtein, M.; Mora-Seró, I. *J. Am. Chem. Soc.* **2004,** *126*, 13550-13559.

(39) Feng, G.-L.; Lai, W.-Y.; Ji, S.-J.; Huang, W. *Tetrahedron Lett.* **2006,** *47*, 7089-7092.

Appendix A: Additional data for chapter 2

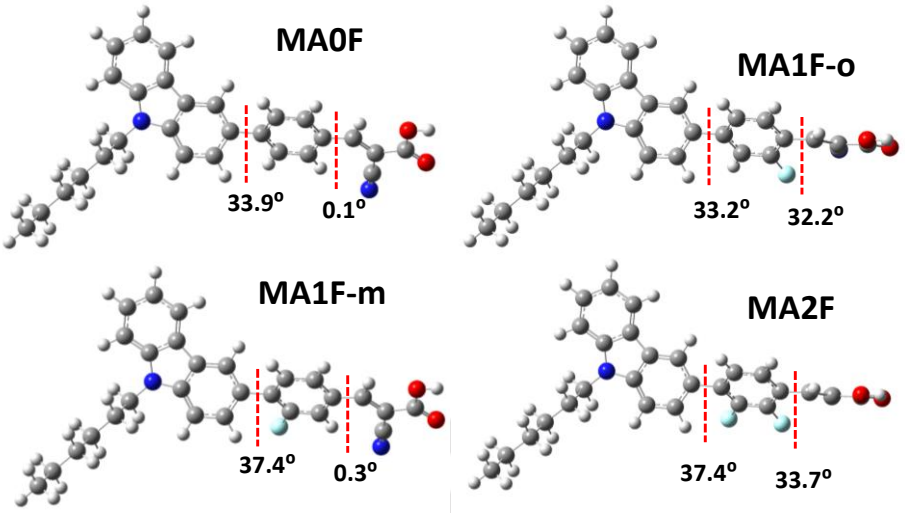

Figure A-1: Optimized structure of dyes showing dihedral angles.

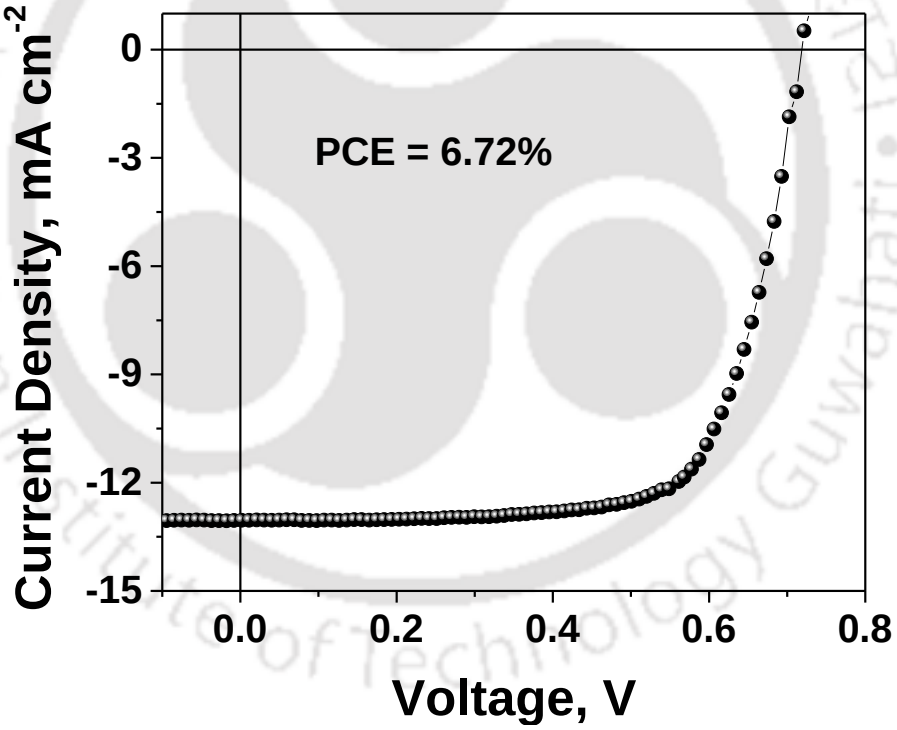

Figure A-2: *J-V* characteristics curve of DSSC device fabricated using N719 dye.

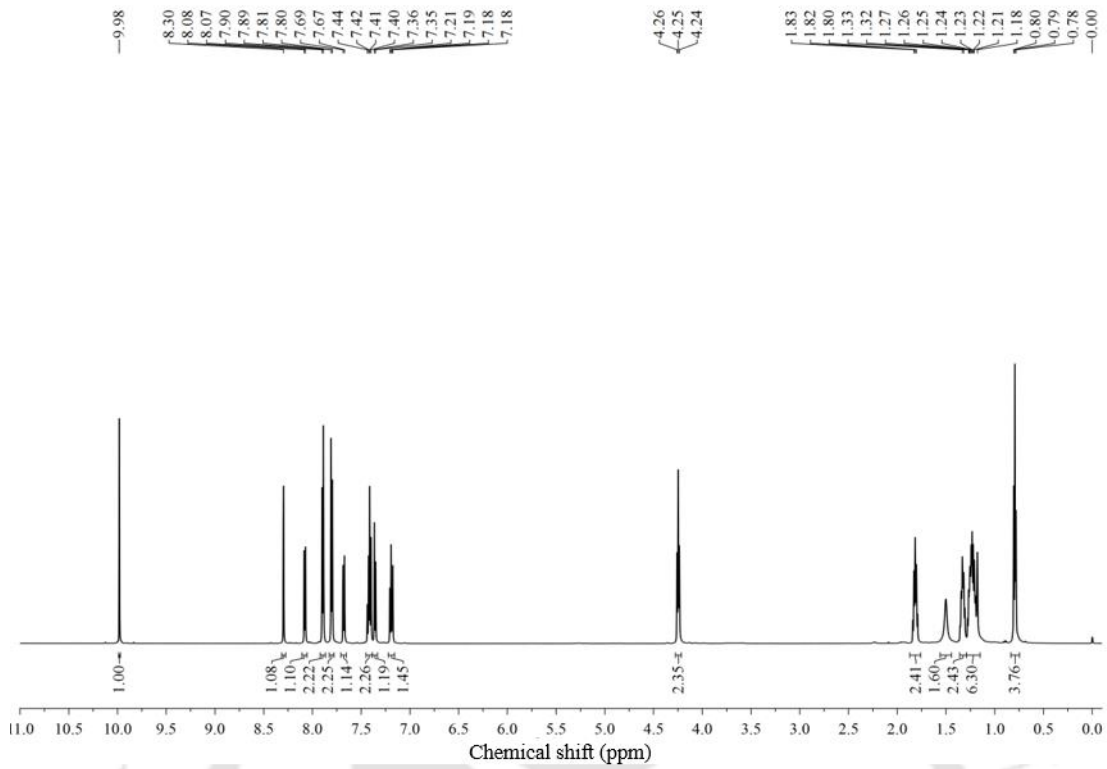

Figure A-3: ^{1}H NMR of 4-(9-hexyl-9H-carbazol-3-yl)benzaldehyde (2a).

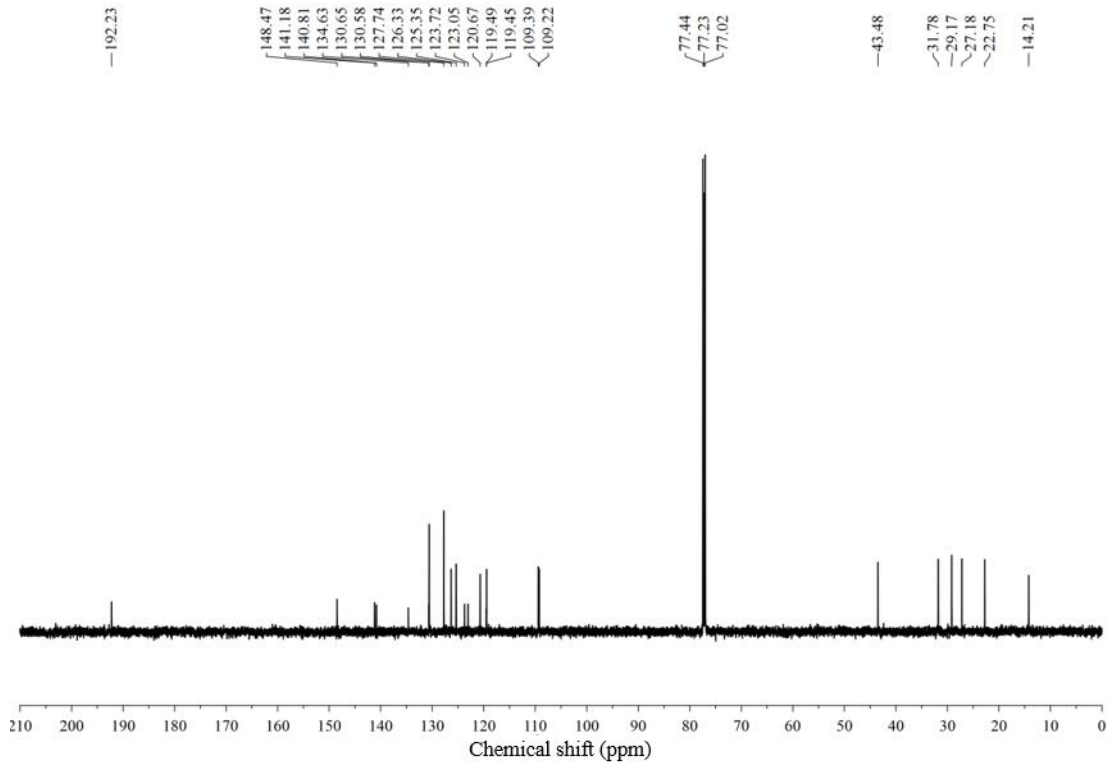

Figure A-4: ^{13}C NMR of 4-(9-hexyl-9H-carbazol-3-yl)benzaldehyde (2a).

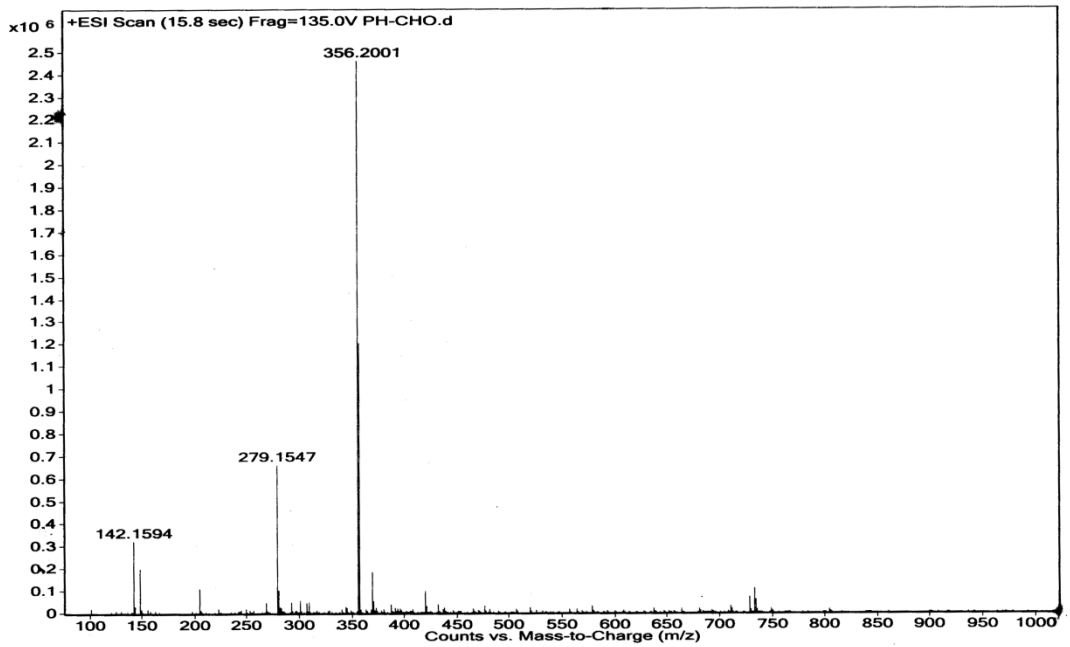

Figure A-5: HRMS (ESI) of 4-(9-hexyl-9H-carbazol-3-yl)benzaldehyde (2a).

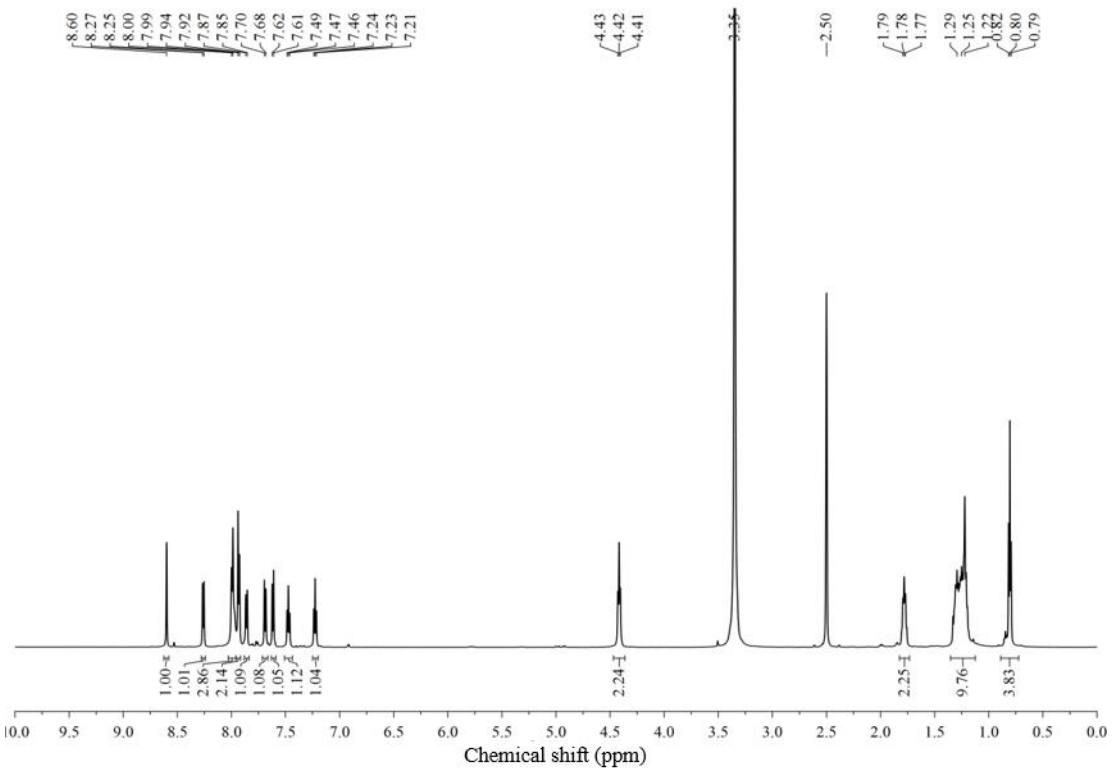

Figure A-6: ^{1}H NMR of 2-cyano-3-(4-(9-hexyl-9H-carbazol-3-yl)phenyl)acrylic acid (MA0F).

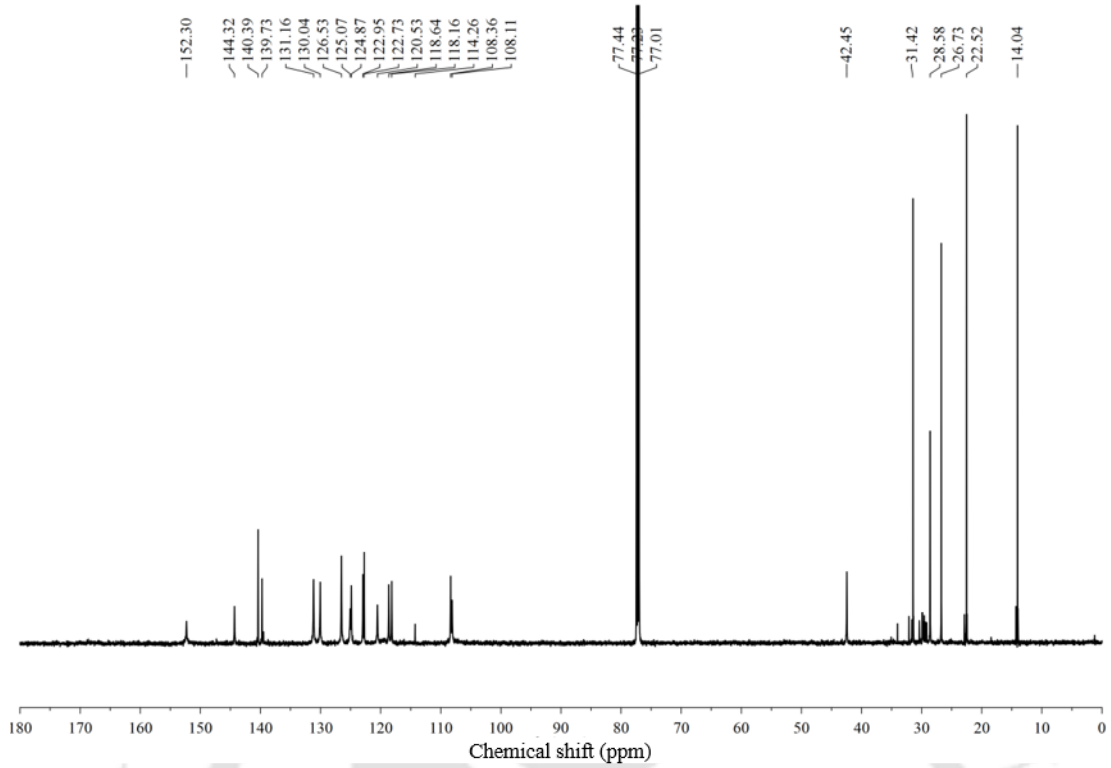

Figure A-7: ^{13}C NMR of 2-cyano-3-(4-(9-hexyl-9H-carbazol-3-yl)phenyl)acrylic acid (MA0F).

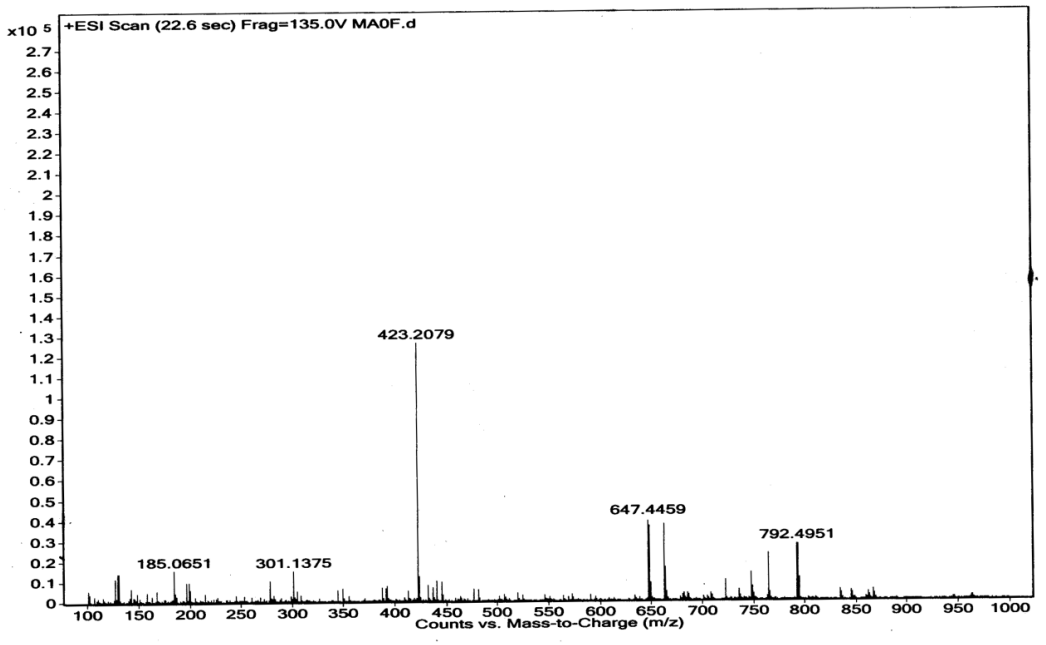

Figure A-8: HRMS (ESI) of 2-cyano-3-(4-(9-hexyl-9H-carbazol-3-yl)phenyl)acrylic acid (MA0F).

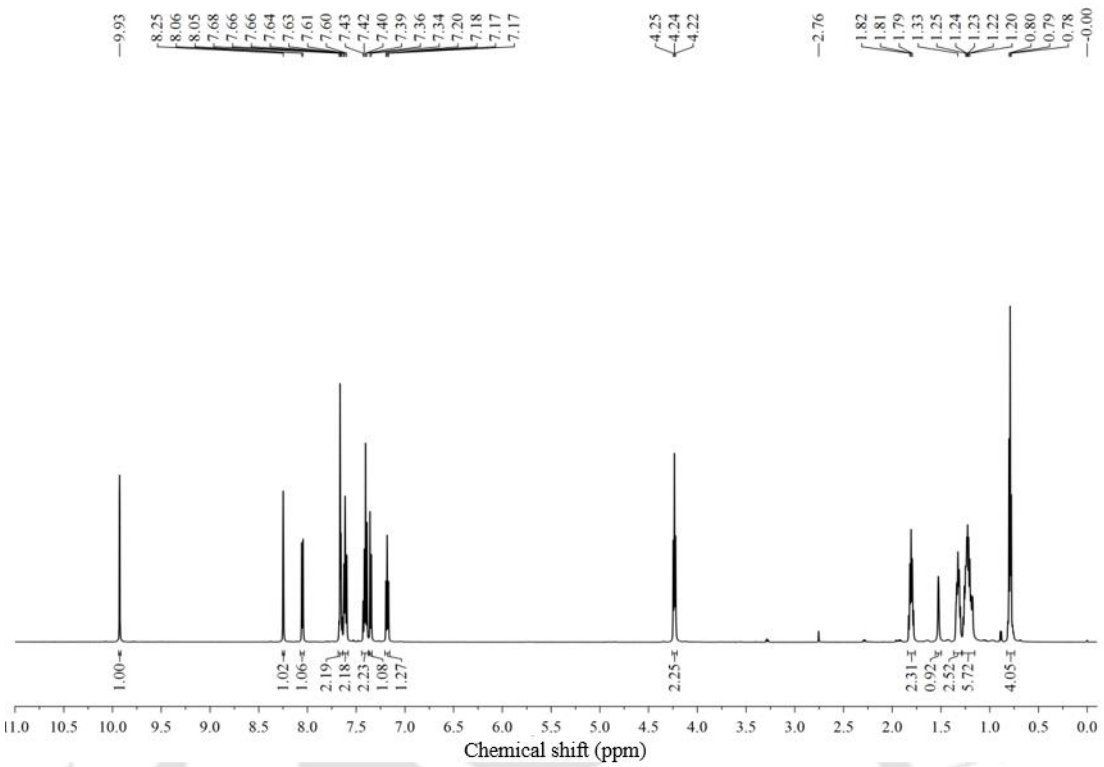

Figure A-9: ^{1}H NMR of 3-fluoro-4-(9-hexyl-9H-carbazol-3-yl)benzaldehyde (2c).

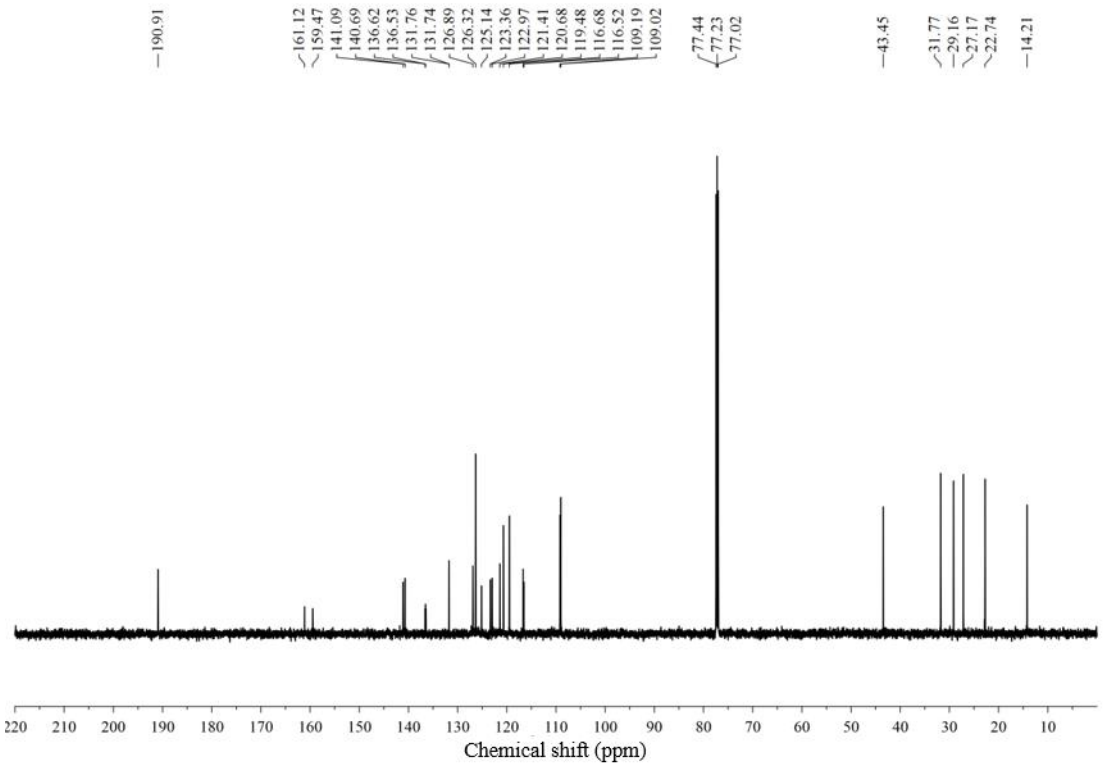

Figure A-10: ^{13}C NMR of 3-fluoro-4-(9-hexyl-9H-carbazol-3-yl)benzaldehyde (2c).

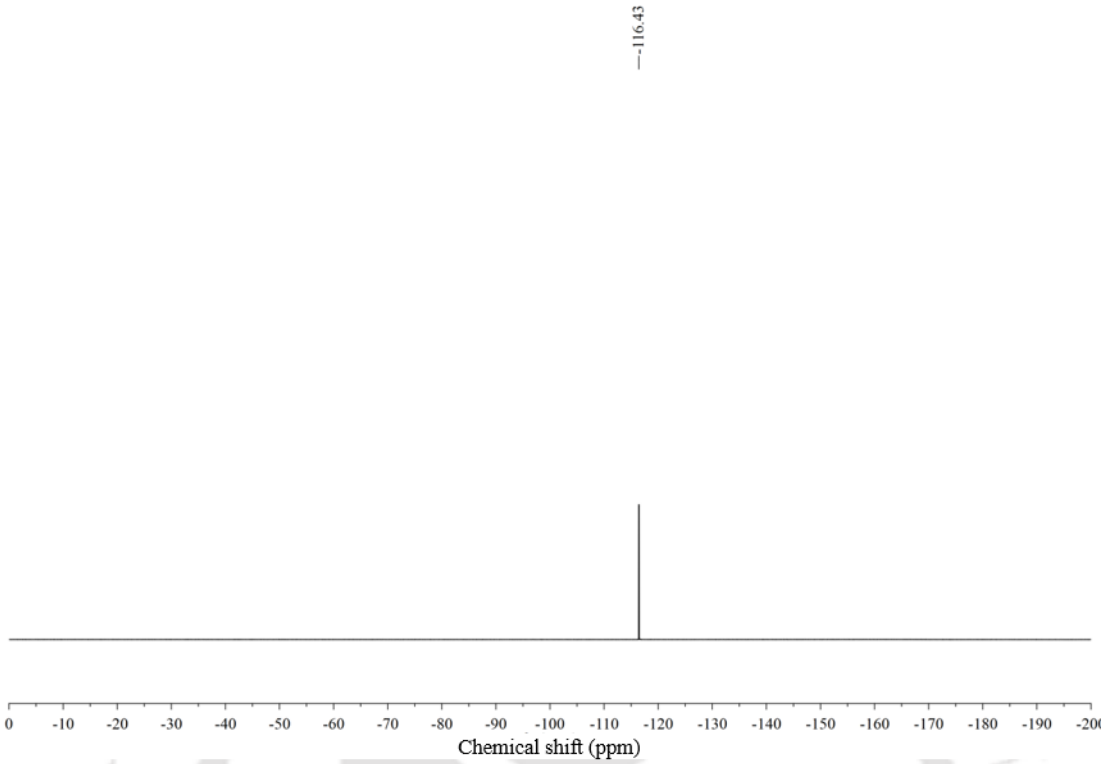

Figure A-11: ^{19}F NMR of 3-fluoro-4-(9-hexyl-9H-carbazol-3-yl)benzaldehyde (2c).

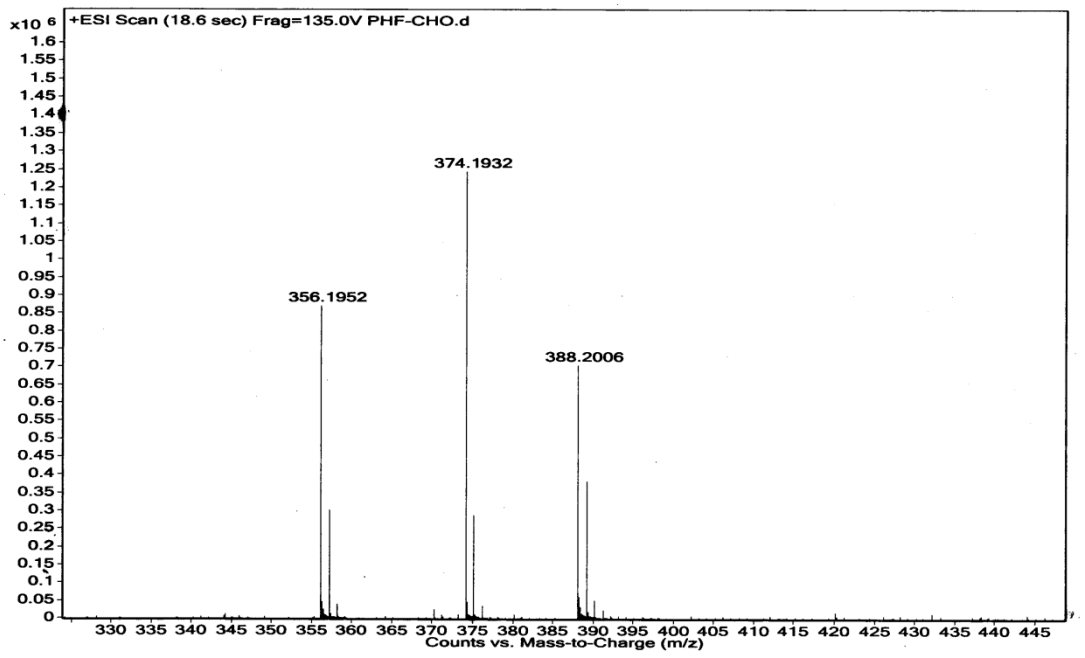

Figure A-12: HRMS (ESI) of 3-fluoro-4-(9-hexyl-9H-carbazol-3-yl)benzaldehyde (2c).

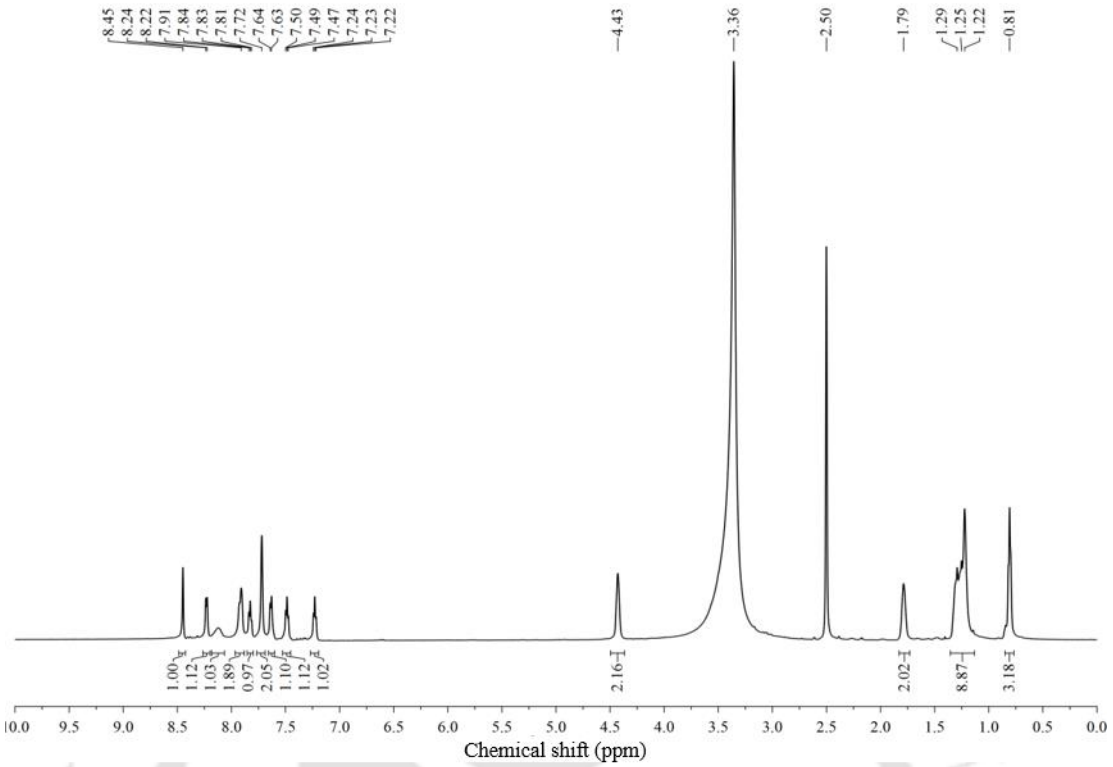

Figure A-13: ^{1}H NMR of 2-cyano-3-(3-fluoro-4-(9-hexyl-9H-carbazol-3-yl)phenyl)acrylic acid (MA1F-m).

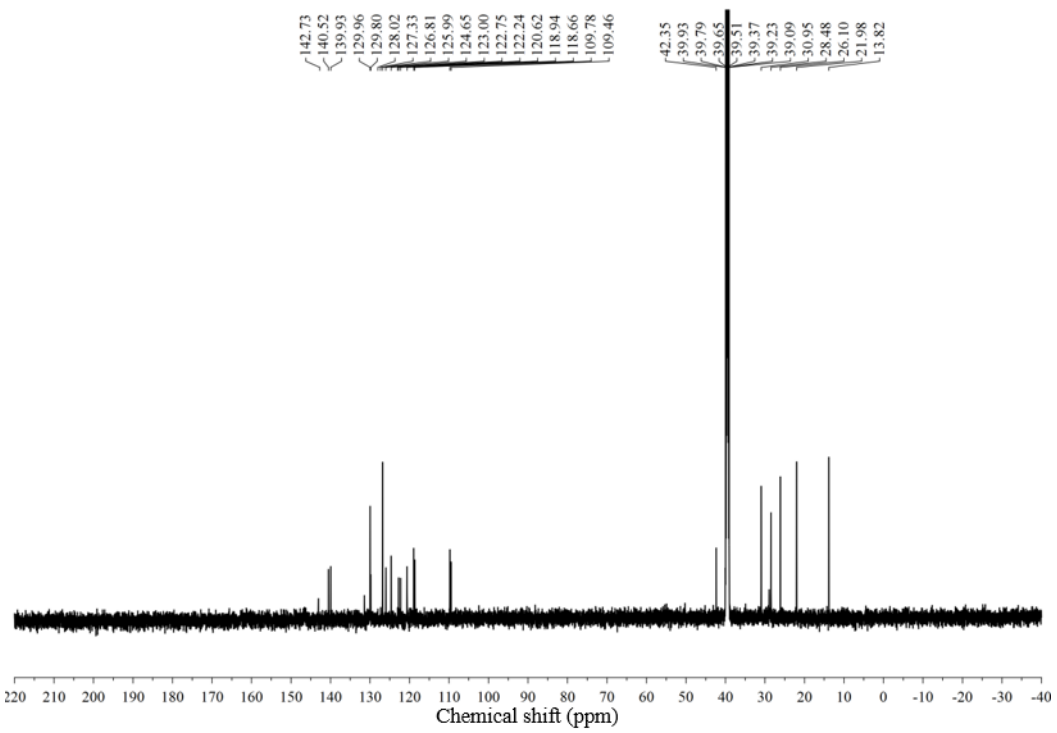

Figure A-14: ^{13}C NMR of 2-cyano-3-(3-fluoro-4-(9-hexyl-9H-carbazol-3-yl)phenyl)acrylic acid (MA1F-m).

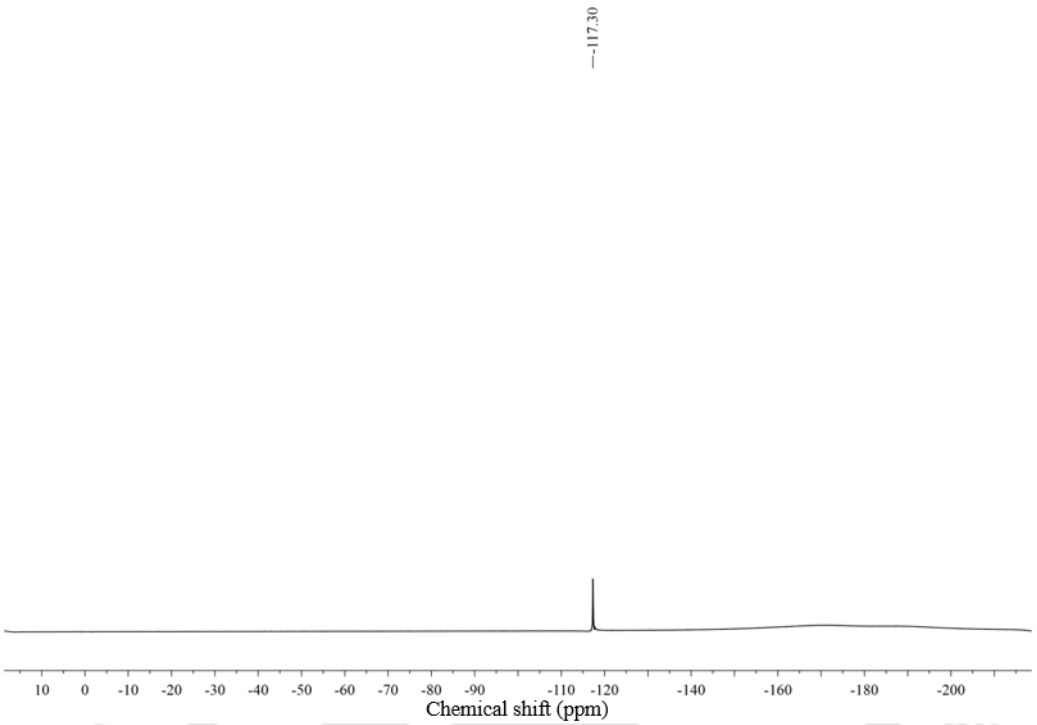

Figure A-15: ^{19}F NMR of 2-cyano-3-(3-fluoro-4-(9-hexyl-9H-carbazol-3-yl)phenyl)acrylic acid (MA1F-m).

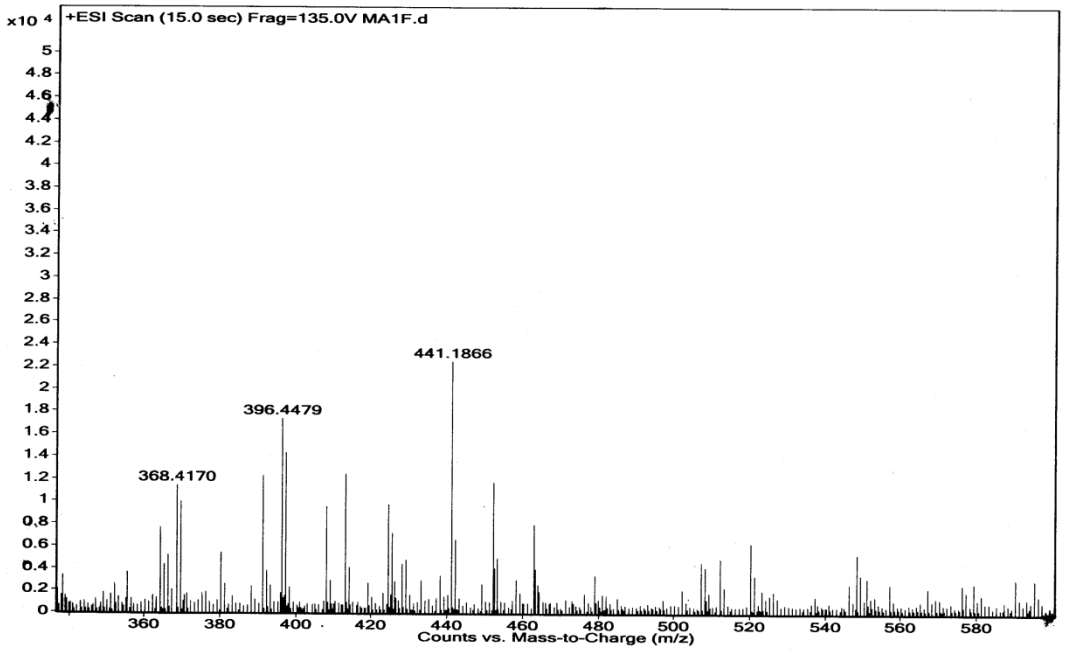

Figure A-16: HRMS (ESI) of 2-cyano-3-(3-fluoro-4-(9-hexyl-9H-carbazol-3-yl)phenyl)acrylic acid (MA1F-m).

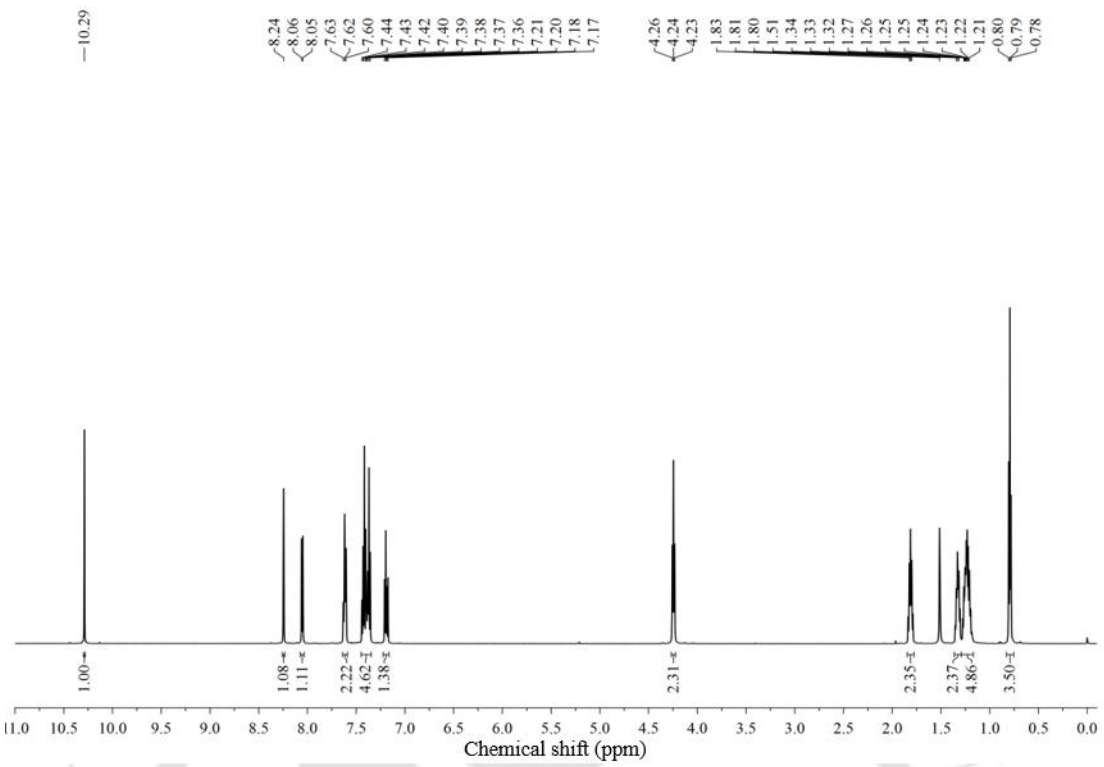

Figure A-17: ^{1}H NMR of 2,3-difluoro-4-(9-hexyl-9H-carbazol-3-yl)benzaldehyde (2d).

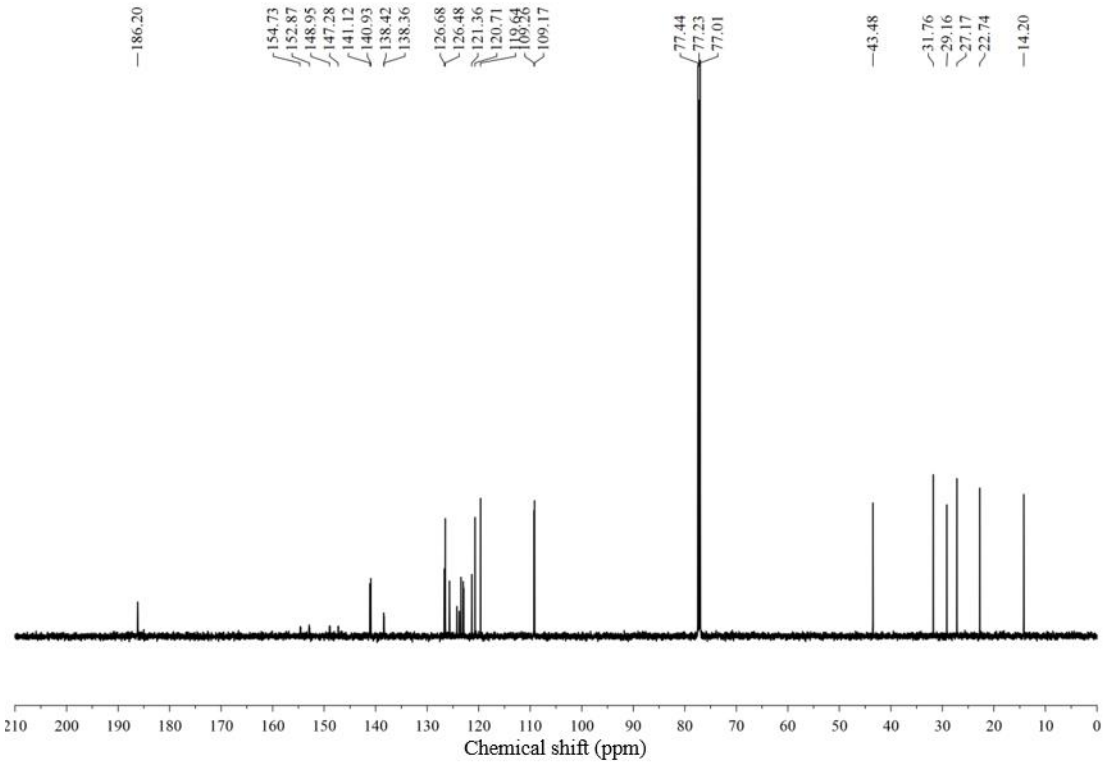

Figure A-18: ^{13}C NMR of 2,3-difluoro-4-(9-hexyl-9H-carbazol-3-yl)benzaldehyde (2d).

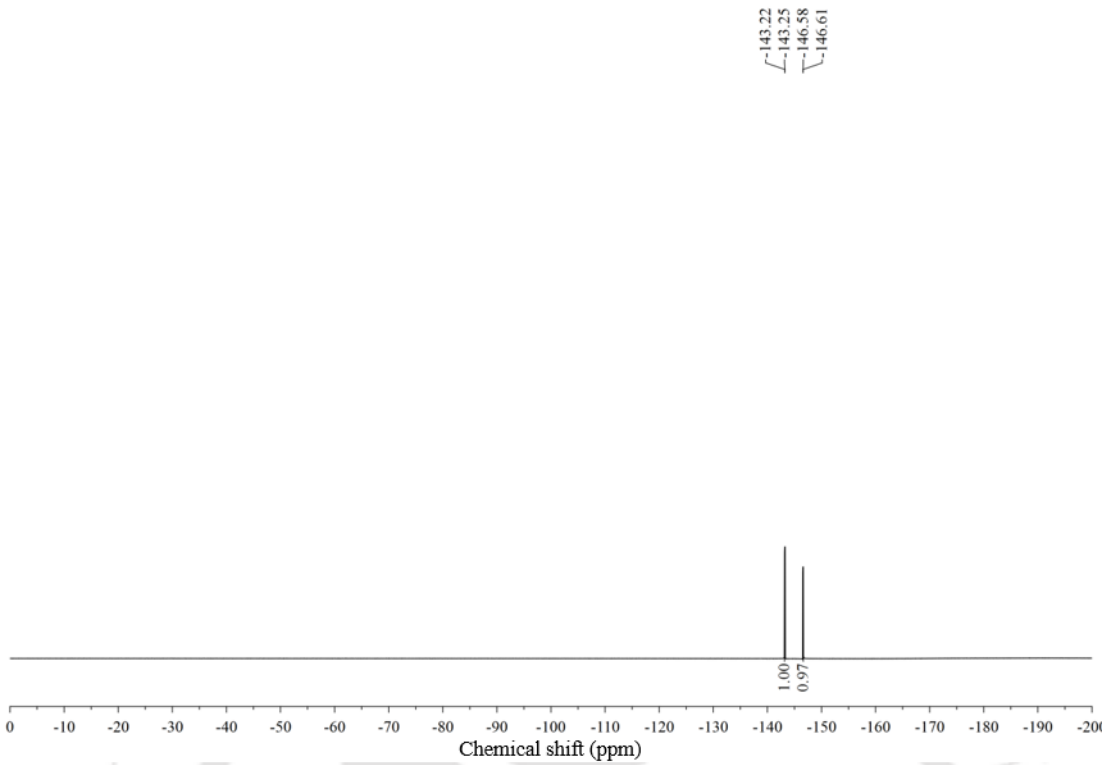

Figure A-19: ^{19}F NMR of 2,3-difluoro-4-(9-hexyl-9H-carbazol-3-yl)benzaldehyde (2d).

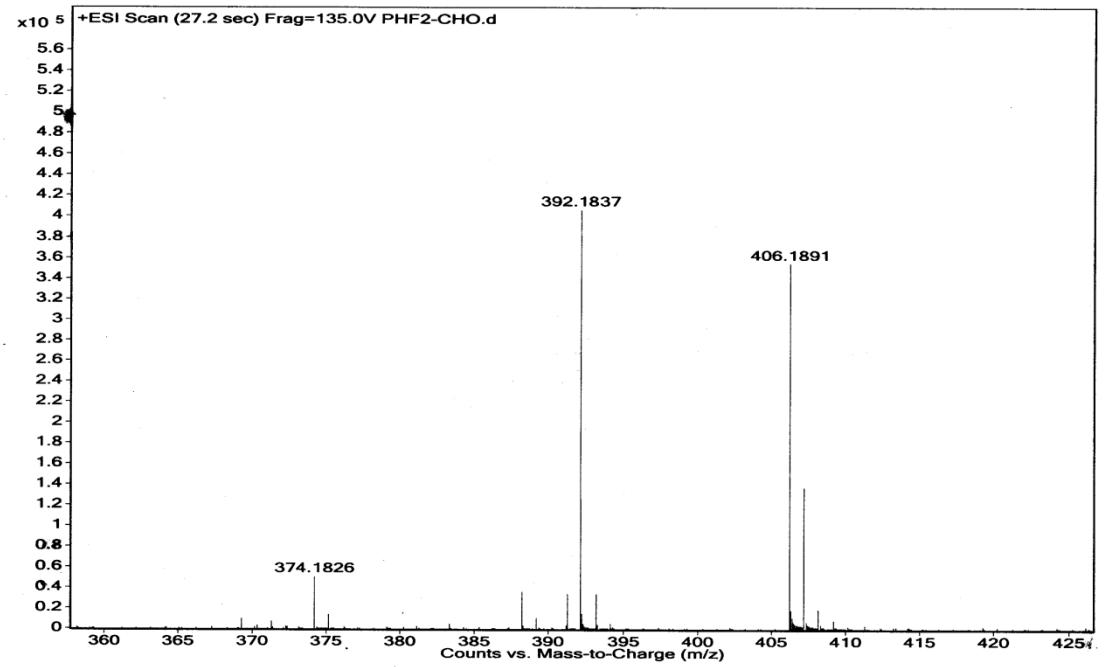

Figure A-20: HRMS (ESI) of 2,3-difluoro-4-(9-hexyl-9H-carbazol-3-yl)benzaldehyde (2d).

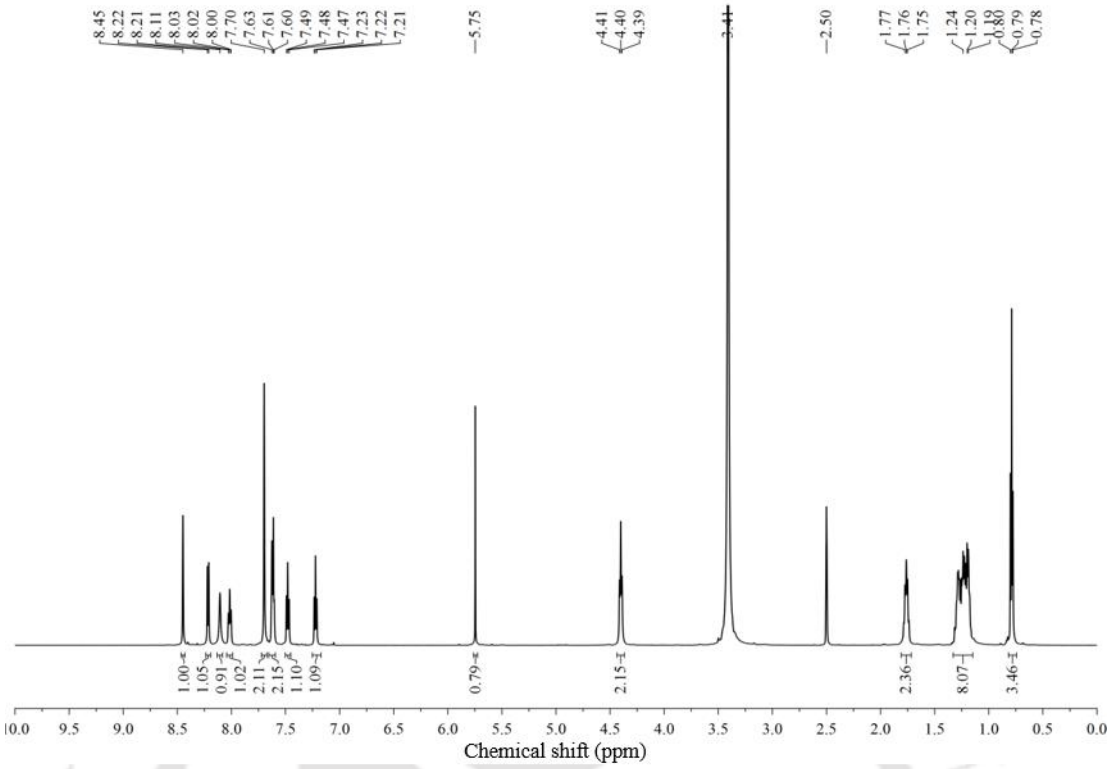

Figure A-21: ^{1}H NMR of 2-cyano-3-(2,3-difluoro-4-(9-hexyl-9H-carbazol-3-yl)phenyl)acrylic acid (MA2F).

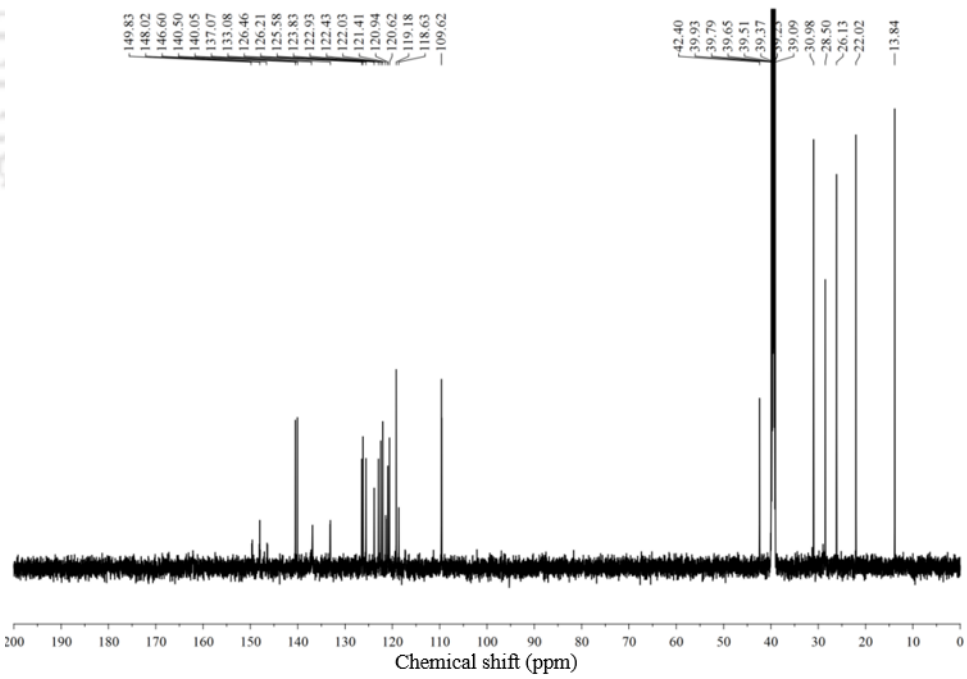

Figure A-22: ^{13}C NMR of 2-cyano-3-(2,3-difluoro-4-(9-hexyl-9H-carbazol-3-yl)phenyl)acrylic acid (MA2F).

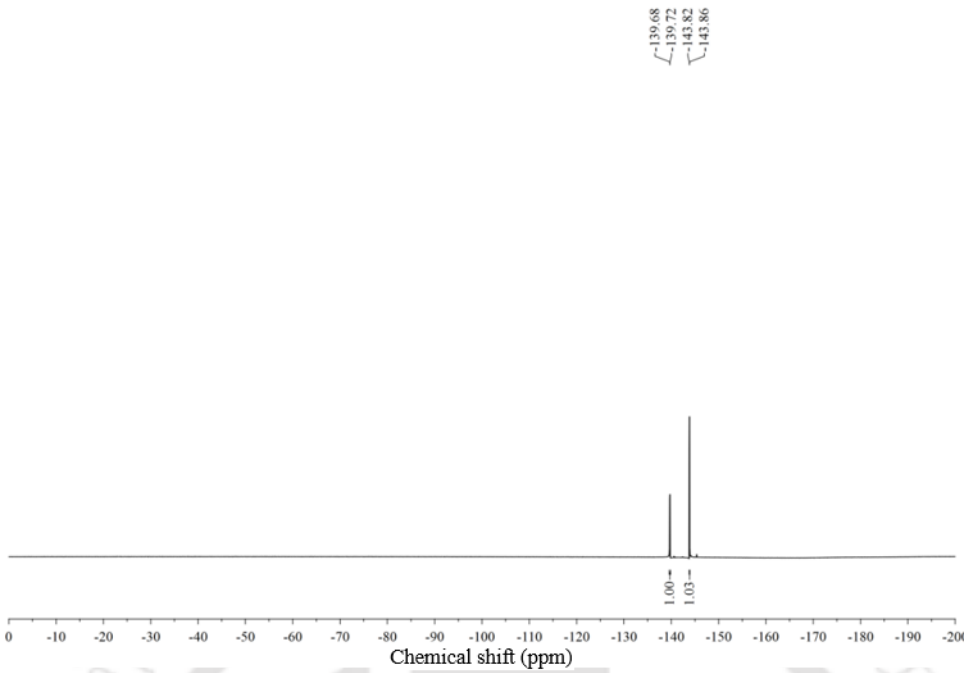

Figure A-23: ^{19}F NMR of 2-cyano-3-(2,3-difluoro-4-(9-hexyl-9H-carbazol-3-yl)phenyl)acrylic acid (MA2F).

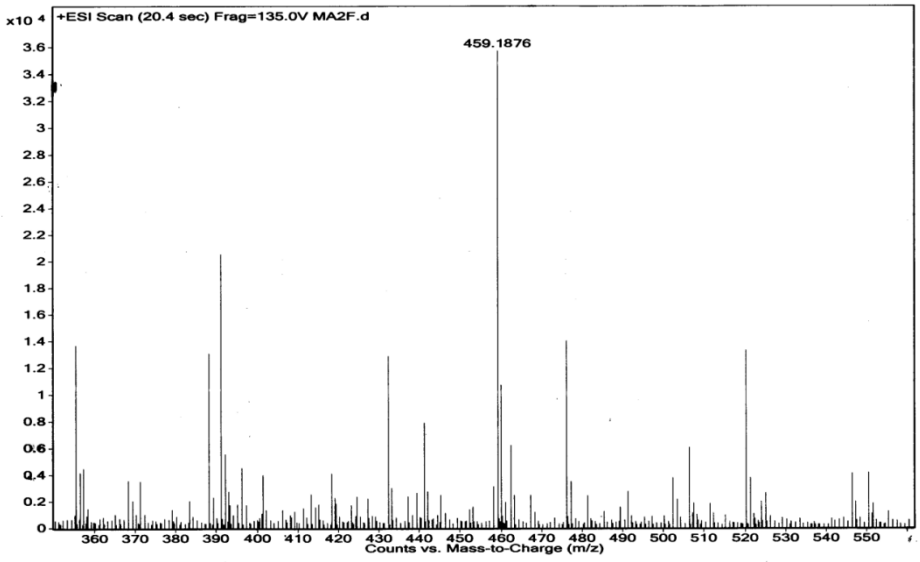

Figure A-24: HRMS (ESI) of 2-cyano-3-(2,3-difluoro-4-(9-hexyl-9H-carbazol-3-yl)phenyl)acrylic acid (MA2F).

CHAPTER 3

Effect of Mono- and Di-anchoring Dyes Based on *o*,*m*-difluoro Substituted Phenylene Spacer in Liquid and Solid State Dye Sensitized Solar Cells

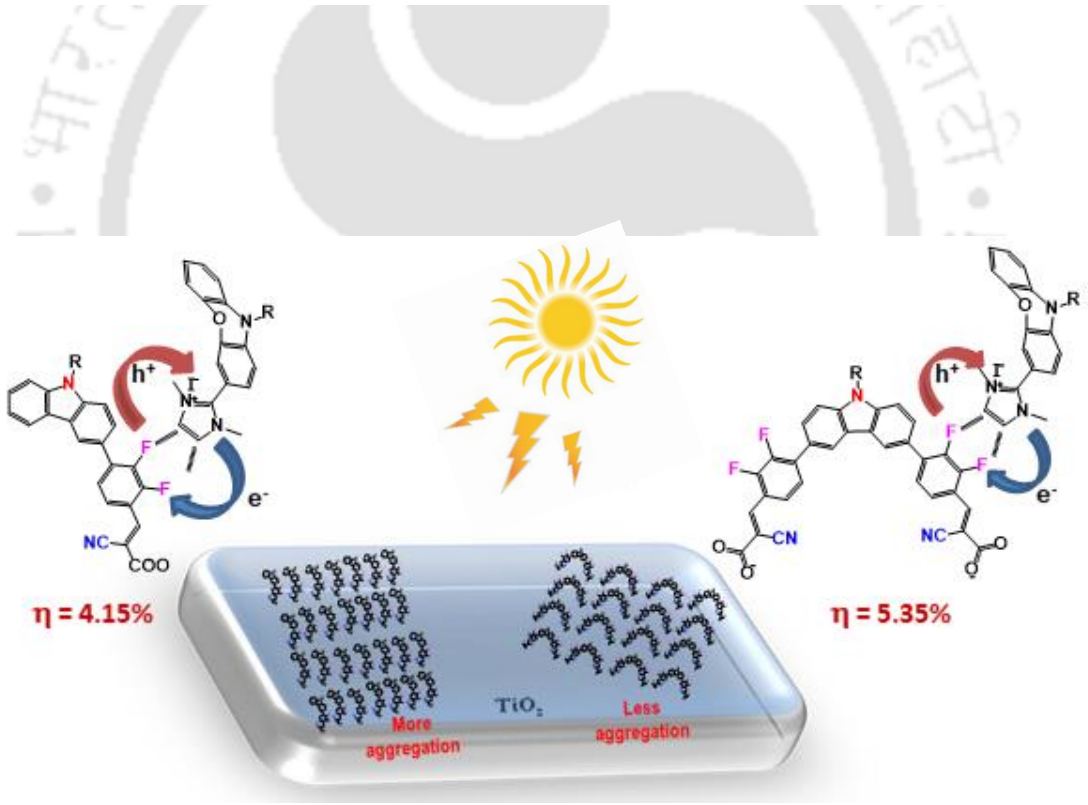

Raju, T. B.; Vaghasiya, J. V.; Afroz, M. A.; Soni, S. S.; Iyer, P. K. *Dyes Pigm.* **2020,** *174*, 108021, DOI: 10.1016/j.dyepig.2019.108021.

Abstract

Novel mono- and di-anchoring organic dyes have been designed and synthesized with *o,m*-difluoro substituted phenylene spacer and were tested for DSSCs in presence of solid-state (SJE-4) as well as liquid (BMImI) electrolytes. The new and simple structures of Cz-D1 and Cz-D2 dyes have same carbazole donor unit with either one or two side substitution of *o,m*-difluoro substituted phenylene π-spacer and cyanoacrylic acid acceptor. The photophysical and electrochemical properties of photosensitizes are investigated in detail and correlated with the solar cell performance. The Cz-D2 dye have ≈20% higher device efficiency than Cz-D1 due to its lower LUMO level, and presence of two acceptor groups which provide efficient electron extraction from carbazole donor, lesser aggregation, high molar extinction coefficient and better charge transfer. Without using any additive, Cz-D2 exhibited an attractive power conversion efficiency (PCE) of 5.35% (Jsc = 10.38 mA cm^{-2}, Voc = 0.750 V and FF = 0.60) in presence of iodide redox electrolyte. These dyes exhibited comparatively less efficiency when used to fabricate a solid-state dye sensitized solar cell in presence of SJE-4 electrolyte due to aggregation between fluorine substituted phenylene spacer and electrolyte through strong H-bonding that might cause more electron recombination/back electron transfer. Good stability was also observed for both the dyes.

3.1 Introduction

Extensive efforts to improve every component of DSSC to achieve higher PCE have been made over the years. To date, highest PCE of >12% has been achieved with porphyrin and Ru based dyes in presence of liquid/solid electrolyte.[1-5] However, for the large-scale application, these dyes are not favorable due to high cost of "Ru" metal, tedious separation process, low molar-extinction coefficients and environmental issues.[6] Recently, scientists have paid attention on metal-free organic dyes due to their low cost, simple preparation, easy purification, high molar-extinction coefficients and environmental friendliness. The advantage of structural diversity in metal-free organic dyes allows easy tuning of optical and electrochemical properties. Although a decent PCE of ~14% has been achieved with metal-free dyes,[7] investigation of novel organic dyes is still challenging and desirable to overcome the energy crisis.

The PCE and stability of a DSSC can be enhanced by controlling the light harvesting, charge recombination, dye regeneration, and electron injection properties of the dye[8] and these factors are strongly associated with the dye structure. Planar units with large conjugation were utilized in the dye structure to improve its light harvesting ability and achieve high absorption.[9-10] Charge recombination with the electrolyte was curtailed by incorporating bulky group or alkyl chains on the dye molecule which prevents the direct contact of electrolyte with the TiO_2 surface.[11] Co-adsorbents such as deoxycholic acid

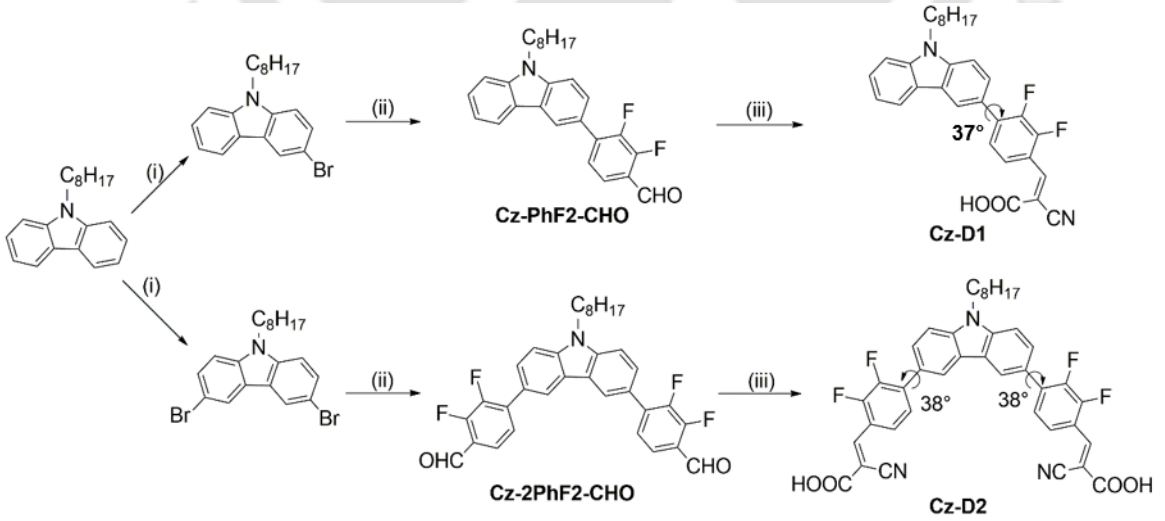

Figure 3.1: Synthetic route of organic sensitizers (i) NBS, THF, 12 h, (ii) 2,3-Difluoro-4-formylphenylboronic acid, $Pd(PPh_3)_4$, K_2CO_3, THF:H_2O = 2:1, Aliquat, 85 °C, 18 h (iii) Cyanoacetic acid, Piperidine, CH_3CN, 85 °C, 8 h.

(DCA) and chenodeoxycholic acid (CDCA) are being used as anti-aggregation agents to suppress dye aggregation over the surface of TiO_2.[12-13] Considering these points, new metal-free organic sensitizers can be designed to achieve high efficiency and stability in DSSCs.

Herein, two new *o,m*-di fluoro substituted phenylene spacer dyes with mono- and di-anchoring groups have been synthesized. The new and simple structure of Cz-D1 and Cz-D2 dyes have same carbazole donor unit, o,m-difluoro substituted phenylene π-spacer and cyanoacrylic acid as acceptor, and only variation is presence of mono- and di-anchors, respectively (Figure 3.1). Fluorine (F) atom was incorporated into π–bridge due to its capability to tune the molecular energy levels (lowering the LUMO level), and improve the electron mobility.[14-17] Linear octyl chain on carbazole moiety was used for the better suppression of dye aggregation on metal oxide surface (TiO_2). It is clear from previous reports that carbazole is the best donor in simple D-π-A dyes with *ortho*/*meta*-F substituted phenylene spacer.[6,18] The planarity of backbone in carbazole based dyes improves charge transfer from donor(D) to acceptor (A), results in high molar extinction coefficients (ε) and long lifetime values. The molecular properties of the newly synthesized dyes were extensively studied and correlated with the photovoltaic performance for both liquid as well as solid state DSSCs (ss-DSSCs). Further, electrochemical impedance spectroscopy (EIS) measurements were used to estimate carrier transport and interfacial charge recombination in the solar cell devices.

3.2 Results and Discussion

Figure 3.2 displays the photophysical properties of Cz-D1 and Cz-D2 dyes in chloroform solution as well as on TiO_2 film and the corresponding characteristic data are summarized in Table 3.1. Both the dyes exhibited two strong distinct absorption bands in $CHCl_3$ solution in the range of 200–350 nm. These peaks correspond to the localized aromatic π-π* transitions of conjugated back bone. Cz-D1 exhibited a weak absorption band in the range of 350–500 nm which is related to the intramolecular charge transfer (ICT) from D to A. Compared to Cz-D1, di-anchor dye Cz-D2 exhibited strong ICT peak as both acceptor units help in efficient electron extraction from carbazole donor and reduces H-aggregation in solution and solid state. Cz-D1 has strong aggregation in $CHCl_3$ and on TiO_2 surface due to the close packing, generally observed in mono-anchoring dyes. Cz-D1 dye has maximum absorption peaks at 239, 288 nm and Cz-D2 dye has maximum

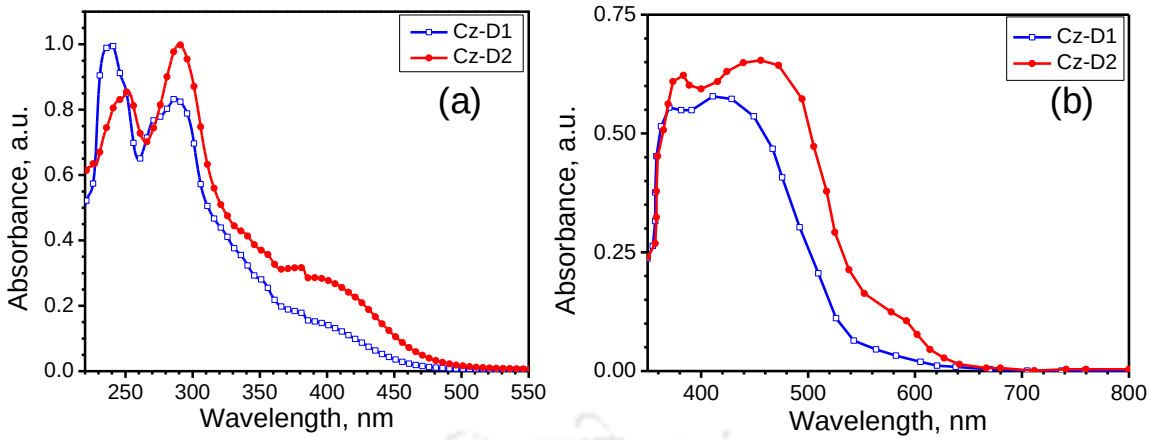

Figure 3.2: Absorption spectra of photosensitizers Cz-D1 and Cz-D2 in $CHCl_3$ solution (a) and on nanocrystalline TiO_2 film (b).

absorption peaks at 253, 290 nm. The absorption spectrum of Cz-D2 dye is slightly red shifted in solution as well as in solid state due to increased effective π-conjugation length and reduced aggregation. The molar absorption coefficient at λ_{max} for Cz-D1 and Cz-D2 were 22,000 $M^{-1}cm^{-1}$ (398 nm) and 30,000 $M^{-1}cm^{-1}$ (401 nm), respectively. The red shift in the absorption and superior molar absorption coefficient resulted in better efficiency of Cz-D2.

Energy levels (HOMO-LUMO) of dyes were investigated by cyclic voltammetry (CV) and the results are shown in Figure 3.3(a) and relevant data are listed in Table 3.1. HOMO level of the photosensitizers were calculated from onset oxidation potential of dyes with Fc/Fc^+ as internal standards (4.8 eV reference energy levels) using $E_{HOMO} = -[(Eox-E_{1/2(ferrocene)}) + 4.8]$ eV formula. Notably, the HOMO level of Cz-D1 and Cz-D2 corresponding to their first onset oxidation potential (Eox = 1.13 V) is at same energy level

Table 3.1: Photophysical, electrochemical and life time properties of carbazole based dyes.

Dye	Solution λ_{max} (nm)[a]	Film λ_{max} (nm)[b]	ε_{max} (M^{-1} cm^{-1})	HOMO (eV)[c]	LUMO (eV)[c]
Cz-D1	239, 288, 398	417	22,000	-5.82	-3.13
Cz-D2	253, 290, 401	453	30,000	-5.82	-3.27

[a]Maximum absorption wavelength of dyes in chloroform solution.

[b]Maximum absorption wavelength of dyes that were absorbed onto the TiO_2 films.

[c]Onset potentials from CV measurements of thin films in 0.1 M Bu_4NPF_6/CH_3CN solution, estimated from $E_{HOMO} = -[(Eox-E_{1/2(ferrocene)}) + 4.8]$ eV and $E_{LUMO} = Eg$ calculated using onset of UV (TiO_2 film)–E_{HOMO}.

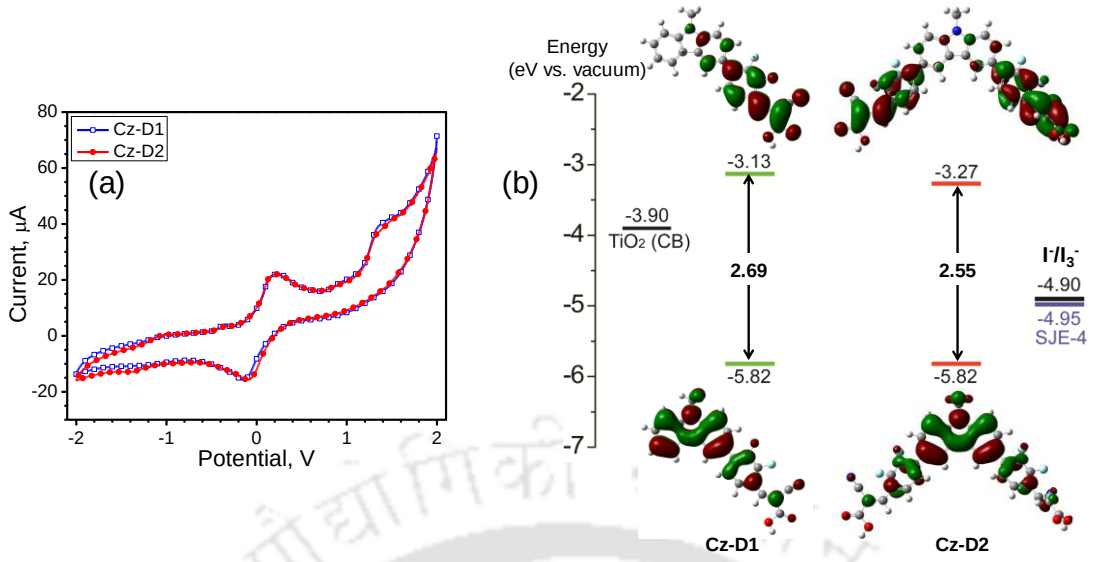

Figure 3.3: (a) Cyclic voltammograms and, (b) Energy level diagram of Photosensitizers compared to the energy levels of TiO_2 and electrolytes including Frontier molecular orbital of the designed dyes obtained from DFT calculations.

of −5.82 eV as same carbazole donor unit is present in both the dyes. The oxidation potential of all photosensitizers versus normal hydrogen electrode (V vs NHE) is more positive than the redox potential of electrolytes, indicating that thermodynamically favorable oxidized photosensitizers can regenerate effectively. The LUMO level of photosensitizers was calculated from the onset absorption spectra of dyes ($E_{LUMO} = Eg - E_{HOMO}$), and are −3.13, and −3.27 eV for Cz-D1 and Cz-D2 dyes, respectively. The LUMO level of Cz-D2 dye is lower than Cz-D1 dye due to the increased acceptor ability. These values are above the conduction band (CB) of the TiO_2 electrode, which is necessary for sufficient driving force to inject the electrons from light-oxidized dye to CB of nanocrystalline TiO_2 surface. Based on the CV results, Figure 3.3(b) illustrates the energy level diagram of dyes. It is clear that the LUMO of Cz-D2 dye matches well with the conduction band of TiO_2 and HOMO matches well with the potential of redox electrolyte (Liquid and SJE-4 electrolyte); this improves *J*sc and results in high PCE.

The electronic distribution of frontier molecular orbitals (HOMO, LUMO) of dyes were calculated by density functional theory (DFT) using B3LYP/6-31G(d,p) level for optimization of dye molecules. The results of computational analysis are presented in Figure 3.3(b). The performance of dyes depends on planarity of backbone and charge transfer from D to A. Moreover, the acceptor moiety and length of alkyl chain also affects the dye performance. In Cz-D1 and Cz-Ds2 dyes, HOMO levels are mainly located on

donor segment and strongly distributed into spacer moiety whereas the LUMO levels are mainly located on acceptor and spacer unit. These results reveal that the better performance of Cz-D2 dye might be due to the well separated HOMO and LUMO orbitals on the donor and acceptor parts, respectively. Proper separation of HOMO and LUMO orbitals is an advantage for charge migration from D to A in photo excited state of dye.

The DSSC devices were fabricated using Cz-D1 and Cz-D2 sensitizers with nanocrystalline TiO_2 anatase semiconductor as the photoanode. The DSSCs device performance parameters, such as short-circuit current density (*J*sc), fill factor (FF), open-circuit photovoltage (*V*oc), and power conversion efficiency (PCE), were measured under 100 mW cm^{-2} (AM 1.5) illumination, and are depicted in Table 3.2. The DSSCs based on Cz-D2, which has bis *o*,*m*-difluoro substituted phenylene spacer and two anchoring units (-$CNCH_2COOH$), features *J*sc and *V*oc values of 10.20 mA cm^{-2} and 0.707 V, respectively. The PCE was calculated to be 5.20% using the equation: PCE = (Pmax/Pin) × 100. In difference, the cell based on Cz-D1, which has single phenylene spacer and –$CNCH_2COOH$ group, has a lower *J*sc value of 7.78 mA cm^{-2} (Figure 3.4(a)).

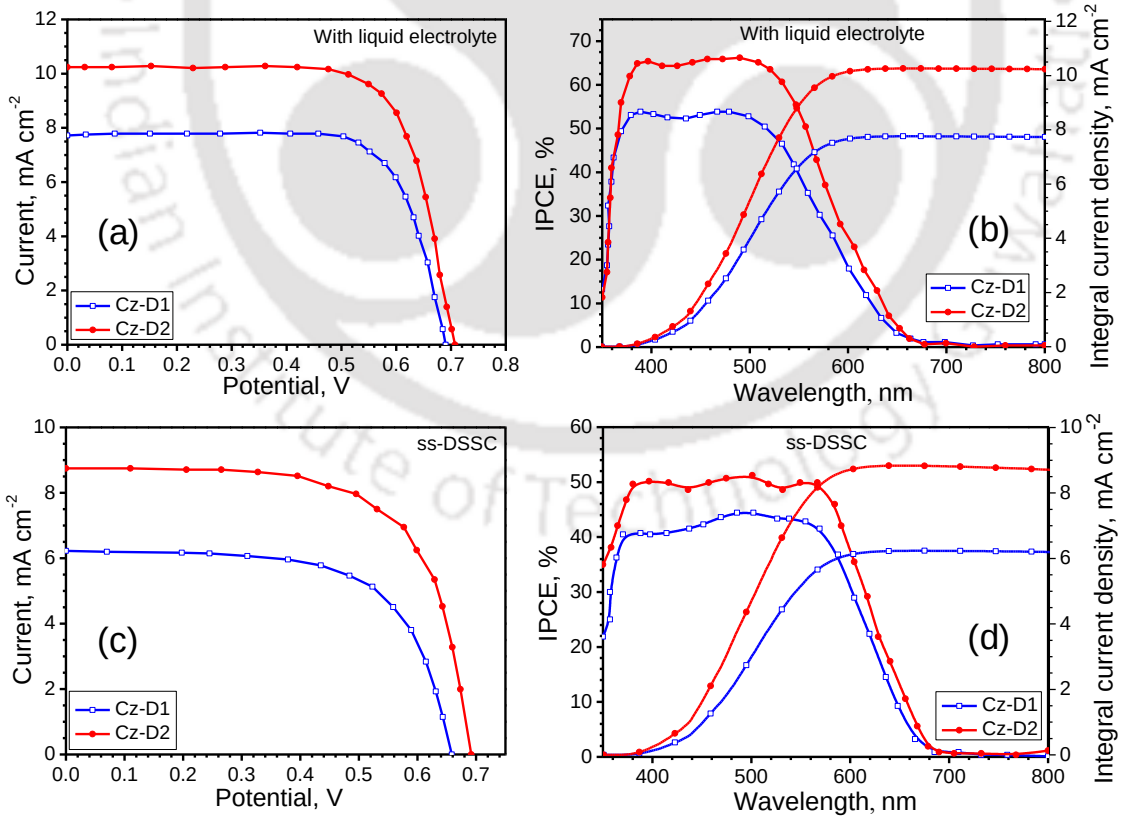

Figure 3.4: (a) *J-V* characteristics of DSSCs based on the liquid electrolyte and (b) corresponding IPCE spectra and integral current density. (c) *J-V* characteristics of DSSCs based on the solid electrolyte and (d) corresponding IPCE spectra and integral current density.

To confirm the different *J*sc results between Cz-D1 and Cz-D2, the IPCE values, which usually depend on charge collection, light harvesting, and electron injection efficiencies were measured. Figure 3.4(b) shows the IPCE intensity curves as a function of the incident light wavelength for the DSSCs based on the new organic sensitizers on nanocrystalline TiO_2 photoanode. Both devices can efficiently convert the light into current in the range of 350–550 nm. The DSSCs containing Cz-D2 sensitizer-based device exhibited a broad and higher IPCE of 66% in the range of 350–650 nm, while the Cz-D1 sensitizer-based device shown blue-shift and lower IPCE of 54% in the range of 350–630 nm. The higher percentage of IPCE was observed for the sensitizer Cz-D2, which is due to its better light harvesting capacity and broad absorption in the visible region. The changes of IPCE curves are consistent with the trend of the absorption spectra on the nanocrystalline TiO_2 photoanode (Figure 3.2(b)). In Cz-D2 dye based device the *J*sc and *V*oc are improved upon substitution of the second *o,m*-difluoro substituted phenylene spacer and acceptor groups. It has a higher PCE because the D-$(\pi$-A$)_2$ system of carbazole based dye has a positive effect on IPCE curve and dye loading on TiO_2 photoanode surface (ε) compared with that of Cz-D1 having one phenylene spacer and acceptor unit. The ε value of Cz-D1 and Cz-D2 were 0.74×10^{-6} and 1.23×10^{-6} mol^{-1} cm^{-1} respectively. The reason for higher loading of Cz-D2 is its better electronic coupling with the TiO_2 matrix due to the presence of two carboxylic acceptor groups.

Under similar condition, ss-DSSCs with Cz-D1 and Cz-D2 dyes and solid organic ionic conductors SJE-4 were also fabricated. The photovoltaic measurement was performed

Table 3.2: Photovoltaic parameters of DSSCs with solid and liquid electrolytes.[a]

Photovoltaic parameters	Cz-D1		Cz-D2	
	A	B	A	B
*J*sc (mA cm^{-2})	7.78 ±(0.12)	6.22 ±(0.20)	10.2 ± (0.18)	8.74 ± (0.25)
*V*oc (V)	0.690 ±(0.05)	0.658 ±(0.06)	0.707 ± (0.05)	0.691± (0.10)
FF (%)	58.0 ±(1.0)	55.0 ±(1.2)	59.2 ± (1.0)	55.0 ± (1.5)
PCE (%)	3.95 ±(0.20)	2.60 ± (0.22)	5.20 ± (0.15)	4.02 ± (0.30)

[a]Performances of DSSCs were measured with 0.20 cm^2 working area (measurements were performed under AM 1.5, 100mW cm^{-2} irradiation). J_{sc} (mA cm^{-2}): short-circuit current, V_{oc} (V): open circuit voltage, FF (%): fill factor and PCE (%): Photo conversion efficiency, A and B indicates liquid-state and solid-state electrolyte based DSSCs, respectively.

at a light intensity of 100 mW cm^{-2}. The results of ss-DSSCs are depicted in Figure 3.4(c) and the corresponding photovoltaic parameters are presented in Table 3.2. A maximum PCE of 4.02% with *J*sc of 8.74 mA cm^{-2} and *V*oc of 0.691 V were obtained for the Cz-D2 sensitizer based ss-DSSCs. It can be noted that reduced *J*sc and *V*oc values compared with liquid based electrolyte were obtained, and same trend was also observed in IPCE spectra (Figure 3.4(d)). The enhanced *V*oc value (in liquid electrolyte) may be explained in terms of the reduction in the back-electron transfer from the nanocrystalline TiO_2 conduction band to the triiodide ions in the electrolyte.[19] Moreover, liquid electrolyte has easy penetration in porous TiO_2 matrix and had better interfacial contact compared to solid electrolyte. In ss-DSSCs, reduced *J*sc was obtained because of low ion transfer via hopping or in other words Grotthuss mechanism rate is slightly lower than liquid based electrolytes.[20-22] Also, pore filling and interface connectivity of solid electrolyte might be low with TiO_2 and counter electrode, leading to a decrease in fill factors and loss of photocurrent. But the long-term stability of solid-state electrolytes is superior compared to liquid electrolyte based DSSCs. Liquid electrolytes have many drawbacks such as; (i) it contains highly volatile organic solvents, (ii) the organic sensitizer bound over TiO_2 surface, after coming in contact with liquid electrolytes start desorbing, (iii) liquid electrolyte is corrosive in nature, and (iv) leakage problem, etc.[3,23-24] Figure 3.5 shows the

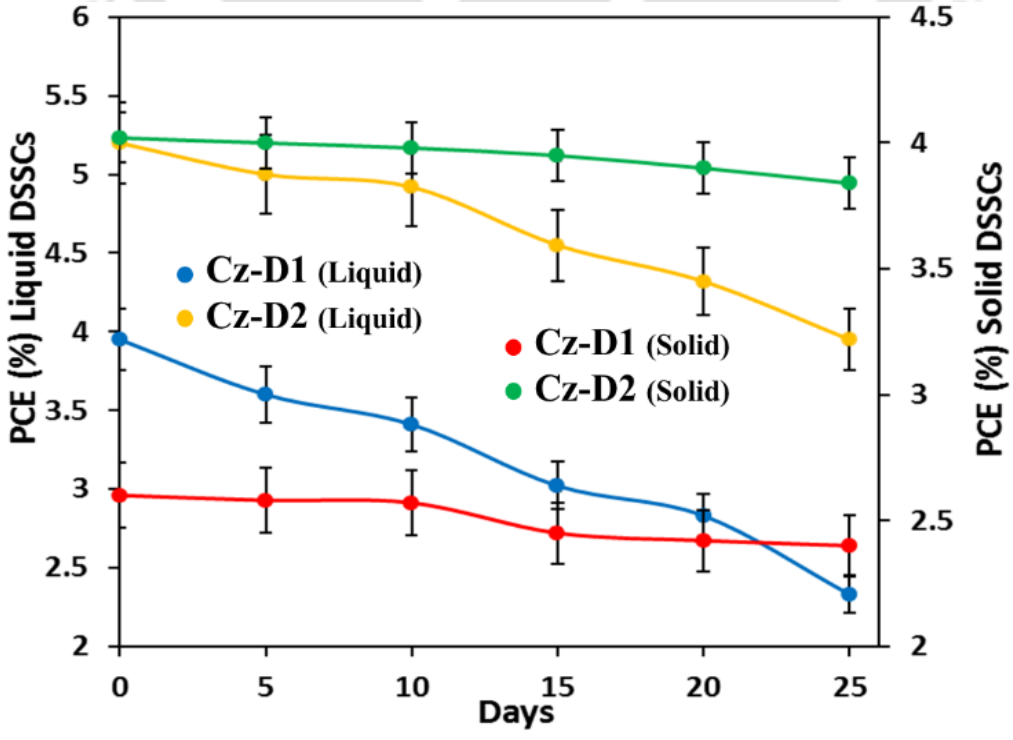

Figure 3.5: Devices stability curve: PCE as a function of time.

stability analysis of liquid and solid electrolyte based DSSCs. To show the stability of the solid organic ionic conductor electrolyte, compared to the liquid electrolyte, a comparison is carried out for four devices (two devices for each dye) fabricated and sealed in the same procedure, except one was filled with solid electrolyte and the other with liquid electrolyte. The PCEs were measured at an interval of 5 days, and after 25 days the liquid-electrolyte based devices displayed that most of its electrolyte in the device was evaporated, whereas the solid-electrolyte based device retained its electrolyte and the PCE was almost unchanged. In Figure 3.5 the PCE as a function of time are illustrated for a period of 25 days, and found that the ss-DSSCs show excellent stability.

The EIS technique was used to study the internal resistance, interfacial properties and charge transfer kinetics of nanocrystalline TiO_2 layers in DSSCs.[25-26] EIS spectra were measured in dark condition using electrochemical workstation (CHI660E, CH instruments, USA). Figure 3.6(a) shows the Nyquist plots of solid and liquid electrolytes based DSSCs. The EIS spectra can be interpreted by fitting it using equivalent circuit (the fitting data are listed in Table 3.3). Each equivalent circuit consisted of several components as shown in inset of Figure 3.6(a): Interfacial resistance (R_{pt}) of electron transfer at Pt/electrolyte interface, recombination resistance (R_k) in TiO_2 matrix, diffusion resistance (RD) in electrolyte and constant phase element (CPE-P), the value of CPE-P is associated with the surface roughness and porosity of the photoelectrode.[18,27-28] Nyquist spectra of the DSSCs showed three semicircles: 1st high frequency region, represents R_{pt}; 2nd mid frequency region, represent R_k and 3rd lower frequency region, represent RD. As shown in Table 3.3, R_{pt} of the DSSCs with liquid electrolyte is lower compared to solid electrolytes. However, R_k was higher for Cz-D2 sensitizer with solid and liquid-electrolytes based devices,

Table 3.3: Electrochemical parameters of DSSC with liquid and solid electrolyte.

Device	State of the Electrolyte	R_{pt} (Ω)[a]	R_k (Ω)[a]	CPE-P (%)[a]	τ (ms)[a]	α_a (mV/decade)[b]	α_c (mV/decade)[b]	J_o (nA cm^{-2})[b]
Cz-D1	Liquid	20.9	229	65	0.83	145.5	235.4	0.69
Cz-D2	Liquid	21.9	323	69	1.68	115.6	220.0	0.82
Cz-D1	Solid	25.1	210	70	0.80	122.4	259.5	0.21
Cz-D2	Solid	24.6	265	70	1.15	115.4	308.3	0.32

[a]Electrochemical Impedance spectroscopy, [b]Data obtain from Tafel polarisation curve.

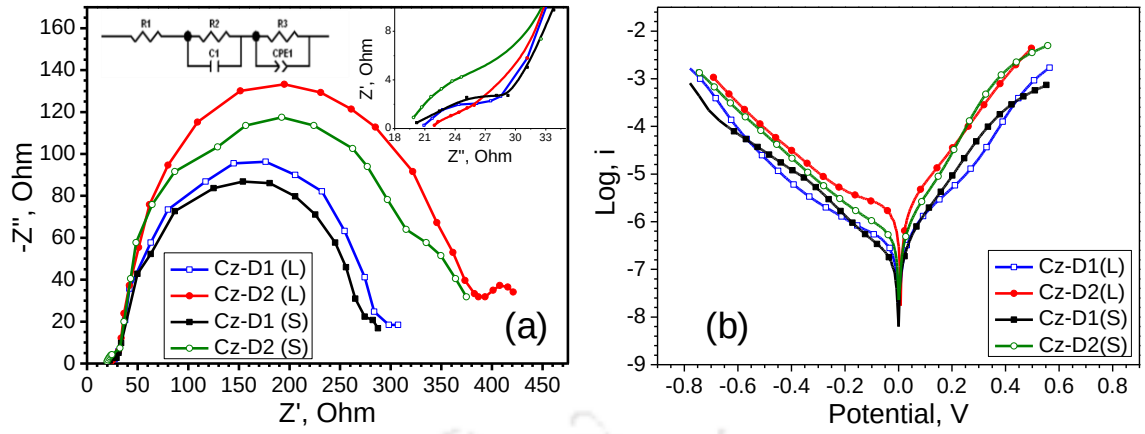

Figure 3.6: (a) Nyquist plots for the fabricated DSSCs based on solid and liquid electrolytes with Cz-D1 and Cz-D2 sensitizers in the dark at Voc (0.65 V). (b) Tafel polarization study of the solid and liquid electrolytes based DSSCs fabricated using new dyes.

compared to Cz-D1 sensitizer-based devices. The electron lifetime (τ_e) of Cz-D2 is also higher in both solid and liquid electrolytes, while a shift of low frequency (mid) corresponds to a longer τ_e and is subjected to a higher value of *V*oc.

Tafel polarization measurement was used to study the interfacial charge transfer properties of the electrolytes on the nanocrystalline TiO_2 matrix. [29] As discussed in previous reports,[18,30-31] the rates of anodic (α_a) and cathodic (α_c) reactions at the TiO_2 photoanode/redox mediator interface can be described by the equation 3.1 (the Butler Volmer Equation).[32-34]

$$j = -J_0 \left(\exp \frac{\alpha_c nF}{RT} (E - E_{eq} \right) - \left(\exp \frac{\alpha_a nF}{RT} (E - E_{eq} \right) \qquad (3.1)$$

Where Eeq is the equilibrium potential of I^-/I_3^- electrolyte, J_0 is the current exchange density and E is the applied voltage. In dark condition the equation simplifies to $J = J_0$ as E becomes Eeq, also J_0 depends on the concentrations of redox couple in the electrolyte and reaction area on the TiO_2 surface. In Figure 3.6(b), Tafel analysis is illustrated which gives an insight into the electrode kinetics of DSSCs based on the solid and liquid electrolytes. In liquid electrolyte system, the J_0 for the I^-/I_3^- redox couple at the TiO_2/electrolyte interface was about 0.69 nA cm^{-2} (Cz-D1) and 0.82 nA cm^{-2} (Cz-D2). It is much higher than that of the DSSCs based on the solid-state electrolyte (Table 3.3).

The solid electrolyte resulted in a decrease of J_0 which increased the charge transfer resistance at electrolyte/TiO_2 surface. Lower α_c slope value was found in the liquid electrolyte based DSSCs as shown in Figure 3.6(b) and Table 3.3. These α_c slope value (lower than solid electrolyte), close to 235 mV $decade^{-1}$ (Cz-D1) and 220 mV $decade^{-1}$ (Cz-

D2), corresponds to the recombination reaction at the sensitized TiO_2 photoanode/I^-/I_3^- electrolyte interface between electrons from the CB of titania and triiodide in the liquid electrolyte. The reduced α_c slope indicates an enhanced reaction of the triiodide at the sensitized TiO_2 photoanode/I^-/I_3^- electrolyte interface.

3.3 Conclusions

In conclusion, we have developed *o,m*-difluoro substituted phenylene spacer and carbazole based dyes Cz-D1 and Cz-D2, consisting mono- and di-anchoring groups. Both dyes exhibited interesting optical, electrochemical and photovoltaic properties. The absorption spectra of planar Cz-D1 dye show strong H-aggregation in solution and dye absorbed on TiO_2. Cz-D2 contain two electron acceptor groups and non-planarity ensuing less aggregation, provide efficient electron extraction from carbazole donor, high molar extinction coefficient, better charge transfer and lower LUMO level resulted in better photovoltaic performance than Cz-D1, in presence of liquid (BMImI) as well as solid (SJE-4) electrolyte systems. Without using any additives, Cz-D2 and Cz-D1 exhibited attractive power conversion efficiency of 5.35% and 4.15%, respectively in presence of iodide redox electrolyte. Both *o,m*-difluoro substituted dyes exhibited less efficiency in presence of SJE-4 solid electrolyte system due to the aggregation between fluorine substituted phenylene spacer and electrolyte through strong H-bonding and resulted in more electron recombination/back electron transfer as confirmed by TD-DFT and EIS measurements. PCE as a function of time for a period of 25 days were also recorded, the mono anchoring Cz-D1 device exhibited better stability than di anchoring Cz-D2 in presence of both electrolyte systems.

3.4 Experimental Section

3.4.1 Materials

All required chemicals used for the synthesis of dyes were purchased from sigma Aldrich, TCI and were used without any further purification unless otherwise explained. Nano-crystalline TiO_2 (<20 nm, 99.8%, anatase), alpha-terpineol, ethyl cellulose, titanium (IV) propoxide, $TiCl_4$, BMImI and tert-butyl pyridine were purchased from Sigma-Aldrich (India) and used as received. Acetonitrile and ethanol were purified using the standard process. Fluorine tin oxide glass (FTO, 12 Ω $\square^{-1}$, Solaronix, SA, Switzerland) and sealing materials (Meltronix tape, thickness 60 μm) were used for the fabrication of the DSSC

device. The alkylation and bromination of carbazole were done according to the published literature procedure.[6,18]

3.4.2 Synthesis

The synthetic procedures of two dyes (Cz-D1, Cz-D2) are shown in Figure 3.1. By using Suzuki coupling reaction, CZ-PhF2-CHO and Cz-2PhF2-CHO were synthesized. The final step to synthesize new dyes (Cz-D1, Cz-D2) was performed by using Knoevenagel condensation reaction method. All the necessary products were purified by column chromatography, characterized by NMR (^{1}H, ^{13}C) and HRMS spectrometry (Data presented in Appendix B, Figure B-2 to 13).

General synthetic procedure of aldehyde

Synthesis of Cz-PhF2-CHO

A 2 M K_2CO_3 solution in THF: H_2O (2:1) was added to the mixture of 3-bromo-9-octyl-9H-carbazole (0.2 mmol) and 2,3-Difluoro-4-formylphenylboronic acid (0.3 mmol) then degassed properly. Finally, in presence of argon, $Pd(PPh_3)_4$ (2 mol%) was added and heated to 85 °C for 18 h. Then the solution was evaporated under reduced pressure. The extracted compound was washed with chloroform and aqueous brine solution. Finally, organic part was dried with anhydrous $MgSO_4$. The desired product was purified by column chromatography (silica gel, EtOAc-hexane 1:2 as eluent).

Synthesis of Cz-2PhF2-CHO

In a clean reaction flask 3,6-dibromo-9-octyl-9H-carbazole (0.2 mmol) and 2,3-Difluoro-4-formylphenylboronic acid (0.5 mmol) taken. Then, 2 M K_2CO_3 solution in THF: H_2O (2:1) was added to the reaction mixture. Finally, in presence of argon, $Pd(PPh_3)_4$ (2 mol%) was added and heated to 85 °C for 18 h. Then the solution was evaporated under reduced pressure. The extracted compound was washed with chloroform and aqueous brine solution. Finally, organic part was dried with anhydrous $MgSO_4$. The desired product was purified by column chromatography (silica gel, EtOAc-hexane 1:2 as eluent).

General synthetic procedure of dyes

Synthesis of Cz-D1

The solution of acetonitrile: chloroform (2:1) was added to the mixture of Cz-PhF2-CHO (0.2 mmol) and cyanoacetic acid (0.3 mmol) and degassed it thoroughly. Finally, in presence of argon atmosphere the piperidine (catalytic amount) was added into the solution. Then the solution was refluxed for 18 h. After cooling to RT, the solution was evaporated under reduced pressure. Extracted compound was washed with chloroform and 0.1 M aq. HCl. Then the organic part was dried with $MgSO_4$. The product was purified by conventional column chromatography (silica gel, EtOAc -hexane 1:2 as eluent) and it was obtained as a yellow-orange solid.

Synthesis of Cz-D2

The solution of acetonitrile: chloroform (2:1) was added to the mixture of Cz-2PhF2-CHO (0.2 mmol) and cyanoacetic acid (0.5 mmol) and degassed it thoroughly. Finally, in presence of argon atmosphere the piperidine (catalytic amount) was added into the solution. Then the solution was refluxed for 18 h. After cooling to RT, the solution was evaporated under reduced pressure. Extracted compound was washed with chloroform and 0.1 M aq. HCl. Then the organic part was dried with $MgSO_4$. The product was purified by conventional column chromatography (silica gel, EtOAc -hexane 1:2 as eluent) and it was obtained as a yellow-orange solid.

2,3-Difluoro-4-(9-octyl-9H-carbazol-3-yl)benzaldehyde [Cz-PhF2-CHO]

Yield = 70%, ^{1}H NMR (400 MHz, $CDCl_3$): δ (ppm) 10.37 (s, 1H), 8.33 (s, 1H), 8.15–8.13 (d, 1H), 7.71–7.69 (t, 3H), 7.53–7.50 (t, 2H), 7.49–7.44 (m, 3H), 7.30–7.27 (d, 1H), 4.33 (t, 2H) 1.91–1.89 (t, 2H), 1.42–1.32 (m, 5H), 1.30–1.24 (m, 9H), 0.89–0.86 (t, 3H). ^{13}C NMR (100 MHz, $CDCl_3$): δ (ppm) 186.14, 154.73, 152.88, 149.15, 146.89, 141.12, 140.93, 138.34, 126.65, 126.48, 125.65, 121.33, 120.70, 119.64, 109.27, 109.17, 43.47, 31.99, 29.56, 29.37, 29.19, 27.51, 22.80, 14.26. HRMS (ESI) m/z: $[M+Na]^+$ calcd for $C_{27}H_{28}F_2NO$ 420.2139, found 420.2123.

4,4'-(9-octyl-9H-carbazole-3,6-diyl)bis(2,3-difluoro benzaldehyde) [Cz-2PhF2-CHO]

Yield = 68%, ^{1}H NMR (400 MHz, $CDCl_3$): δ (ppm) 10.37 (s, 1H), 8.37 (s, 1H), 7.75–7.64 (m, 4H), 7.56–7.53 (d, 2H), 7.48–7.46 (m, 4H), 4.37 (t, 2H) 1.94–1.92 (t, 2H), 1.56 (t, 1H), 1.44–1.25 (m, 9H), 0.89–0.84 (t, 3H). ^{13}C NMR (100 MHz, $CDCl_3$): δ (ppm) 186.13,

141.39, 137.31, 132.32, 128.79, 128.71, 127.34, 125.66, 123.31, 123.06, 121.51, 114.13, 109.61, 43.69, 31.96, 29.89, 29.54, 29.35, 27.49, 22.78, 14.24, 14.26. HRMS (ESI) m/z: $[M]^+$ calcd for $C_{34}H_{29}F_4NO_2$ 559.2134, found 559.2141.

(Z)-2-Cyano-3-(2,3-difluoro-4-(9-octyl-9H-carbazol-3-yl)phenyl)acrylic acid [Cz-D1]

Yield = 73%, ^{1}H NMR (400 MHz, DMSO‐ d6): δ (ppm) 8.86–8.42 (d, 2H), 8.30 (s, 1H), 8.24–8.22 (d, 2H), 8.10 (S, 2H), 8.02 (s, 1H), 7.71–7.70 (m, 4H), 7.62.7.61 (m, 6H), 7.56–7.48 (m, 7H), 7.23 (m, 3H), 4.41 (t, 2H), 1.57 (m, 5H), 1.33–1.15 (t, 6H), 0.84–0.78 (m, 4H), 1.30–1.24 (m, 9H), 0.89–0.86 (t, 3H). ^{13}C NMR (150 MHz, DMSO‐ d6): δ (ppm) 149.54, 148.03, 146.33, 140.51, 140.06, 136.79, 133.09, 126.47, 126.22, 125.59, 123.84, 122.94, 122.44, 122.04, 121.42, 120.95, 120.63, 119.19, 118.64, 109.58, 50.91, 30.99, 28.51, 27.22, 26.14, 24.16, 22.03, 13.85. HRMS (ESI) m/z: [M − H]- calcd for $C_{30}H_{28}F_2N_2O_2$ 485.2041, found 485.2031.

(2Z,2′E)-3,3'-((9-octyl-9H-carbazole-3,6-diyl)bis(2,3-difluoro-4,1-phenylene))bis(2-cyanoacrylic acid) [Cz-D2]

Yield = 68%, ^{1}H NMR (400 MHz, $CDCl_3$): δ (ppm) 8.32–8.18 (m, 2H), 7.92 (s, 1H), 7.75–7.68 (m, 3H), 7.56–7.40 (m, 3H), 7.17–7.10 (d, 2H). ^{13}C NMR (100 MHz, $CDCl_3$): δ (ppm) 149.10, 146.82, 140.39, 133.99, 132.19, 128.92, 126.29, 122.99, 122.73, 121.16, 120.68, 117.88, 117.06, 114.29, 109.39, 108.64, 51.17, 31.91, 29.88, 29.15, 27.32, 26.57, 22.74, 14.23. MALDI-TOF m/z: $[M-2H]^+$ calcd for $C_{40}H_{31}F_4N_3O_4$ 691.6696, found 691.6610.

3.4.3 Preparation of electrolytes

The electrolyte contains solid organic ionic conductor (SJE-4, Figure B-1), iodide source (BMImI), iodine and TBP (tert-butyl pyridine). The molar proportion of composition was usually 0.03 (SJE-4): 0.04 (BMImI): 0.05 (I2): 0.5 (TBP). All components were mixed in acetonitrile solvent.

3.4.4 Fabrication of DSSCs

The preparation of TiO_2 photoelectrode was done as per our previously reported method.[6,18] The dye solar cells were assembled by placing a Pt-coated FTO on the (Cz-D1 & Cz-D2) dyes sensitized TiO_2 photo-electrode using a hot-melt Surlyn film. A solution of electrolytes in acetonitrile was injected into the interior space of the device from the predrilled holes on the Pt-based counter electrode and sealed using epoxy resin. In solid

state devices the same procedure was followed and after filling the electrolyte, devices were kept in a vacuum oven at 50 °C for at least 6 h to remove the organic solvent. The same process was repeated three times to ensure that the TiO_2 porous film was filled with a compact layer of the SJE-4. The active area of all DSSC devices was 0.20 cm^2.

3.4.5 Characterization

^1H and ^{13}C NMR spectra were recorded on Varian AS-400 MHz or Bruker Ascend 600 MHz spectrometer with TMS as internal standard using $CDCl_3$ or DMSO-d_6 solvent with chemical shifts reported in ppm. MALDI-TOF-MS experiment was performed on AB SCIEX, U.S.A. instrument with a 4800 plus MALDI TOF/TOF Analyzer. The UV-vis absorption spectra and PL spectra experiments were done in Perkin-Elmer Model lambda-750 UV-Vis spectrometer and Horiba Fluoromax-4 spectro-fluorometer respectively. High resolution mass spectrometry (HRMS) was performed using Q-Tof MS analyzer spectrometer. Cyclic Voltammetry (CV) was performed on CH instruments 611D model with three standard electrochemical cells. Thin film of dyes was coated on glassy carbon electrode, it was used as a working electrode, Ag/Ag^+ electrode as the reference and Pt wire for counter electrode. 0.1 M tetrabutyl ammonium hexaflurophosphate ($TBAPF_6$) was used as supporting electrolyte dissolved in acetonitrile solvent. CV curves were standardized by using ferrocene as the standard. The photocurrent density *vs* photovoltage ($J-V$) curves of the DSSCs were acquired with a Keithley 2450 source meter under standard AM 1.5 solar illuminations (solar simulator, Photoemission Tech., 80AAA) at intensity of 100 mW cm^{-2}. The electrochemical impedance spectra (EIS) measurement for DSSCs was performed using electrochemical workstation (CHI660E, CH instruments, USA) under dark condition. The spectra were performed at various forward bias voltages -0.65 V in the frequency range 100 KHz to 0.1 Hz. IPCE curves of DSSCs were measured by SR 300, Optosolar, Gemany, where a 250 W, Xe lamp was used as the light source. Tafel polarization curves were obtained by using CHI660E electrochemical analyzer by sweeping potential ±0.60 in dark with 10 mV s^{-1} scan rate.

3.5 References

(1) Chen, W.-C.; Kong, F.-T.; Li, Z.-Q.; Pan, J.-H.; Liu, X.-P.; Guo, F.-L.; Zhou, L.; Huang, Y.; Yu, T.; Dai, S.-Y. *ACS Appl. Mater. Interfaces* **2016,** *8*, 19410-19417.

(2) Li, C.; Luo, L.; Wu, D.; Jiang, R.; Lan, J.; Wang, R.; Huang, L.; Yang, S.; You, J. *J. Mater. Chem. A* **2016,** *4*, 11829-11834.

(3) Mathew, S.; Yella, A.; Gao, P.; Humphry-Baker, R.; Curchod, B. F. E.; Ashari-Astani, N.; Tavernelli, I.; Rothlisberger, U.; Nazeeruddin, M. K.; Grätzel, M. *Nat. Chem.* **2014,** *6*, 242-247.

(4) Xie, Y.; Tang, Y.; Wu, W.; Wang, Y.; Liu, J.; Li, X.; Tian, H.; Zhu, W.-H. *J. Am. Chem. Soc.* **2015,** *137*, 14055-14058.

(5) She, Z.; Cheng, Y.; Zhang, L.; Li, X.; Wu, D.; Guo, Q.; Lan, J.; Wang, R.; You, J. *ACS Appl. Mater. Interfaces* **2015,** *7*, 27831-27837.

(6) Raju, T. B.; Vaghasiya, J. V.; Afroz, M. A.; Soni, S. S.; Iyer, P. K. *Org. Electron.* **2016,** *39*, 371-379.

(7) Kakiage, K.; Aoyama, Y.; Yano, T.; Oya, K.; Fujisawa, J.-i.; Hanaya, M. *Chem. Commun.* **2015,** *51*, 15894-15897.

(8) Lü, X.; Mou, X.; Wu, J.; Zhang, D.; Zhang, L.; Huang, F.; Xu, F.; Huang, S. *Adv. Funct. Mater.* **2010,** *20*, 509-515.

(9) Ren, Y.; Liu, J.; Zheng, A.; Dong, X.; Wang, P. *Adv. Sci.* **2017,** *4*, 1700099.

(10) Huang, Z.-S.; Zang, X.-F.; Hua, T.; Wang, L.; Meier, H.; Cao, D. *ACS Appl. Mater. Interfaces* **2015,** *7*, 20418-20429.

(11) Kimura, M.; Masuo, J.; Tohata, Y.; Obuchi, K.; Masaki, N.; Murakami, T. N.; Koumura, N.; Hara, K.; Fukui, A.; Yamanaka, R.; Mori, S. *Chem. Eur. J.* **2013,** *19*, 1028-1034.

(12) Jia, H.-L.; Huang, M.-Z.; Peng, Z.-J.; Wang, D.-M.; Zhang, G.-H.; Guan, M.-Y. *Dalton Trans.* **2017,** *46*, 15124-15129.

(13) Han, L.; Islam, A.; Chen, H.; Malapaka, C.; Chiranjeevi, B.; Zhang, S.; Yang, X.; Yanagida, M. *Energy Environ. Sci.* **2012,** *5*, 6057-6060.

(14) Roy, C.; Bura, T.; Beaupré, S.; Légaré, M.-A.; Sun, J.-P.; Hill, I. G.; Leclerc, M. *Macromolecules* **2017,** *50*, 4658-4667.

(15) Cho, N.; Han, J.; Song, K.; Kang, M.-S.; Jun, M.-J.; Kang, Y.; Ko, J. *Tetrahedron* **2014,** *70*, 427-433.

(16) Paek, S.; Cho, N.; Song, K.; Jun, M.-J.; Lee, J. K.; Ko, J. *J. Phys. Chem. C* **2012,** *116*, 23205-23213.

(17) Chen, D.-Y.; Hsu, Y.-Y.; Hsu, H.-C.; Chen, B.-S.; Lee, Y.-T.; Fu, H.; Chung, M.-W.; Liu, S.-H.; Chen, H.-C.; Chi, Y.; Chou, P.-T. *Chem. Commun.* **2010,** *46*, 5256-5258.

(18) Bhim Raju, T.; Vaghasiya, J. V.; Afroz, M. A.; Soni, S. S.; Iyer, P. K. *Phys. Chem. Chem. Phys.* **2016,** *18*, 28485-28491.

(19) Park, S. S.; Won, Y. S.; Choi, Y. C.; Kim, J. H. *Energy Fuels* **2009,** *23*, 3732-3736.

(20) Wu, J.; Lan, Z.; Lin, J.; Huang, M.; Huang, Y.; Fan, L.; Luo, G. *Chem. Rev.* **2015,** *115*, 2136-2173.

(21) Vaghasiya, J. V.; Sonigara, K. K.; Prasad, J.; Beuvier, T.; Gibaud, A.; Soni, S. S. *J. Mater. Chem. A* **2017,** *5*, 5373-5382.

(22) Song, D.; Cho, W.; Lee, J. H.; Kang, Y. S. *J. Phys. Chem. Lett.* **2014,** *5*, 1249-1258.

(23) Yella, A.; Lee, H.-W.; Tsao, H. N.; Yi, C.; Chandiran, A. K.; Nazeeruddin, M. K.; Diau, E. W.-G.; Yeh, C.-Y.; Zakeeruddin, S. M.; Grätzel, M. *Science* **2011,** *334*, 629-634.

(24) Li, B.; Wang, L.; Kang, B.; Wang, P.; Qiu, Y. *Sol. Energy. Mater. Sol. Cells.* **2006,** *90*, 549-573.

(25) Bisquert, J. *J. Phys. Chem. B* **2002,** *106*, 325-333.

(26) Huang, S. Y.; Schlichthörl, G.; Nozik, A. J.; Grätzel, M.; Frank, A. J. *J. Phys. Chem. B* **1997,** *101*, 2576-2582.

(27) Adachi, M.; Sakamoto, M.; Jiu, J.; Ogata, Y.; Isoda, S. *J. Phys. Chem. B* **2006,** *110*, 13872-13880.

(28) Vaghasiya, J. V.; Sonigara, K. K.; Fadadu, K. B.; Soni, S. S. *Perspect. Sci.* **2016,** *8*, 46-49.

(29) Huo, Z.; Zhang, C.; Fang, X.; Cai, M.; Dai, S.; Wang, K. *J. Power Sources* **2010,** *195*, 4384-4390.

(30) Fadadu, K. B.; Soni, S. S. *Electrochim. Acta* **2013,** *88*, 270-277.

(31) Vekariya, R. L.; Sonigara, K. K.; Fadadu, K. B.; Vaghasiya, J. V.; Soni, S. S. *ACS Omega* **2016,** *1*, 14-18.

(32) Soderberg, J. N.; Co, A. C.; Sirk, A. H. C.; Birss, V. I. *J. Phys. Chem. B* **2006,** *110*, 10401-10410.

(33) Petrii, O. A.; Nazmutdinov, R. R.; Bronshtein, M. D.; Tsirlina, G. A. *Electrochim. Acta* **2007,** *52*, 3493-3504.

(34) Vaghasiya, J. V.; Sonigara, K. K.; Suresh, L.; Panahandeh-Fard, M.; Soni, S. S.; Tan, S. C. *Nano Energy* **2019,** *60*, 457-466.

Appendix B: Additional data for chapter 3

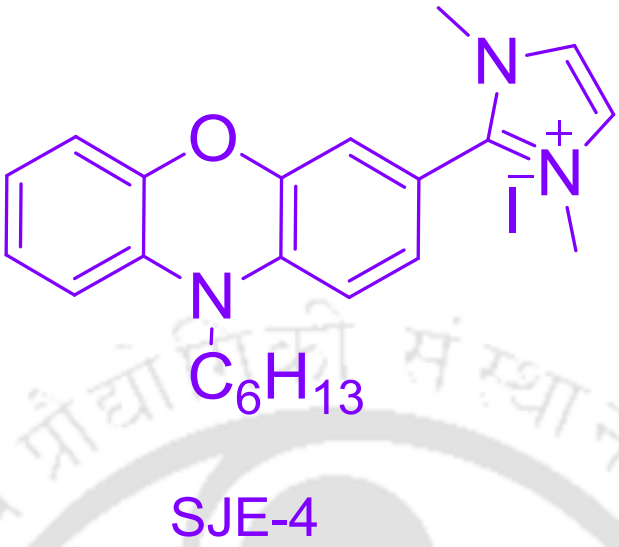

Figure B-1: Structure of SJE-4 electrolyte.

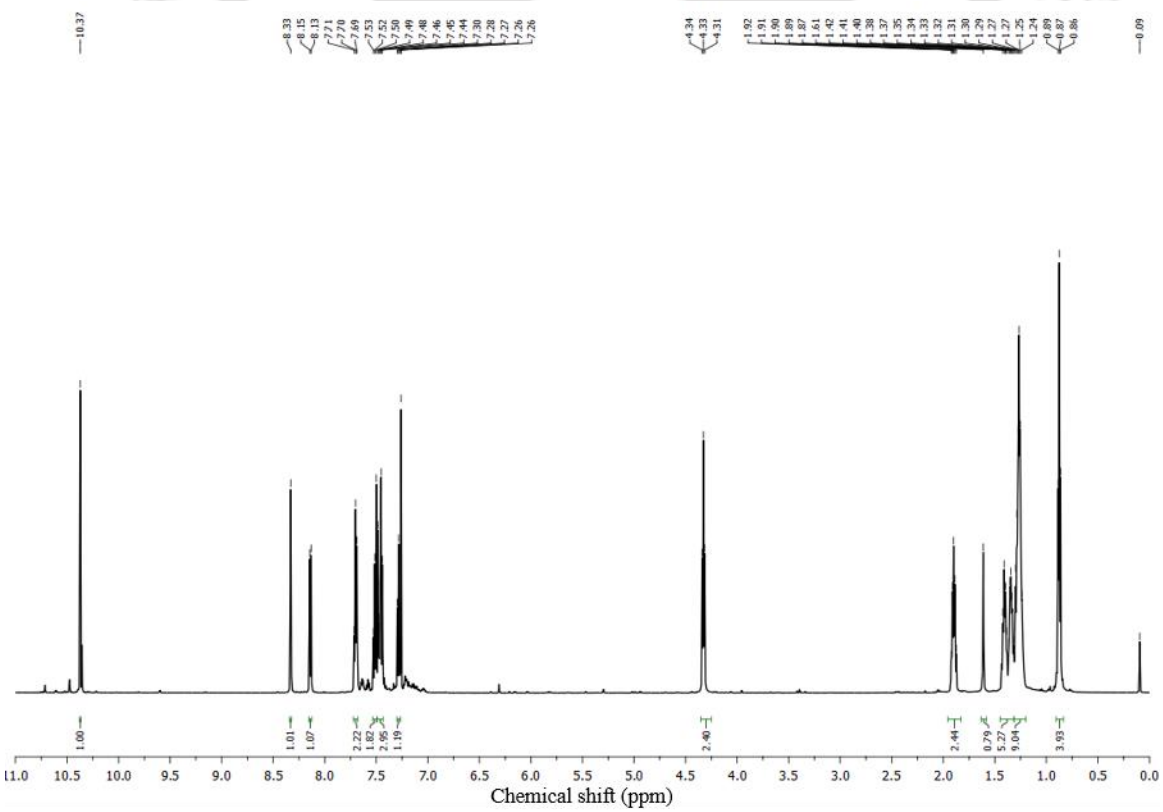

Figure B-2: ^{1}H-NMR spectrum of Cz-PhF2-CHO.

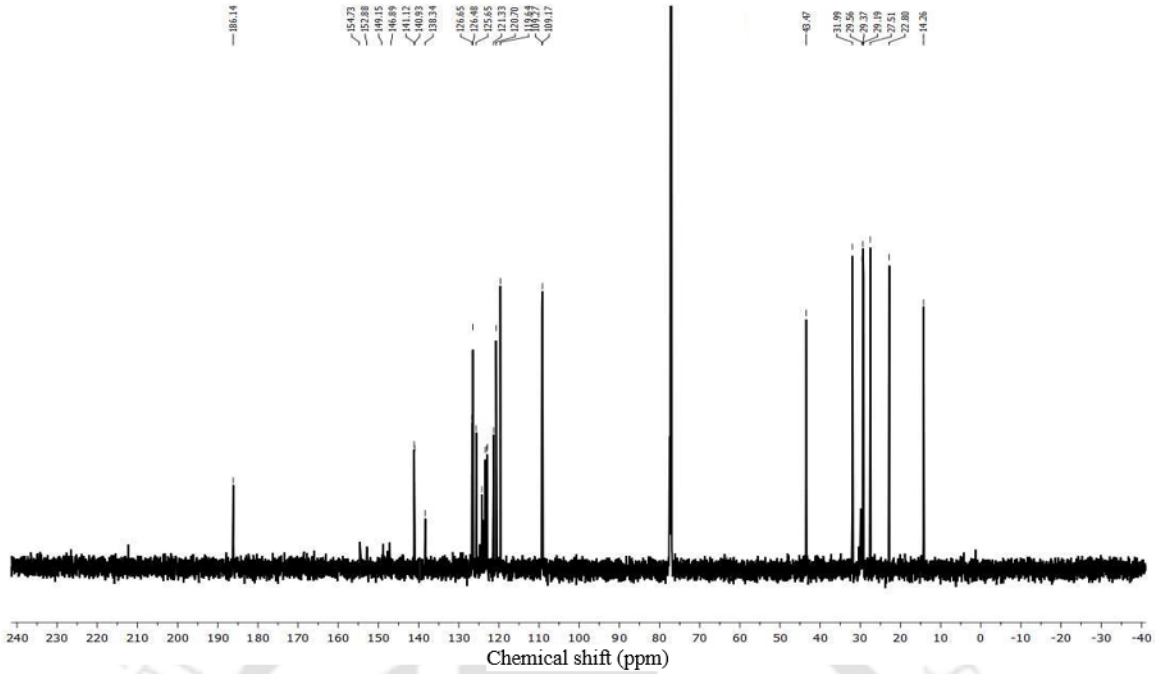

Figure B-3: ^{13}C-NMR spectrum of Cz-PhF2-CHO.

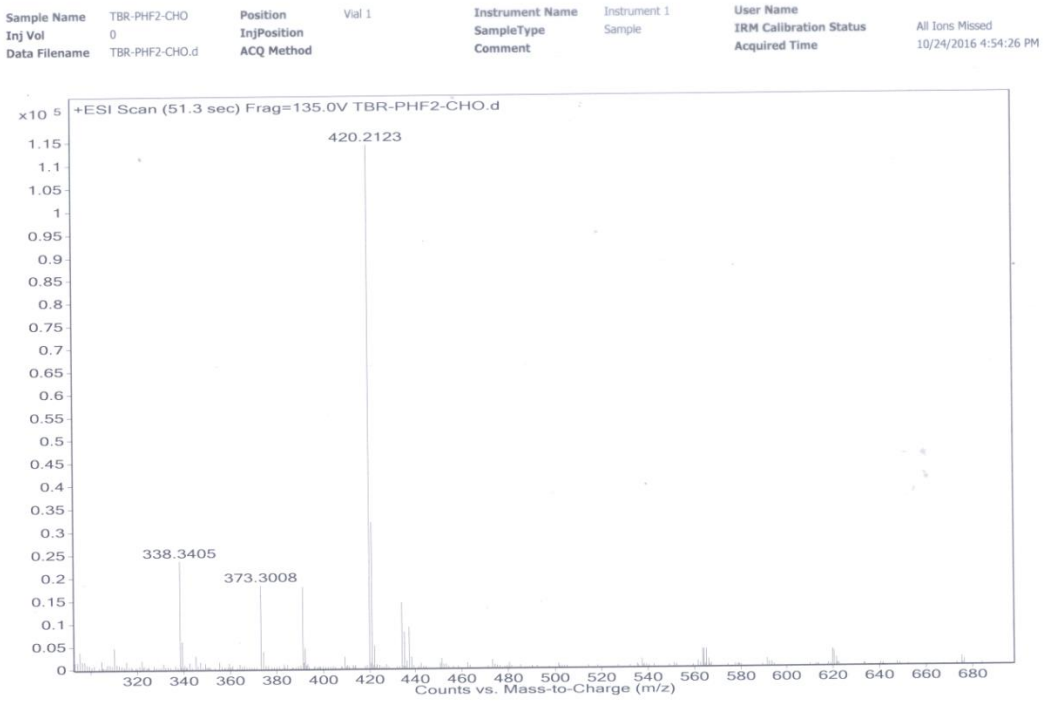

Figure B-4: ESI-MS spectrum of Cz-PhF2-CHO.

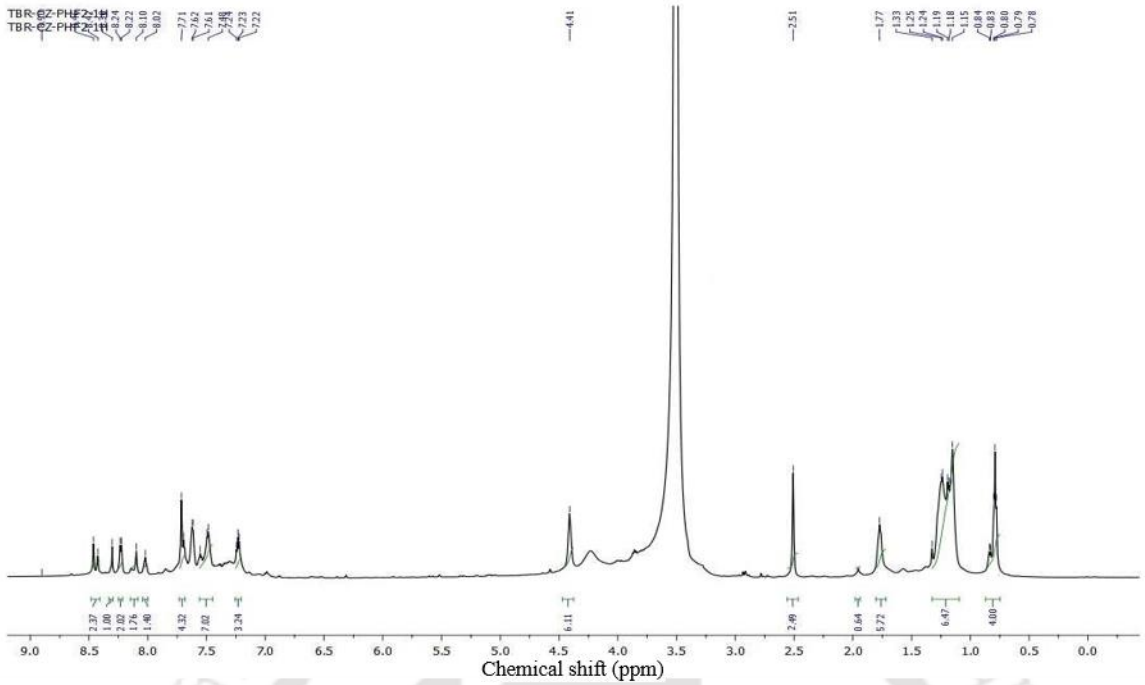

Figure B-5: ^{1}H-NMR spectrum of Cz-D1.

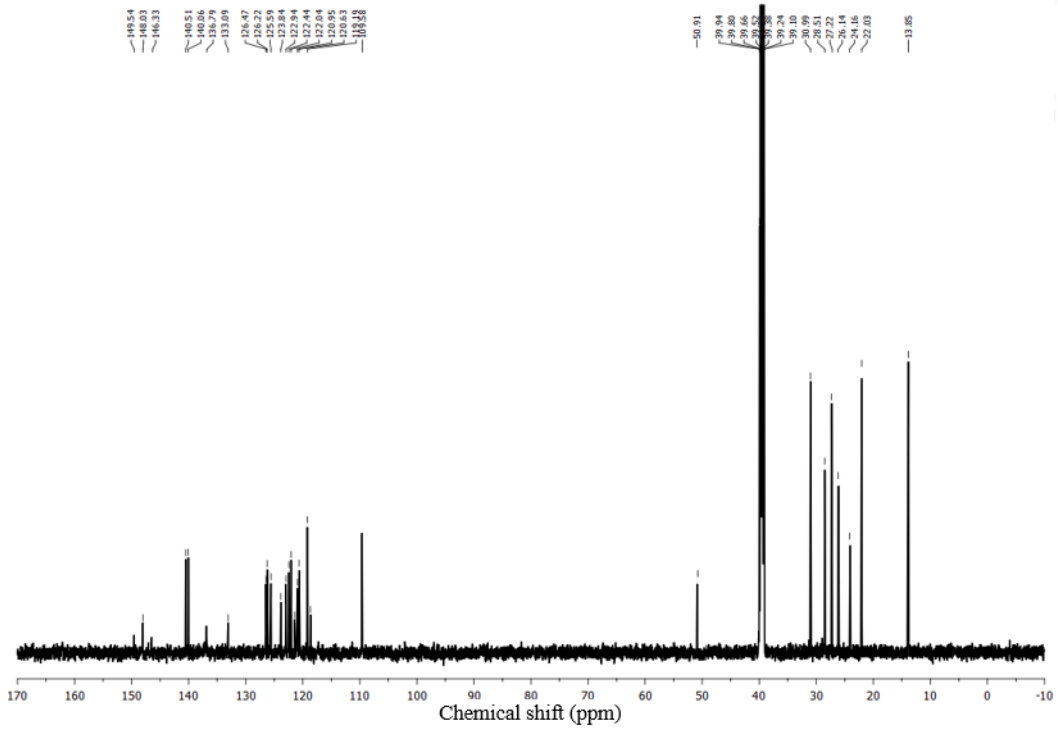

Figure B-6: ^{13}C-NMR spectrum of Cz-D1.

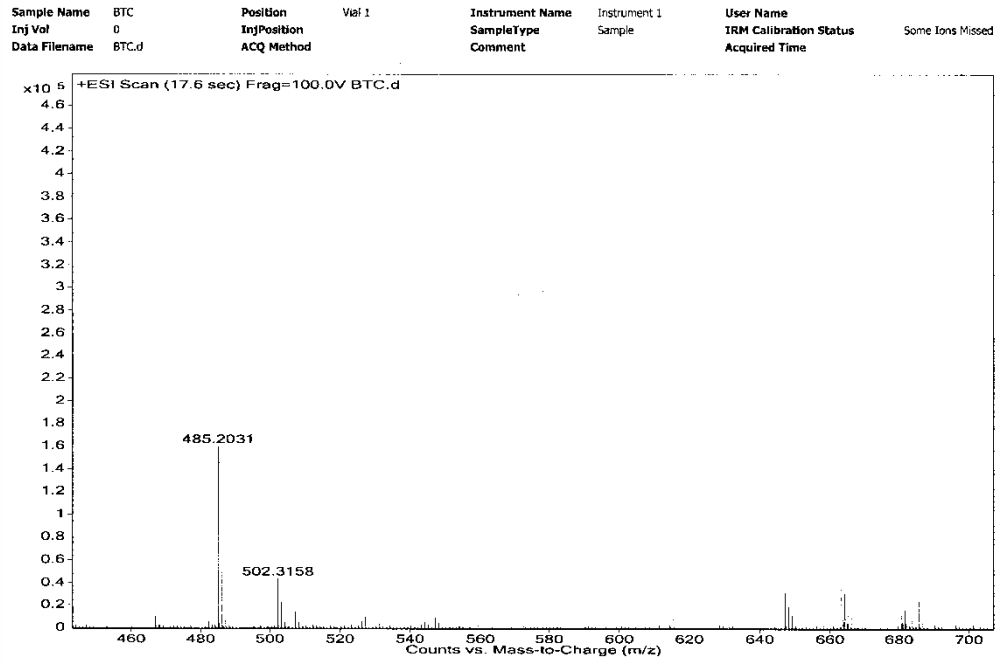

Figure B-7: ESI-MS spectrum of Cz-D1.

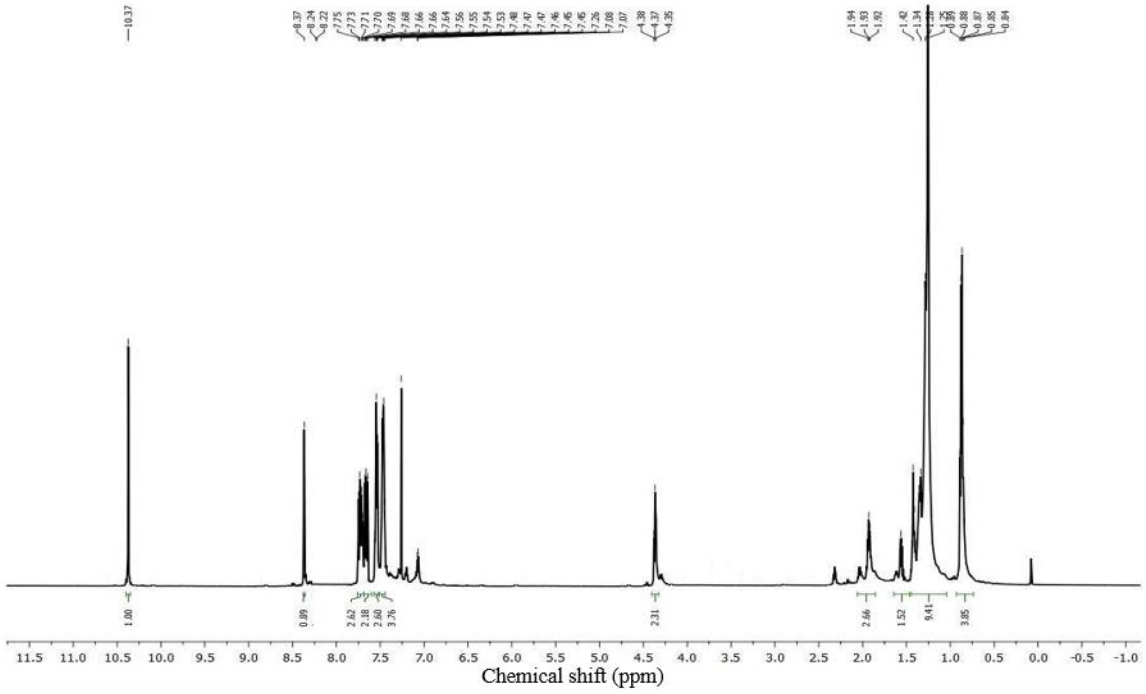

Figure B-8: ^{1}H-NMR spectrum of Cz-2PhF2-CHO.

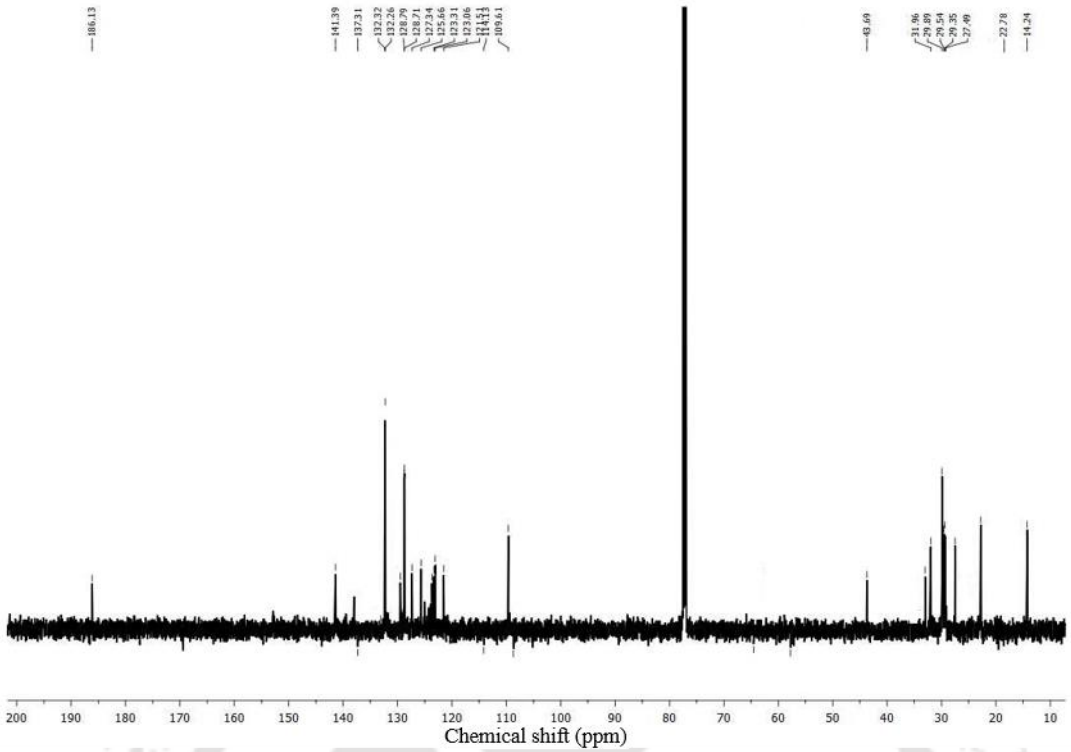

Figure B-9: ^{13}C-NMR spectrum of Cz-2PhF2-CHO.

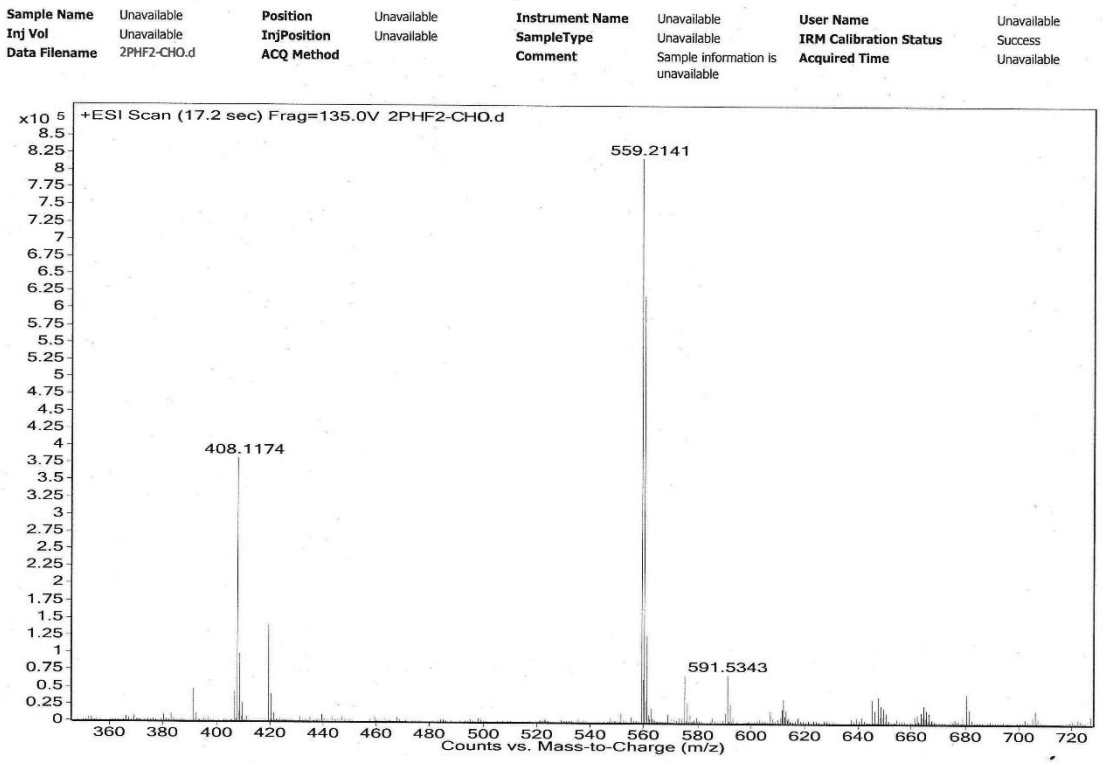

Figure B-10: ESI-MS spectrum of Cz-2PhF2-CHO.

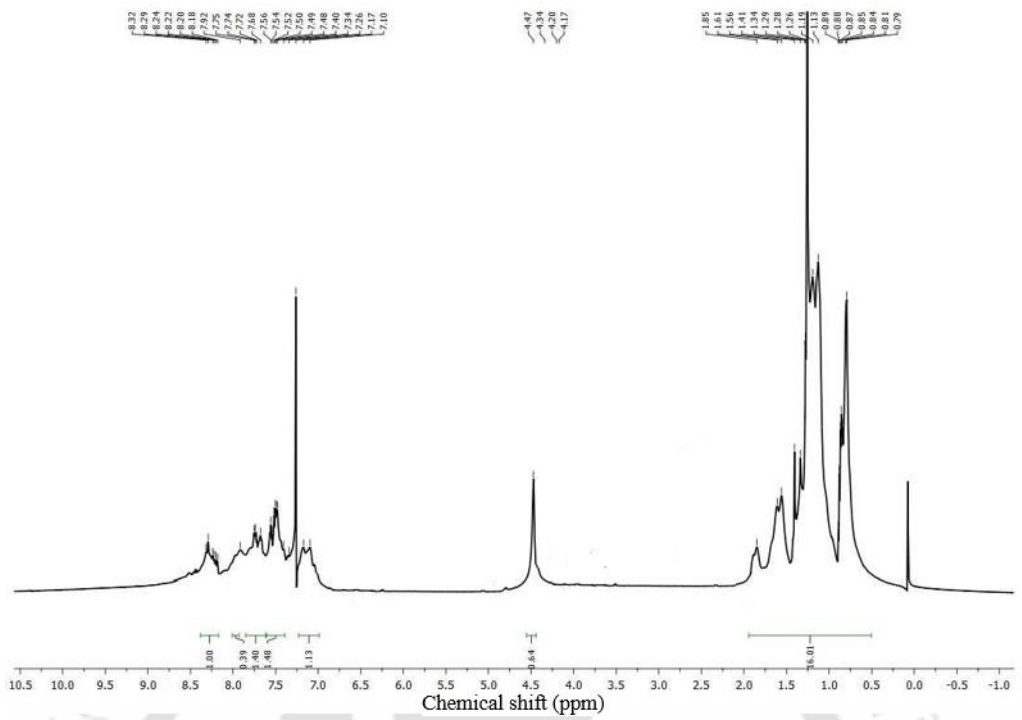

Figure B-11: ^{1}H-NMR spectrum of Cz-D2.

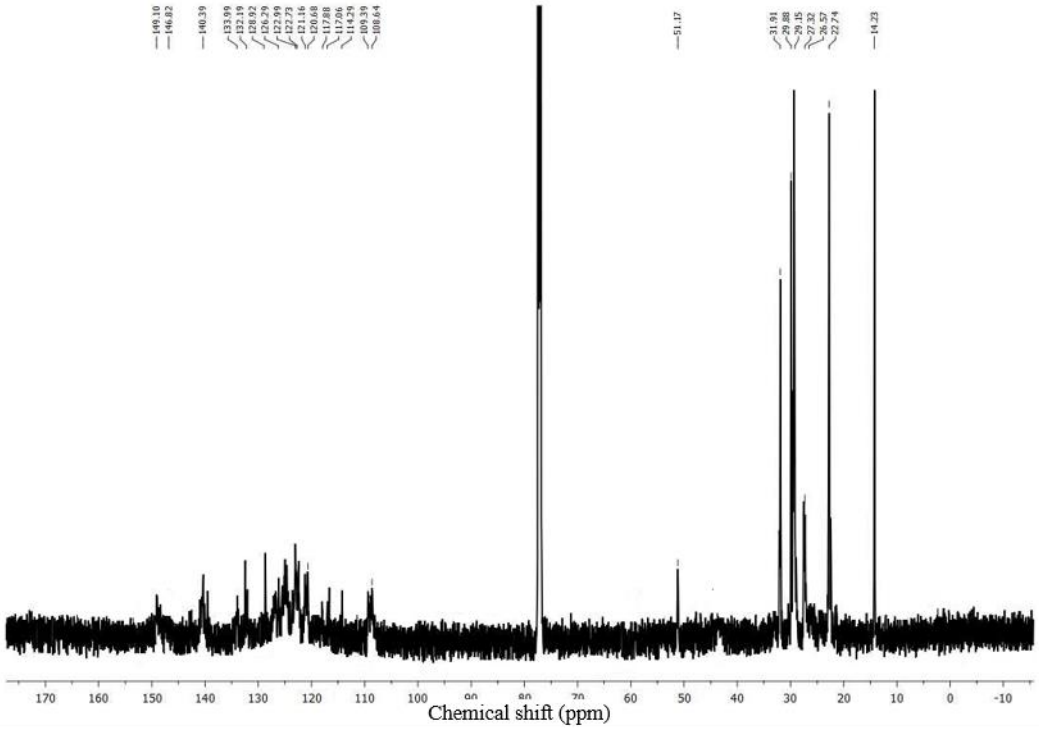

Figure B-12: ^{13}C-NMR spectrum of Cz-D2.

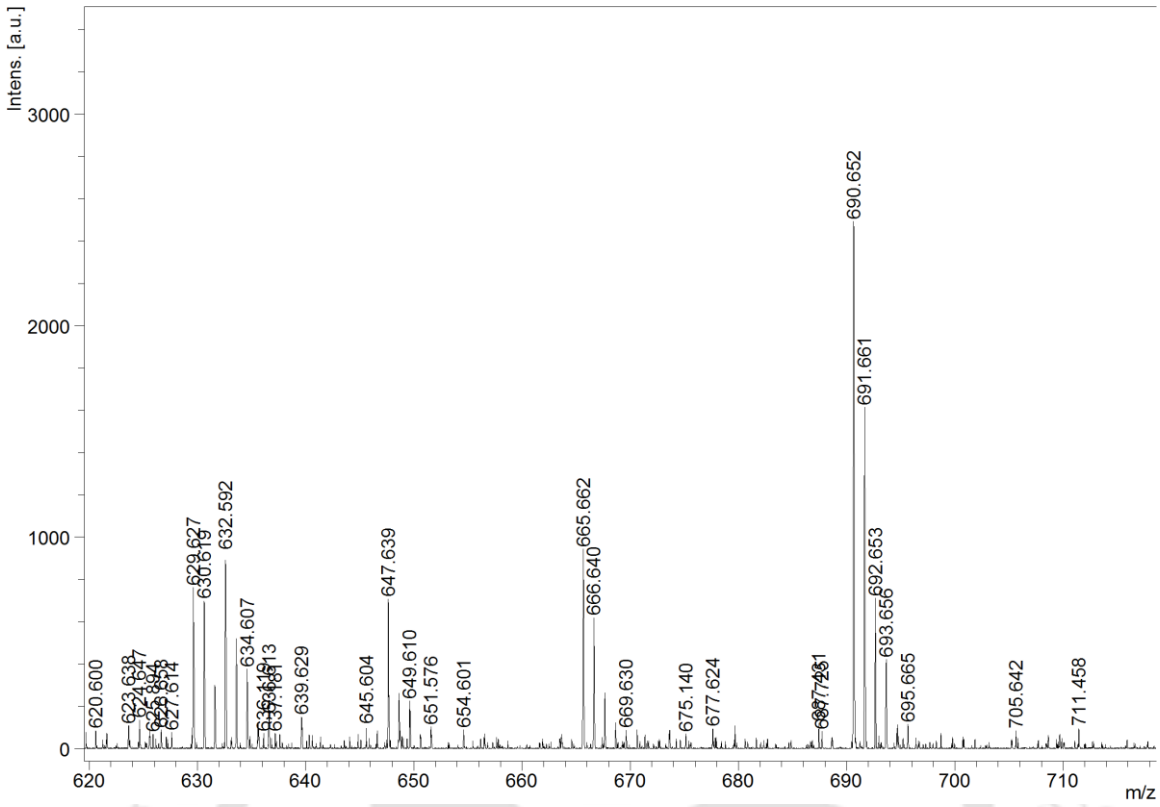

Figure B-13: MALDI-TOF spectrum of Cz-D2.

CHAPTER 4

Crystallization and Grain Growth Regulation through Lewis Acid-Base Adduct Formation in Hot Cast Perovskite-based Solar Cells

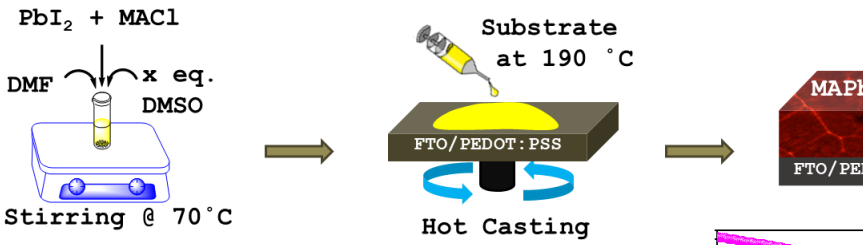

DMSO eq. (x)	0	0.5	1	1.5	2	3	4	Pure DMSO
Ave. Grain size (µm)	44	72	88	154	123	122	89	65

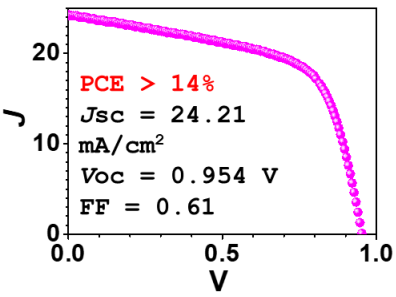

Afroz, M. A.; Gupta, R. K.; Garai, R.; Hossain, M.; Tripathi, S. P.; Iyer, P. K. *Org. Electron.* **2019,** *74*, 172-178, DOI: 10.1016/j.orgel.2019.07.007.

Abstract

The precise control of perovskite crystallization process that could provide smooth films with large grains is a prerequisite for solar cell fabrication to achieve higher efficiencies. To regulate this crystallization process and to achieve it multiple times remains a humongous challenge. This process has been reproducibly demonstrated in this chapter through efficient molecular exchange via a Lewis acid-base adduct formation. In this work, a Lewis acid-base adduct approach in concurrence with hot casting technique was employed to efficiently control the perovskite crystallization by judiciously adding dimethyl sulfoxide (DMSO) to a precursor solution of lead iodide (PbI_2) and methyl ammonium chloride (MACl) in dimethylformamide (DMF). High quality perovskite films were fabricated by precisely controlling the volume of DMSO which resulted in low recombination rate and which had better light harvesting ability. Uniform films of $MAPbCl_xI_{3-x}$ having large grain size were formed reproducibly on addition of 1.5 equivalents (eq.) DMSO to the precursor solution. Perovskite solar cells fabricated using this solution resulted in maximum power conversion efficiency (PCE) of 14.11% with enhanced stability as compared to the reduced PCE values obtained with other DMSO ratios and pure DMF solution cast films.

4.1 Introduction

During the last decade, the rapid growth of perovskite solar cells (PSCs) has become feasible owing to the inexpensive perovskite materials, ease of fabrication, and high power conversion efficiency (PCE).[1-7] The organic-inorganic mixed perovskites of methyl ammonium lead halide ($MAPbX_3$, $MA = CH_3NH_3^+$, $X = I^-$, Br^- or Cl^-) possess outstanding properties of an active material for photovoltaic application, such as strong absorption with high extinction coefficient, large diffusion length and lifetime of charge carriers, and low recombination rate along with the ability to tune its band gap and crystallinity.[8-11] Optimization of the methods for perovskite film formation,[4,12-14] development of new materials for enhanced performance,[3,5-9] and flexibility of device architectures[15-16] have facilitated the PSCs to advance from an initial efficiency of 3.8 % to a certified 23.3 %[17] recently, making them the fastest growing photovoltaic technology to date. Along with good chemical composition, smooth perovskite films with good crystallinity and large size grains are extremely preferred for high efficiency PSCs through reduction in non-radiative recombination sites.[18] In order to improve the quality of perovskite films, some approaches like use of different additives in perovskite precursor solution[19-21] to enhance crystallization of perovskite films, passivation of the perovskite film[22-23] and application of new methods such as solvent annealing,[24] vacuum-flash solution processing,[25] solvent- and vacuum free route[26] have been reported.

Modulation of the perovskite precursor solution through Lewis acid-base adduct formation is a successful approach to obtain perovskite film with high quality both in one-step[27-29] as well as two-step methods.[30-31] In this approach a Lewis acid-base adduct intermediate is formed between lead halide (a Lewis acid) and polar aprotic solvent N,N-dimethylformamide (DMF, a Lewis base) before conversion to the perovskite film. The quality of perovskite film depends on the intermediate formed and can be controlled by employing strong Lewis bases in combination with DMF. Generally used Lewis bases having lone pairs on oxygen, nitrogen, and sulfur atoms are Dimethyl sulfoxide (DMSO), N-methyl pyrrolidone (NMP), hexamethylphosphoramide (HMPA), urea, thiourea etc.[27,31-34] Perovskite film is formed by the removal of Lewis base from the intermediate, which can be done through solvent extraction,[32] intramolecular exchange[35] or by annealing.[36] There are various reports where the grain size and crystallinity of the perovskite films have been regulated by adding these bases to the precursor solution. The amount of a Lewis base to

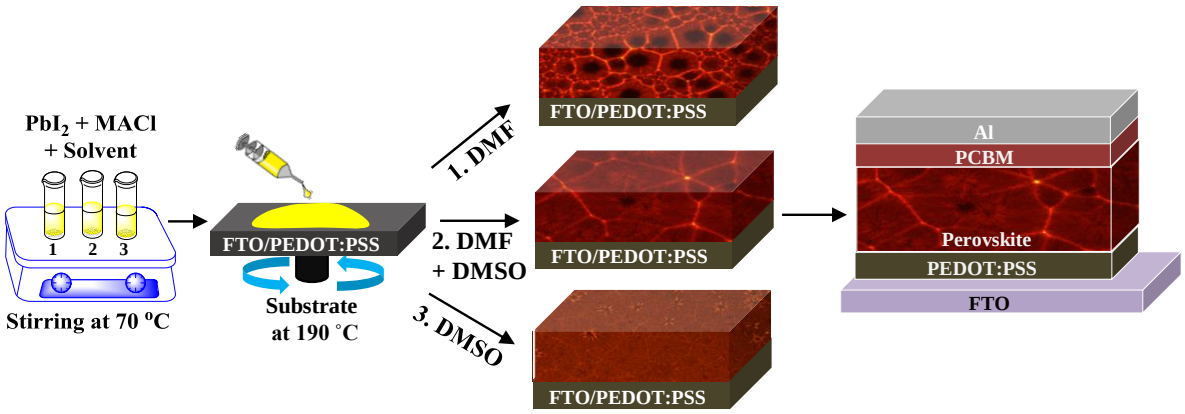

Figure 4.1: Schematic illustration of perovskite solar cell fabrication utilizing Lewis acid-base approach with hot casting method. Different amount of DMSO was added to the precursor solution of PbI_2: MACl in DMF and hot casting at 190 ˚C was carried out to form perovskite films.

be used depends on the donor number, which in turn is a measure of electron pair donating ability of a Lewis base.[37] For a particular base, however, the optimum amount to obtain good quality perovskite film also depends on the fabrication process of the film.[28,38-39] Recently, hot casting method for perovskite film formation had been reported where the precursor solution was coated on a pre-heated substrate following single step method. This method resulted in an excellent quality perovskite film with good crystallinity and large grains.[40]

Considering these advantages, the Lewis acid base approach was combined with the hot casting technique to control the grain growth of perovskite films by varying the amount of DMSO carefully. Different amounts of DMSO (0.5, 1.0, 1.5, 2.0, 3.0, 4.0 equivalents proportionate to PbI_2) were mixed with the precursor solution of PbI_2 and MACl in DMF (Figure 4.1). These precursors were chosen since the beneficial role of chloride-containing precursors has been well demonstrated previously for solar cell applications.[41-42] The results of these solutions were compared with the reference solution where no DMSO was added and the solution of precursors in pure DMSO. 1.5 eq. DMSO was found to generate large sized grains and high-performance solar cells due to good light harvesting and slow recombination rates.

4.2 Results and Discussion

The interactions of Lewis base, DMSO with PbI_2 were investigated with the help of FTIR transmission spectroscopy. The FTIR spectra of DMSO, DMSO + PbI_2 and DMSO + Perovskite are presented in Figure 4.2(a). The perovskite material used in the study was

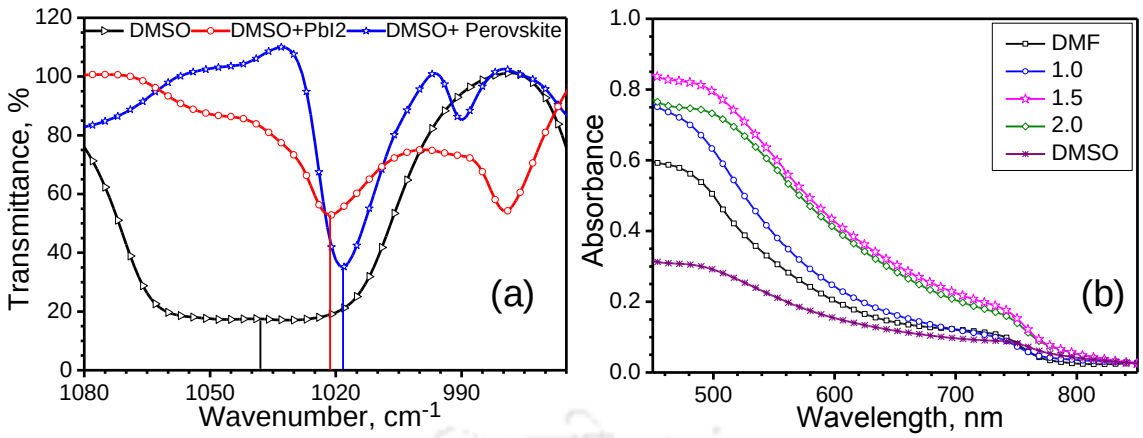

Figure 4.2: (a) FTIR spectra of the liquid DMSO, DMSO + PbI_2 (powder), and DMSO + Perovskite (powder) (b) UV-vis spectra of perovskite films fabricated through hot casting method using different equivalents of DMSO (pure DMF, 1.0, 1.5, 2.0 eq. of DMSO in DMF and pure DMSO) in the perovskite precursor solution.

$MAPbCl_xI_{3-x}$. A broad peak observed at 1045 cm^{-1} for S-O stretching (υ_{S-O}) shifted to 1022 cm^{-1} for DMSO + PbI_2 adduct. Further shift in the υ_{S-O} to 1018 cm^{-1} was observed for DMSO + Perovskite adduct.[28] The shift in the stretching vibration frequency confirms the interaction between the solvent and PbI_2 in adducts. The shift in υ_{S-O} from 1045 cm^{-1} to 1022 cm^{-1} is noted for the 1:1 adduct of PbI_2 and DMSO.[43] As the vibration frequency has a direct relation with square root of force constant (K), the decreased υ_{S-O} indicates a decrease in force constant, due to the reduced strength of S-O bond as a result of the adduct formation. Thus, the stretching frequencies for adducts are shifted towards lower wavenumber with respect to that of DMSO. The υ_{S-O} for DMSO + Perovskite is further decreased as compared to DMSO + PbI_2 due to the better interactions with both MA^+ as well as Pb_2^+ Lewis acids. This interaction results in the slow growth of perovskite crystals and hence good crystallinity and large grain formation was expected. To evaluate the effect of Lewis base on absorption, UV-vis absorption of the hot casted perovskite films was performed (Figure 4.2(b)). There was an enhancement in the absorption intensity of perovskite film with increasing amount of DMSO up to 1.5 eq., however further addition led to reduced absorption. A negligible red shift was also observed in the absorption onset when the perovskite film was grown with the help of DMSO. This improvement in the absorption intensity with the incorporation of DMSO might be attributed to high-quality perovskite films with large grains and good crystallinity. The band gap of all the perovskite films was ≈1.6 eV as obtained from absorption spectra (Figure 4.2(b)).

The perovskite film formation through Lewis adduct can be divided as: intercalation of Lewis base into PbI_2 molecule to form solvate complex, ion exchange to form perovskite,

and dissolution-recrystallization during grain growth.[28,30] When DMSO was added, due to its strong donating ability, it replaces the DMF molecules from the DMF·PbI_2·MACl adduct. Therefore, the overall strength of Pb-O bond between the solvent and PbI_2 becomes stronger. This resulted in the slow molecular exchange between MA^+ and solvent and hence slower conversion rate to form the perovskite film. As a result of slow formation rate, large grain size perovskites are likely to be obtained. However, larger quantities of Lewis base would solubilize the perovskite grains in the dissolution-recrystallization step, thereby generating films with smaller grain size.[30,44] The slow conversion rate of perovskite formation could be confirmed by XRD experiment. The solvate complex films prepared from pure DMF as well as pure DMSO were characterized by XRD (Figure 4.3(a)). The as-cast film from DMF solution showed characteristic peaks at 6.6˚ and 9.6˚, whereas, the film casted from DMSO solution showed peaks at 6.6˚ and 9.3˚ respectively.[45-46] After 24 h, XRD experiments were repeated on the same films to realize that a new peak at 14.2˚ corresponding to perovskite was observed in the case of DMF, but no such peaks could be seen for DMSO film. This important observation confirmed that the presence of DMSO retards the perovskite formation. Figure 4.3(b) illustrates the XRD spectra of solvate complexes with different amount of DMSO added to the precursor solution. It can be observed that with 0.5 eq. solution, the DMF adduct dominates over the DMSO adduct (very small peak at 9.3˚) and with 1.0 eq. solution, small amount of DMF adduct remained in the film. With further addition, only DMSO adducts were formed. The XRD spectra of hot casted perovskite films are illustrated in Figure 4.3(c). All the spectra showed identical patterns with characteristic peaks of 14.2˚ and 28.6˚ for 110 and 220 planes of tetragonal $MAPbI_3$ respectively. Peaks at 15.6˚ and 32.0˚ correspond to the 110 and 220 planes of $MAPbCl_3$. Importantly no PbI_2 peak was present due to the use of hot casting method, which is highly beneficial for the improved device performance.[40] The composition of the

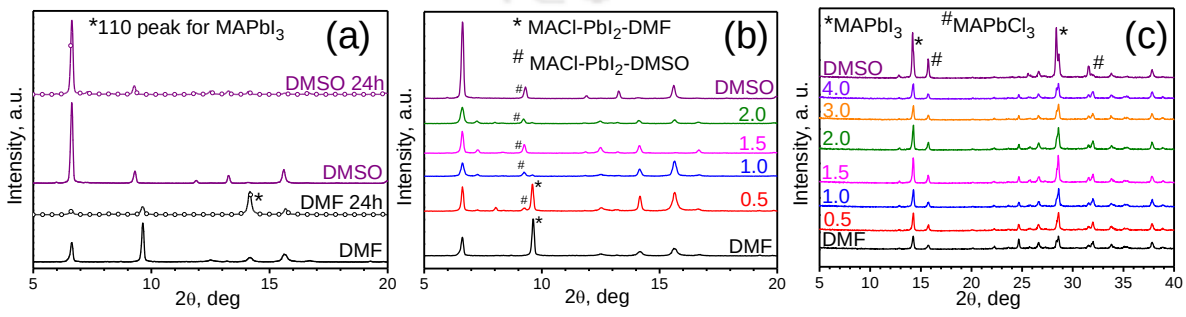

Figure 4.3: X-ray diffraction patterns of (a) DMF and DMSO adduct as cast and after 24 hours, (b) Adduct films with different amount of DMSO, and (c) Hot casted perovskite films from different precursor solutions.

Table 4.1: Composition of perovskites calculated from the XRD.

Perovskite	$MAPbI_3/MAPbCl_3$	$MAPbCl_3$ percent
DMF	3.08	24.5
0.5	2.80	26.3
1	3.08	24.5
1.5	3.29	23.3
2	3.15	24.1
3	2.95	25.3
4	2.86	25.9
DMSO	2.34	29.9

perovskites was also calculated from the XRD peak ratio corresponding to $MAPbI_3$ (14.2˚) and $MAPbCl_3$ (15.6˚). No major change was realized in the percentage of $MAPbCl_3$; it ranges from 23.3-26.3 % for films fabricated with DMF containing precursors and is slightly higher for pure DMSO film (29.9%) (Table 4.1).

Optical microscopic characterization was performed to perceive the influence of DMSO amount (0.5, 1.0, 1.5, 2.0, 3.0, 4.0 eq. to that of PbI_2), when added to the precursor solution. The precursor solutions were spin casted on the FTO/PEDOT:PSS substrates inside a glove box and the as-casted, solvate intermediate films were analyzed by optical microscopy. Films from pure DMF as well as pure DMSO were also prepared for comparison. Small crystallites were observed on the film casted from pure DMF, which grow slowly on addition of up to 1.0 eq. DMSO. Further addition of DMSO showed rod shaped solvate complex on the film surface and it covered the entire film when 4.0 eq. DMSO was added (Figure 4.4). These rod-shaped crystallites disappeared in the film formed only with DMSO solution that may be because of the dissolution in excess solvent. To understand the influence of DMSO on the grain size, the hot casted perovskite films were then analyzed using optical microscopy (Figure 4.5(a-h)). It was observed that the grain sizes of the perovskite films grow progressively with the addition of up to 1.5 eq. DMSO and reduced on further addition. The initial increase in grain size is attributed to the strong Lewis basicity of DMSO which reduced the conversion rate through the Pb-O bond formation with lead iodide. However, DMSO quantity of more than 2.0 eq. is likely to

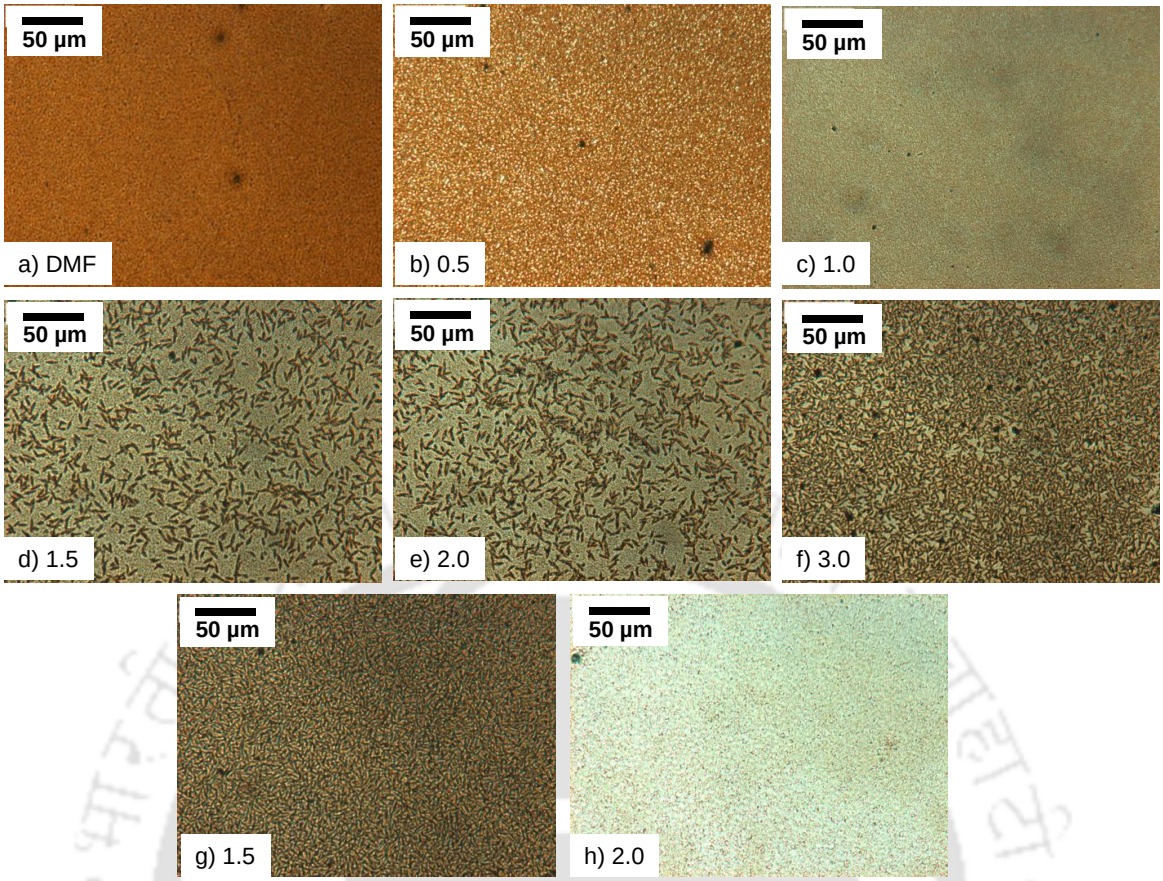

Figure 4.4: Optical microscopic images of MACl·PbI_2·DMSO solvate complex films prepared using precursor solutions in (a) pure DMF, (b-g) 0.5, 1.0, 1.5, 2.0, 3.0 & 4.0 equivalents of DMSO in DMF respectively and (h) pure DMSO.

dissolve the grains of perovskite film in the dissolution−recrystallization step, contributing to the grain size reduction. The average grain size was also calculated by taking the distribution of 50 grains obtained from four different optical microscopic images. The distribution of grain sizes is shown in Figure 4.5(i). (Their Gaussian fit is presented in Figure C-1, Appendix C). The average grain size for perovskite film prepared from pure DMF solution was 44 µm, and with 0.5, 1.0, 1.5, 2.0, 3.0, & 4.0 eq. of DMSO added to the precursor solution, the grain sizes were 72, 88, 154, 123, 112, & 89 µm respectively. The average grain size of perovskite film fabricated from precursor solution in pure DMSO was 65 µm. This variation clearly indicated that the size of perovskite grains depended on the amount of DMSO added to the precursor solution in DMF. The maximum grain size obtained in our case was for 1.5 eq. of DMSO. This was further confirmed by FESEM analysis (Figure C-2, Appendix C) and the results were comparable to the optical microscopy. A decrease in the root mean square (RMS) roughness of the perovskite films

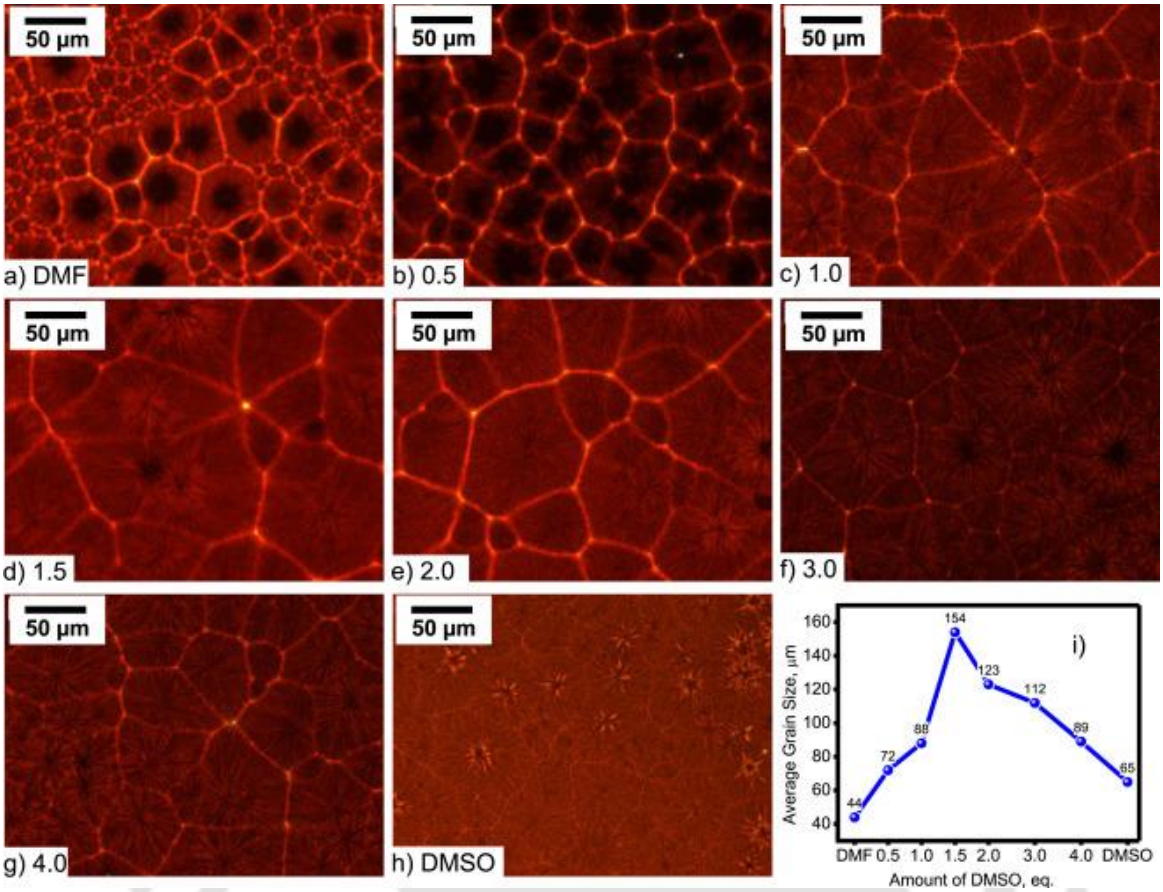

Figure 4.5: Optical microscopic images of perovskite films fabricated from different precursors using hot casting method (a) pure DMF, (b-g) 0.5, 1.0, 1.5, 2.0, 3.0 & 4.0 equivalents of DMSO in DMF respectively and (h) pure DMSO, and (i) average grain size distribution.

were also observed in AFM topography as DMSO is added into the precursor solution (Figure C-3, Appendix C).

To correlate the effect of DMSO on hot casting method with the solar cell performance, solar cell devices with inverted configuration of FTO/PEDOT:PSS/$MAPbI_{3-x}Cl_x$/PCBM/Al were fabricated and the results for best devices are demonstrated in Figure 4.6 and corresponding parameters are listed in Table 4.2. The data showed that with the increased amount of DMSO from 0 to 1.5 eq., the PCE enhanced from 8.65 % to 14.11 %. However, further addition of DMSO to the precursor resulted in the decrease in its PCE. The PSCs fabricated from 1.5 eq. DMSO outperformed other devices with short circuit current density (J_{sc}) of 24.21 mA cm^{-2}, open circuit voltage (V_{oc}) of 0.954 V, fill factor (FF) of 0.61, and PCE of 14.11 %. The devices prepared either from pure DMF (J_{sc} = 18.13 mA cm^{-2}, V_{oc} = 0.852 V, FF = 0.56, and PCE = 8.65 %) or pure DMSO (J_{sc} = 19.39 mA cm^{-2}, V_{oc} = 0.812 V, FF = 0.45, and PCE = 7.09 %) resulted in poor performance. A statistical summary of a series of devices is presented as box chart in Figure 4.7(a-d) and corresponding average

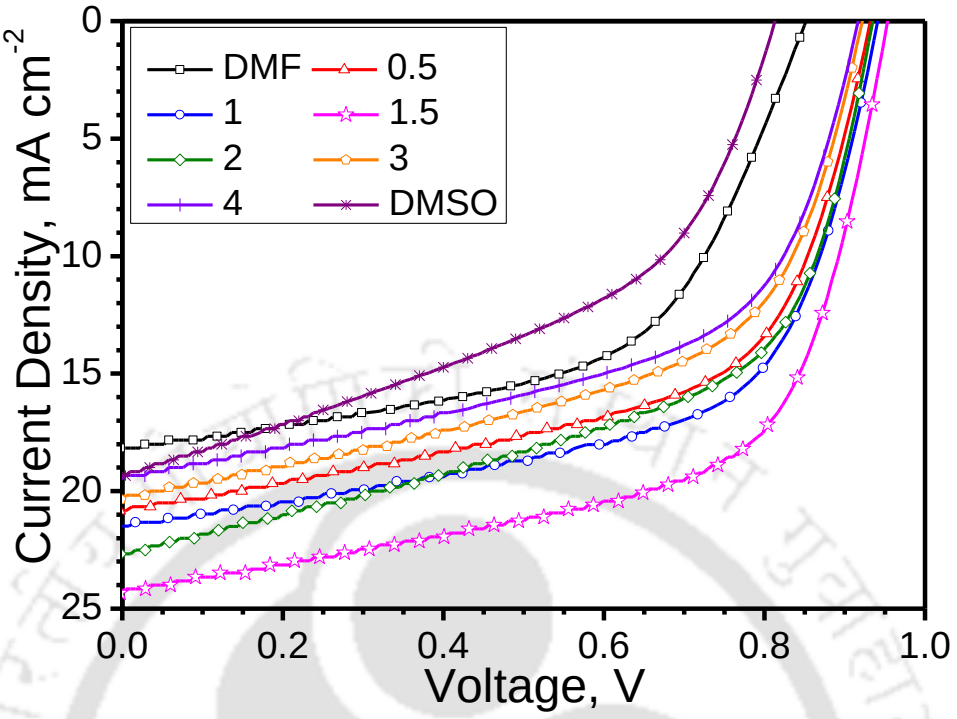

Figure 4.6: *J-V* curves of perovskite solar cells (FTO/PEDOT:PSS/MAPbI$_{3-x}$Cl$_x$/PCBM/Al) fabricated through Lewis acid-base adduct using hot casting method.

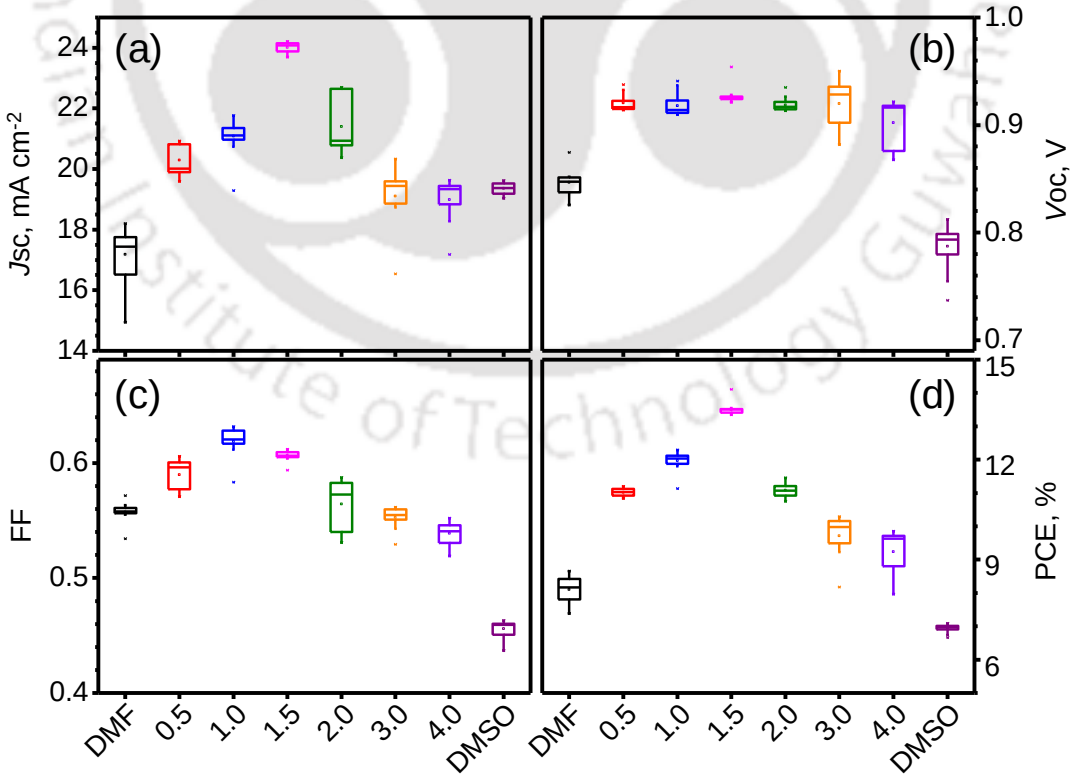

Figure 4.7: Box chart showing statistical distribution of solar cell parameters of 20 devices (a) *J*sc, (b) *V*oc, (c) FF and (d) PCE.

Table 4.2: *J-V* parameters of hot casted PSCs under AM1.5G standards.

Device	Jsc (mA cm^{-2})	Voc (V)	FF	Max. PCE, % (Ave. PCE, %)[a]
DMF	18.13	0.852	0.56	8.65 (8.11 ± 0.41)
0.5	20.82	0.932	0.57	11.20 (11.02 ± 0.12)
1.0	21.48	0.941	0.60	12.13 (11.97 ± 0.27)
1.5	24.21	0.954	0.61	14.11 (13.50 ± 0.16)
2.0	22.67	0.935	0.54	11.45 (11.08 ± 0.19)
3.0	20.33	0.922	0.54	10.18 (9.72 ± 0.67)
4.0	19.46	0.917	0.54	9.70 (9.24 ± 0.61)
DMSO	19.39	0.812	0.45	7.09 (6.95 ± 0.11)

[a]Average PCE of 20 devices with their standard deviation given in parenthesis.

values of PCEs are listed in Table 4.2. This data also followed the same trend as best devices. There was no significant change in the V_{oc} value of devices (Figure 4.7(b)) as it does not depend on the grain size if the grains are bigger than 20 µm.[40] The enhancement in the PCE is mainly due to the significant improvement in the J_{sc}. The increase in J_{sc} is attributed to the enhancement in the light harvesting ability and slower recombination process.

The IPCE spectra of PSCs fabricated from pure DMF, pure DMSO, and 1.5 eq. DMSO solutions are given in Figure 4.8(a) and the integrated J_{sc} values obtained from it are listed in Table C-1, Appendix C. The IPCE spectra also shows that the PSCs fabricated from 1.5 eq. DMSO has better charge transport property than that of pure DMF or pure DMSO devices, which was expected with the better current density obtained in the former case. The IPCE values are lesser than expected and this inconsistency may be attributed to the slow response of the steady state current density[47] (Figure 4.8(b)) and difference in measurement conditions. The *J-V* characterization was performed inside an argon filled glove box with a water content less than 5 ppm, whereas, the IPCE measurement was done at ambient condition with a relative humidity of around 70%. The steady state current (SSC) measurements were also performed by applying voltage at a maximum power point. (Figure 4.8(b)) The PSCs fabricated from 1.5 eq. DMSO solution exhibited better stabilized output

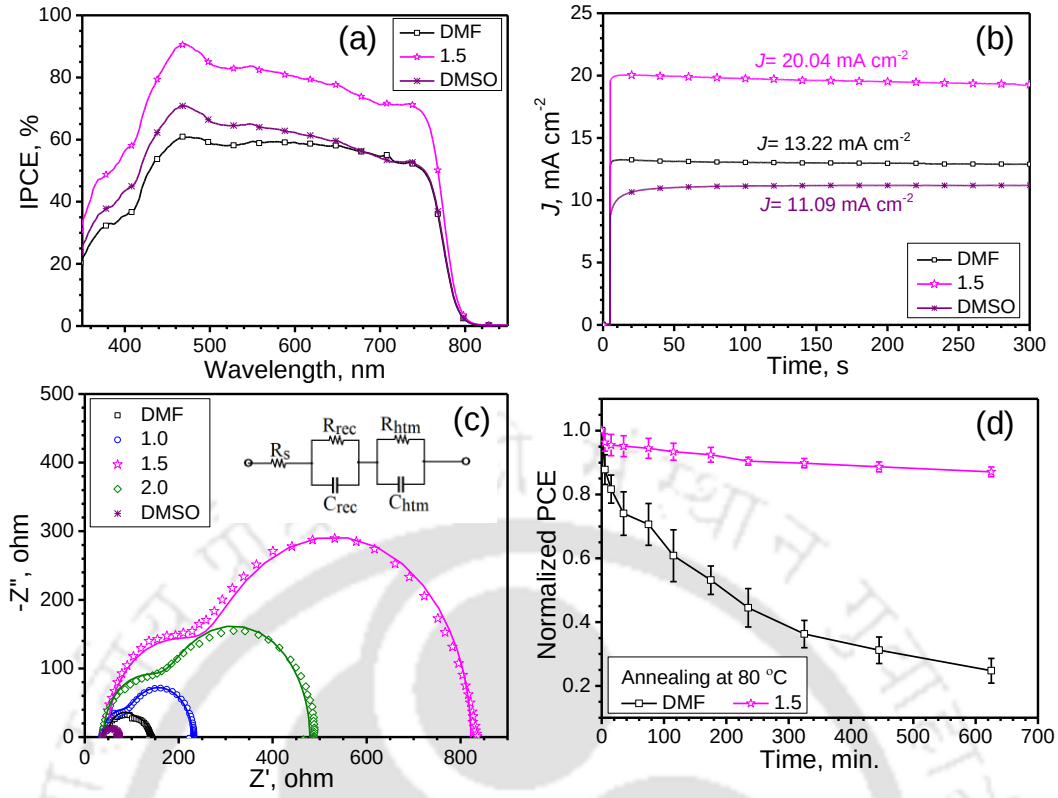

Figure 4.8: (a) IPCE spectra of different device. (b) Steady state current analysis performed at maximum power point, (c) Impedance spectra with equivalent circuit diagram in inset (d) Thermal Stability of PSCs at 80 ˚C for DMF and with 1.5 eq DMSO device carried out inside the glovebox for different durations.

as compared to that of pure DMF or pure DMSO. Values obtained from SSC measurements were lower than those obtained from *J-V* measurement, as observed widely in PSCs having hysteresis behavior.[46] Figure 4.8(c) shows the impedance spectra of the PSCs recorded at 0.8 V under dark conditions for various concentration of DMSO in a frequency ranging from 1 Hz up to 1 MHz. The obtained curves were fitted (solid line) using a model (inset of Figure 4.8(c)) to analyze the recombination resistance (R_{rec}) and transportation resistance (R_{htm}) in the fabricated PSCs.[48-49] R_s gives the series resistance between the two electrodes, R_{rec} in parallel to recombination capacitance (C_{rec}) contributes to the recombination process of the device and R_{htm} in parallel to the capacitance due to HTM (C_{htm}) is associated with the diffusion of holes across the HTM, i.e. PEDOT:PSS. Two semi circles were observed in the impedance spectra. The one in low frequency region was due to the charge recombination effect whereas the one in high frequency was due to the transport effect through HTM. The results obtained from fitting of the equivalent circuit of impedance spectra are summarized in Table 4.3. The R_{rec} was found to increase till 1.5 eq. DMSO (559.7 Ω) was added and thereafter it was found to decrease. This signifies least

Table 4.3: Impedance spectroscopy parameters.

Device	R_{rec} (Ω)	R_s (Ω)	R_{htm} (Ω)
DMF	29.4	38.7	62.63
1.0	136.1	37.9	55.28
1.5	559.7	43.2	213.7
2.0	305.9	39.6	133.3
DMSO	6.9	48.1	25.64

recombination current in the 1.5 eq. DMSO, thus giving the highest efficiency. Similarly, the R_{htm} for 1.5 eq. DMSO (213.7 Ω) was also higher than any other concentration of DMSO signifying better hole diffusion through PEDOT:PSS in the device. Both these can be very well correlated to the grain size of the perovskite film which was also the maximum for 1.5 eq. DMSO (154 μm), and had the least effect of recombination due to minimum grain boundaries. Slow recombination and better hole diffusion resulted in the higher V_{oc} and FF[31] for 1.5 eq. DMSO PSC.

To study the impact of DMSO addition on the stability of perovskite solar cell, the thermal stability test was carried out by heating the devices at 80 ˚C inside the glove box and measuring the device performance at different time intervals. As shown in the graph of

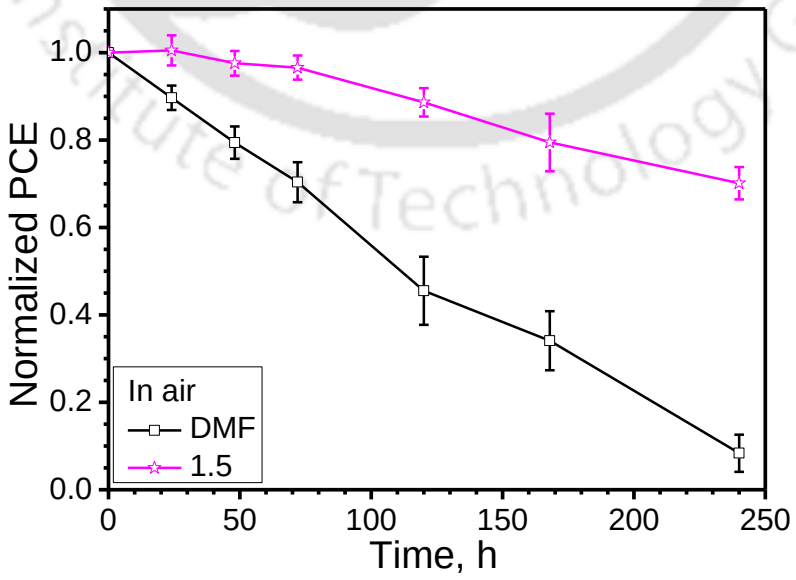

Figure 4.9: Air stability test of perovskite solar cell fabricated from pure DMF and 1.5 eq DMSO solutions.

normalized PCE Vs time (Figure 4.8(d)), the average loss in the PCE of solar cell fabricated from pure DMF solution was >75% and for 1.5 eq. DMSO the loss was <13% after 625 minutes. The degradation of perovskite films at grain boundaries takes place at a much faster rate compared to the grain surface,[50-51] therefore the improved stability observed in case of DMSO modified perovskite as compared to the control cell with only DMF might be attributed to the bigger grain size. The air stability test was also performed (Figure 4.9) which confirmed the improved stability for the device fabricated from 1.5 eq DMSO solution.

4.3 Conclusions

In summary, a facile approach of Lewis acid-base adduct formation was applied in combination with hot casting method to obtain a series of perovskite films with different average grain sizes using different amounts of DMSO. It was observed that the crystallinity and morphology of the solvent engineered perovskite film strongly depends on the amount of Lewis base and the processing condition which in turn influences the photovoltaic performance significantly. The film fabricated with 1.5 eq. DMSO precursor solution exhibited smooth film with large grain size. As a result, the maximum PCE of 14.11 % with improved stability could be obtained at these conditions as compared to 8.65 % efficiency for pure DMF casted films. The present work delivers an effective way to fabricate efficient perovskite solar cell. Further work via Lewis acid base approach and hot casting method to improve the PCE and stability of the cells can be performed by including some amount of FAI with MAI that is comparable to DMSO in terms of size.

4.4 Experimental Section

4.4.1 Materials

Methylammonium chloride (MACl, 98.0 %) was purchased from TCI chemicals, lead iodide (PbI_2, 99.0 %), Fluorine-doped tin oxide (FTO) substrates (150 nm, 7 Ω $\square^{-1}$) were obtained from Sigma-Aldrich, (6,6)-Phenyl-C_{61}-butyric Acid Methyl Ester (PCBM, >99.5 %) was purchased from LUMTEC, DMF (99.5 %) and DMSO (99.0 %) were purchased from Qualigens and were distilled in our laboratory using literature procedure[52] before use. The hole transporting material (HTM) Poly(3,4-ethylenedioxythiophene)-poly(styrenesulfonate) (PEDOT:PSS, PVP AI 4083) was received from Clevios.

4.4.2 Fabrication of Perovskite solar cell

The patterned FTO substrates were cleaned by subsequent sonication in Milli-Q water, acetone, and 2-propanol and then exposed to a UV ozone treatment system for 15 min before the deposition of PEDOT:PSS film. A thin film of PEDOT:PSS was first deposited by spin-coating on the cleaned FTO at 5000 rpm for 30 s followed by heat treatment for 20 min at 150 ˚C. The perovskite films were coated in a one-step hot casting method described in detail elsewhere.[40] In short; the substrates were preheated to 190 ˚C and transferred to the spin coater chuck followed by spin coating for 30 s at a speed of 4000 rpm. Different amount of DMSO was added into the precursor solution of equimolar PbI_2 and MACl in DMF (200 mg mL^{-1} PbI_2 concentration), which was stirred overnight at 70 ˚C. Solution in pure DMSO was also made for comparison. After perovskite film, an electron transporting layer (ETL) was coated from a 20 mg mL^{-1} solution of PCBM in chlorobenzene (CB) at 1000 rpm for 30 s. Finally, to complete the solar cell fabrication Aluminum (80 nm) was deposited in a thermal evaporator at a rate of <5 $Å s^{-1}$. The active area of the PSCs was 0.06 cm^2.

4.4.3 Characterization

The perovskite films were characterized by optical microscopy (Leica DM 2500P polarizing optical microscope with QICAM FAST1394 camera), X-ray diffraction (XRD, Bruker, D8 Advance XRD with Cu-Kα [α = 1.54 Å]), atomic force microscopy (AFM, Agilent 5500-STM instrument), Scanning electron microscopy (SEM, JEOL JSM-7610F) and UV-vis absorption spectroscopy (Perkin Elmer Lamda-35). The PbI_2-DMSO and MACl-PbI_2-DMSO Lewis adducts were studied using Fourier transform infrared spectroscopy (FTIR, Perkin-Elmer-Spectrum). The current density−voltage (*J*−*V*) characteristic curves were recorded with a Keithley 2400 source meter in argon atmosphere by illuminating the device with a solar simulator (Newport, Oriel Sol 3A solar simulator, AM 1.5G, 100 mW cm^{-2}) using a shadow mask of 6 mm^2 area. The steady state current analysis and impedance spectroscopic measurement were performed using an electrochemical workstation (CH Instruments 760D). An Oriel IQE-200 instrument was used to record the incident photon-to-current efficiency (IPCE) in ambient condition.

4.5 References

(1) Lee, M. M.; Teuscher, J.; Miyasaka, T.; Murakami, T. N.; Snaith, H. J. *Science* **2012,** *338*, 643-647.

(2) Kim, H.-S.; Lee, C.-R.; Im, J.-H.; Lee, K.-B.; Moehl, T.; Marchioro, A.; Moon, S.-J.; Humphry-Baker, R.; Yum, J.-H.; Moser, J. E.; Grätzel, M.; Park, N.-G. *Sci. Rep.* **2012,** *2*, 591.

(3) Yang, W. S.; Noh, J. H.; Jeon, N. J.; Kim, Y. C.; Ryu, S.; Seo, J.; Seok, S. I. *Science* **2015,** *348*, 1234-1237.

(4) Burschka, J.; Pellet, N.; Moon, S.-J.; Humphry-Baker, R.; Gao, P.; Nazeeruddin, M. K.; Grätzel, M. *Nature* **2013,** *499*, 316-319.

(5) Jeon, N. J.; Noh, J. H.; Yang, W. S.; Kim, Y. C.; Ryu, S.; Seo, J.; Seok, S. I. *Nature* **2015,** *517*, 476-480.

(6) Green, M. A.; Ho-Baillie, A.; Snaith, H. J. *Nat. Photonics* **2014,** *8*, 506-514.

(7) Rong, Y.; Ku, Z.; Mei, A.; Liu, T.; Xu, M.; Ko, S.; Li, X.; Han, H. *J. Phys. Chem. Lett.* **2014,** *5*, 2160-2164.

(8) Eperon, G. E.; Stranks, S. D.; Menelaou, C.; Johnston, M. B.; Herz, L. M.; Snaith, H. J. *Energy Environ. Sci.* **2014,** *7*, 982-988.

(9) Noh, J. H.; Im, S. H.; Heo, J. H.; Mandal, T. N.; Seok, S. I. *Nano Lett.* **2013,** *13*, 1764-1769.

(10) Im, J.-H.; Lee, C.-R.; Lee, J.-W.; Park, S.-W.; Park, N.-G. *Nanoscale* **2011,** *3*, 4088-4093.

(11) Xing, G.; Mathews, N.; Lim, S. S.; Yantara, N.; Liu, X.; Sabba, D.; Grätzel, M.; Mhaisalkar, S.; Sum, T. C. *Nat. Mater.* **2014,** *13*, 476-480.

(12) Liu, M.; Johnston, M. B.; Snaith, H. J. *Nature* **2013,** *501*, 395-398.

(13) Jeon, N. J.; Noh, J. H.; Kim, Y. C.; Yang, W. S.; Ryu, S.; Seok, S. I. *Nat. Mater.* **2014,** *13*, 897-903.

(14) Xiao, Z.; Bi, C.; Shao, Y.; Dong, Q.; Wang, Q.; Yuan, Y.; Wang, C.; Gao, Y.; Huang, J. *Energy Environ. Sci.* **2014,** *7*, 2619-2623.

(15) Jeng, J.-Y.; Chiang, Y.-F.; Lee, M.-H.; Peng, S.-R.; Guo, T.-F.; Chen, P.; Wen, T.-C. *Adv. Mater.* **2013,** *25*, 3727-3732.

(16) Tavakoli, M. M.; Tsui, K.-H.; Zhang, Q.; He, J.; Yao, Y.; Li, D.; Fan, Z. *ACS Nano* **2015,** *9*, 10287-10295.

(17) National Renewable Energy Laboratory (NREL). https://www.nrel.gov/pv/assets/pdfs/pv-efficiency-chart.20190103.pdf (accessed January 2019).

(18) De Marco, N.; Zhou, H.; Chen, Q.; Sun, P.; Liu, Z.; Meng, L.; Yao, E.-P.; Liu, Y.; Schiffer, A.; Yang, Y. *Nano Lett.* **2016,** *16*, 1009-1016.

(19) Shi, Y.; Wang, X.; Zhang, H.; Li, B.; Lu, H.; Ma, T.; Hao, C. *J. Mater. Chem. A* **2015,** *3*, 22191-22198.

(20) Gong, X.; Li, M.; Shi, X.-B.; Ma, H.; Wang, Z.-K.; Liao, L.-S. *Adv. Funct. Mater.* **2015,** *25*, 6671-6678.

(21) Liang, P.-W.; Liao, C.-Y.; Chueh, C.-C.; Zuo, F.; Williams, S. T.; Xin, X.-K.; Lin, J.; Jen, A. K.-Y. *Adv. Mater.* **2014,** *26*, 3748-3754.

(22) Jiang, L.-L.; Wang, Z.-K.; Li, M.; Zhang, C.-C.; Ye, Q.-Q.; Hu, K.-H.; Lu, D.-Z.; Fang, P.-F.; Liao, L.-S. *Adv. Funct. Mater.* **2018,** *28*, 1705875.

(23) Jiang, Y.; Li, J.; Xiong, S.; Jiang, F.; Liu, T.; Qin, F.; Hu, L.; Zhou, Y. *J. Mater. Chem. A* **2017,** *5*, 17632-17639.

(24) Wang, Y.; Li, S.; Zhang, P.; Liu, D.; Gu, X.; Sarvari, H.; Ye, Z.; Wu, J.; Wang, Z.; Chen, Z. D. *Nanoscale* **2016,** *8*, 19654-19661.

(25) Li, X.; Bi, D. Q.; Yi, C. Y.; Decoppet, J. D.; Luo, J. S.; Zakeeruddin, S. M.; Hagfeldt, A.; Gratzel, M. *Science* **2016,** *353*, 58-62.

(26) Chen, H.; Ye, F.; Tang, W.; He, J.; Yin, M.; Wang, Y.; Xie, F.; Bi, E.; Yang, X.; Grätzel, M.; Han, L. *Nature* **2017,** *550*, 92-95.

(27) Lee, J.-W.; Kim, H.-S.; Park, N.-G. *Acc. Chem. Res.* **2016,** *49*, 311-319.

(28) Ahn, N.; Son, D.-Y.; Jang, I.-H.; Kang, S. M.; Choi, M.; Park, N.-G. *J. Am. Chem. Soc.* **2015,** *137*, 8696-8699.

(29) Pham, N. D.; Tiong, V. T.; Chen, P.; Wang, L.; Wilson, G. J.; Bell, J.; Wang, H. *J. Mater. Chem. A* **2017,** *5*, 5195-5203.

(30) Han, Q.; Bai, Y.; Liu, J.; Du, K.-z.; Li, T.; Ji, D.; Zhou, Y.; Cao, C.; Shin, D.; Ding, J.; Franklin, A. D.; Glass, J. T.; Hu, J.; Therien, M. J.; Liu, J.; Mitzi, D. B. *Energy Environ. Sci.* **2017,** *10*, 2365-2371.

(31) Cao, X.; Li, C.; Li, Y.; Fang, F.; Cui, X.; Yao, Y.; Wei, J. *Nanoscale* **2016,** *8*, 19804-19810.

(32) Fei, C.; Li, B.; Zhang, R.; Fu, H.; Tian, J.; Cao, G. *Adv. Energy Mater.* **2017,** *7*, 1602017.

(33) Zhang, Y.; Gao, P.; Oveisi, E.; Lee, Y.; Jeangros, Q.; Grancini, G.; Paek, S.; Feng, Y.; Nazeeruddin, M. K. *J. Am. Chem. Soc.* **2016,** *138*, 14380-14387.

(34) Jo, Y.; Oh, K. S.; Kim, M.; Kim, K.-H.; Lee, H.; Lee, C.-W.; Kim, D. S. *Adv. Mater. Interfaces* **2016,** *3*, 1500768.

(35) Cao, X. B.; Li, Y. H.; Fang, F.; Cui, X.; Yao, Y. W.; Wei, J. Q. *RSC Adv.* **2016,** *6*, 70925-70931.

(36) Jesper Jacobsson, T.; Correa-Baena, J.-P.; Pazoki, M.; Saliba, M.; Schenk, K.; Grätzel, M.; Hagfeldt, A. *Energy Environ. Sci.* **2016,** *9*, 1706-1724.

(37) Cao, X. B.; Li, C. L.; Zhi, L. L.; Li, Y. H.; Cui, X.; Yao, Y. W.; Ci, L. J.; Wei, J. Q. *J. Mater. Chem. A* **2017,** *5*, 8416-8422.

(38) Zhu, L.; Xu, Y.; Zhang, P.; Shi, J.; Zhao, Y.; Zhang, H.; Wu, J.; Luo, Y.; Li, D.; Meng, Q. *J. Mater. Chem. A* **2017,** *5*, 20874-20881.

(39) Tu, Y.; Wu, J.; He, X.; Guo, P.; Luo, H.; Liu, Q.; Lin, J.; Huang, M.; Huang, Y.; Fan, L.; Lan, Z. *Appl. Surf. Sci.* **2017,** *403*, 572-577.

(40) Nie, W.; Tsai, H.; Asadpour, R.; Blancon, J. C.; Neukirch, A. J.; Gupta, G.; Crochet, J. J.; Chhowalla, M.; Tretiak, S.; Alam, M. A.; Wang, H. L.; Mohite, A. D. *Science* **2015,** *347*, 522-5.

(41) Yu, H.; Wang, F.; Xie, F.; Li, W.; Chen, J.; Zhao, N. *Adv. Funct. Mater.* **2014,** *24*, 7102-7108.

(42) Williams, S. T.; Zuo, F.; Chueh, C.-C.; Liao, C.-Y.; Liang, P.-W.; Jen, A. K. Y. *ACS Nano* **2014,** *8*, 10640-10654.

(43) Wharf, I.; Gramstad, T.; Makhija, R.; Onyszchuk, M. *Can. J. Chem.* **1976,** *54*, 3430-3438.

(44) Wu, W.-Q.; Chen, D.; McMaster, W. A.; Cheng, Y.-B.; Caruso, R. A. *ACS Appl. Mater. Interfaces* **2017,** *9*, 31959-31967.

(45) Li, B.; Li, M.; Fei, C.; Cao, G.; Tian, J. *J. Mater. Chem. A* **2017,** *5*, 24168-24177.

(46) Chan Choi, Y.; Lee, S. W.; Jo, H. J.; Kim, D.-H.; Sung, S.-J. *RSC Adv.* **2016,** *6*, 104359-104365.

(47) Cao, X.; Zhi, L.; Li, Y.; Fang, F.; Cui, X.; Yao, Y.; Ci, L.; Ding, K.; Wei, J. *J. Mater. Chem. C* **2017,** *5*, 7458-7464.

(48) Christians, J. A.; Fung, R. C. M.; Kamat, P. V. *J. Am. Chem. Soc.* **2014,** *136*, 758-764.

(49) Dong, Q. Q.; Wang, Z. W.; Zhang, K. C.; Yu, H.; Huang, P.; Liu, X. D.; Zhou, Y.; Chen, N.; Song, B. *Nanoscale* **2016,** *8*, 5552-5558.

(50) Wang, Q.; Chen, B.; Liu, Y.; Deng, Y. H.; Bai, Y.; Dong, Q. F.; Huang, J. S. *Energy Environ. Sci.* **2017,** *10*, 516-522.

(51) Chiang, C.-H.; Wu, C.-G. *ChemSusChem* **2016,** *9*, 2666-2672.

(52) Armarego, W. L. F.; Chai, C. L. L. *Purification of laboratory chemicals*, Elsevier Science: Amsterdam, 2003.

Appendix C: Additional data for chapter 4

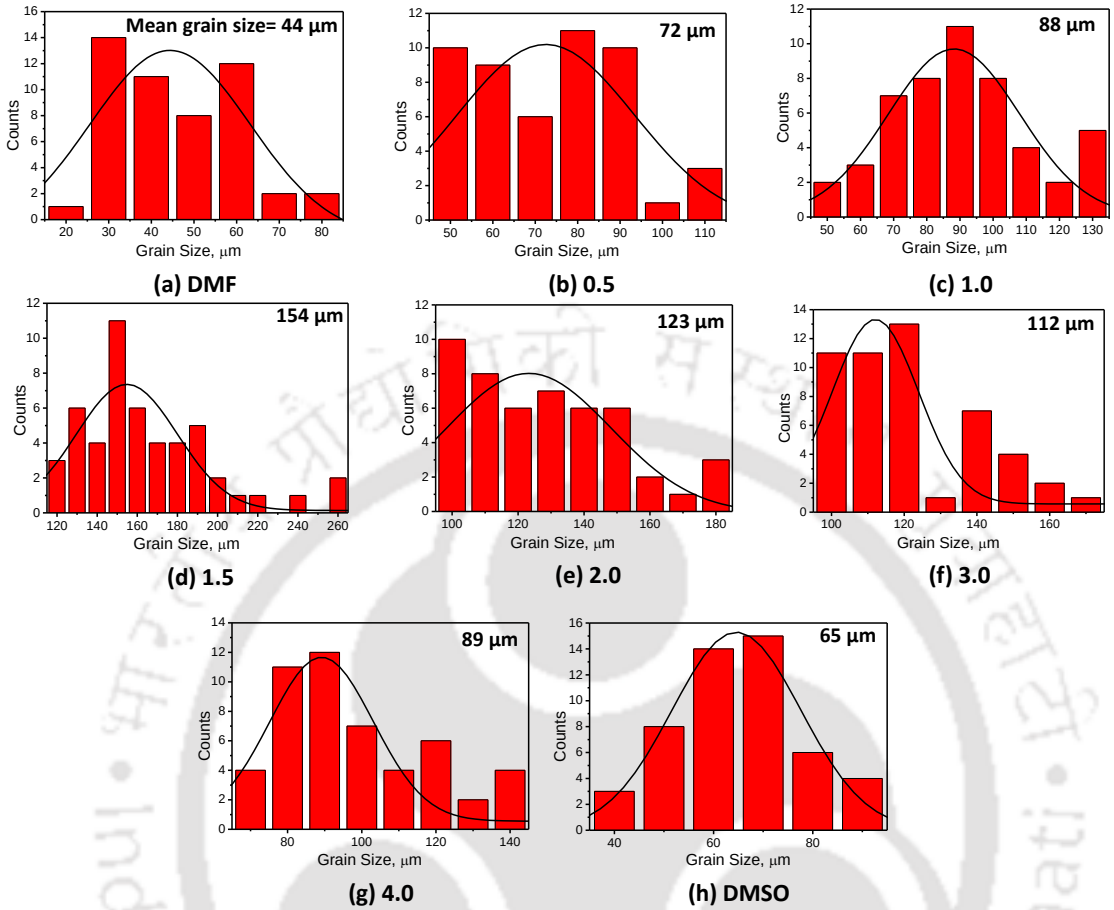

Figure C-1: Grain size distribution (red bar) with Gaussian fit (black line) of $MAPbCl_xI_{3-x}$ perovskite films prepared using precursor solutions in **(a)** pure DMF, **(b-g)** 0.5, 1.0, 1.5, 2.0, 3.0 & 4.0 equivalents of DMSO in DMF respectively and **(h)** pure DMSO using hot casting method.

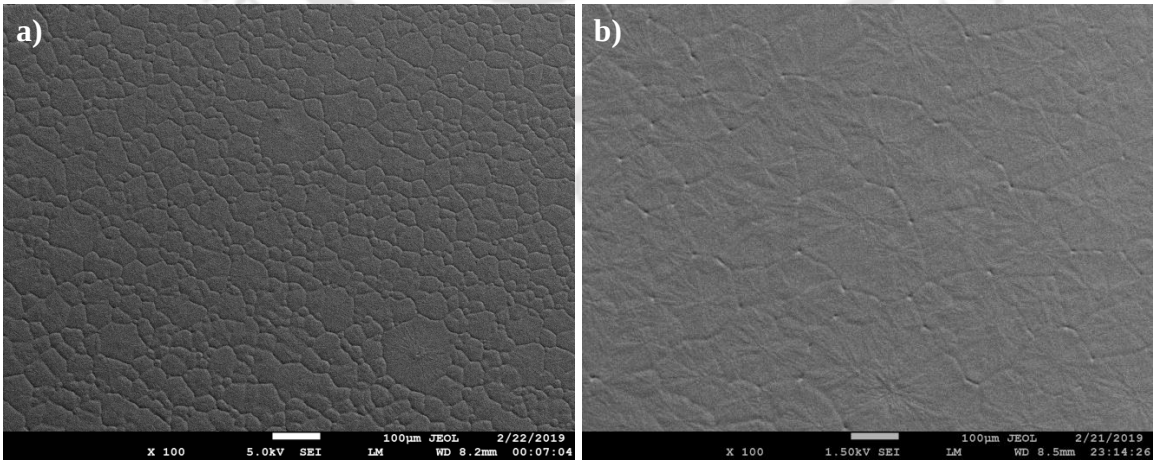

Figure C-2: FESEM images of perovskite films coated from (a) pure DMF and (b) 1.5 eq DMSO in DMF solutions using hot casting method.

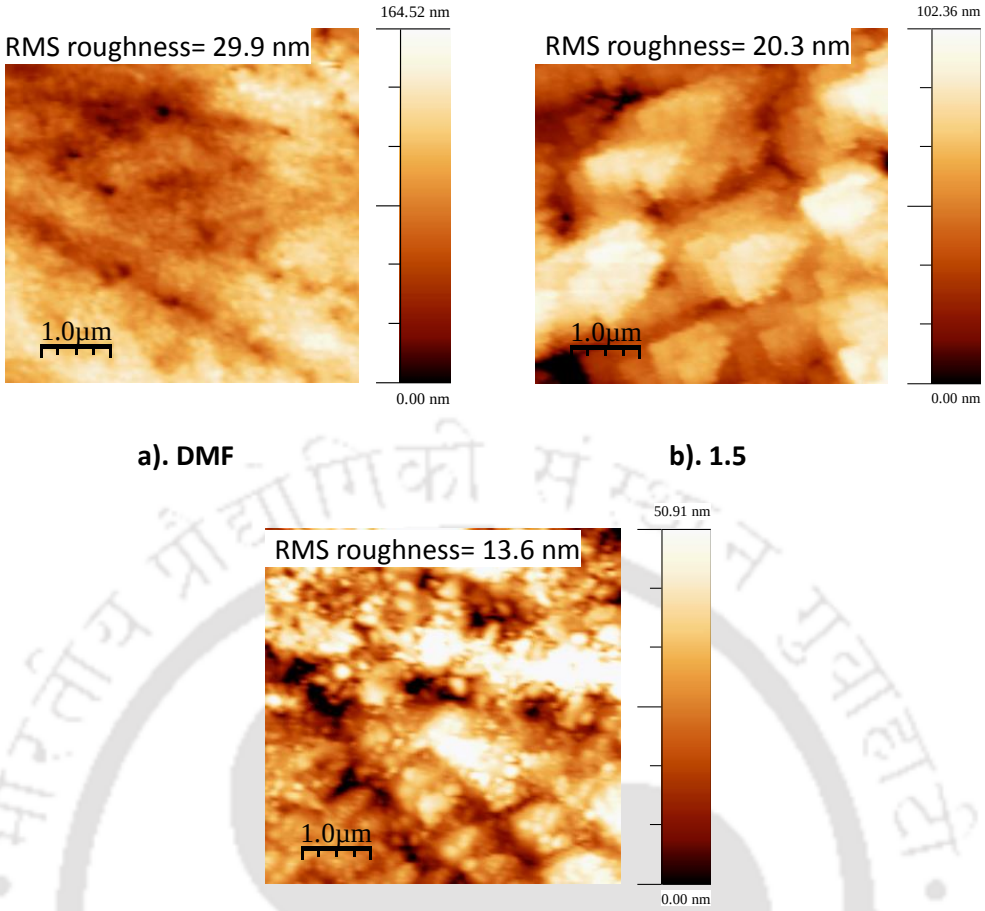

Figure C-3: Topographical AFM images of different perovskite films prepared using precursor solutions in (a) pure DMF, (b) 1.5 equivalents of DMSO in DMF and (c) pure DMSO using hot casting method.

Table C-1: Integrated *J*sc values calculated from IPCE spectra.

Device	Integrated J_{sc} from IPCE ($mA\ cm^{-2}$)
DMF	13.986
1.5	19.489
DMSO	14.950

CHAPTER 5

Oxalic Acid Induced Perovskite Formation for High Performance and Improved Stability Solar Cells

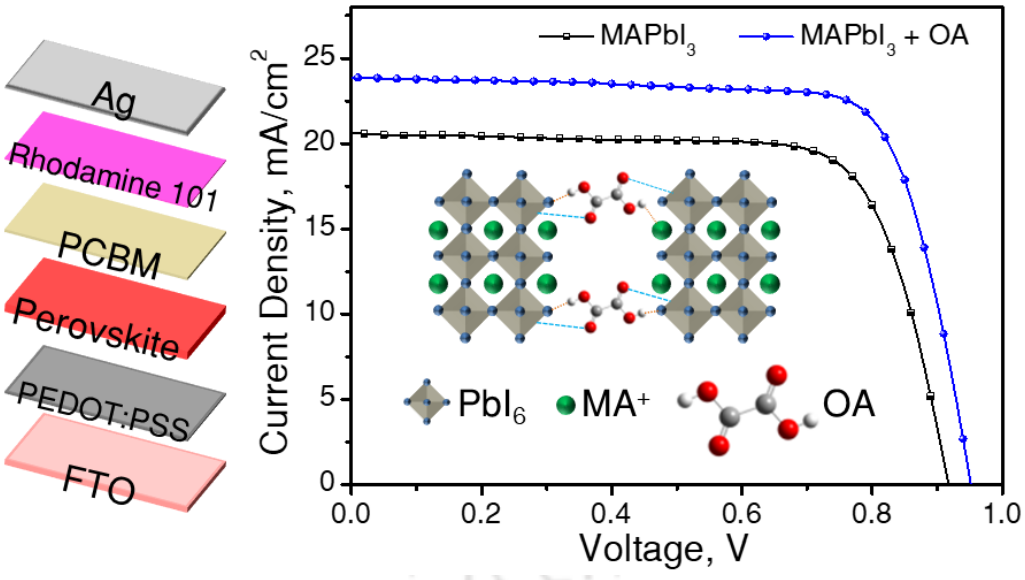

Afroz, M. A.; Ghimire, N.; Reza, K. M.; Bahrami, B.; Bobba, R. S.; Gurung, A.; Chowdhury, A. H.; Iyer, P. K.; Qiao, Q. *ACS Appl. Energy Mater*. **2020,** *3*, 2432-2439, DOI: 10.1021/acsaem.9b02111.

Abstract

Achieving long-term stability along with high power conversion efficiency is the biggest obstacle for the pursuit of organic-inorganic perovskite solar cells towards commercialization. In this chapter, additive assisted perovskite crystal growth has been demonstrated as an effective strategy to improve both power conversion efficiency and thermal stability of methylammonium lead triiodide ($MAPbI_3$) perovskite solar cells. For this, oxalic acid (OA) with two bifacial carboxylic acid groups was employed as additive into the perovskite precursor solution which facilitate the crystallization process leading to increase in grain size, reduced grain boundaries and trap states. Subsequently, devices fabricated with the OA additive, showed power conversion efficiency of 17.12%, compared to control device with 14.06%. Furthermore, enhanced thermal stability was achieved for the OA modified PSCs compared to that of pristine device. The device without OA additive retained 14% of the initial PCE after only 9 hours of heat treatment at 100 ˚C, whereas, for the same condition, OA modified device retained 90% after 9 h and even 70% of after 19 h. These observations suggest that OA assisted morphological improvement of perovskite can offer an efficient approach to further improve the performance as well as stability of the PSCs.

5.1 Introduction

Photovoltaic devices based on organic-inorganic metal halide hybrid perovskites also known as perovskite solar cells (PSCs) have fascinated researchers owing to their appealing optoelectronic properties, solution-based low-cost processing and high power conversion efficiency (PCE).[1-6] Since the first report on PSCs with PCE of 3.8 % in 2009, a substantial increase in PCE to 25.2% has been achieved, outperforming widely deployed multi-crystalline silicon at cell level.[7-8] This growth has been possible through extensive efforts of developing new materials and device engineering, including investigations on crystal formation,[9-11] solvents,[12-13] additives,[14-15] and interface engineering.[16-18] Precise control of morphology, crystallinity and charge transport properties of perovskite films with proper device engineering is crucial to realize high efficiency and stability in PSCs.[19] However, the hybrid perovskite has non-coordinated ions present reasonably; particularly the I^- ions that can easily migrate into perovskite films inside grains,[20] through grain boundaries and even out of the perovskite layer. These ions coming out of perovskite film destroy the metal electrode, which can further lead to formation of many defects and thus resulting in the disintegration of perovskite layer.[21] Formation of these defects occur preferentially at grain boundaries and over the surfaces of perovskite layer and act as centers of non-radiative recombination, thereby reducing the lifetime of charge carriers to finally result in low PCE of PSCs.[22] In addition, the grain boundaries and these defects-formed regions are attacked easily by oxygen or moisture, accelerating the deterioration of perovskite film.[23] This demands the development of perovskite films with improved crystallinity, less grain boundaries, larger grains as well as full surface coverage that can minimize the amount of defects and recombination and hence improve the PCE and stability of PSCs.

Numerous attempts have been made to achieve perovskite layer with high quality. Notable improvements have been observed in the crystallinity, surface coverage, and grain size of perovskite films via Ostwald ripening,[24] solvent annealing,[25] solvent engineering,[26-28] gas treatment,[29] and through additives.[30-31] Among these approaches, additive assisted perovskite crystal growth has been particularly effective to enhance the performance of PSCs as well as its stability. A ligand, 2-aminoethanethiol was used in the perovskite precursor to interconnect lead iodide (PbI_2) and methylammonium iodide (MAI), that led to simultaneous growth of PbI_2 and MAI crystals and ensured a dense perovskite film with improved stability.[32] Similarly, the use of butylphosphonic acid 4-ammonium chloride resulted in the crosslinking of perovskite grains with neighboring one, through strong

hydrogen bond formation of the perovskite surface with $–NH_3^+$ and $–PO(OH)_2$ terminal groups, which showed better moisture stability with improved photovoltaic performance.[33] Other additives such as poly(ethylene glycol),[34] poly(propylene carbonate),[35] poly(methyl methacrylate)[36] have also been used to prepare perovskite layer with large grain size and improved stability via chelation or cross-linking between functional groups of additives and perovskite grains. In these additives, the functional groups utilized, for example ammonium ($-NH_2$), carboxyl (−COOH), and hydroxyl (−OH) groups were separated with flexible carbon chain and modulated the crystallization process of perovskite formation by interaction with Pb^{+2} or I^- ions of perovskite. Simultaneously, strong hydrogen bonds of such functional groups can also inhibit the ions migration in perovskite film, and enhance the stability and minimize hysteresis in PSCs.[37] Although improvements have been achieved in the crystallization process by incorporation of additives into the perovskite precursors to attain high-quality large-grain perovskite films with uniform morphology and smooth surface,[32-33,36] the poor stability of PSCs has still remained a key challenge that need to be solved. Also, among the functional groups utilized, carboxyl group is a good choice having a carbonyl group with lone pairs at oxygen as well as a hydroxyl group. The carbonyl group can control the crystallization process during the perovskite formation and the hydrogen bond of hydroxyl group can suppress ion migration.[38]

In this work, oxalic acid (OA) is introduced as an effective additive into perovskite precursor solution to positively impact both photovoltaic performance and stability of PSCs. OA also known as ethanedioic acid is a dicarboxylic acid having two carboxyl groups attached directly through a single bond. The presence of the two-carbonyl group of the OA modulated the crystallization process to enable enlargement of grains and minimize the grain boundaries. In addition, the two hydroxyl groups in the OA can significantly passivate the perovskite film by strongly coordinating with iodide. This bidirectional OA assisted growth enables a substantial improvement in the quality of perovskite films, leading to an enhancement in PCE to 17.12% compared to control device with 14.06%. Furthermore, a remarkable improvement in stability under heat at 100 ºC was obtained with OA incorporation, where the OA modified PSCs exhibited much higher PCE retention of 70% after 19 h versus control device with 14% after just 9 h which can be attributed to the strong interaction between the OA and the perovskite.

5.2 Results and Discussion

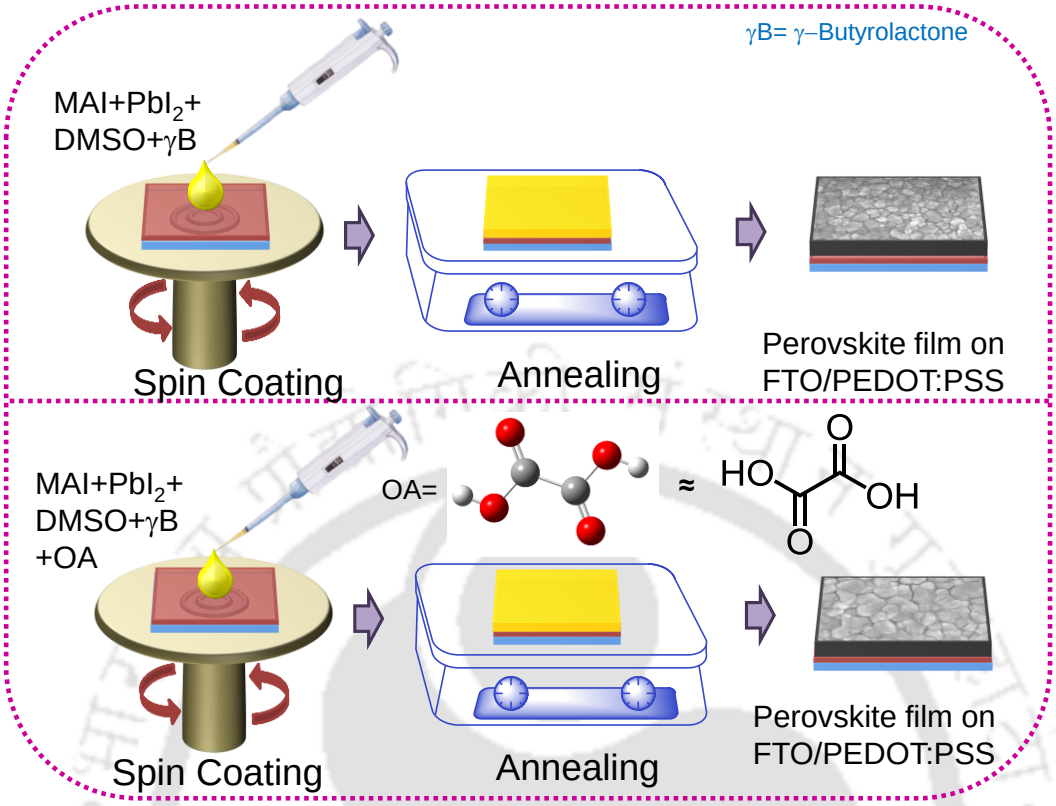

Figure 5.1: Schematic representing the perovskite film fabrication process.

The fabrication process of perovskite films is depicted in Figure 5.1. In short, the films were prepared using single step method from precursor solution (PbI_2+MAI in γ-butyrolactone/DMSO) with OA additive in different concentrations (0, 3, 5, 7, and 10 mg mL^{-1}). To confirm the interaction of the OA in perovskite, Fourier transform infrared (FTIR) experiment was performed. The FTIR spectra of OA, $MAPbI_3$, and $MAPbI_3$ with OA are presented in Figure 5.2(a,b). A peak at 1685 cm^{-1} was observed for the stretching vibration of carbonyl group ($\upsilon_{C=O}$) present in the OA, which moved to 1654 cm^{-1} in $MAPbI_3$ with OA (Figure 5.2(b)). This shift in the $\upsilon_{C=O}$ value towards lower wavenumber verifies the interaction between the lone pairs present at carbonyl oxygen and lead ions of $MAPbI_3$. Therefore, it is expected to modulate the crystallization kinetics and improve morphology of perovskite films.[39]

The morphological study was performed with FESEM to understand the effect of OA addition as shown in Figure 5.3(a-e). It was perceived that with the addition of OA into the perovskite precursor solution, it enhanced the quality of perovskite film and enlarged grain

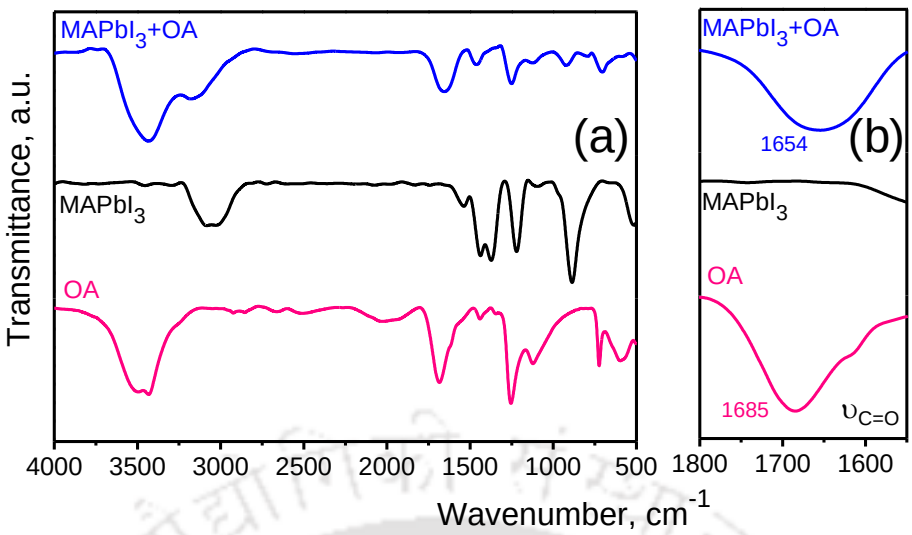

Figure 5.2: (a) FTIR spectra of OA, $MAPbI_3$ and OA modified $MAPbI_3$ (b) Expansion of FTIR spectra in 5.2 (a) to show stretching vibration of carbonyl group.

size. The control perovskite film without OA addition shows small grains with size ranging from 50-250 nm (Figure 5.3(a)). The grain size improved with small amount of OA incorporation and optimum amount of 5 mg mL^{-1} resulted in smooth and uniform perovskite layer with grain size of ~400- 600 nm (Figure 5.3(c). However, further increase in the concentration resulted in non-uniform grains with many pinholes observed at the surface of the perovskite layer. Therefore, it is clear that OA can significantly regulate the course of crystallization and improve the morphology of perovskite films. The PbI_2 present

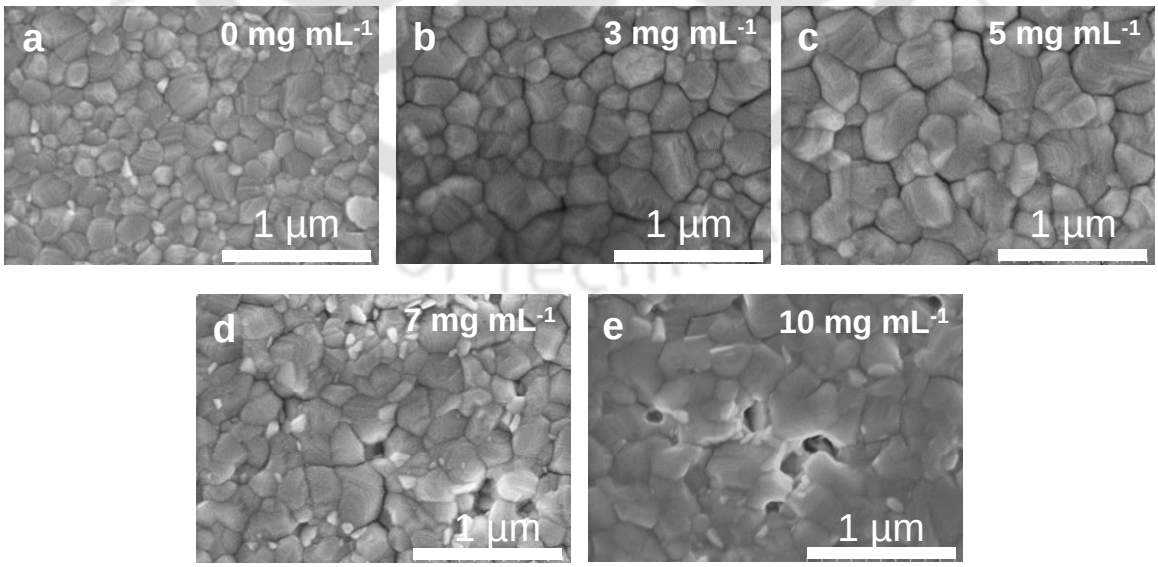

Figure 5.3: FESEM images of $MAPbI_3$ perovskite films (a) without and (b-e) with different amount of OA additive.

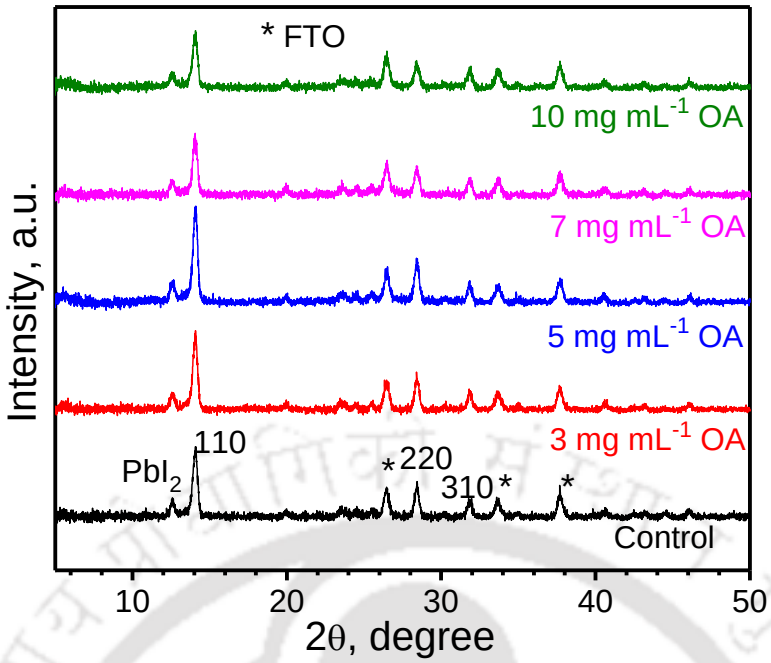

Figure 5.4: XRD patterns of pristine and 5 mg mL^{-1} OA modified $MAPbI_3$ perovskite film.

in the precursor solution form an intermediate complex with the solvent and ion exchange with MAI takes place during solvent removal by anti-solvent treatment and annealing process.[39] When the OA is added to the precursor solution, the two carbonyl groups present in it strongly interacts with Pb^{+2} (Lewis acid-base interaction) and forms a complex. This complex, during the solvent removal by annealing, converted to perovskite through ion exchange with MAI. Therefore, the presence of OA elongated the crystallization process and resulted in large grain perovskite film formation. The bifacial nature of OA could also lead to improved interconnection of the adjacent perovskite grains by crosslinking and enhances the grain size. However, large amount of OA doping might lead to excess intermediate formation, which may impede the perovskite film formation process and lead to poor quality film with many pinholes.

X-ray diffraction (XRD) study was performed to estimate the influence of OA on the crystallinity of the $MAPbI_3$ perovskite films. Figure 5.4 illustrates the XRD curves of the perovskite films without and with different amount of OA. The diffraction peaks observed at 2θ value of 14.10˚, 28.41˚, and 31.81˚ for all $MAPbI_3$ films can be assigned to the (110), (220), and (310) diffractions, respectively.[38] The signals marked with asterisk are indexed to FTO substrate. The absolute intensities of (110) diffraction peak for perovskite films prepared with OA addition (up to 5 mg mL^{-1}) became stronger compared to pristine film,

which confirm that small amount of OA could improve the crystallinity of perovskite film. It is well established that the crystallinity of the perovskite layer is a key factor to determine the performance of PSC. Presence of defects in the perovskite layer leads to trap formation and charge recombination.[22] Further addition of OA (7 and 10 mg mL^{-1}) resulted in the intensities of (110) peaks, that were weaker compared to the pristine perovskite film because of poor quality perovskite films having small grains and many pinholes (Figure 5.3(d,e)).

The UV-vis spectra of $MAPbI_3$ perovskite films with different amount of OA addition is presented in Figure 5.5(a). The intensities of optical absorption for perovskite films were gradually enhanced with the amount of OA up to 5 mg mL^{-1} due to good quality perovskite films formation with large grains and improved crystallinity. However, addition of OA more than 5 mg mL^{-1} resulted in lower absorption intensity, which is ascribed to the poor quality of the perovskite film. The photoluminescence (PL) experiment is very useful to explore the recombination properties in perovskite layer. The PL emission of perovskite film coated on glass substrate without hole and/or electron transporting layer comes primarily due to recombination of excitons inside the film. As illustrated in Figure 5.5(b), the $MAPbI_3$ perovskite film prepared with 5 mg mL^{-1} OA has higher emission intensity relative to the pristine perovskite film, which demonstrate that the non-radiative recombination of the carriers has been efficiently suppressed owing to lower defect density and high quality of perovskite film with OA as evident from XRD and SEM measurements.[40-41] This suppression of non-radiative recombination suggesting lower

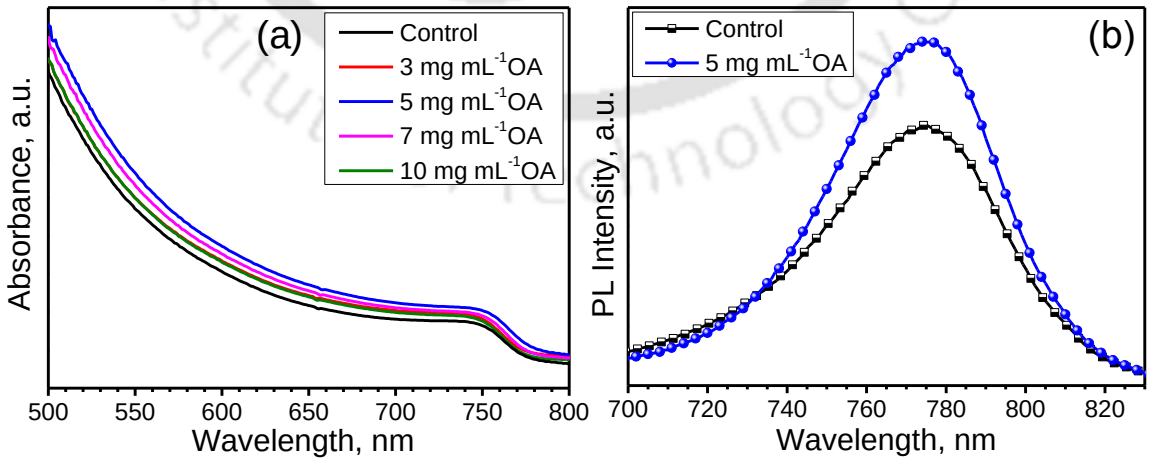

Figure 5.5: (a) UV-vis absorption spectra of $MAPbI_3$ perovskite films without and with different amount of OA additive. (b) Steady state PL emission spectra of pristine and 5 mg mL^{-1} OA modified $MAPbI_3$ perovskite film.

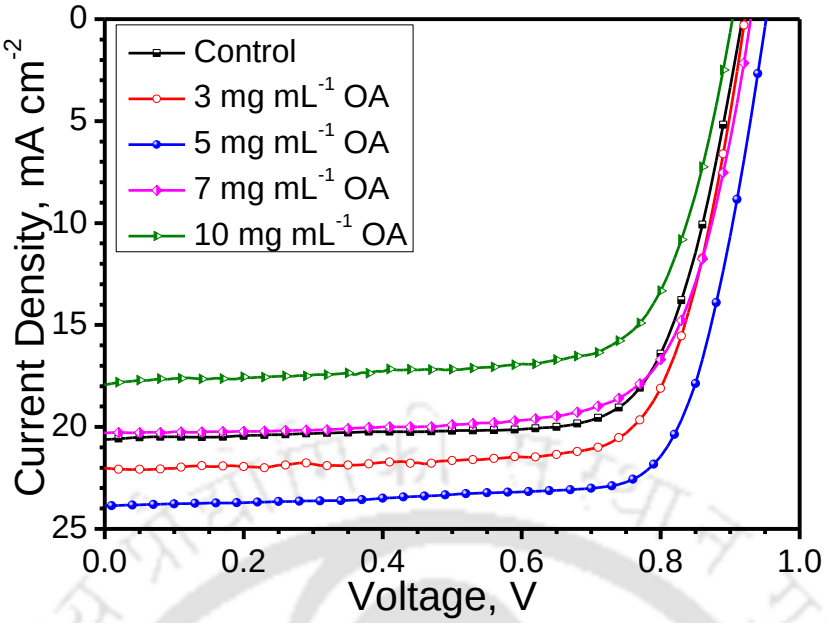

Figure 5.6: Photocurrent density vs voltage (*J*-*V*) curves of PSCs fabricated without and with different amount of OA additive.

defect/trap density can lead to improved open circuit voltage (V_{oc}) of PSCs because of reduced band bending of the perovskite affected by trap states.[41]

The *J*−*V* curves of PSCs without and with different amount of OA are illustrated in Figure 5.6 and the corresponding photovoltaic performance parameters are summarized in Table 5.1. The best PCE obtained for pristine $MAPbI_3$ based PSC was 14.06% with a short circuit current density (*J*sc) of 20.58 mA cm^{-2}, an open circuit voltage (*V*oc) of 0.920 V and

Table 5.1: Photovoltaic performance parameters of the PSCs fabricated without and with different amount of OA additive.

Device	*J*sc (mA cm^{-2})	*V*oc (V)	FF	PCE, Best (Average) (%)
Control	20.58	0.920	0.74	14.06 (13.34±0.35)[a]
OA3	22.09	0.930	0.74	15.23 (14.61±0.44)[b]
OA5	23.89	0.960	0.75	17.12 (16.46±0.48)[a]
OA7	20.29	0.930	0.73	13.79 (12.97±0.48)[b]
OA10	17.93	0.910	0.72	11.68 (11.15±0.59)[b]

[a] Average of 50 devices. [b]Average of 15 devices

a fill factor (FF) of 0.74. The performance of PSC improved gradually with the addition of OA and the highest PCE of 17.12% (*J*sc= 23.89 mA cm^{-2}, *V*oc= 0.960 V, & FF= 0.75) was attained for 5 mg mL^{-1}. This enhancement in the performance can be mainly ascribed to the superior quality of perovskite film obtained for 5 mg mL^{-1} having large grains, good crystallinity and lower trap states. However, as expected, the PSCs with 7 mg mL^{-1} or higher incorporation of OA resulted in poor performance due to formation of small grains, and pinholes in the perovskite films. Further investigations were carried out for PSCs with 5 mg mL^{-1} OA due to their superior performance and their characteristics were compared with control devices fabricated with pristine $MAPbI_3$ film. A minimum hysteresis behavior was obtained in both the PSCs without and with 5 mg mL^{-1} OA as shown in Figure 5.7(a) (Photovoltaic data presented in Table 5.2). The typical incident photon to current conversion efficiency (IPCE) curves of PSCs without and with OA (5 mg mL^{-1}) is presented in Figure 5.7(b). The PSCs with OA exhibited higher IPCE values in the wavelength range of 300-800 compared to the control cell, which can be ascribed to the better charge transport, collection and improved absorption. The values of integrated *J*sc calculated from

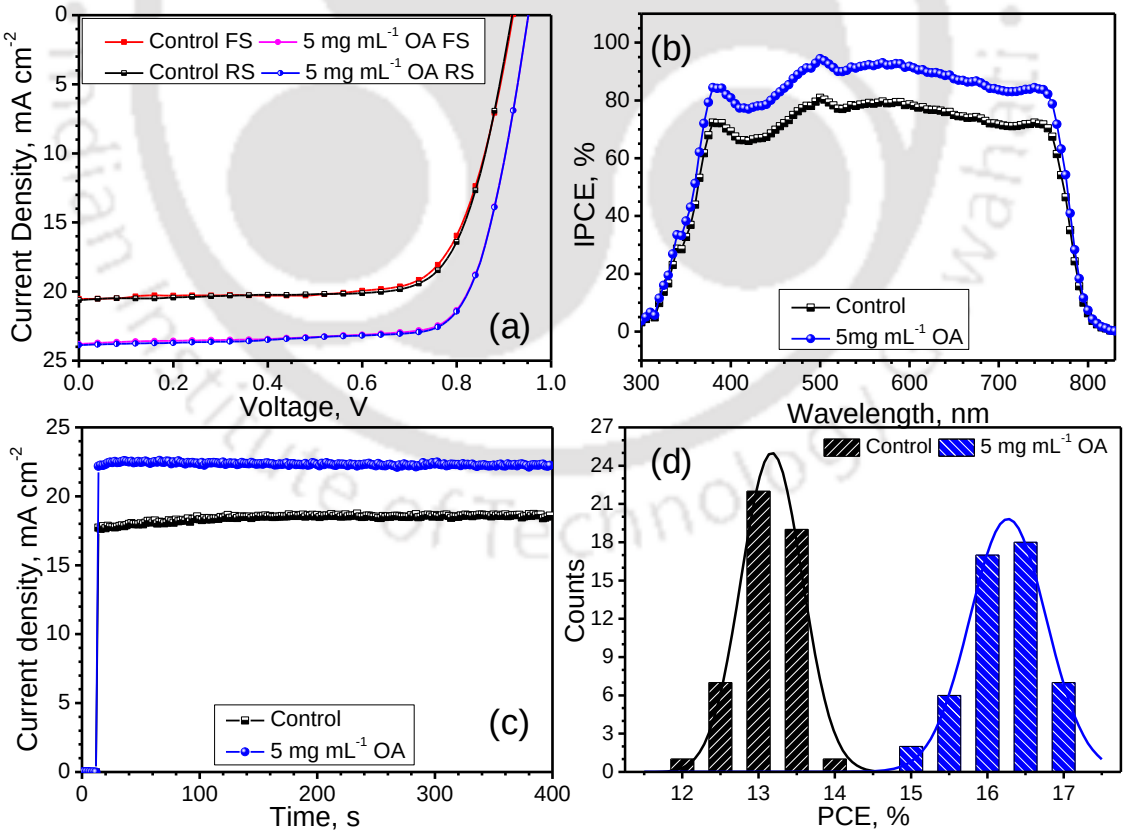

Figure 5.7: (a) *J-V* curves (b) IPCE spectra of PSCs without and with 5 mg mL^{-1} OA additive (c) Steady state current obtained by holding the bias at 0.8 V for PSCs without and with OA (d) Statistics of PCE for 50 PSCs devices each, fabricated without and with OA.

Table 5.2: Photovoltaic performance parameters of PSCs without and with 5mg mL^{-1} OA scanned in forward as well as reverse directions.

Device	Scan	*J*sc (mA cm^{-2})	*V*oc (V)	FF	PCE (%)
Control	Forward	20.64	0.92	0.73	13.82
	Reverse	20.58	0.92	0.74	14.06
OA5	Forward	23.83	0.95	0.75	17.07
	Reverse	23.89	0.96	0.75	17.12

the IPCE spectra are 19.05 and 22.25 mA cm^{-2} for control and OA devices, respectively. The values agree with the values obtained from the *J*-*V* curves. The results were further validated by recording the steady state current density at a potential about the maximum power point for PSCs without and with OA additive. Both the devices, without and with OA, showed steady state current densities of about 18.58 and 22.49 mA cm^{-2}, respectively (Figure 5.7(c)). These steady state current density values are consistent with the *J*-*V* results (Figure 5.7(a)). Statistical variation of the photovoltaic performance of the devices were analyzed based on a series of 50 devices each for control as well as OA assisted PSCs, as shown in the histogram (Figure 5.7(d)). The average PCE of the pristine $MAPbI_3$ based PSCs was 13.34% ± 0.35, whereas OA induced growth of perovskite film resulted in an average PCE of 16.47% ± 0.48.

The interfacial charge transfer kinetics and recombination properties of photovoltaic devices can be investigated by utilizing the electrochemical impedance spectroscopy (EIS). The Nyquist plots of the control and OA modified PSCs, estimated at a bias of 0.8 V and in the frequency range of 1 Hz – 1 MHz under dark condition are presented in Figure 5.8(a). The Nyquist plot was fitted using an equivalent circuit model as illustrated in the inset of Figure 5.8(a). A semicircle can be observed for both the devices which correspond to the charge transfer at FTO/PEDOT: PSS/$MAPbI_3$/PCBM interfaces, relates to the recombination resistance (Rct).[38] Rct estimated from the Nyquist plot, for OA based device was much larger than the pristine PSCs, indicating the defect passivation or recombination suppression contributed by OA. Therefore, OA facilitates the charge injection to HTL and ETL thereby improving the *V*oc and *J*sc.[42]

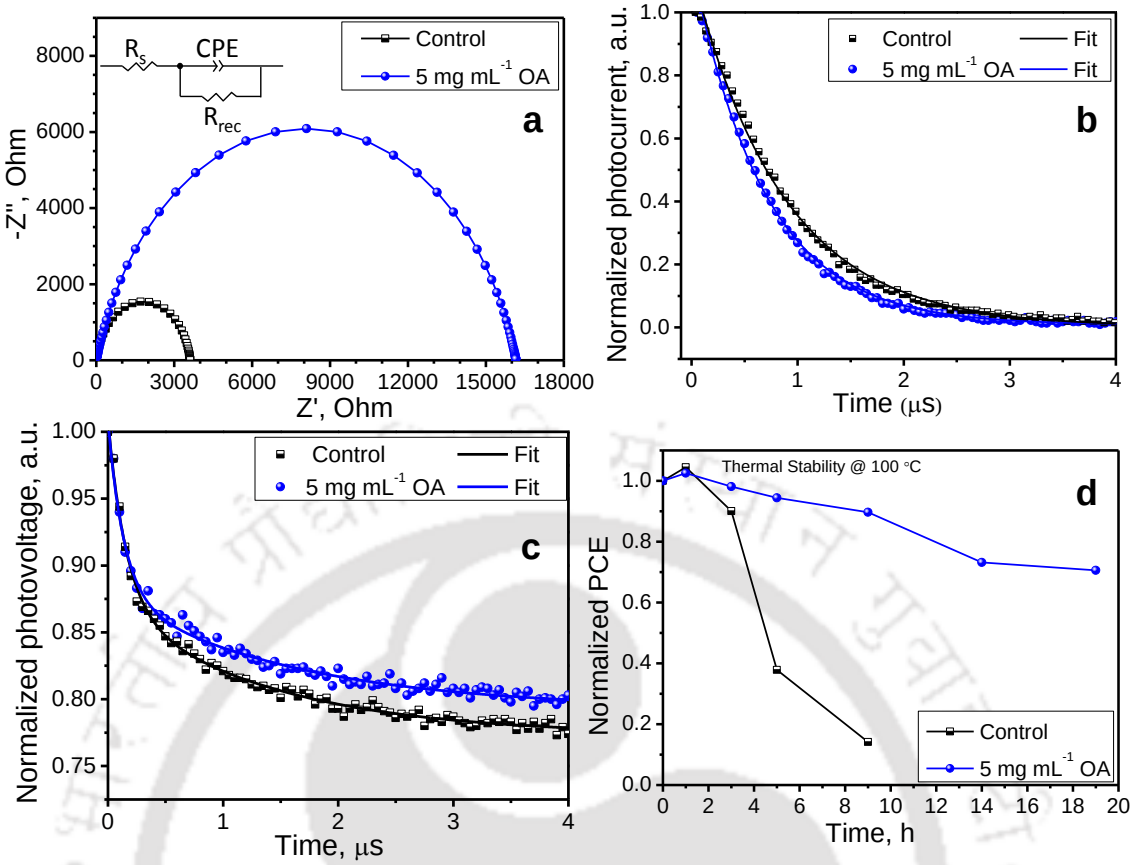

Figure 5.8: (a) Nyquist plot, (b) Transient photocurrent, (c) Transient photo-voltage and (d) thermal stability at 100 ˚C for PSCs without and with OA addition.

To further understand the carrier dynamics across the PSCs, transient photocurrent (TPC) and transient photo-voltage (TPV) experiments were performed for the pristine and the OA modified devices.[43] As shown in the TPC curves (Figure 5.8(b)), the OA-based device showed a faster decay compared to the pristine device. The charge transport time (τ_t, obtained by fitting the TPC curves with mono- exponential function A $\exp^{-t/\tau}$) for the OA based device was 0.68 μs whereas, a higher value of 0.86 μs was obtained for the control device. The fast decay for OA based devices indicates enhancement in the charge transport properties through interfaces. Further, the carrier recombination rates under open circuit condition in PSCs can be correlated from the TPV curves. A much slow decay was observed for the OA based device compared to the control device (Figure 5.8(c)). The charge recombination lifetime (τ_r) estimated from the TPV decay curves was prolonged for the OA based device than that of the control device from 1.38 μs to 1.58 μs, indicating the prohibition of carrier recombination in OA based device. This is mainly attributed to the reduced trap density that is consistent with the higher *V*oc observed from the OA treated device.

The thermal stability of PSCs is a critical factor affecting their applicability. To evaluate the effect of OA addition on device stability, the thermal stability test at 100 ˚C was performed inside the glove box.[44] Figure 5.8(d) shows the normalized PCE vs time plot for PSCs with and without OA additive. No device encapsulation was used. The PSC without OA retained only 14% of its initial PCE after heat treatment of the device at 100 ˚C for 9 h. However, under the same condition, the OA based device retained 90% of its initial PCE after 9 h and 70% after 19 h. The attenuation in the loss of PCE is essentially ascribed to the reduced degradation of the perovskite layer.[45-46] These results show that the perovskite layer prepared with OA results in improved thermal stability, which is related to the superior morphology obtained.

5.3 Conclusions

In summary, $MAPbI_3$ perovskite film with improved morphology having large grains, low grain boundaries and minimized defects was achieved by incorporating OA into the precursor solution of perovskite. As a result, a substantial improvement in the PCE from 14.06% to 17.12% was observed by incorporation of OA in its optimum concentration. More importantly, the thermal stability of the PSCs was also enhanced with the OA addition. The OA modified PSC retained 70% of its initial PCE after 19 h of heating at 100 ˚C, whereas the PCE for pristine device was reduced to 14% of its initial value after only 9 hours. This improvement in the stability and PCE has been achieved by utilizing the Lewis acid-base interaction between carbonyl group of OA with Pb^{+2} ions, and the hydrogen bonding interaction of hydroxyl group present in OA with iodide and MA^+ ions. This study provides an effective way to prepare perovskite film with superior morphology and low traps to achieve high efficiency and stability of PSCs.

5.4 Experimental Section

5.4.1 Materials

Fluorine-doped tin oxide (FTO) substrates (sheet resistance: 15 Ω $\square^{-1}$, size: 1.5 x 1.5 cm^2, thickness: 2.2 mm) were purchased from Hartford Glass Co, USA. Lead (II) iodide (PbI_2, 99%) was obtained from Acros Organics. Methylammonium iodide (MAI or CH_3NH_3I) was obtained from GreatCell Solar. Anhydrous Oxalic Acid ($(COOH)_2$) was purchased from Spectrum Chemical Mfg. Corp. PEDOT: PSS (Clevios P VP AI 4083) was obtained from Heraeus. PCBM (99.5%) was received from Nano-C, and Rhodamine 101

dye was procured from Sigma-Aldrich. All the solvents used were anhydrous and obtained from commercial sources.

5.4.2 Device Fabrication

On a pre-cleaned FTO substrate, the PEDOT: PSS layer was first spin coated at 4500 rpm for 60 s followed by baking at 140 ˚C for 10 min. The PEDOT: PSS coated substrates, after cooling down to room temperature, were transferred to a glove box filled with nitrogen. Perovskite precursor solutions were prepared by mixing 209 mg of MAI, 581 mg of PbI_2, and different amount of oxalic acid (0, 3, 5, 7, & 10 mg) in a mixed solvent (300 µL of DMSO and 700 µL of γ- butyrolactone). Sixty microliters of these precursor solutions were spin coated on top of the PEDOT:PSS films at 750 rpm for 20 s followed by 4000 rpm for 60 s. During the second step of spin coating, 40 s before the end, 160 µL of anhydrous toluene was dripped over the precursor film. The substrates were then annealed on a hotplate at 80 ˚C for 10 min. After cooling down to room temperature, a 20 mg mL^{-1} solution of PCBM in chlorobenzene was spun at 2000 rpm for 40 s over the perovskite film and annealed at 80 ˚C for 5 min. A very thin layer of rhodamine was then spin coated from a 0.5 mg mL^{-1} solution in IPA at a spin speed of 4000 rpm for 40 s. Finally, ~100 nm of silver was evaporated using a shadow mask under a vacuum in the order of 10^{-6} mbar to achieve an active area of 0.16 cm^2.

5.4.3 Characterization

Fourier transform infrared (FTIR, Perkin-Elmer-Spectrum) spectroscopy was used to study the interaction of OA and perovskite. The morphology of perovskite samples was examined on a scanning electron microscope (SEM, Hitachi S-4800). Perovskite grain orientation was measured using X-ray diffraction (XRD, Rigaku SmartLab system, 2.2 kW, Cu-Kα = 1.54 Å). Optical and photoluminescence spectra were recorded using an UV-vis spectrometer (Hitachi, U-3010) and a fluorescence spectrophotometer (HORIBA Jobin Yvon, fluoromax-4 with a 405 nm laser excitation), respectively. An Ametek VERSASTAT3- 200 potentiostat was used in the frequency range 1 Hz–1 MHz with amplitude of 20 mV in dark condition at maximum power point to perform EIS analysis. Photocurrent density-voltage (*J-V*) performance of the PSCs was measured in ambient environment without encapsulation using a Xenon arc lamp with a filter under AM 1.5 conditions, which were calibrated using a standardized silicon solar cell from NREL (S1133-14). External quantum efficiency measurements were done using the Newport

monochromator, Model 74125 and the Xenon lamp (Newport, Model 67005). The transient photocurrent and photovoltage investigations were made utilizing nitrogen laser pulse (OBB's Model OL- 4300) at 377 nm to pump a dye laser (model 1011) for generating a short pulse. This pulsed laser worked as a source of excitation with <1 ns pulse duration and ~4 Hz frequency. The dynamics curves of TPC and TPV measurements were recorded on a digital oscilloscope in open condition at around 1 MΩ resistor for TPV and in short-circuit condition at 50-Ω resistor for TPC.

5.5 References

(1) Green, M. A.; Ho-Baillie, A.; Snaith, H. J. *Nat. Photonics* **2014,** *8*, 506-514.

(2) Seo, J.; Noh, J. H.; Seok, S. I. *Acc. Chem. Res.* **2016,** *49*, 562-572.

(3) Zhao, Y. X.; Zhu, K. *Chem. Soc. Rev.* **2016,** *45*, 655-689.

(4) Chiang, C.-H.; Nazeeruddin, M. K.; Grätzel, M.; Wu, C.-G. *Energy Environ. Sci.* **2017,** *10*, 808-817.

(5) Khatiwada, D.; Venkatesan, S.; Adhikari, N.; Dubey, A.; Mitul, A. F.; Mohammad, L.; Iefanova, A.; Darling, S. B.; Qiao, Q. *J. Phys. Chem. C* **2015,** *119*, 25747-25753.

(6) Wu, Q.; Zhou, W.; Liu, Q.; Zhou, P.; Chen, T.; Lu, Y.; Qiao, Q.; Yang, S. *ACS Appl. Mater. Interfaces* **2016,** *8*, 34464-34473.

(7) Kojima, A.; Teshima, K.; Shirai, Y.; Miyasaka, T. *J. Am. Chem. Soc.* **2009,** *131*, 6050-+.

(8) National Renewable Energy Laboratory (NREL). https://www.nrel.gov/pv/assets/pdfs/best-research-cell-efficiencies.20190703.pdf (accessed 07 July 2019).

(9) Chen, H. N. *Adv. Funct. Mater.* **2017,** *27*.

(10) Ahn, N.; Kwak, K.; Jang, M. S.; Yoon, H.; Lee, B. Y.; Lee, J. K.; Pikhitsa, P. V.; Byun, J.; Choi, M. *Nat. Commun.* **2016,** *7*.

(11) Dubey, A.; Kantack, N.; Adhikari, N.; Reza, K. M.; Venkatesan, S.; Kumar, M.; Khatiwada, D.; Darling, S.; Qiao, Q. *J. Mater. Chem. A* **2016,** *4*, 10231-10240.

(12) Ahn, N.; Son, D. Y.; Jang, I. H.; Kang, S. M.; Choi, M.; Park, N. G. *J. Am. Chem. Soc.* **2015,** *137*, 8696-8699.

(13) Chen, J. Z.; Xiong, Y. L.; Rong, Y. G.; Mei, A. Y.; Sheng, Y. S.; Jiang, P.; Hu, Y.; Li, X.; Han, H. W. *Nano Energy* **2016,** *27*, 130-137.

(14) He, Y. T.; Wang, W. H.; Qi, L. M. *ACS Appl. Mater. Interfaces* **2018,** *10*, 38985-38993.

(15) Mabrouk, S.; Bahrami, B.; Gurung, A.; Reza, K. M.; Adhikari, N.; Dubey, A.; Pathak, R.; Yang, S.; Qiao, Q. *Sustainable Energy & Fuels* **2017,** *1*, 2162-2171.

(16) Fan, R. D.; Huang, Y.; Wang, L. G.; Li, L.; Zheng, G. H. J.; Zhou, H. P. *Adv. Energy Mater.* **2016,** *6*.

(17) Mabrouk, S.; Zhang, M.; Wang, Z.; Liang, M.; Bahrami, B.; Wu, Y.; Wu, J.; Qiao, Q.; Yang, S. *J. Mater. Chem. A* **2018,** *6*, 7950-7958.

(18) Elbohy, H.; Bahrami, B.; Mabrouk, S.; Reza, K. M.; Gurung, A.; Pathak, R.; Liang, M.; Qiao, Q.; Zhu, K. *Adv. Funct. Mater. 0*, 1806740.

(19) Al-Dainy, G. A.; Bourdo, S. E.; Saini, V.; Berry, B. C.; Biris, A. S. *Energy Technology* **2017,** *5*, 373-401.

(20) Zhao, Y. C.; Zhou, W. K.; Ma, W.; Meng, S.; Li, H.; Wei, J.; Fu, R.; Liu, K. H.; Yu, D. P.; Zhao, Q. *Acs Energy Letters* **2016,** *1*, 266-272.

(21) Besleaga, C.; Abramiuc, L. E.; Stancu, V.; Tomulescu, A. G.; Sima, M.; Trinca, L.; Plugaru, N.; Pintilie, L.; Nemnes, G. A.; Iliescu, M.; Svavarsson, H. G.; Manolescu, A.; Pintilie, I. *Journal of Physical Chemistry Letters* **2016,** *7*, 5168-5175.

(22) Nie, W. Y.; Tsai, H. H.; Asadpour, R.; Blancon, J. C.; Neukirch, A. J.; Gupta, G.; Crochet, J. J.; Chhowalla, M.; Tretiak, S.; Alam, M. A.; Wang, H. L.; Mohite, A. D. *Science* **2015,** *347*, 522-525.

(23) You, J. B.; Yang, Y. M.; Hong, Z. R.; Song, T. B.; Meng, L.; Liu, Y. S.; Jiang, C. Y.; Zhou, H. P.; Chang, W. H.; Li, G.; Yang, Y. *Applied Physics Letters* **2014,** *105*.

(24) Zhu, W. D.; Bao, C. X.; Wang, Y. R. Q.; Li, F. M.; Zhou, X. X.; Yang, J.; Lv, B. H.; Wang, X. Y.; Yu, T.; Zou, Z. G. *Dalton Trans.* **2016,** *45*, 7856-7865.

(25) Xiao, Z. G.; Dong, Q. F.; Bi, C.; Shao, Y. C.; Yuan, Y. B.; Huang, J. S. *Adv. Mater.* **2014,** *26*, 6503-6509.

(26) Numata, Y.; Kogo, A.; Udagawa, Y.; Kunugita, H.; Ema, K.; Sanehira, Y.; Miyasaka, T. *ACS Appl. Mater. Interfaces* **2017,** *9*, 18739-18747.

(27) Dubey, A.; Adhikari, N.; Mabrouk, S.; Wu, F.; Chen, K.; Yang, S.; Qiao, Q. *J. Mater. Chem. A* **2018,** *6*, 2406-2431.

(28) Afroz, M. A.; Gupta, R. K.; Garai, R.; Hossain, M.; Tripathi, S. P.; Iyer, P. K. *Org. Electron.* **2019,** *74*, 172-178.

(29) Hao, F.; Stoumpos, C. C.; Liu, Z.; Chang, R. P. H.; Kanatzidis, M. G. *J. Am. Chem. Soc.* **2014,** *136*, 16411-16419.

(30) Liang, P. W.; Liao, C. Y.; Chueh, C. C.; Zuo, F.; Williams, S. T.; Xin, X. K.; Lin, J. J.; Jen, A. K. Y. *Adv. Mater.* **2014,** *26*, 3748-3754.

(31) Vickers, E. T.; Graham, T. A.; Chowdhury, A. H.; Bahrami, B.; Dreskin, B. W.; Lindley, S.; Naghadeh, S. B.; Qiao, Q.; Zhang, J. Z. *ACS Energy Letters* **2018,** *3*, 2931-2939.

(32) Li, B.; Fei, C. B.; Zheng, K. B.; Qu, X. H.; Pullerits, T.; Cao, G. Z.; Tian, J. J. *J. Mater. Chem. A* **2016,** *4*, 17018-17024.

(33) Li, X.; Dar, M. I.; Yi, C.; Luo, J.; Tschumi, M.; Zakeeruddin, S. M.; Nazeeruddin, M. K.; Han, H.; Gratzel, M. *Nat Chem* **2015,** *7*, 703-11.

(34) Zhao, Y. C.; Wei, J.; Li, H.; Yan, Y.; Zhou, W. K.; Yu, D. P.; Zhao, Q. *Nat. Commun.* **2016,** *7*.

(35) Han, T. H.; Lee, J. W.; Choi, C.; Tan, S.; Lee, C.; Zhao, Y. P.; Dai, Z. H.; De Marco, N.; Lee, S. J.; Bae, S. H.; Yuan, Y. H.; Lee, H. M.; Huang, Y.; Yang, Y. *Nat. Commun.* **2019,** *10*.

(36) Bi, D. Q.; Yi, C. Y.; Luo, J. S.; Decoppet, J. D.; Zhang, F.; Zakeeruddin, S. M.; Li, X.; Hagfeldt, A.; Gratzel, M. *Nature Energy* **2016,** *1*.

(37) Fu, R.; Zhao, Y. C.; Li, Q.; Zhou, W. K.; Yu, D. P.; Zhao, Q. *Chem. Commun.* **2017,** *53*, 1829-1831.

(38) Hou, X.; Huang, S. M.; Wei, O. Y.; Pan, L. K.; Sun, Z.; Chen, X. H. *ACS Appl. Mater. Interfaces* **2017,** *9*, 35200-35208.

(39) Su, L. J.; Xiao, Y. M.; Han, G. Y.; Lu, L. P.; Li, H. G.; Zhu, M. L. *J. Power Sources* **2019,** *426*, 11-15.

(40) Xiang, W. C.; Chen, Q.; Wang, Y. Y.; Liu, M. J.; Huang, F. Z.; Bu, T. L.; Wang, T. S.; Cheng, Y. B.; Gong, X.; Zhong, J.; Liu, P.; Yao, X.; Zhao, X. J. *J. Mater. Chem. A* **2017,** *5*, 5486-5494.

(41) Zhang, X.; Yuan, S. J.; Lu, H. Z.; Zhang, H. T.; Wang, P. F.; Cui, X. L.; Zhang, Y.; Liu, Q.; Wang, J.; Zhan, Y. Q.; Sun, Z. Y.; Huang, W. *ACS Appl. Mater. Interfaces* **2017,** *9*, 36810-36816.

(42) Guan, L.; Jiao, N.; Guo, Y. *J. Phys. Chem. C* **2019,** *123*, 14223-14228.

(43) Chen, Y. H.; Li, N. X.; Wang, L. G.; Li, L.; Xu, Z. Q.; Jiao, H. Y.; Liu, P. F.; Zhu, C.; Zai, H. C.; Sun, M. Z.; Zou, W.; Zhang, S.; Xing, G. C.; Liu, X. F.; Wang, J. P.; Li, D. D.; Huang, B. L.; Chen, Q.; Zhou, H. P. *Nat. Commun.* **2019,** *10*.

(44) Meng, L.; You, J. B.; Yang, Y. *Nat. Commun.* **2018,** *9*.

(45) Lee, J. W.; Kim, D. H.; Kim, H. S.; Seo, S. W.; Cho, S. M.; Park, N. G. *Adv. Energy Mater.* **2015,** *5*.

(46) Niu, G. D.; Guo, X. D.; Wang, L. D. *J. Mater. Chem. A* **2015,** *3*, 8970-8980.

CHAPTER 6

Benzene Carboxylic Acid Derivative Assisted Passivation of Perovskites for Stable and High-Performance Inverted Perovskite Solar Cells

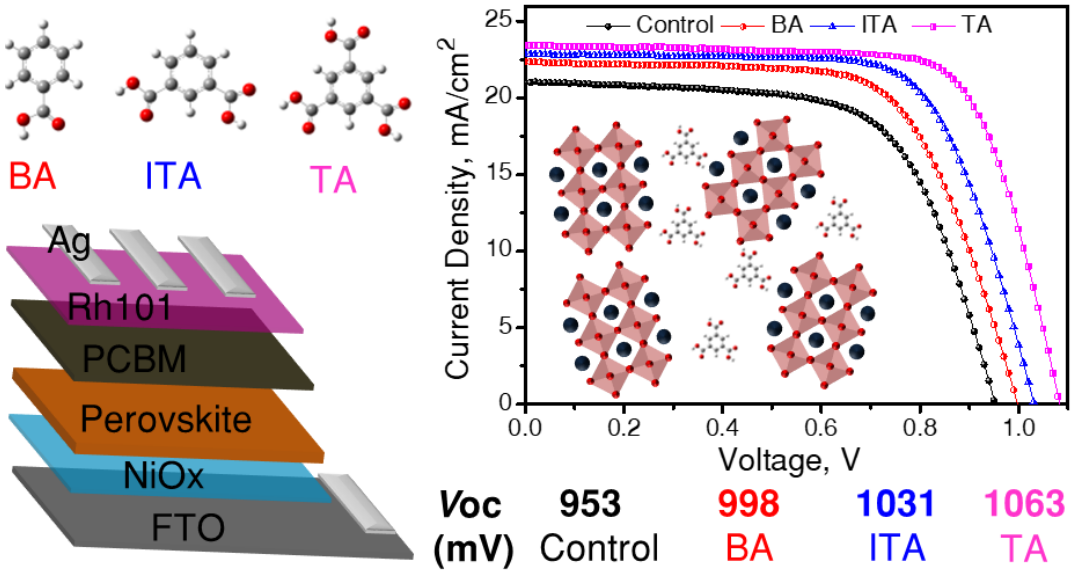

Afroz, M. A.; Garai, R.; Gupta, R. K.; Iyer, P. K. (submitted)

Abstract

Trap states formation in perovskite films during their preparation is a key limitation restricting the device performance and stability of perovskite solar cells. These trap states, also termed as defects, are generally present at the surface of perovskite film and on grain boundaries and work as charge recombination centres, thereby influencing the device performance. Herein, a unique methodology of trap state passivation in accord with crystallization control has been demonstrated using multiple carboxylic acid functionalized small aromatic molecules. Three benzene carboxylic acids (BCA), viz. Benzoic acid (BA), Isophthalic acid (ITA), and Trimesic acid (TA) (with one, two, and three carboxylic acid groups, respectively), have been utilized as additives in the precursor solution that resulted in high quality perovskite films with large grains and reduced trap states. Perovskite films generated in presence of these BCA additives strongly influenced the charge transfer dynamics and resulted in improved performance and stability of the devices by lowering the photo generated charge recombination. TA incorporated devices, gave highest power conversion efficiency (PCE) of 18.08% with a significant improvement in the open circuit voltage (*V*oc) to 1.063 V (an enhancement of ≈110 mV) compared to the control device, that showed PCE of 13.01% and *V*oc of 0.952 V. Additionally, the devices were also endowed with enhanced thermal stability. Furthermore, an effective trap state passivation by tuning the concentration of –COOH group within the same aromatic core has been established. These BCA functionalized molecules simultaneously reduce trap states through passivation and effectively controls crystallization thereby demonstrating the broad universality of using specific BCA additives to enhance perovskite based solar cells.

6.1 Introduction

The perovskite films prepared using solution processing methods are polycrystalline and have non-coordinated ions as defects. These defects are majorly present at grain boundaries and on the surfaces of perovskite film, which work as recombination centres, hence greatly influence the performance of PSCs.[1-2] Besides being harmful to device performance, these defects can also elevate the penetration of moisture and oxygen into perovskite and contribute significantly to the inherent instability of perovskite films[3] and subsequently result in an unsatisfactory lifetime of PSCs under operating conditions.[4-5] Poor device stability is presently one of the most serious difficulties for commercialization of the PSCs. The solution processed polycrystalline perovskite films have multiple times higher defect density compared to the single-crystalline film.[6] Thus, it is highly desired to minimize the quantity of defects in the perovskite films to simultaneously improve the device performance as well as their long-term durability.

To enhance the perovskite film quality and reduce trap states, different approaches have been established, such as solvent engineering of precursor solution,[7] development of coating procedure,[8] composition engineering,[9] off-stoichiometric passivation,[10] anti-solvent engineering,[11-12] utilizing organic molecules in anti-solvent,[13-14] interface engineering[15-17] and additive engineering.[18-20] Among these methods, additive engineering is one of the effective approaches for achieving high quality perovskite films because of the vast diversity present in their functionality and structure.[21-22] D-π-A molecules with –COOH group, PCBM and C60-PEG have been added in the anti-solvent for defect passivation.[13-14] The use of these molecules in anti-solvent helps in passivation of surface defects only. Numerous materials have been investigated as additives in perovskite precursor solution including organic halide salts, metal halide salts, inorganic acids, fullerenes, polymers, and nanoparticles.[21,23-27] Some of the reported additives were used to only enhance film stability or charge transport.[21,28] However, few others were used to improve the perovskite film either by controlling the kinetics of nucleation and grain growth or by the passivation of trap/defect states. The fast crystallization of perovskite film during solution processing results in small grains with a large number of grain boundaries and defects.[29] Therefore, it is essential to appropriately control and regulate the crystallization kinetics via tuning the interaction of additive with perovskite precursor judiciously. Many additives, such as MACl,[24] NH_4SCN,[30] MASCN,[31] HBr,[25] HI,[32] and hypophosphorous acid,[33] were only effective in regulating crystal growth, yet they were

very less effective for passivation of defects. On the other hand, some of the additives such as IT-4F,[34] F4TCNQ,[35] PVP (poly(4-vinylpyridine)),[36] polyamic acid & polyimide,[37] fullerene derivatives and ITIC,[21,27] organic dye (AQ310),[38] p-type conjugated polymers PBDB-T,[39] P3HT[26] were only effective in passivating the defects of perovskite films whereas no improvement was observed in crystallization. One of the possible ways to simultaneously obtain an improved perovskite film with good morphology as well as reduced defects is to use multiple additives having different functions into perovskite precursor. However, only a few studies on the simultaneous addition of different additives have been reported.[40-42] Multiple functions, such as simultaneous enhancement of the perovskite grains morphology and its defects passivation was also achieved with a single additive, for instance, side-chain liquid crystalline polymer (SCLCP),[43] N-doped graphene,[29] and carbonized bamboo-derived carbon nanodots (CNDs).[42] Thus, the use of additive with simultaneous capabilities of crystallization control and trap state passivation is a promising approach to realize high quality perovskite films.

In this chapter, improved perovskite morphology with effective defect passivation has been achieved by controlled addition of benzene carboxylic acid (BCA) derivatives in the perovskite precursor solution. Three different BCA derivatives, viz. benzoic acid (BA), isophthalic acid (ITA), and trimesic acid (TA), have been used in this study. The concentration of each BCA derivative was first optimized independently by adding different amounts in the perovskite precursor and performing the detailed study on crystallization and morphology control simultaneously. Further, these additives in their optimum concentration were compared to examine the effect of –COOH substitution on trap passivation. An increased concentration of –COOH group was optimized by additional substitution on the same aromatic core. Interestingly, it was observed that the samples with the additive BA statistically showed a small improvement in the *V*oc to that of control samples, whereas a pronounced enhancement in the *V*oc was achieved with ITA and TA. By adding 1.8% TA (5.4% –COOH), the PCE was improved to 17.22%±0.42 (champion efficiency, 18.08%) versus control (12.16%±0.39, champion efficiency= 13.01%).

6.2 Results and discussion

FESEM analysis was performed to assess the effect of BA, ITA, and TA addition on the perovskite film. A good quality perovskite film with large grains, minimal pinholes and a smaller number of grain boundaries is a key factor to fabricate highly efficient PSCs. A

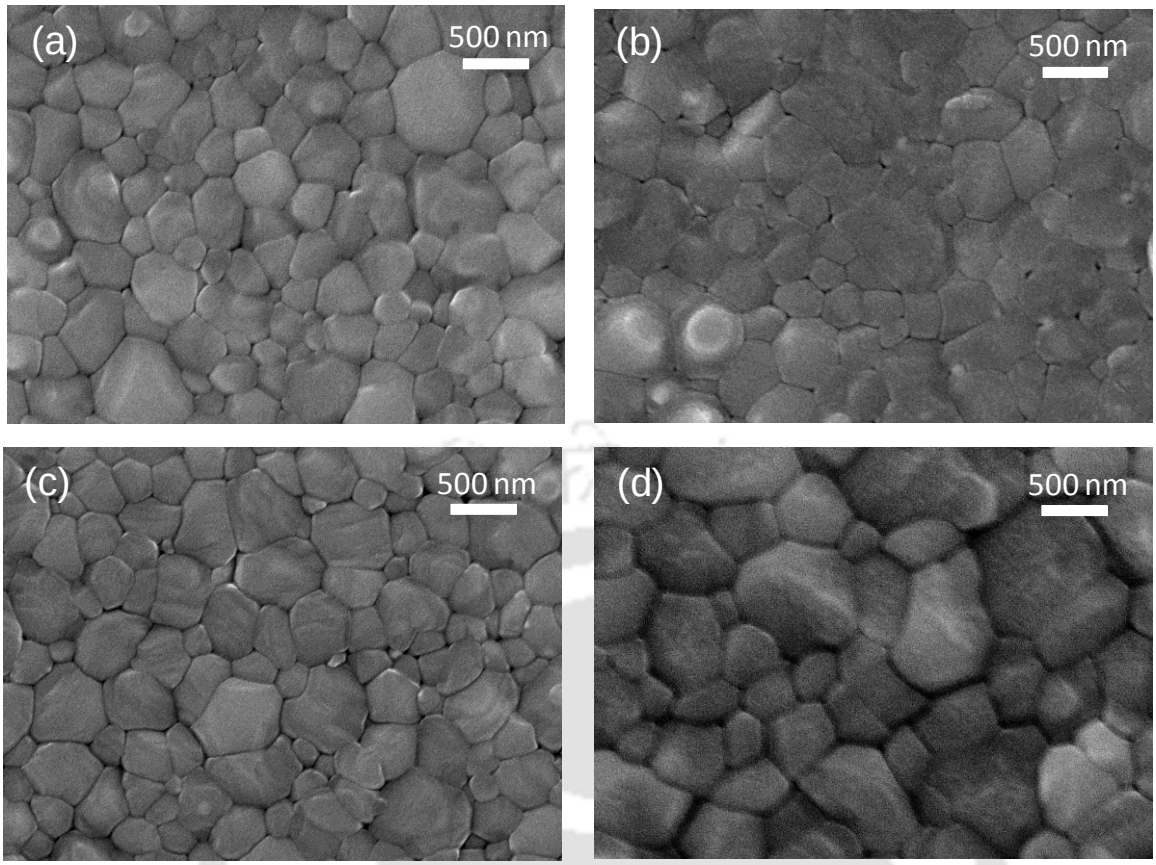

Figure 6.1: FESEM image of perovskite film with (a) no additive, (b) 1.6% BA, (c) 3.2 % BA and (d) 4.8% BA additive.

smooth perovskite film could improve light harvesting and provide better charge-transport channels. Figure 6.1 shows the FESEM images of pristine and different amounts of BA incorporated (1.6, 3.2, and 4.8 mol %) perovskite film. It was observed that the grain size of perovskites increased on optimizing the concentration of BA. The pristine perovskite film without BA display most of the grains with size range 100-300 nm whereas, perovskite obtained with 3.2% BA addition resulted in grain sizes in the range 400-600 nm. The grain size increases on further addition of BA, but the film became non-uniform and less smooth. These results prove that BA is an effective additive that can modulate the crystallization process and control the perovskite film morphology. Generally, perovskite film is formed from its precursor solution having PbI_2-solvent intermediate complex through ion exchange by MAI. The perovskite crystallization occurs when the solvent is removed during anti-solvent treatment followed by annealing process.[44] Addition of BA to the precursor solution modulates the crystallization by forming a complex through strong interaction of its carboxylic groups with Pb^{+2}. Formation of this complex extends the crystallization and results in large grain perovskite film. However, higher concentration of BA may lead to

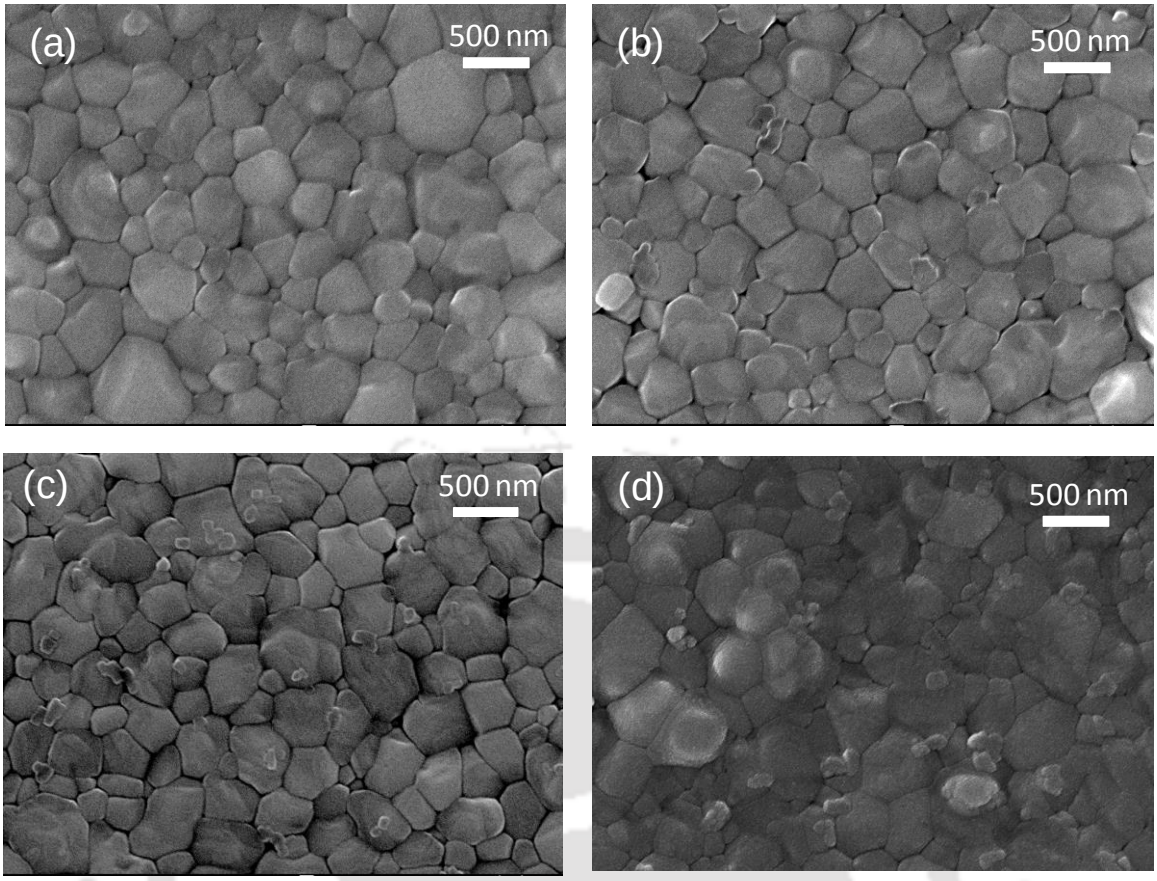

Figure 6.2: FESEM image of perovskite film with (a) no additive, (b) 1.2% ITA, (c) 2.4 % ITA and (d) 3.6% ITA.

formation of excess intermediates, which may result in non-uniform poor-quality perovskite films. When the FESEM analysis for perovskite film modified with ITA was performed (Figure 6.2), an improvement in the perovskite film quality ensued, although it was not as proficient as in the case of BA. In this case, small particles of ITA can also be seen on the surface (with 1.2%), and their quantity increases with the additive concentration (2.4 & 3.6%). This might be helpful in the passivation of grain boundaries. TA addition resulted in both, enlargement in the grain size as well as the appearance of TA on the surface (Figure 6.3). When the TA concentration increased up to 0.9%, the grain size increased with the presence of some small TA particles on the surface. Further increase in concentration to 1.8% resulted in rod-shaped TA on the surface of perovskite film. With 2.7% addition, an uneven perovskite film with small grains were formed. It is clear from the FESEM analysis that all these acids have an impact on the morphology and grain size of the perovskite films.

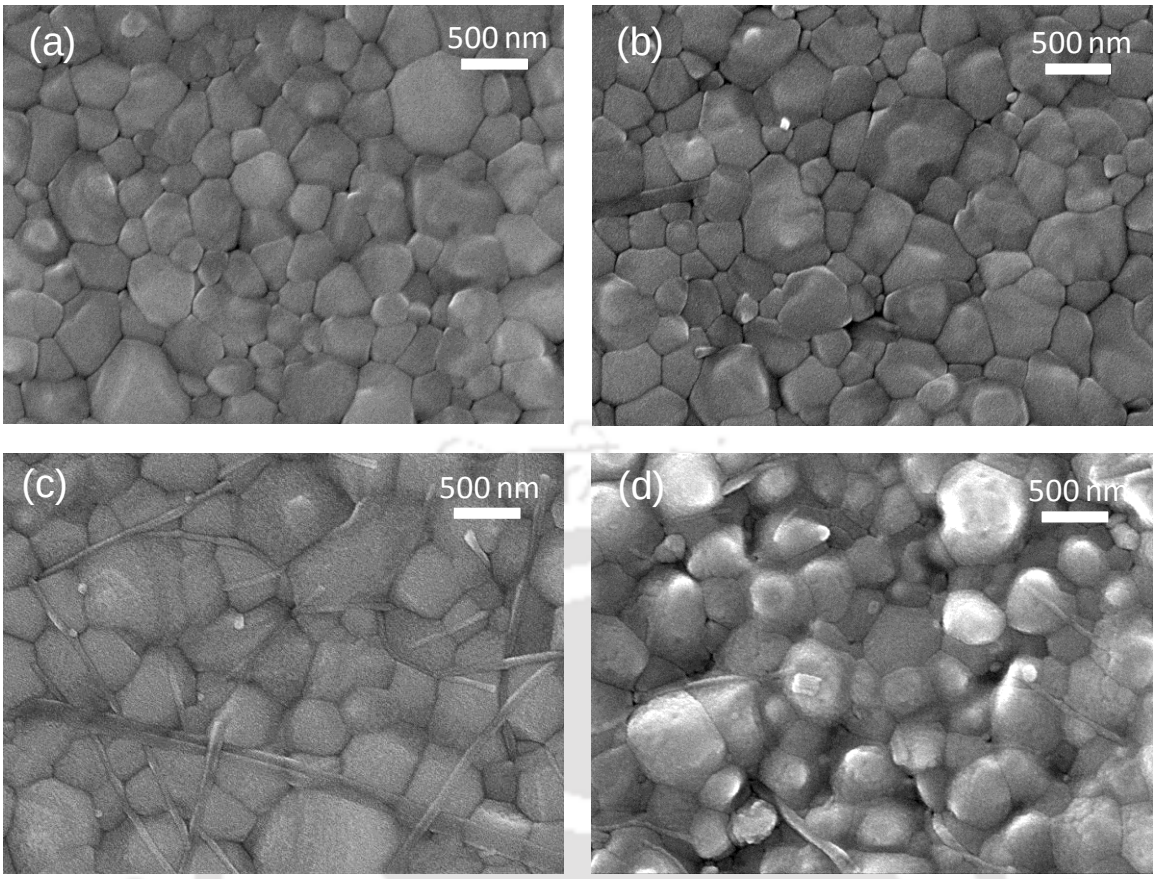

Figure 6.3: FESEM image of perovskite film with (a) no additive, (b) 0.9% TA, (c) 1.8% TA and (d) 2.7% TA.

XRD spectra of the pristine and modified perovskite films prepared by adding different amounts of BA are shown in Figure 6.4(a). The peaks at 2θ value of 14.08˚, 28.44˚, 31.88˚ corresponds to (1 1 0), (2 2 0), & (3 1 0) diffraction peaks of $MAPbI_3$. The absence of peak at around 12.6˚ confirmed the complete conversion of lead iodide to the perovskite. The peak intensities for the modified perovskite first increased up to 3.2% BA additive, and further addition resulted in reduction of peak intensity. The other two additives, ITA and TA, also showed a similar trend (Figure D-1, Appendix D). This confirms that the addition of these acids into the perovskite precursor solution proved beneficial to improve the crystallinity of the perovskite film. The interaction of BA with perovskite confirmed by Fourier transform infrared (FTIR) spectroscopy. The FTIR spectra of BA and perovskite modified with BA are presented in Figure 6.4(b,c). The stretching vibration of carbonyl group ($\upsilon_{C=O}$) appeared at 1741 cm^{-1}, which shifted to 1720 cm^{-1} for $MAPbI_3$ with BA. This shift is attributed to the coordination of lone pairs present at oxygen of –COOH group with the Pb ions of perovskite.[44] Therefore, the interaction of BA can affect the perovskite crystallization and improve the morphology.

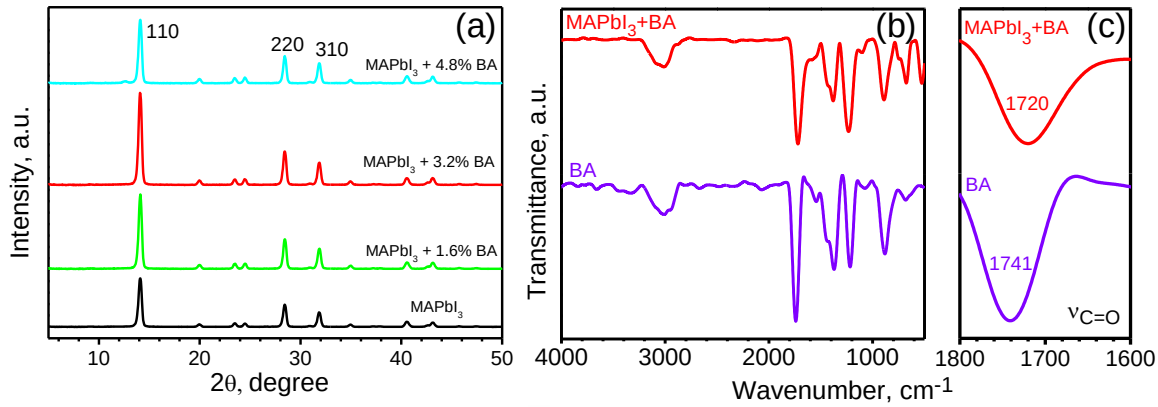

Figure 6.4: (a) XRD spectra of perovskite films prepared without and with different amount of BA additive. (b) Full and (c) magnified FTIR spectra of BA and perovskite with BA additive.

Photovoltaic cells of p-i-n configuration having the architecture FTO/NiO_x/Perovskite (without or with BCA)/PCBM/Rhodamine 101/Ag were fabricated for each carboxylic acid with varying concentration in the active layer (Figure 6.5). The *J-V* characteristics curves for BA, ITA, and TA with various concentrations are presented in Figure D-2, Appendix D. The photovoltaic parameters are compiled in Table D-1, Table D-2, and Table D-3 of Appendix D for BA, ITA and TA, respectively. The control device without any carboxylic acid additive displayed best PCE of 13.01% (average PCE of 12.16% for 40 cells) with J_{sc}, V_{oc} and FF values of 21.00 mA cm^{-2}, 952.6 mV and 65%, respectively. For BA, the PCE

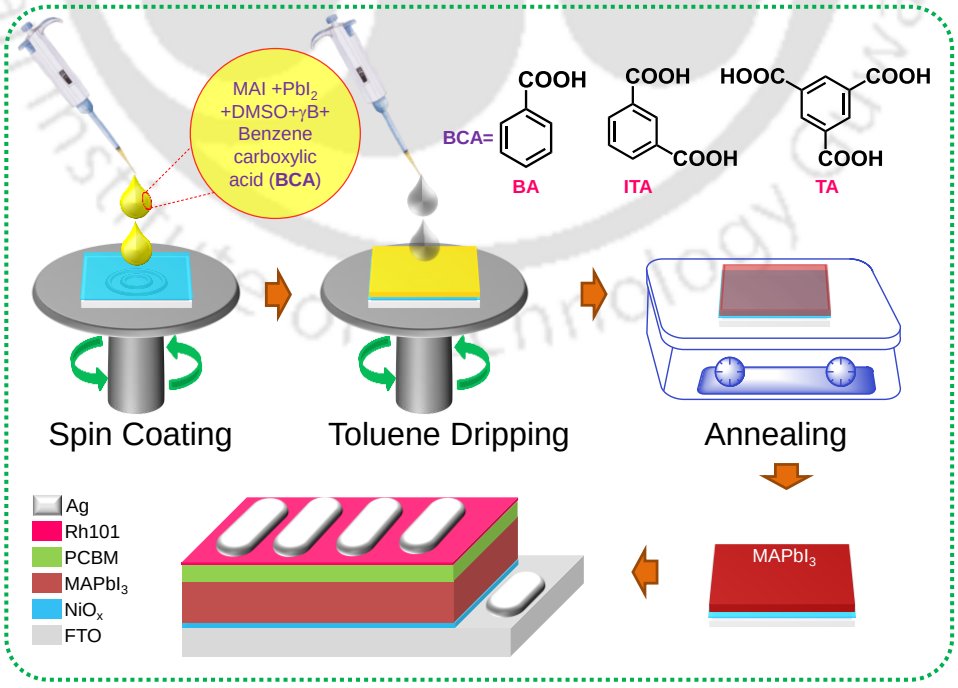

Figure 6.5: Schematic showing the fabrication process of perovskite solar cell and the final inverted device structure.

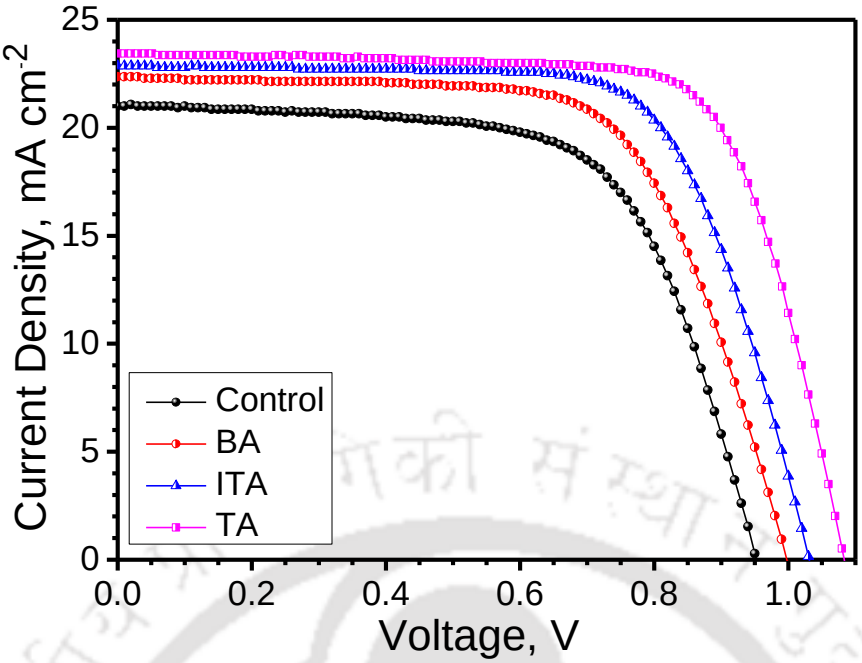

Figure 6.6: *J-V* curves of PSCs without and with optimum concentrations of BA, ITA and TA additive.

was found to increase for 1.6% and 3.2% addition due to improved perovskite film having large size grains, good crystallinity, and reduced trap states. However, the PCE reduced when it was added in excess. The highest PCE of 14.76% (average PCE of 13.90% for 40 cells) was recorded for BA with 3.2% addition. Similar improvements were observed when ITA and TA were added to the perovskite active layer. Highest PCEs of 16.39% and 18.08% were observed for ITA and TA-modified solar cells in their optimum concentrations, respectively (average PCEs of 40 cells for ITA was 15.39%, and for TA it was 17.22%). The best *J-V* curves for control device along with BA, ITA, and TA based

Table 6.1: Perovskite solar cell performance for control, BA, ITA and TA based devices.

Device	PCE, Best (Average)[a] (%)	FF (%)	*Voc* (mV)	*Jsc*, (mA cm^{-2}
Control	13.01 (12.16 ± 0.39)	65.0	952.6	21.00
BA	14.76 (13.90 ± 0.39)	66.2	997.7	22.36
ITA	16.39 (15.39 ± 0.40)	69.5	1031.1	22.86
TA	18.08 (17.22 ± 0.42)	72.6	1063.4	23.43

[a]Average of 40 devices

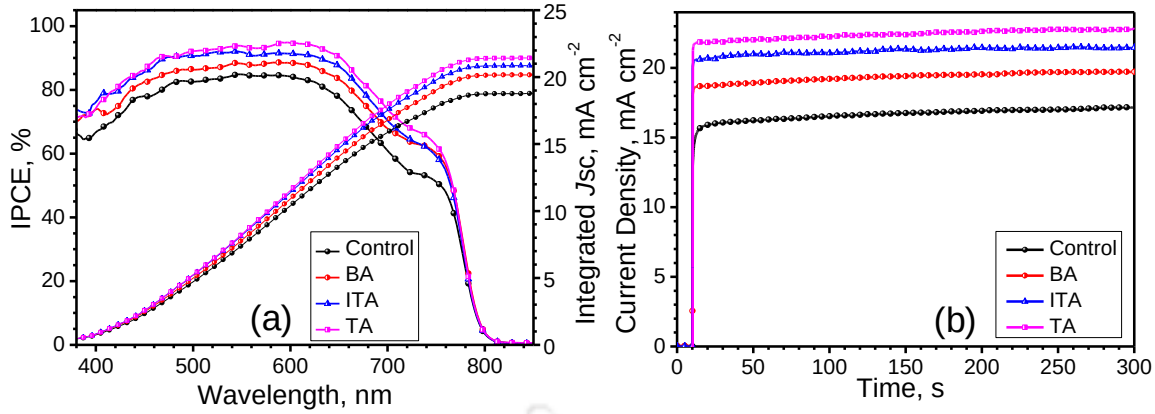

Figure 6.7: (a) IPCE curves and (b) steady state current measured at 0.75V for PSCs without and with optimum concentrations of BA, ITA and TA additive.

solar cells in their optimum concentrations are presented in Figure 6.6 and the corresponding photovoltaic data are listed in Table 6.1. It is evident that the improvement in PCE is mostly contributed from the increase in the value of *V*oc for all the three cases, and attributed to the reduced trap states. However, there is a slight enhancement in *J*sc and FF as well ascribed to improved grain size, crystallinity, and morphology of perovskite films. Figure 6.7(a) shows the IPCE spectra of control, ITA, and TA based devices. A wide response to incident photons was observed in the range of 400 to 800 nm. The higher IPCE of modified PSCs than the pristine one indicates that more photo-generated electrons are transferred to the electrodes. The higher IPCE of modified PSCs might be due to the presence of lower traps resulting in better charge transport and collection. Therefore, the addition of BA, ITA, and TA, through trap passivation, prevents the recombination of electrons. The *J*sc values obtained from IPCE spectra are consistent with those found in *J-V* curves. Moreover, steady-state current measurements were performed to validate the working condition of PSCs. All the devices show fast response time at a bias of 750 mV (Figure 6.7(b)). The currents observed for modified PSCs are more than the pristine $MAPbI_3$ and follow the same order as seen in *J*−*V* curves.

To further understand the variation and repeatability of the results related to device performance, box-chart for ten photovoltaic cells each with varying concentrations of BA, ITA, and TA, is presented in Figure D-3, Appendix D. Individually, it can be observed that the variation of PCE (≈1%) is almost similar to the control devices in low concentration for all the additives. However, when added in excess the variation of the PCE increases. To compare the photovoltaic parameters of all the additives in their optimum concentration,

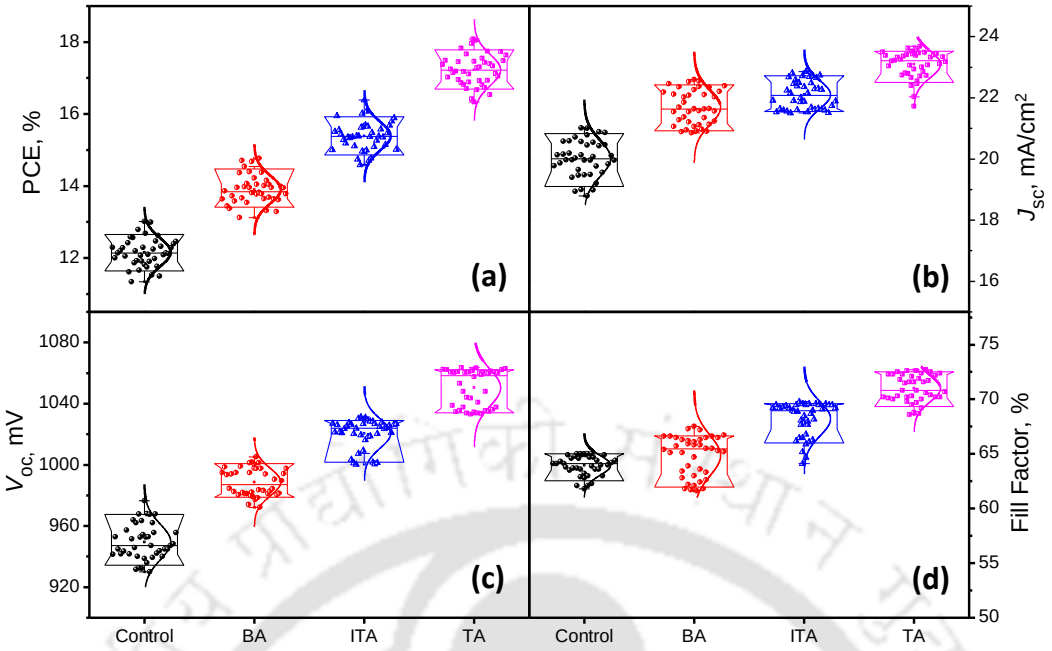

Figure 6.8: Box chart of 40 devices each of control, BA, ITA and TA: (a) PCE, (b) Jsc, (c) Voc and (d) fill factor.

box chart of the control device as well as BA, ITA and TA modified devices are presented in Figure 6.8. Though the variation in PCE is nearly similar, the deviation in *V*oc and *J*sc is found to be improved in case of all the modified devices. The variation of FF for BA and ITA modified devices is more, but the same has reduced for the TA-modified devices compared to that of the control devices. A histogram plot displaying the range of PCE and the corresponding number of devices is also presented in Figure D-4, Appendix D.

The UV-vis absorption spectra of the $MAPbI_3$ films were estimated to understand the effect of additives on absorption. As illustrated in Figure 6.9(a), there is no change in absorption beyond 550 nm wavelength. However, an enhancement in the absorption has been observed in the region of 400-550 nm wavelengths. TA based perovskite film exhibited the highest absorption among all. The improvement in the absorption might be ascribed to the improved morphology of perovskite film, having fewer grain boundaries and pinholes obtained with additives. Photoluminescence (PL) spectroscopy was used to explore the charge-carrier dynamics (Figure 6.9(b)). Perovskite film coated over glass substrate gave PL emission primarily due to exciton recombination inside the film. The enhancement in the PL intensity for perovskite films with BA, ITA and TA additives offers strong evidence that the non-radiative recombination has been suppressed due to reduced

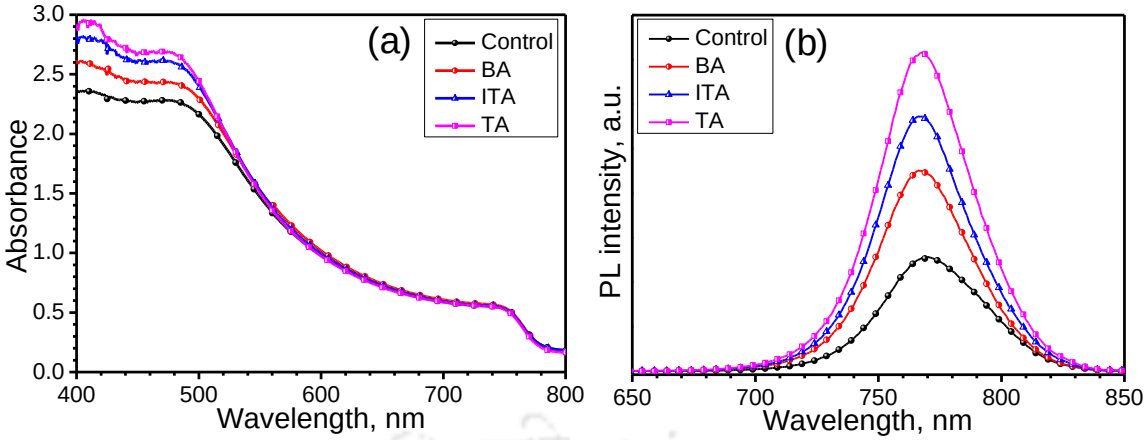

Figure 6.9: (a) UV-vis absorption spectra, (b) PL spectra of perovskite films prepared without and with optimum concentrations of BA, ITA and TA additive.

defect density. Moreover, a blue shift in the PL peaks was also observed from 770 nm to 766 nm, attributed to the trap passivation of the perovskite film surface induced by these additives through deep trap filling.[45]

To further confirm the trap passivation, EIS experiment was performed for the PSC without and with BA, ITA, TA additives. The experiments were executed at a bias voltage from 0.65-0.90 V and amplitude of 10 mV sinusoidal voltage in the frequency range of 1 Hz to 1 MHz under dark condition. The parameters like recombination resistance (R_{rec}), capacitance (C), and trap density of states (DOS) were estimated from the EIS data. A

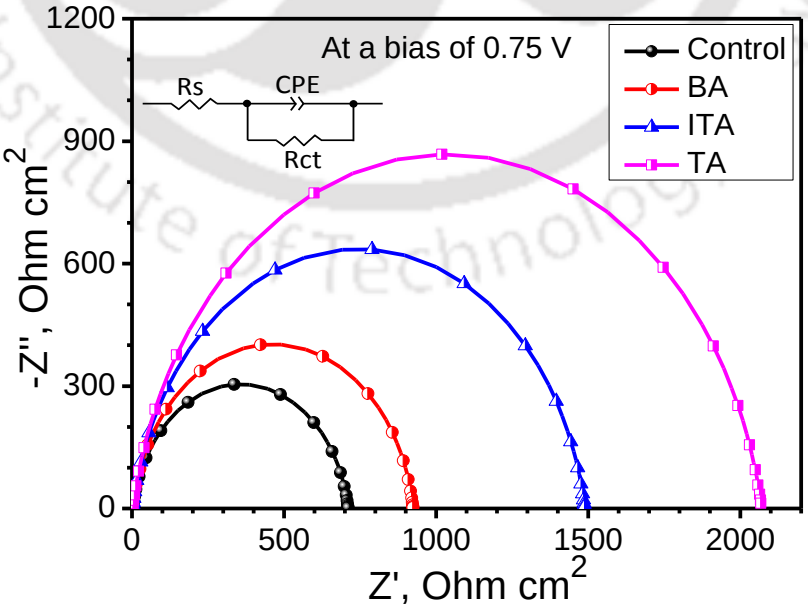

Figure 6.10: Nyquist plots obtained from impedance spectroscopy performed at 0.75V for PSCs without and with optimum concentrations of BA, ITA and TA additive.

semicircle was obtained in the Nyquist plots of PSCs (Figure 6.10), which is related to the R_{rec} at the interfaces of perovskite and charge transfer layers (HTL, ETL) as well as over the perovskite film. The R_{rec} values were obtained by fitting the EIS curves using an equivalent circuit (inset of Figure 6.10). The R_{rec} of modified devices is higher compared to the pristine one and increased in the order of pristine<BA<ITA<TA. Figure 6.11(a) represents variation of R_{rec} with bias voltage for control and TA based devices and follows a linear relation with *V*oc. The results show that the charge recombination was effectively controlled through defect passivation by using additives, facilitating the charge injection that resulted in increased V_{OC} as well as J_{SC}. The semi log plot of C as a function of voltage is illustrated in Figure 6.11(b). A relatively lower value of C, compared to the control device, was observed for TA based device. Further, the capacitance versus frequency curve (Figure 6.11(c)) was used to investigate the presence of traps in PSCs. The capacitance observed at the lower frequency region confirms the presence of traps in both the devices. The lower capacitance observed for TA based device compared to the control device indicates that the addition of TA can minimize electronic trap states.[46] The values of C

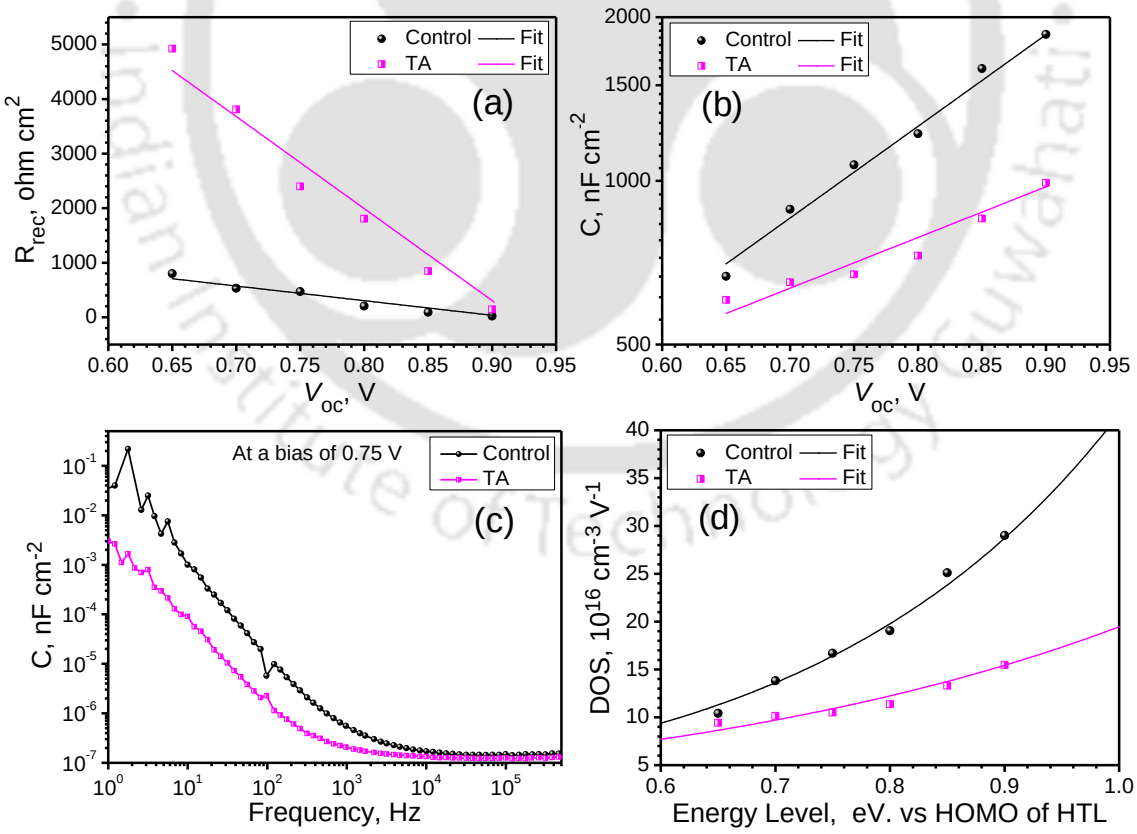

Figure 6.11: (a) Recombination resistance (R_{rec}) and (b) Capacitance (C) with varying bias, (c) Variation of C with frequency and (d) Trap density of states (DOS) versus electron energy level for control and TA based devices.

manifest the amount of charge carriers stored at the traps, interfaces and hence hold proportionality with the trap density of states (DOS).[36,47] Therefore, DOS values calculated from the capacitance versus voltage data are shown in Figure 6.11(d). The DOS values obtained in the order of 10^{16} $cm^{-3}V^{-1}$ match well with the reported literature and verifies the superior quality of perovskite film.[36] At a particular bias voltage, the relatively lower value of DOS for TA based PSC confirms trap passivation. The lower traps lead to higher performance of the PSCs.

The effectiveness of the trap state passivation can also be correlated from a substantial enhancement in the *V*oc after passivation. A distinctive improvement in the *V*oc (≈110 mV) has been achieved in this work, which is higher than the recent reports with NiOx as hole transport layer as illustrated in Figure 6.12 and Table 6.2. Therefore, the improved morphology led to the effective passivation of trap states resulting in improved *V*oc and hence ≈40% enhancement in the PCE with TA modification. This improvement in the performance of PSCs has become possible through utilization of increased concentration of –COOH group by additional substitution on the same aromatic core.

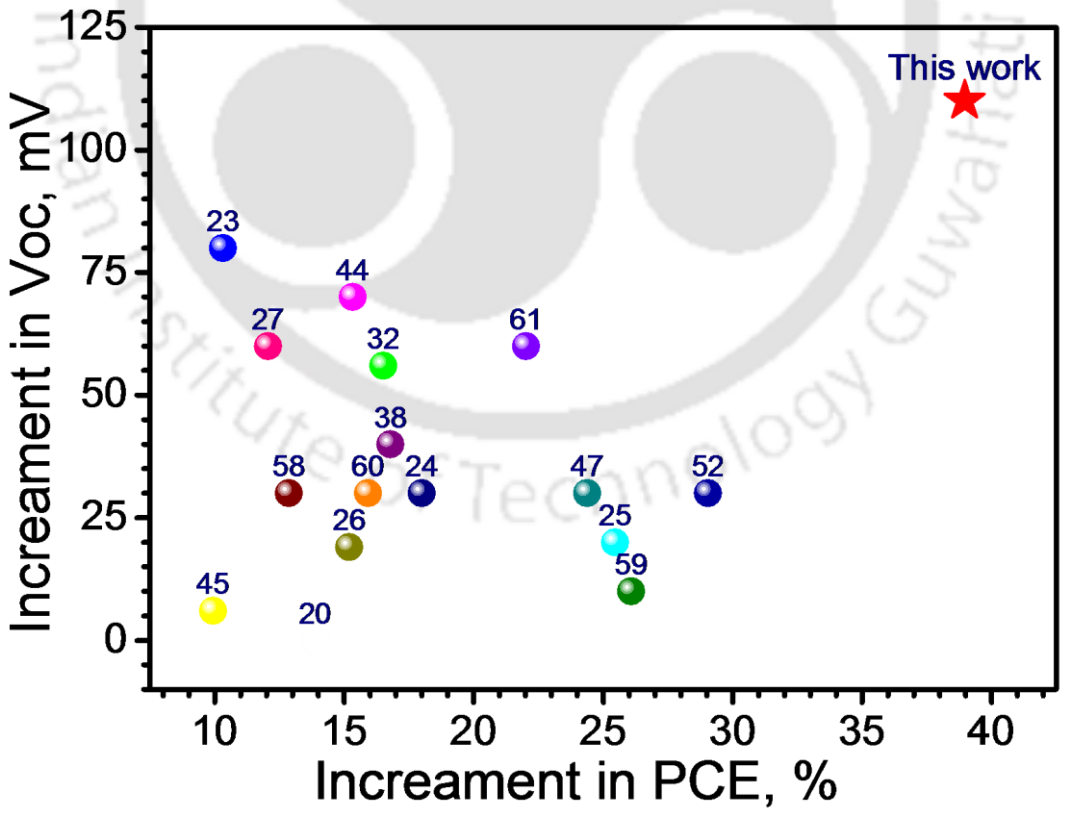

Figure 6.12: Summary of PCE and Voc improvement in representative report with NiOx hole transport layer (The number labels represent references).

Table 6.2: A comparison table of solar cell performance in this work with the recently reported literature having NiOx as hole transport layer.

Device configuration	Perovskite	PCE, % (*Voc*, V)		*Voc* increment, mV	Reference
		Control	Modified		
FTO/NiOx/Perovskite/PCBM/Rh101/Ag	$CH_3NH_3PbI_3$	13.01 (0.953)	18.08 (1.063)	110	This work
FTO/SnOx/Perovskite/spiro-OMeTAD/Ag	$CH_3NH_3PbI_3$	13.57 (1.018)	15.81 (1.074)	56	[22]
FTO/NiOx/Perovskite/PCBM/BCP/Ag	$CH_3NH_3PbI_3$	18.52 (1.066)	20.43 (1.146)	80	[13]
ITO/NiOx/Perovskite/PCBM/$Ca(acac)_2$/Ag	$CH_3NH_3PbI_3$	14.53 (1.02)	18.23 (1.04)	20	[15]
FTO/Li-NiOx/perovskite/PCBM/BCP/Ag	$CH_3NH_3PbI_3$	15.91 (1.05)	18.35 (1.12)	70	[34]
ITO/NiOx/Perovskite/PCBM/BCP/Ag	$CH_3NH_3PbI_3$	15.1 (1.054)	16.6 (1.060)	6	[35]
ITO/NiOx/Perovskite/PCBM/PTN-Br/Ag	$CH_3NH_3PbI_3$	15.14 (1.004)	17.44 (1.023)	19	[16]
ITO/NiOx/perovskite/PCBM/BCP/Ag	$Cs_{0.1}FA_{0.7}MA_{0.2}I_{3-x}Br_x$	15.01 (1.01)	17.41 (1.04)	30	[14]
ITO/NiOx/Perovskite/PCBM/BCP/Ag	$MAPbI_{3-x}Cl_x$	16.56 (1.08)	19.34 (1.12)	40	[28]
ITO/NiOx/Perovskite/C60/BCP/Ag	$CH3NH3PbI_{3-x}Cl_x$	17.81 (1.06)	20.10 (1.09)	30	[48]
FTO/NiOx/Perovskite/PCBM/PEI/Ag	$CH_3NH_3PbI_3$	14.26 (1.033)	17.98 (1.043)	10	[49]
ITO/NiOx/Perovskite/PCBM/BCP/Ag	$CH_3NH_3PbI_3$	14.35 (1.03)	17.85 (1.06)	30	[37]
ITO/NiOx/Perovskite/PCBM/BCP/Ag	$CH_3NH_3PbI_3$	15.11 (1.04)	19.50 (1.07)	30	[42]
ITO/NiOx/Perovskite/PCBM/BCP/Ag	$CH_3NH_3PbI_3$	15.70 (1.04)	18.2 (1.07)	30	[50]
FTO/NiOx/Perovskite/PCBM/PEI/Ag	$CH_3NH_3PbI_3$	15.44 (1.05)	18.84 (1.11)	60	[51]
ITO/NiOx//perovskite/PC61BM/BCP/Ag	$CH_3NH_3PbI_3$	16.92 (1.042)	18.96 (1.102)	60	[17]
FTO/NiOx/perovskite/PCBM/PEI/Ag	$CH_3NH_3PbI_3$	15.14 (1.02)	17.24 (1.02)	0	[10]

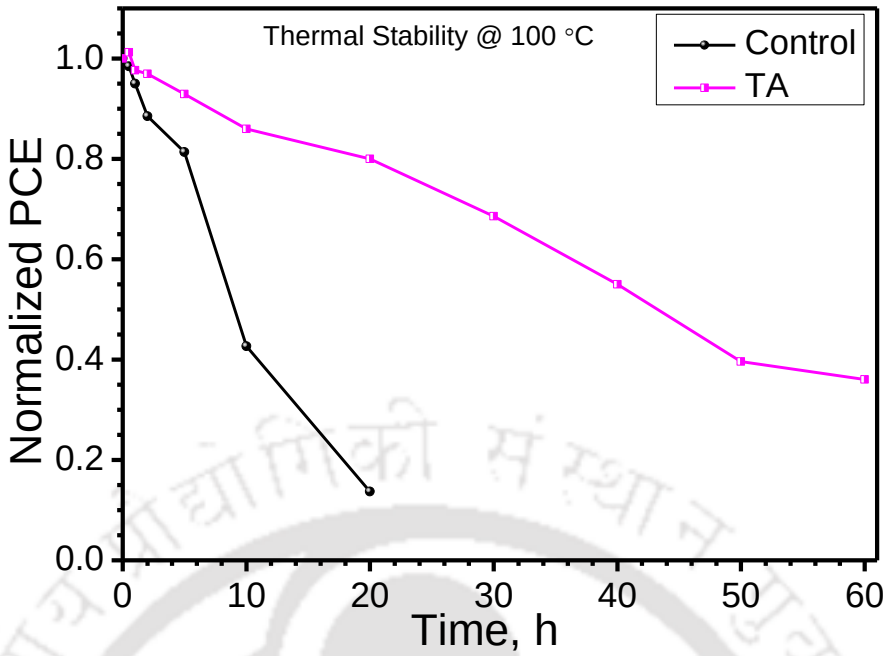

Figure 6.13: Thermal stability test of PSCs without and with TA modification.

The thermal stability test is an important characteristic for the PSCs, determining their applicability. Figure 6.13 shows the normalized PCE of PSCs without and with TA additive. The experiment was performed by heating the devices at 100 °C inside the glove box. The PCE of the pristine $MAPbI_3$ device retained only 13 % of its initial PCE after 20 h, whereas, the PCE of PSC with additive can retain ~80% under the same test conditions after 20 h and around 40% after 60 h. Therefore, it is clear that the carboxylic acid derivatives can prevent the decomposition of $MAPbI_3$ even at elevated temperatures by simultaneously improving the morphology and crystallinity of the perovskite film and effectively reducing the trap states.

6.3 Conclusions

In summary, an effective and simple strategy to passivate trap states simultaneously with morphology and crystallization control by utilizing three different benzene carboxylic acid derivatives (BA, ITA, and TA) was demonstrated. The synergistic effect of controlled crystal growth and defect passivation endowed the devices with multiple improvements viz. high-quality perovskite layer with large grains, good morphology, reduced traps and lower recombination. The influence of these acids depends on the number of –COOH groups present on them as well as the appropriate concentration of these passivation agents. It is also noteworthy that a higher concentration of –COOH group could be utilized by

substituting it on the aromatic core. The maximum PCE of 18.08% is the highest value obtained for PSC with an optimum concentration of TA (with three –COOH groups). This increase in the PCE is mainly attributed to substantial enhancement in *V*oc (≈110 mV increment), along with a rise in FF and *J*sc. Moreover, the device thermal stability also improved drastically with the addition of TA confirming the retention of morphology even at elevated temperature. It is established here that the presence of carboxylic acid groups was effective in achieving good morphology perovskite films with reduced trap states and ion migration. The reduction in the trap density has been successfully investigated from PL and EIS measurements. These investigations provide very useful insights for the strategic utilization of multi-functional small molecule additives to simultaneously passivate the defects and improve the morphology of perovskite films and retain at high temperature and have broad general applications.

6.4 Experimental Section

6.4.1 Materials

FTO glass substrates (13 Ω $\square^{-1}$), PbI_2 (99.8%), benzoic acid (99.5%), isophthalic acid (99%), trimesic acid (95%), rhodamine 101 inner salt and silver (99.99%, 1 mm wire) were acquired from Sigma-Aldrich. Methylammonium iodide (MAI) was purchased from GreatCell Solar. PCBM (99.5%) was purchased from Lumtec. Nickel nitrate hexahydrate ($Ni(NO_3)_2 \cdot 6H_2O$, 98%) and ethylene diamine (99%) were purchased from Merck. Ethylene glycol (98%) was received from Fisher Scientific. All the solvents (anhydrous) were purchased from different commercial sources and used without further purification.

6.4.2 Device Fabrication

NiO_x precursor solution was prepared by dissolving 1M Nickel nitrate hexahydrate and 1M Ethylenediamine in Ethylene Glycol. Then the NiO_x layer was spin coated as hole transporting layer on the pre-cleaned FTO at 3000 rpm for 40 sec and then baked at 300 °C for 60 min in ambient. The $MAPbI_3$ precursor solution was prepared in a glovebox by stirring MAI and PbI_2 (1:1 ratio) in a mixed solvent of γ-butyrolactone and DMSO (7:3, v/v) at 70 °C, where the concentration of Pb^{2+} was kept at 1.26 M. The solution was heated overnight and filtered with a 0.45 μm filter prior to spin coating. For the modified devices, different concentrations of additives (1.6, 3.2, 4.8 mol % of BA, 1.2, 2.4, 3.6 mol % of ITA or 0.9, 1.8, 2.7 mol % of TA) were incorporated into the precursor solution. In terms of –

COOH concentration, BA solution have 1.6, 3.2, 4.8 mol % –COOH, ITA solution have 2.4, 4.8, 7.2 mol % –COOH, and TA solution have 2.7, 5.4, 8.1 mol % –COOH. The filtered precursor solution was spin coated on the NiO_x coated FTO in a two-step program, i.e., 750 rpm for 20 sec followed by 4000 rpm for 60 sec. In the second step, 160 µL anhydrous toluene was dripped after 20 sec as anti-solvent, and the substrates were annealed at 80 °C for 10 min. Then, 12 mg mL^{-1} PCBM solution was coated at 1200 rpm as ETL and again annealed at 80 °C for 5 min. After that, a thin layer of rhodamine 101 inner salt (0.5 mg mL^{-1} in isopropanol) was spin coated at 4000 rpm. Finally, Ag was thermally deposited by using a shadow mask to yield an active area of 0.12 cm^2.

6.4.3 Characterization

The perovskite films were analyzed by UV-vis absorption spectroscopy (Perkin Elmer Lamda-35), FTIR spectroscopy (Perkin-Elmer-Spectrum), and fluorescence spectroscopy (HORIBA Jobin Yvon, fluoromax-4 with a 405 nm laser excitation). The XRD patterns of the samples were recorded using a Rigaku Micromax-007HF diffractometer equipped with Cu Kα irradiation (λ = 1.54184 Å). The perovskite film morphology was studied by scanning electron microscopy (SEM, JEOL JSM-7610F). A Keithley 2400 source meter was used to measure the current density−voltage (*J*−*V*) characteristic curves in an argon filled glove box by illuminating the device under a solar simulator (AM 1.5G, 100 mW cm^{-2}, Oriel Sol 3A solar simulator, Newport). The incident photon-to-current efficiency (IPCE) was obtained by using an Oriel IQE-200 instrument under ambient condition. Electrochemical measurements were performed with a CH Instrument 760D. The impedance spectroscopy was performed by applying a sinusoidal perturbation of 10 mV in the frequency range of 1 Hz–1 MHz under dark condition.

6.5 References

(1) de Quilettes, D. W.; Vorpahl, S. M.; Stranks, S. D.; Nagaoka, H.; Eperon, G. E.; Ziffer, M. E.; Snaith, H. J.; Ginger, D. S. *Science* **2015,** *348*, 683-686.

(2) Wetzelaer, G.-J. A. H.; Scheepers, M.; Sempere, A. M.; Momblona, C.; Ávila, J.; Bolink, H. J. *Adv. Mater.* **2015,** *27*, 1837-1841.

(3) Yang, J.; Liu, X.; Zhang, Y.; Zheng, X.; He, X.; Wang, H.; Yue, F.; Braun, S.; Chen, J.; Xu, J.; Li, Y.; Jin, Y.; Tang, J.; Duan, C.; Fahlman, M.; Bao, Q. *Nano Energy* **2018,** *54*, 218-226.

(4) Park, N.-G.; Grätzel, M.; Miyasaka, T.; Zhu, K.; Emery, K. *Nat. Energy* **2016,** *1*, 16152.

(5) Domanski, K.; Alharbi, E. A.; Hagfeldt, A.; Grätzel, M.; Tress, W. *Nat. Energy* **2018,** *3*, 61-67.

(6) Shi, D.; Adinolfi, V.; Comin, R.; Yuan, M.; Alarousu, E.; Buin, A.; Chen, Y.; Hoogland, S.; Rothenberger, A.; Katsiev, K.; Losovyj, Y.; Zhang, X.; Dowben, P. A.; Mohammed, O. F.; Sargent, E. H.; Bakr, O. M. *Science* **2015,** *347*, 519-522.

(7) Lee, J.-W.; Dai, Z.; Lee, C.; Lee, H. M.; Han, T.-H.; De Marco, N.; Lin, O.; Choi, C. S.; Dunn, B.; Koh, J.; Di Carlo, D.; Ko, J. H.; Maynard, H. D.; Yang, Y. *J. Am. Chem. Soc.* **2018,** *140*, 6317-6324.

(8) Li, X.; Bi, D.; Yi, C.; Décoppet, J.-D.; Luo, J.; Zakeeruddin, S. M.; Hagfeldt, A.; Grätzel, M. *Science* **2016,** *353*, 58-62.

(9) Chen, J.; Rong, Y.; Mei, A.; Xiong, Y.; Liu, T.; Sheng, Y.; Jiang, P.; Hong, L.; Guan, Y.; Zhu, X.; Hou, X.; Duan, M.; Zhao, J.; Li, X.; Han, H. *Adv. Energy Mater.* **2016,** *6*, 1502009.

(10) Liao, K.; Yang, J.-a.; Li, C.; Li, T.; Hao, F. *ACS Appl. Mater. Interfaces* **2019,** *11*, 39882-39889.

(11) Zhao, P.; Kim, B. J.; Ren, X.; Lee, D. G.; Bang, G. J.; Jeon, J. B.; Kim, W. B.; Jung, H. S. *Adv. Mater.* **2018,** *30*, 1802763.

(12) Xiao, M.; Huang, F.; Huang, W.; Dkhissi, Y.; Zhu, Y.; Etheridge, J.; Gray-Weale, A.; Bach, U.; Cheng, Y.-B.; Spiccia, L. *Angew. Chem., Int. Ed.* **2014,** *53*, 9898-9903.

(13) Wu, T.; Wang, Y.; Li, X.; Wu, Y.; Meng, X.; Cui, D.; Yang, X.; Han, L. *Adv. Energy Mater.* **2019,** *9*, 1803766.

(14) Fu, Q.; Xiao, S.; Tang, X.; Chen, Y.; Hu, T. *ACS Appl. Mater. Interfaces* **2019,** *11*, 24782-24788.

(15) Zhao, Z. Q.; You, S.; Huang, J.; Yuan, L.; Xiao, Z. Y.; Cao, Y.; Cheng, N.; Hu, L.; Liu, J. F.; Yu, B. H. *J. Mater. Chem. C* **2019,** *7*, 9735-9742.

(16) Tu, J.; Liu, C.; Fan, Y.; Liu, F.; Chang, K.; Xu, Z.; Li, Q.; Chen, Y.; Li, Z. *J. Mater. Chem. A* **2019,** *7*, 15662-15672.

(17) Wang, S.-Y.; Chen, C.-P.; Chung, C.-L.; Hsu, C.-W.; Hsu, H.-L.; Wu, T.-H.; Zhuang, J.-Y.; Chang, C.-J.; Chen, H. M.; Chang, Y. J. *ACS Appl. Mater. Interfaces* **2019,** *11*, 40050-40061.

(18) Gao, L.; Wang, L.; Ding, X.; Zhao, E.; Yang, S.; Zhao, Y.; Li, Y.; Wang, S.; Ma, T. *J. Mater. Chem. A* **2018,** *6*, 4365-4373.

(19) Zheng, H.; Zhu, L.; Hu, L.; Yang, S.; Chen, S.; Alsaedi, A.; Hayat, T.; Huang, Y.; Pan, X.; Dai, S. *J. Mater. Chem. A* **2018,** *6*, 9930-9937.

(20) Wu, Z.; Raga, S. R.; Juarez-Perez, E. J.; Yao, X.; Jiang, Y.; Ono, L. K.; Ning, Z.; Tian, H.; Qi, Y. *Adv. Mater.* **2018,** *30*, 1703670.

(21) Li, T.; Pan, Y.; Wang, Z.; Xia, Y.; Chen, Y.; Huang, W. *J. Mater. Chem. A* **2017,** *5*, 12602-12652.

(22) Guan, L.; Jiao, N.; Guo, Y. *J. Phys. Chem. C* **2019,** *123*, 14223-14228.

(23) Pan, J.; Mu, C.; Li, Q.; Li, W.; Ma, D.; Xu, D. *Adv. Mater.* **2016,** *28*, 8309-8314.

(24) Xie, F.; Chen, C.-C.; Wu, Y.; Li, X.; Cai, M.; Liu, X.; Yang, X.; Han, L. *Energy Environ. Sci.* **2017,** *10*, 1942-1949.

(25) Huang, J.; Wang, M.; Ding, L.; Yang, Z.; Zhang, K. *RSC Adv.* **2016,** *6*, 55720-55725.

(26) Zeng, Q.; Zhang, X.; Feng, X.; Lu, S.; Chen, Z.; Yong, X.; Redfern, S. A. T.; Wei, H.; Wang, H.; Shen, H.; Zhang, W.; Zheng, W.; Zhang, H.; Tse, J. S.; Yang, B. *Adv. Mater.* **2018,** *30*, 1705393.

(27) Niu, T.; Lu, J.; Munir, R.; Li, J.; Barrit, D.; Zhang, X.; Hu, H.; Yang, Z.; Amassian, A.; Zhao, K.; Liu, S. *Adv. Mater.* **2018,** *30*, 1706576.

(28) Zhang, F.; Guang, S.; Ye, M.; Xu, K.; Guo, W.; Liu, X.; Xu, H. *ACS Appl. Mater. Interfaces* **2018,** *10*, 36841-36850.

(29) Hadadian, M.; Correa-Baena, J.-P.; Goharshadi, E. K.; Ummadisingu, A.; Seo, J.-Y.; Luo, J.; Gholipour, S.; Zakeeruddin, S. M.; Saliba, M.; Abate, A.; Grätzel, M.; Hagfeldt, A. *Adv. Mater.* **2016,** *28*, 8681-8686.

(30) Zhang, X.; Wu, G.; Fu, W.; Qin, M.; Yang, W.; Yan, J.; Zhang, Z.; Lu, X.; Chen, H. *Adv. Energy Mater.* **2018,** *8*, 1702498.

(31) Han, Q.; Bai, Y.; Liu, J.; Du, K.-z.; Li, T.; Ji, D.; Zhou, Y.; Cao, C.; Shin, D.; Ding, J.; Franklin, A. D.; Glass, J. T.; Hu, J.; Therien, M. J.; Liu, J.; Mitzi, D. B. *Energy Environ. Sci.* **2017,** *10*, 2365-2371.

(32) Heo, J. H.; Song, D. H.; Han, H. J.; Kim, S. Y.; Kim, J. H.; Kim, D.; Shin, H. W.; Ahn, T. K.; Wolf, C.; Lee, T.-W.; Im, S. H. *Adv. Mater.* **2015,** *27*, 3424-3430.

(33) Zhang, W.; Pathak, S.; Sakai, N.; Stergiopoulos, T.; Nayak, P. K.; Noel, N. K.; Haghighirad, A. A.; Burlakov, V. M.; deQuilettes, D. W.; Sadhanala, A.; Li, W.; Wang, L.; Ginger, D. S.; Friend, R. H.; Snaith, H. J. *Nat. Commun.* **2015,** *6*, 10030.

(34) Guo, Y.; Ma, J.; Lei, H.; Yao, F.; Li, B.; Xiong, L.; Fang, G. *J. Mater. Chem. A* **2018,** *6*, 5919-5925.

(35) Liu, C.; Huang, Z.; Hu, X.; Meng, X.; Huang, L.; Xiong, J.; Tan, L.; Chen, Y. *ACS Appl. Mater. Interfaces* **2018,** *10*, 1909-1916.

(36) Zuo, L.; Guo, H.; deQuilettes, D. W.; Jariwala, S.; De Marco, N.; Dong, S.; DeBlock, R.; Ginger, D. S.; Dunn, B.; Wang, M.; Yang, Y. *Sci. Adv.* **2017,** *3*, 1700106.

(37) Yu, Y.-Y.; Tseng, C.; Chien, W.-C.; Hsu, H.-L.; Chen, C.-P. *J. Phys. Chem. C* **2019,** *123*, 23826-23833.

(38) Li, X.; Chen, C.-C.; Cai, M.; Hua, X.; Xie, F.; Liu, X.; Hua, J.; Long, Y.-T.; Tian, H.; Han, L. *Adv. Energy Mater.* **2018,** *8*, 1800715.

(39) Qin, P.-L.; Yang, G.; Ren, Z.-w.; Cheung, S. H.; So, S. K.; Chen, L.; Hao, J.; Hou, J.; Li, G. *Adv. Mater.* **2018,** *30*, 1706162.

(40) Wu, Y.; Xie, F.; Chen, H.; Yang, X.; Su, H.; Cai, M.; Zhou, Z.; Noda, T.; Han, L. *Adv. Mater.* **2017,** *29*, 1701073.

(41) Wang, P.; Jiang, Q.; Zhao, Y.; Chen, Y.; Chu, Z.; Zhang, X.; Zhou, Y.; You, J. *Sci. Bull.* **2018,** *63*, 726-731.

(42) Hsu, H.-L.; Hsiao, H.-T.; Juang, T.-Y.; Jiang, B.-H.; Chen, S.-C.; Jeng, R.-J.; Chen, C.-P. *Adv. Energy Mater.* **2018,** *8*, 1802323.

(43) Arivunithi, V. M.; Reddy, S. S.; Sree, V. G.; Park, H.-Y.; Park, J.; Kang, Y.-C.; Shin, E.-S.; Noh, Y.-Y.; Song, M.; Jin, S.-H. *Adv. Energy Mater.* **2018,** *8*, 1801637.

(44) Su, L.; Xiao, Y.; Han, G.; Lu, L.; Li, H.; Zhu, M. *J. Power Sources* **2019,** *426*, 11-15.

(45) Yang, J.; Xiong, S.; Qu, T.; Zhang, Y.; He, X.; Guo, X.; Zhao, Q.; Braun, S.; Chen, J.; Xu, J.; Li, Y.; Liu, X.; Duan, C.; Tang, J.; Fahlman, M.; Bao, Q. *ACS Appl. Mater. Interfaces* **2019,** *11*, 13491-13498.

(46) Meng, X.; Ho, C. H. Y.; Xiao, S.; Bai, Y.; Zhang, T.; Hu, C.; Lin, H.; Yang, Y.; So, S. K.; Yang, S. *Nano Energy* **2018,** *52*, 300-306.

(47) O'Regan, B. C.; Scully, S.; Mayer, A. C.; Palomares, E.; Durrant, J. *J. Phys. Chem. B* **2005,** *109*, 4616-4623.

(48) Cheng, J.; Zhang, H.; Zhang, S.; Ouyang, D.; Huang, Z.; Nazeeruddin, M. K.; Hou, J.; Choy, W. C. H. *J. Mater. Chem. A* **2018,** *6*, 23865-23874.

(49) Zhang, H.; Chen, H.; Stoumpos, C. C.; Ren, J.; Hou, Q.; Li, X.; Li, J.; He, H.; Lin, H.; Wang, J.; Hao, F.; Kanatzidis, M. G. *ACS Appl. Mater. Interfaces* **2018,** *10*, 42436-42443.

(50) Ma, Y.; Zhang, H.; Zhang, Y.; Hu, R.; Jiang, M.; Zhang, R.; Lv, H.; Tian, J.; Chu, L.; Zhang, J.; Xue, Q.; Yip, H.-L.; Xia, R.; Li, X. a.; Huang, W. *ACS Appl. Mater. Interfaces* **2019,** *11*, 3044-3052.

(51) Hsiao, K.-C.; Jao, M.-H.; Li, B.-T.; Lin, T.-H.; Liao, S. H.-C.; Wu, M.-C.; Su, W.-F. *ACS Appl. Energy Mater.* **2019,** *2*, 4821-4832.

Appendix D: Additional data for chapter 6

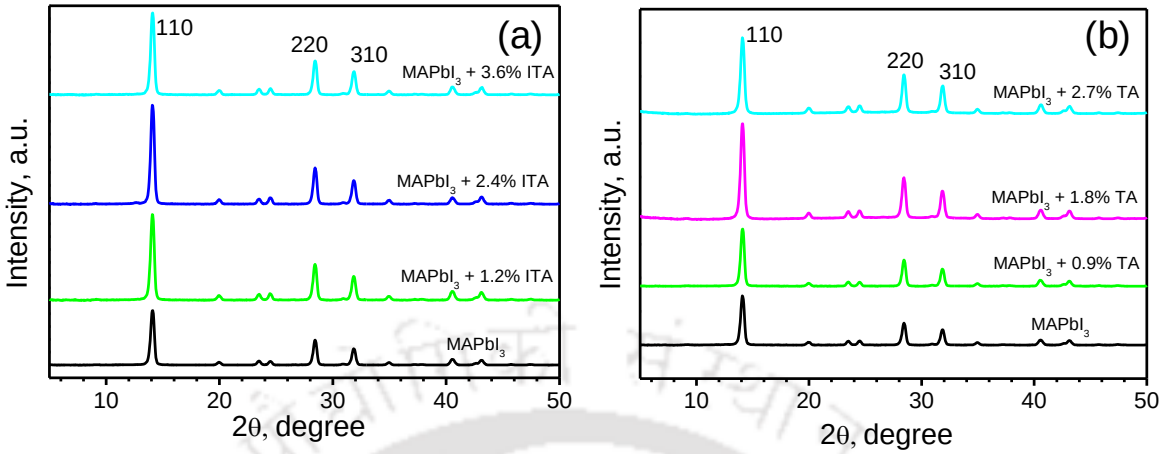

Figure D-1: XRD spectra of perovskite films prepared without and with different amount of (a) ITA additive and (b) TA additive.

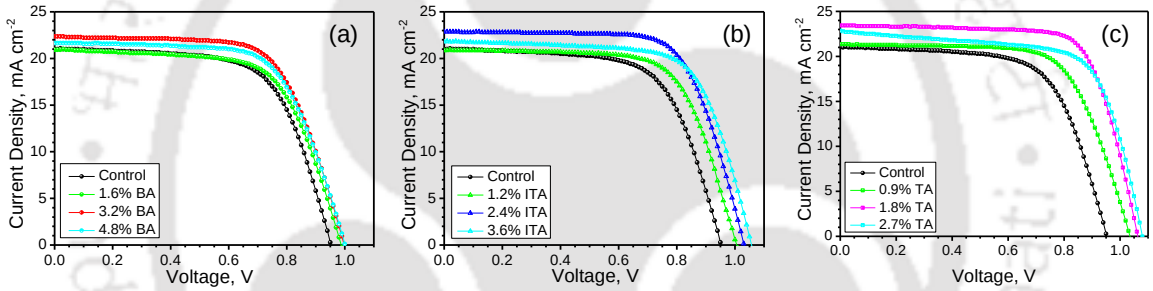

Figure D-2: *J-V* curves of PSCs without and with different concentration of (a) BA, (b) ITA and (c) TA additives.

Table D-1: Photovoltaic parameters of PSCs with different concentration of BA additive.

Device	PCE, Best (Average)[a] (%)	FF (%)	*Voc* (mV)	*Jsc*, (mA cm^{-2})
Control	13.01 (12.22 ± 0.41)	65.0	952.6	21.00
1.6% BA	13.48 (12.77 ± 0.42)	65.2	987.6	20.93
3.2% BA	14.76 (13.95 ± 0.40)	66.2	997.7	22.36
4.8% BA	14.27 (13.29 ± 0.62)	65.9	1001	21.64

[a]Average of 10 devices

Table D-2: Photovoltaic parameters of PSCs with different concentration of ITA additive.

Device	PCE, Best (Average)[a] (%)	FF (%)	*Voc* (mV)	*Jsc* (mA cm^{-2})
Control	13.01 (12.22 ± 0.41)	65.0	952.6	21.00
1.2% ITA	14.28 (13.57 ± 0.46)	68.0	1006.3	20.86
2.4% ITA	16.39 (15.46 ± 0.46)	69.5	1031.1	22.86
3.6% ITA	15.87 (14.48 ± 0.74)	68.9	1056.9	21.79

[a]Average of 10 devices

Table D-3: Photovoltaic parameters of PSCs with different concentration of TA additive.

Device	PCE, Best (Average)[a] (%)	FF (%)	*Voc* (mV)	*Jsc* (mA cm^{-2})
Control	13.01 (12.22 ± 0.41)	65.0	952.6	21.00
0.9% TA	14.91 (14.27 ± 0.44)	67.4	1035.5	21.36
1.8% TA	18.08 (17.29 ± 0.43)	72.6	1063.4	23.43
2.7% TA	16.81 (15.81 ± 0.62)	68.2	1079.9	22.86

[a]Average of 10 devices

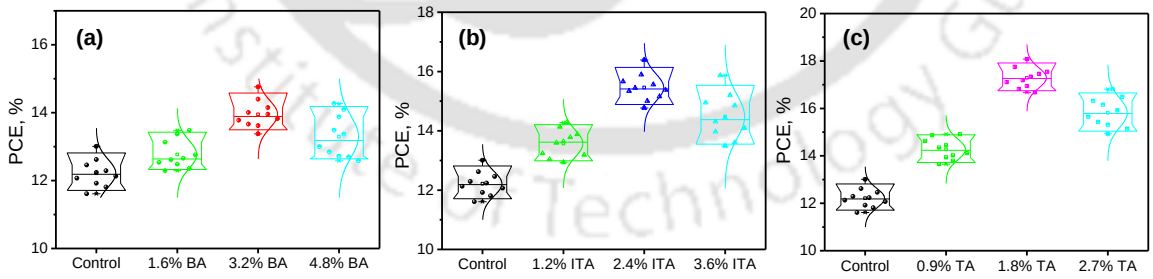

Figure D-3: Box chart of PCE for 10 devices of each concentration: (a) BA, (b) ITA and (c) TA additives.

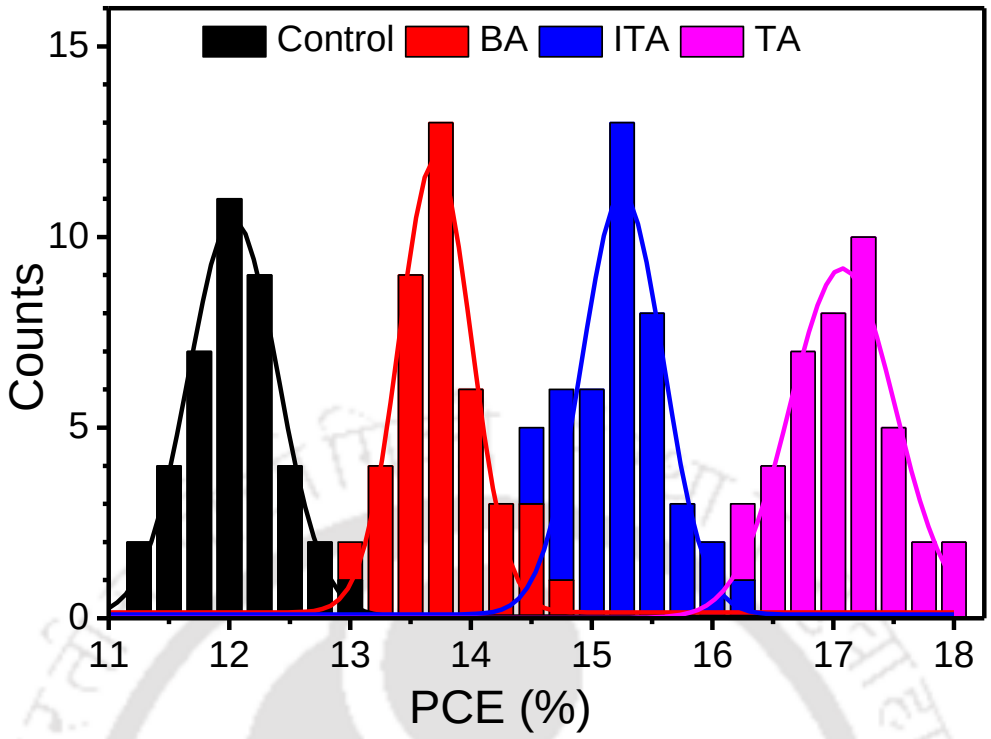

Figure D-4: Histogram of 40 devices each for control, BA, ITA and TA based devices.

CHAPTER 7

Conclusions and Prospects

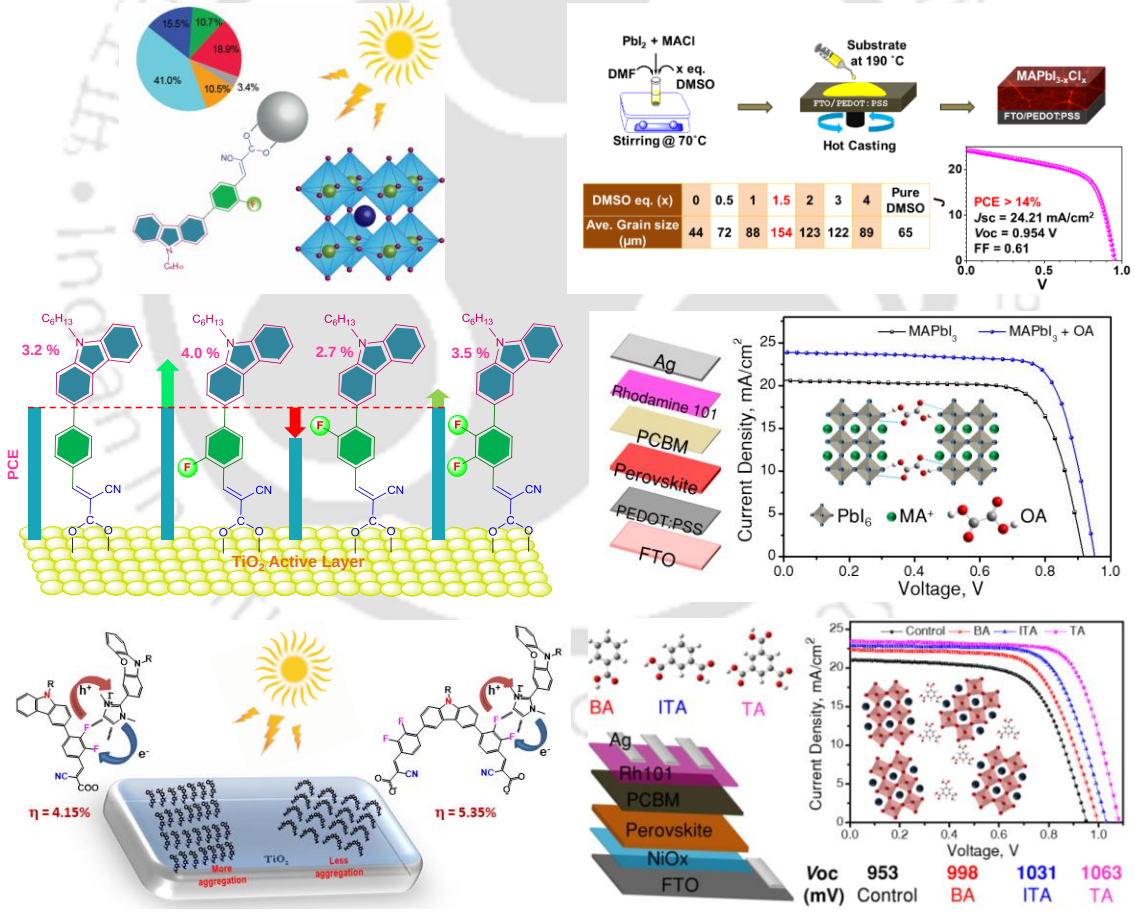

7.1 Conclusions

The increasing quest for clean energy is expected to raise the status of solar energy as the real competitor of fossil fuels to overcome the societal energy needs. Dye sensitized and perovskite solar cells have become one of the most promising photovoltaics that has led the third-generation photovoltaic technologies. This thesis focused to overcome the limitations of dye sensitized solar cells and discuss the structure property relationship of metal-free organic photosensitizer dye in the first part. Later, attempt was made to study crystallization and trap states in perovskite films to improve the performance and stability of perovskite solar cells mainly through additive engineering.

The first chapter of this thesis discussed the need for energy, a brief history of dye sensitized and perovskite solar cells development, their device structure and working principle including different components. Then different techniques used for the measurement of solar cell performance is explained. Finally, rules to engineering photosensitizer dye and perovskite is presented.

In the second chapter, effect of fluorine substitution and position on phenylene spacer in carbazole based organic sensitizers for dye sensitized solar cells was examined. A detailed study of optoelectronic property and solar cell performance is offered with respect to the structure property relationship of dyes.

The third chapter dealt with the dye aggregation over the photoanode through molecular design. The effect of mono- and di-anchoring dyes based on *o,m*-difluoro substituted phenylene spacer in liquid and solid state dye sensitized solar cells was described in this chapter. The molecular properties of the newly synthesized dyes are discussed and correlated with the photovoltaic performance for both liquid as well as solid state dye sensitized solar cells. Finally, carrier transport and interfacial charge recombination in the solar cell devices has been unveiled.

Chapter four demonstrated crystallization and grain growth regulation through Lewis acid-base adduct formation in hot cast perovskite-based solar cells. An insight on the crystallization process of perovskite film along with requirements to achieve large grains and good crystallinity has been provided. The effect of Lewis base concentration in the perovskite precursor solution on the solar cell performance had been studied.

Chapter five described use of oxalic acid with bifacial carboxylic acid group for crystallization control of perovskite films. Oxalic acid modulated the crystallization

process to enable enlargement of grains and minimize the grain boundaries. The detailed study on how oxalic acid controls the perovskite formation along with device performance and stability has been given.

Finally, chapter six elucidated the effect of benzene carboxylic acid derivatives in the passivation of perovskite film. These organic molecules with carboxylic acid group are effective in achieving good morphology perovskite films with reduced trap states and ion migration. The strategy to utilize additives for realizing simultaneous passivation of the defects and improvement of perovskite films morphology had been explained.

7.2 Prospects

Extensive studies on DSSCs have been carried out to solve many issues, such as absorption ability, light scattering, interfacial contacts and reactions, associated with them. Different methods developed to improve the performance of DSSCs comprise development of new photosensitizers with tuned properties, preparation of nanocomposites and development of state-of-the-art nanostructures for photoanode. These approaches have made significant advancement in the field of DSSCs. Still, several challenges remain to further improve the efficiency, stability and to scale up the fabrication.

With regard to photosensitizers, a large number of metal-free organic dyes have been developed with tuned properties which suits n-type DSSCs. But very less effort has been made to develop dyes for p-type DSSCs. Further progress in dyes with broad absorption spectra and a high extinction coefficient, appropriate for p-type DSSC, can also help in improving the efficiency. With the advancement of p-type DSSC, a boost in the growth of efficient tandem solid state DSSCs can be achieved.

In terms of perovskite solar cells, tremendous progress has been made on all fronts so far, but the question still knocking is how far is it from commercialization success? For further developments, the following strategies and challenges could be considered.

Further improvements in PCE can be achieved by identifying the recombination processes, both in bulk as well as at interfaces, and through trap passivation. It can be believed that further understanding of the perovskite composition in structure evolution and its distribution may lead to improvement in the PCE by curtailing recombination and increasing *V*oc and FF.

The stability of perovskite solar cells becomes more important for the purpose of commercialization than pushing the PCE higher. The stability of perovskite materials can be improved in two ways; (i) by increasing the intrinsic structural stability of perovskite material, and (ii) by increasing the environmental stability through improvement in the bonding/interaction of the cations (MA+, FA+) with the lead halide. A perovskite with ideal cubic structure is required for better structural stability. Formation of such cubic perovskite structures geometrically involves tolerance factor τ between 0.97 and 0.99, such as, the triple cation $(Cs/FA/MA)Pb(I/Br)_3$, perovskite. The solution processed perovskite fabrication results in many defects and strains in the film. Fabrication of polycrystalline perovskite films without strain in crystal structure and with desired crystals orientation along more air-stable crystal facets is anticipated to raise the intrinsic stability of films and hence the solar cells significantly.

It has been identified that weak interaction organic molecular ions with the inorganic sub-lattice is accountable for the thermal degradation of perovskites. Therefore, the thermal stability of perovskites can be further enhanced by developing strategies to strengthen the interaction between organic cations and the inorganic part. The poor stability against humidity are being controlled by the use of large size cation to form 2D/3D mixed perovskites. A deeper study to further understand the interaction of the large cations with the inorganic sub-lattice (PbI_6^{4-}) are required. Finally, investigation and development of other materials used in the fabrication of perovskites (HTL, ETL etc.) and for sealing/encapsulation should establish a significant step towards overall long-term stability.

Toxicity of lead poses a potential threat to commercialization of Pb-based perovskite photovoltaics. Although, tin (Sn)-based perovskites have shown the possibility to be used in solar cells, their stability is far behind the Pb perovskites. Some additives such as SnF_2, $SnCl_2$, H_3PO_2 have been found to enhance the stability of Sn perovskites. Further exploration to understand Sn perovskites might lead to improvement in the performance and stability of these Pb-free PSCs further.

In summary, the work presented in this thesis demonstrates the strategies to design metal-free organic dyes for high performance and stability. It also shows the approaches to prepare high quality organic-inorganic perovskite films with large grains, less grain boundaries, a smaller number of pinholes, and minimized trap states. These strategies were designed with the aim to improve the performances as well as stability of solar cells. I

believe that the developments presented in this thesis will motivate future researchers to contribute towards highly efficient and stable perovskite solar cells.

Mohammad Adil Afroz

m.afroz@iitg.ac.in/afroz.madil@gmail.com
CHEL304, Department of Chemistry
Indian Institute of Technology Guwahati
Guwahati-781039, Assam, India
+91 8011 024 014

EDUCATION

Indian Institute of Technology Guwahati — Guwahati, Assam
- PhD in Chemistry — Expected July 2020

Indian Institute of Technology Delhi — New Delhi, Delhi
- M Tech Polymer Science and Technology, CGPA **7.9**/10 — 2013

Aligarh Muslim University — Aligarh, Uttar Pradesh
- MSc Industrial Chemistry, **75.2%** — 2011
- BSc (Hons) Industrial Chemistry, **72.7%** — 2009

RESEARCH EXPERIENCE

Indian Institute of Technology Guwahati — Guwahati, Assam
Graduate student (Doctoral) with Prof. Parameswar K Iyer — 2013- present
- Crystallization and Grain Growth Regulation through Lewis Acid-Base Adduct Formation in Hot Cast Perovskite-based Solar Cells. Passivation of perovskites layer using different additives in the precursor solution.
- Investigating the effect of fluorine substituted spacer in carbazole based organic dyes on their optical, electrochemical and photovoltaic properties
- Exploring different solvents for halogen-free solvent processing of P3HT:PCBM based bulk heterojunction solar cells

South Dakota State University — Brookings, South Dakota
Short term Researcher with Prof. Qiquan Qiao — April- September 2018
- Performance and stability enhancement in perovskite solar cell through bulk passivation

Indian Institute of Technology Delhi — New Delhi, Delhi
Graduate student (Master's) with Dr. Josemon Jacob — 2012- 2013
- Poly(N-vinylimidazole) and its quaternary ammonium salts (polymeric ionic liquids) were synthesized and characterized. Effect of iodine doping on their thermal properties were analyzed

University of Madras, National Centre for Ultrafast Processes — Chennai, Tamil Nadu
Summer Research Fellow with Prof. Perumal Ramamurthy — May-July 2010
- Investigation on Proton-Coupled Electron Transfer in Pyridine Linked Acridinedione Derivatives were carried out

TECHNICAL SKILLS/ TEACHING EXPERIENCE

Indian Institute of Technology Guwahati Guwahati, Assam

Central Instrument Facility
- Authorized operator of Field Emission Electron Microscope (FESEM) — 2014- 2018

Department of Chemistry

- Guided Two summer projects — May-July 2017
- Guided Two master's projects — 2015-2016, 2014-2015
- Guided Six undergraduate projects — 2016-2017, 2015-2016, 2014-2015
- Teaching Assistant, undergraduate Laboratory work — July- November 2014

RESEARCH INTEREST

- Perovskite Solar Cells
- Bulk Heterojunction Solar Cells
- Dye Sensitized Solar Cells
- Chemical Sensors
- Perovskite LEDs

PUBLICATIONS

1. **Afroz, M. A.**; Garai, R.; Gupta, R. K.; Iyer, P. K. Benzene Carboxylic Acid Derivative Assisted Passivation of Perovskites for Stable and High-Performance Inverted Perovskite Solar Cells (submitted).
2. **Afroz, M. A.**; Ghimire, N.; Reza, K. M.; Bahrami, B.; Bobba, R. S.; Gurung, A.; Chowdhury, A. H.; Iyer, P. K.; Qiao, Q. Thermal Stability and Performance Enhancement of Perovskite Solar Cells Through Oxalic Acid-Induced Perovskite Formation. *ACS Appl. Energy Mater*. **2020**, *3* (3), 2432–2439. DOI: https://doi.org/10.1021/acsaem.9b02111.
3. Gupta, R. K.; Garai, R.; **Afroz, M. A.**; Iyer, P. K. Regulating Active Layer Thickness and Morphology for High Performance Hot-casted Polymer Solar Cells. DOI: https://doi.org/10.1039/D0TC00822B.
4. Garai, R.; **Afroz, M. A.**; Gupta, R. K.; Choudhury, A.; Iyer, P. K. High-performance Ambient-Condition-Processed Polymer Solar Cells and Organic Thin-Film Transistors. *ACS Omega* **2020**, 5 (6), 2747–2754. DOI: https://doi.org/10.1021/acsomega.9b03347.
5. Zehra, N.; Kalita, A.; Malik, A. H.; Barman, U.; **Afroz, M. A.**; Iyer, P. K. Conjugated Polymer-Based Electrical Sensor for Ultra-trace Vapor Phase Detection of Nerve Agent Mimics. *ACS Sens*. **2020**, *5* (1), 191-198. DOI: https://doi.org/10.1021/acssensors.9b02031.
6. Raju, T. B.[1]; Vaghasiya, J. V. [1]; **Afroz, M. A. [1]**; Soni, S. S.; Iyer, P. K. Effect of mono- and di-anchoring dyes based on o,m-difluoro substituted phenylene spacer in liquid and solid state dye sensitized solar cells. *Dyes Pigm.* **2019**, 108021, DOI: https://doi.org/10.1016/j.dyepig.2019.108021.
7. **Afroz, M. A.**; Gupta, R. K.; Garai, R.; Hossain, M.; Tripathi, S. P.; Iyer, P. K. Crystallization and grain growth regulation through Lewis acid-base adduct formation in hot cast perovskite-based solar cells. *Org. Electron.* **2019,** *74*, 172-178, DOI: https://doi.org/10.1016/j.orgel.2019.07.007.
8. Ratha, R.; Singh, A.; **Afroz, M. A.**; Gupta, R. K.; Baumgarten, M.; Müllen, K.; Iyer, P. K. 6,7-Di(thiophen-2-yl)naphtho[2,3-c][1,2,5]thiadiazole and 4,6,7,9-tetra (thiophen-2-yl)naphtho[2,3-c][1,2,5]thiadiazole as new acceptor units for D-A type co-polymer for polymer solar cells. *Synth. Met.* **2019,** *252*, 113-121, DOI: https://doi.org/10.1016/j.synthmet.2019.04.013.
9. Ratha, R.; **Afroz, M. A.**; Gupta, R. K.; Iyer, P. K. Functionalizing benzothiadiazole with non-conjugating ester groups as side chains in a donor–acceptor polymer improves

solar cell performance. *New J. Chem.* **2019,** *43* (10), 4242-4252, DOI: 10.1039/C8NJ05850D.

10. Tanwar, A. S.; Adil, L. R.; **Afroz, M. A.**; Iyer, P. K. Inner Filter Effect and Resonance Energy Transfer Based Attogram Level Detection of Nitroexplosive Picric Acid Using Dual Emitting Cationic Conjugated Polyfluorene. *ACS Sens.* **2018,** *3* (8), 1451-1461, DOI: 10.1021/acssensors.8b00093.
11. Sharma, B.; Singh, A.; **Afroz, M. A.**; Iyer, P. K.; Jacob, J. Direct arylation polymerization approach for the synthesis of narrow band gap cyclopentadithiophene based conjugated polymer and its application in solar cell devices. *Synth. Met.* **2017,** *226*, 56-61, DOI: 10.1016/j.synthmet.2017.02.002.
12. Raju, T. B.; Vaghasiya, J. V.; **Afroz, M. A.**; Soni, S. S.; Iyer, P. K. Twisted donor substituted simple thiophene dyes retard the dye aggregation and charge recombination in dye-sensitized solar cells. *Org. Electron.* **2017,** *50*, 25-32, DOI: 10.1016/j.orgel.2017.07.019.
13. **Afroz, M. A.**; Sonigara, K. K.; Raju, T. B.; Soni, S. S.; Iyer, P. K. Effect of fluorine substitution and position on phenylene spacer in carbazole based organic sensitizers for dye sensitized solar cells. *Phys. Chem. Chem. Phys.* **2017,** *19* (42), 28579-28587, DOI: 10.1039/c7cp05226j.
14. Tanwar, A. S.; Hussain, S.; Malik, A. H.; **Afroz, M. A.**; Iyer, P. K. Inner Filter Effect Based Selective Detection of Nitroexplosive-Picric Acid in Aqueous Solution and Solid Support Using Conjugated Polymer. *ACS Sens.* **2016,** *1* (8), 1070-1077, DOI: 10.1021/acssensors.6b00441.
15. Raju, T. S.; Vaghasiya, J. V.; **Afroz, M. A.**; Soni, S. S.; Iyer, P. K. Influence of m-fluorine substituted phenylene spacer dyes in dye-sensitized solar cells. *Org. Electron.* **2016,** *39*, 371-379, DOI: 10.1016/j.orgel.2016.10.024.
16. Raju, T. B.; Vaghasiya, J. V.; **Afroz, M. A.**; Soni, S. S.; Iyer, P. K. Design, synthesis and DSSC performance of o-fluorine substituted phenylene spacer sensitizers: effect of TiO_2 thickness variation. *Phys. Chem. Chem. Phys.* **2016,** *18* (41), 28485-28491, DOI: 10.1039/c6cp05641e.
17. Hussain, S.; Malik, A. H.; **Afroz, M. A.**; Iyer, P. K. Ultrasensitive detection of nitroexplosive - picric acid via a conjugated polyelectrolyte in aqueous media and solid support. *Chem. Commun.* **2015,** *51* (33), 7207-7210, DOI: 10.1039/c5cc02194d.

FELLOWSHIPS AND AWARDS

- Bhaskara Advance Solar Energy Fellowship, Indo-US science and technology forum and DST, Government of India, April- September 2018
- Junior and Senior Research Fellowship, Ministry of Human Resource Development, Government of India, 2013-2018
- Institute Best Poster Award, Research Conclave '16, IIT Guwahati, Guwahati, Assam, March 2016
- Departmental Best Poster Award, Research Conclave '16, IIT Guwahati, Guwahati, Assam, March 2016
- M Tech Assistantship, Ministry of Human Resource Development, Government of India, 2011-2013
- Summer Research Fellowship, jointly by Indian Academy of Sciences (IAS), Indian National Science Academy (INSA) and National Academy of Sciences (NASI), India, May- July 2010

CONFERENCES/SYMPOSIUMS/WORKSHOPS

1. "Carboxylic acid functionalized small molecule assisted passivation of perovskites for stable and high-performance inverted perovskite solar cells" given oral talk at the 6th International Conference on Advanced Nanomaterials and Nanotechnology, Centre for Nanotechnology, IIT Guwahati, Guwahati, Assam, December 18-21, 2019
2. Attended six days "short course on Flexible Electronics" organized jointly by Samtel Centre for Display Technology, IIT Kanpur and Ministry of Electronics & Information Technology (MeitY) Govt. of India, Kanpur, UP, July 3-8, 2017
3. "Design, synthesis and DSSC performance of o-fluorine substituted phenylene spacer sensitizers: effect of TiO_2 thickness variation" presented poster at the 20th CRSI National Symposium in Chemistry, Department of Chemistry, Gauhati University, Guwahati, Assam, February 3-5, 2017
4. Attended the full agenda of ACS on Campus, IIT Guwahati, Guwahati, Assam, January 16, 2017
5. Attended FICS 2016, Department of Chemistry, IIT Guwahati, Guwahati, Assam, December 8-10, 2016
6. Participated in 2nd National Workshop on NEMS/MEMS and Theranostics Devices, Centre for Nanotechnology, IIT Guwahati, Guwahati, Assam, March 21-22, 2016
7. "Ultrasensitive Detection of Nitro Explosive–Picric Acid via Conjugated Polyelectrolyte in Aqueous Media and Solid Support" presented poster at the Research Conclave'16, IIT Guwahati, Guwahati, Assam, March 17-20, 2016
8. Participated in 68th Annual Session of Indian Institute of Chemical Engineers, CHEMCON 2015, IIT Guwahati, Guwahati, Assam, December 27-30, 2015
9. Attended 4th International Conference on Advanced Nanomaterials and Nanotechnology, Centre for Nanotechnology, IIT Guwahati, Guwahati, Assam, December 8-11, 2015
10. Participated in 2–Day Familiarization Workshop on Nanofabrication Technologies, Tezpur University, Tezpur, Assam, April 25-26, 2015
11. Attended 3rd International Conference on Advanced Nanomaterials and Nanotechnology, Centre for Nanotechnology, IIT Guwahati, Guwahati, Assam, December 1-3, 2013
12. Participated in workshop on Sensors and its Applications, Institute of Advanced Study in Science & Technology (IASST), Guwahati, Assam, November 15, 2013
13. Attended International Conference on Chemistry: Frontiers and Challenges, Department of Chemistry, AMU, Aligarh, Uttar Pradesh, March 5-6, 2011

-----End-----